

Kenzo Hiraoka *Editor*

Fundamentals of Mass Spectrometry

 Springer

Fundamentals of Mass Spectrometry

Kenzo Hiraoka
Editor

Fundamentals of Mass Spectrometry

 Springer

Editor
Kenzo Hiraoka
Clean Energy Research Center
University of Yamanashi
Kofu, Japan

ISBN 978-1-4614-7232-2 ISBN 978-1-4614-7233-9 (eBook)
DOI 10.1007/978-1-4614-7233-9
Springer New York Heidelberg Dordrecht London

Library of Congress Control Number: 2013940059

© Springer Science+Business Media New York 2013

This work is subject to copyright. All rights are reserved by the Publisher, whether the whole or part of the material is concerned, specifically the rights of translation, reprinting, reuse of illustrations, recitation, broadcasting, reproduction on microfilms or in any other physical way, and transmission or information storage and retrieval, electronic adaptation, computer software, or by similar or dissimilar methodology now known or hereafter developed. Exempted from this legal reservation are brief excerpts in connection with reviews or scholarly analysis or material supplied specifically for the purpose of being entered and executed on a computer system, for exclusive use by the purchaser of the work. Duplication of this publication or parts thereof is permitted only under the provisions of the Copyright Law of the Publisher's location, in its current version, and permission for use must always be obtained from Springer. Permissions for use may be obtained through RightsLink at the Copyright Clearance Center. Violations are liable to prosecution under the respective Copyright Law.

The use of general descriptive names, registered names, trademarks, service marks, etc. in this publication does not imply, even in the absence of a specific statement, that such names are exempt from the relevant protective laws and regulations and therefore free for general use.

While the advice and information in this book are believed to be true and accurate at the date of publication, neither the authors nor the editors nor the publisher can accept any legal responsibility for any errors or omissions that may be made. The publisher makes no warranty, express or implied, with respect to the material contained herein.

Printed on acid-free paper

Springer is part of Springer Science+Business Media (www.springer.com)

Preface

Mass spectrometry has progressed remarkably in the last half century. In the history of liquid chromatography mass spectrometry (LC-MS), for example, liquid flowing out from an LC column was vaporized and gaseous analytes were ionized by a dc corona discharge (APCI: [1]); the analytes in vaporized LC effluent were concentrated by a jet separator and ionized by electron ionization [2]; sample solutions were simply sprayed through the heated capillary into vacuum and analytes were ionized [3]; LC effluent was nebulized by helium gas into vacuum. The dried sample particulates accelerated by jet expansion collided with the heated wall leading to the collision-induced desorption of analytes that were ionized by electron ionization or chemical ionization (Particle beam: [4]). In 1979, [5] achieved a significant milestone in the history of mass spectrometry; they coupled a high electric field with liquid nebulization. This method can be regarded as an early-stage pneumatically assisted electrospray. Electrospray ionization [6] and matrix-assisted laser desorption ionization (MALDI) [7] triggered the explosive development of mass spectrometry.

Mass spectrometers of various kinds (e.g., quadrupole, time of flight, ion trap, Fourier-transform, and Orbitrap) have been the subject of marvelous improvements these days and this situation accentuates the importance of mass spectrometry as the indispensable analytical method in modern science and technology. Needless to say, mass spectrometry is an integrated science; it is based on physics, quantum mechanics, thermodynamics, physical chemistry, photochemistry, electromagnetism, instrumentation, and so on. Unfortunately, however, because mass spectrometry is nowadays widely applied in many fields as one of the most important analytical tools, there is less chance to learn about its fundamentals, and the aim of this book is to fill in this knowledge gap.

In this book, the fundamentals of mass spectrometry are explained in detail. We are confident that this book will be an excellent guide for students and researchers who are engaged in mass spectrometry and related fields because it provides answers to the question what is going on in the “black box” of highly sophisticated mass spectrometers. In addition, the fundamental knowledge is indispensable for creating new concepts for ionization

and instrumentation in order to be able to contribute to the next generation mass spectrometry. This book will be extremely useful for satisfying these future demands.

The editor (K.H.) would like to appreciate Dr. K. Howell of Springer USA for his patient encouragement in publishing this book.

Kofu, Japan

Kenzo Hiraoka

References

1. Carroll DI, Dzidic I, Stillwell RN, Haegele KD, Horning EC (1974) *Anal Chem* 47:2369
2. Takeuchi T, Hirata Y, Okumura Y (1978) *Anal Chem* 50:659
3. Blakley CR, Carmody JJ, Vestal ML (1980) *J Am Chem Soc* 102:5931
4. Willoughby RC, Browner RF (1984) *Anal Chem* 56:2625
5. Iribarne JV, Thomson BA (1976) *J Chem Phys* 64:2287
6. Yamashita M, Fenn JB (1984) *J Phys Chem* 88:4451, 4671
7. Tanaka K, Waki H, Ido Y, Akita S, Yoshida Y, Yoshida T (1988) *Rapid Commun Mass Spectrom* 2:151

Contents

1	Collision Theory: Basic Explanation for Collisions in Mass Spectrometry	1
	Shigeo Hayakawa	
2	Unimolecular Dissociations in Mass Spectrometry	29
	Toshihide Nishimura	
3	Fundamental Aspects of the Photoionization of Molecules	55
	Kenichiro Tanaka and Inosuke Koyano	
4	Chemical Reactions Induced by Core Electron Excitations ...	61
	Shin-ichi Wada and Kenichiro Tanaka	
5	Superexcited States of Molecules	81
	Noriyuki Kouchi	
6	Ion Mobility Spectrometry with Mass Spectrometry	89
	Toshiki Sugai	
7	Gas-Phase Ion/Molecule Reactions	109
	Kenzo Hiraoka	
8	Fundamentals of Electrospray	145
	Kenzo Hiraoka	
9	MALDI: A Very Useful UV Light-Induced Process... That Still Remains Quite Obscure	173
	Rosa Erra-Balsells	
10	Cluster SIMS	199
	Kenzo Hiraoka	
	Index	231

Collision Theory: Basic Explanation for Collisions in Mass Spectrometry

1

Shigeo Hayakawa

1.1 Introduction

Recent developments in mass spectrometry have had far-reaching effects not only on physical and chemical studies of gaseous molecules and ions but also on biological studies, including proteomics and metabolomics. In mass spectrometry, collisions are very important elementary processes in ionization, collision-induced dissociation, and mobility, whose methods are useful for the development of proteomics and metabolomics. In this chapter, to understand the basis of collision, the concepts of center-of-mass system, laboratory system, cross section, kinetic energy release, and impact parameter are explained. The cross sections, which provide the magnitude of elementary reactions, depend on reaction species, collision energies, and reaction processes. I present these dependences with the support of various examples.

1.2 Collisions in Mass Spectrometry

In mass spectrometry, molecular collisions are closely related to such phenomena as ionization and collision dissociation. A molecular collision depends heavily on the type of reaction and its behavior varies widely depending on whether it involves electrons, ions, or neutral elements. Moreover, differences also appear in the reaction depending on internal energy and collision energy. Several books have been published on collisions related to mass spectrometry; detailed discussions can be found in *Metastable Ion* [1], *Collision Spectroscopy* [2], *Mass Spectrometry/Mass Spectrometry* [3], and *Molecular Reaction Dynamics* [4]. This chapter explains the basics of collision theory focusing on the collision between electrons or ions and molecules, which bears the closest relation with mass spectrometry, and explains the meanings of values so that readers can evaluate such values by themselves.

S. Hayakawa (✉)

Department of Chemistry, Graduate School of Science, Osaka Prefecture University,
1-1, Gakuen-cho, Nakaku, Sakai, Osaka, Japan
e-mail: hayakawa@c.s.osakafu-u.ac.jp

Collision theory relates to reactions among electrons, atoms, molecules, ions, and the like. The following equation must be solved from the viewpoint of quantum mechanics. In particular, the wave function $\Psi(\mathbf{R}, t)$ of a collision must be a function of time (t):

$$\hat{H} \Psi(\mathbf{R}, t) = \left(\sum_j \frac{\hbar^2}{2m_j} \nabla_j^2 + V(\mathbf{R}(t)) \right) \Psi(\mathbf{R}, t) = i\hbar \frac{\partial}{\partial t} \Psi(\mathbf{R}, t), \quad (1.1)$$

where, \hat{H} denotes the Hamiltonian that corresponds to the sum of kinetic and potential energies, j designates every particle regardless of whether an electron or atomic nucleus, m_j is the mass of the respective particle, and the vector \mathbf{R} is a variable that includes all positions. Since a collision is not in the steady state, it is difficult to obtain a rigorous solution of (1.1) for the multiparticle system corresponding to the collision of atoms and molecules. De Broglie's material wave is given by:

$$\lambda = \frac{h}{p} = \frac{h}{mv}. \quad (1.2)$$

The matter wave wavelength of an electron with energy of 100 eV is 1.2×10^{-10} m and that of a hydrogen atom with energy of 1 keV is 9.1×10^{-13} m. For this reason, provided that we do not consider collisions between electrons or those involving extremely small energy, collisions handled by mass spectrometry involving ions and heavy particles show a matter wave behavior only for short wavelengths. Therefore it is certain that they exhibit a classical behavior until the atomic order of magnitude of 1×10^{-10} m. Since collisions handled by mass spectrometry fit these conditions, we can describe them in terms of classical motion.

1.3 Laboratory (Lab) System and Center-of-Mass (CM) System

A collision is a process in which two particles interact with each other. By transforming the Lab (laboratory) system into a CM (center-of-mass) system, the collision can be described in terms of the center of mass of a single particle, i.e., in a central force field. The Lab system is a system used by the experimenter for measurement, and the CM system is a system that considers only the interactions between particles. In a two-body collision, there is no interaction other than the one between the two colliding particles, and therefore the total momentum and total energy of the two particles are conserved. To illustrate the relation between Lab and CM systems, Fig. 1.1a describes a collision in terms of momentum vectors, while Fig. 1.1b does so in terms of velocity vectors. In the Lab system, velocity is denoted by \mathbf{V} , while in the CM system it is denoted by \mathbf{v} . As shown in Fig. 1.1a, if a particle

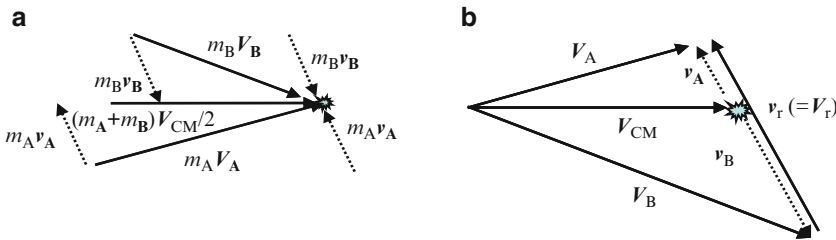


Fig. 1.1 Relation between momentum (a) and velocity (b) in a laboratory (Lab) and center-of-mass (CM) system

with mass m_A and velocity V_A collides with a particle with mass m_B and velocity V_B , V_{CM} is given by the following equation:

$$V_{CM} = \frac{(m_A V_A + m_B V_B)}{(m_A + m_B)}. \quad (1.3)$$

From the principle of conservation of momentum, V_{CM} is conserved before and after the collision, and therefore in the CM system the total momentum is 0. The relative velocity v_r between the two particles before the collision does not differ in the Lab and CM systems. Using the reduced mass $\mu = (m_A m_B)/(m_A + m_B)$, the velocities v_A of particle A and v_B of particle B are given respectively by (1.4a) and (1.4b):

$$v_A = V_A - V_{CM} = \frac{m_B(V_A - V_B)}{(m_A + m_B)} = \frac{\mu}{m_A} v_r. \quad (1.4a)$$

$$v_B = -\frac{\mu}{m_B} v_r. \quad (1.4b)$$

In the CM system, the momenta of the two particles have the same value and opposite directions. The velocities differ due to their different masses, being inversely proportional to their respective masses, pointing in mutually opposite directions. This relates to the fact that the total momentum in the CM system is 0. The energy in the CM system $E_{(CM)}$ is obtained as the sum of the kinetic energies of the two particles:

$$E_{(CM)} = \frac{1}{2} m_A v_A^2 + \frac{1}{2} m_B v_B^2 = \frac{m_A}{2} \left(\frac{\mu}{m_A} v_r \right)^2 + \frac{m_B}{2} \left(\frac{\mu}{m_B} v_r \right)^2 = \frac{1}{2} \mu v_r^2. \quad (1.5)$$

The energy $E_{(CM)}$ of the CM system expressed by (1.5) corresponds to the amount of energy that may be transformed into internal energy; only this energy can cause ionization or dissociation.

This idea can be applied to a collision of energy 70 eV between a molecule of mass $m_{Tar} = 100 u$ and an electron of mass $m_e = 5.5 \times 10^{-4} u$. We can consider the molecule to be still, with a motion approximately equivalent to its thermal energy (0.03 eV). In this case, the energy of the CM system is given by:

$$\begin{aligned} E_{(CM)} &= \frac{1}{2} \mu v_r^2 = \frac{1}{2} \mu V_r^2 = \frac{m_T}{m_e + m_T} \frac{1}{2} m_e V_r^2 = \frac{m_T}{m_e + m_T} E_{Total} \\ &= \frac{100}{5.5 \times 10^{-4} + 100} 70 \approx 70 \text{ (eV)}. \end{aligned} \quad (1.6)$$

Thus, the collision energy is $E_{(CM)} = 70$ eV, which is almost the same as in the Lab system. This result indicates that in collisions involving particles that are extremely light compared to their targets such as in electron ionization, almost the whole kinetic energy is converted into the collision energy of a CM system.

For incident ions with momentum 5 keV and mass ($m_{Inc} = 1,000 u$) colliding with He ($m_{Tar} = 4 u$) inside a collision chamber, the collision energy in a CM system is obtained by:

$$E_{(CM)} = \frac{1}{2} \mu v_r^2 = \frac{4 u}{4 u + 1,000 u} \frac{1}{2} (1,000 u) V_r^2 = \frac{4}{4 + 1,000} \times 5,000 \text{ (eV)} = 20 \text{ eV}. \quad (1.7)$$

The collision energy in the CM system is 20 eV, which corresponds to 0.4 % of 5 keV in the Lab system. Even if the collision energy is the same in a Lab system, if the target used is Xe, which has a mass of approximately 130 u , the collision energy in the CM system becomes 58 eV, which is about three times larger than that using a He target. This indicates that the probability of activation/dissociation due to collision may increase.

In low-energy collisions of the order of 5 eV such as those used in ion trap equipment, if the mass of the incident ions is 1,000 u and the targets are He atoms, the largest excitation energy in a single collision will be 0.02 eV. In order to dissociate a normal molecule with a binding energy of the order of 5 eV, multiple collisions would be necessary. In a collision-excited reaction, since it is almost impossible for all the collision energy to be converted into excitation energy, an even larger number of collisions are necessary. On the other hand, by reducing the collision energy to a level below the excitation energy, it is possible to practically stop the occurrence of internal excitation of ion species, resulting in smaller kinetic energy. This can be used for converging the kinetic energy of ions in mobility experiments.

1.4 Kinetic Energy Release

When an ion with mass M , velocity V_{Lab} , and kinetic energy E_{Lab} in a Lab system spontaneously dissociates itself into fragments of masses m and $M - m$, the total kinetic energy $E_{(\text{CM})}$ of the two particles in the CM system is called Kinetic Energy Release (KER). The opposite reaction to the dissociation is a combination of two colliding particles in the collision of the previous section, with the entire kinetic energy in the CM system being converted into internal energy. The collision-driven dissociation in mass spectrometry can be regarded as an extremely fast excitation process combined with spontaneous dissociation. One of the excited particles releases part of its internal energy as kinetic energy and dissociates itself into two fragments, as shown in Fig. 1.2. The relation between relative velocity and energy in a CM system is given by (1.5). Therefore, if we replace the relative velocity v_r by v'_r and $E_{(\text{CM})}$ by KER in (1.5), the velocity v'_r of the fragment in the CM system will be given by:

$$v'_r = \sqrt{\frac{2 \text{KER}}{\mu}} = \sqrt{\frac{2M \text{KER}}{m(M-m)}}, \quad (1.8)$$

where, m and M correspond respectively to m_A and $m_A + m_B$ in (1.5).

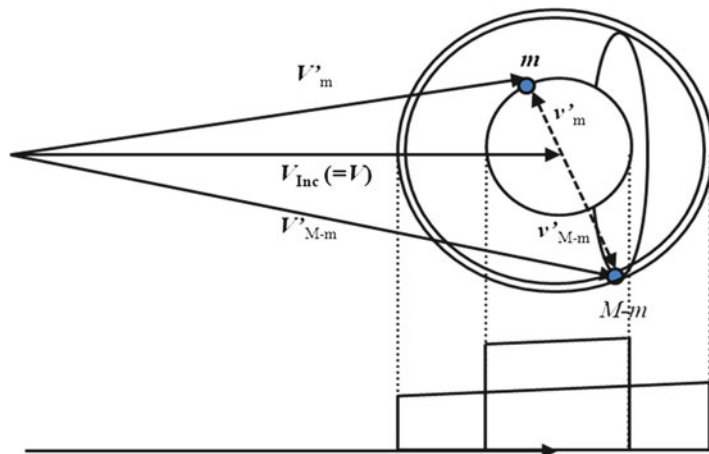


Fig. 1.2 Peak velocity distribution due to kinetic energy release

In a spontaneous dissociation with constant KER, the distribution shows equal probabilities through all directions of the CM system. Therefore, the distribution of fragments in a Lab system can be obtained by integrating the dissociated sphere. As shown in Fig. 1.2, the distribution of velocities forms a slightly high rectangle in the direction of movement, and so does the distribution of energies.

The Lab system energy range ΔE_{Lab} corresponding to the largest peak width can be expressed as follows, as a first-order approximation:

$$\Delta E_{\text{Lab}} = 2 \left(\frac{4m(M-m)E_{\text{Lab}} \text{KER}}{M^2} \right)^{(1/2)}. \quad (1.9)$$

If the kinetic energy of fragments is analyzed using an electrostatic energy analyzer or the like, the mass width d is related to the Lab-system energy range ΔE_{Lab} as follows:

$$d = \frac{\Delta E_{\text{Lab}}}{E_{\text{Lab}}} M. \quad (1.10)$$

By solving (1.9) and (1.10) for KER, KER can be obtained from mass width d as follows:

$$\text{KER} = \frac{E_{\text{Inc}}}{16m(M-m)} d^2. \quad (1.11)$$

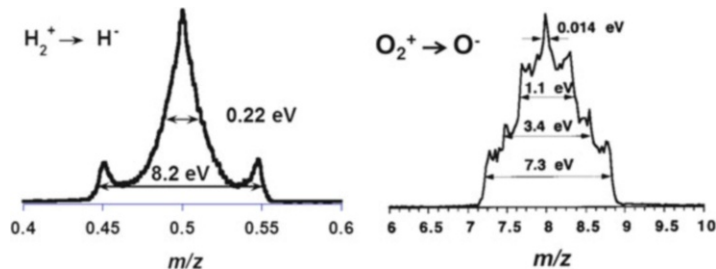
The actual KER can be calculated using the following equation [5], considering the mass width d_0 of ion peaks of the incident particles:

$$\text{KER} = \frac{E_{\text{Inc}}}{16m(M-m)} \left(d^2 - \left(\frac{m}{M} d_0 \right)^2 \right). \quad (1.12)$$

Consider an ion with kinetic energy 5 keV and mass 100 u dissociating into fragments of masses 90 and 10 u at KER 5 eV. According to (1.9), the kinetic energy variation of the ion with mass 90 u in a Lab system is approximately 190 eV. This difference is considerably larger than 5 eV, which is the KER of a CM system. The reason for such amplification is that velocity is expressed as a vectorial quantity and corresponds to the square root of energy. In concrete terms, the square root of 0.1 % is approximately 3 %. The amplification of the KER value is obtained by measurements performed in a Lab system. Even when the kinetic energy release is extremely small, it can be obtained from the width of the dissociation spectrum peak in a Lab system.

Figure 1.3 shows an enlarged illustration of dissociation peaks of the electron transfer dissociation spectrum measured using a single-magnetic-field charge inversion mass spectrometer [6, 7]. Figure 1.3a, b are respectively detected as H^- and O^- ions that result from electron transfer between H and O with alkali metals. These, in turn, result from dissociation of excited H_2 and O_2 , which are generated by electron transfer between H_2^+ and O_2^+ and alkali metal targets. As shown in this figure, even in the case of dissociation of ions with the same mass into fragments of equal mass, different KER dissociation processes can be identified due to differences in peak width. Figure 1.3a shows the overlap of a central triangular peak and a peak with a large central concave broadening, and Fig. 1.3b represents the overlap of four types of peaks. If all peaks showing expanded KER are detected, they become rectangular. However, if they have a large KER, a broadening occurs in the vertical direction in addition to the direction of movement. Fragments with considerable broadening in the vertical

Fig. 1.3 Enlarged illustration of dissociation peak measured using charge inversion mass spectrometry in a single magnetic field. The values in the figure represent kinetic energy release



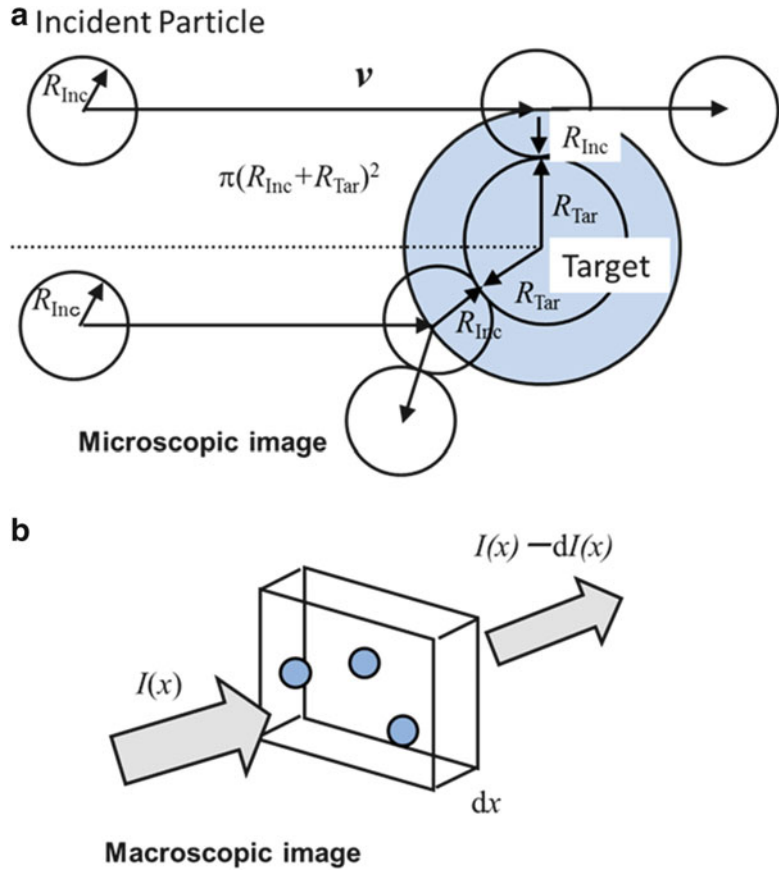
direction often do not reach the detector. In that case, the peak with large KER exhibits a concavity in the central region called “dishing” such as the one with an 8.2 eV in Fig. 1.3a. A large visual difference exists between the apparent mass width and the KER value shown in the figure. This is because KER is proportional to the square of the mass width d as expressed by (1.11), which must be obtained accurately in order to obtain the KER value. The actual value of KER shows variations and may also suffer the effect of dishing. The KER value with the highest probability is usually calculated by obtaining the mass width for half the peak height (Full Width at Half Maximum: FWHM). The triangular peak in the center of Fig. 1.3a represents the overlap of peaks with a broadening of KER values. For narrow peaks which have a small KER value, it is necessary to calculate KER using (1.12), which considers the broadening of the incident ions, in order to reduce errors.

1.5 Collision Cross Section

Reactions in mass spectrometry occur due to interactions among electrons, atoms, molecules, and ions, and the value per unit area used to evaluate the scale of the interaction is the collision cross section. The problem of scattering at the atomic and molecular level is a phenomenon that must be understood in the framework of quantum theory. However, in order to understand the concept of collision cross section, we first consider collisions between hard balls of rigid spheres with no wave characteristics such as in the case of billiard balls. Let us first consider a collision with velocity v occurring between an incident particle (Inc) with radius R_{Inc} and a target particle (Tar) with radius R_{Tar} , as shown in Fig. 1.4a. A collision occurs if the incident particle approaches the target closer than $R_{\text{Inc}} + R_{\text{Tar}}$, but if it passes at a larger distance, it just continues its motion without interaction. It is possible to state that a collision occurs when the distance between the particles equals the sum of their radii $R_{\text{Inc}} + R_{\text{Tar}}$. Looking from the direction of movement of the incident particle, collision occurs within the area of radius $R_{\text{Inc}} + R_{\text{Tar}}$. Therefore, the collision cross section is $\pi(R_{\text{Inc}} + R_{\text{Tar}})^2$. Since the collision also causes a change in the direction of movement, it is also called scattering cross section. If the collision is considered in this classical framework, the cross section remains constant regardless of the collision velocity v . However, if the particles exhibit wave properties such as in the case of atoms and electrons, it is no longer possible to assume fixed sizes for incident and target particles. Nevertheless, changes in the direction of movement can be observed due to interactions, and therefore the concept of collision cross section has the same classical meaning. The scattering cross section can be experimentally obtained by measuring the reduction of incident particles traveling at a constant velocity in a collision chamber, with constant density.

A schematic diagram for a macroscopic image is shown in Fig. 1.4b. As shown in the figure, consider the beam strength $I(x)$ expressed as a function of distance x traveled inside a collision

Fig. 1.4 Schematic diagram of the measurement of scattering cross section



chamber of length L in the direction of movement. The reduction in strength $-dI(x)$ of the incident beam for a displacement dx is proportional to the strength $I(x)$ of the beam, the density of targets D , and distance dx . $D dx$ corresponds to density times distance and expresses the number of targets in a narrow region dx along the direction of movement. The small circles of Fig. 1.4b correspond to $\pi(R_{Inc} + R_{Tar})^2$ in Fig. 1.4a. An incident beam that enters the circle changes direction and is scattered. The rate of numerical change $dI(x)/I(x)$ in the incident beam represents the region where scattering occurs, and is obtained as the product of the area where the incident beam collides with a single target (collision cross section σ [$\text{m}^2 \text{U}^{-1}$]) by $D dx$ [m^{-2}], according to:

$$\frac{dI(x)}{I(x)} = -\sigma D dx. \quad (1.13)$$

If (1.13) is integrated from $x = 0$ until length L of the collision chamber, the ratio of particles that are not scattered to the number of incident particles is given by:

$$\frac{I_{OUT}}{I_{IN}} = \exp(-\sigma LD). \quad (1.14)$$

The scattering cross section σ is obtained by:

$$\sigma = -\frac{\log_e(I_{OUT}/I_{IN})}{LD} = \frac{\log_e(I_{IN}/I_{OUT})}{LD}, \quad (1.15)$$

where, given L , which is the length of the collision chamber, and D , which is the density of targets, if we can measure the strength of the incident beam I_{IN} and that of the output beam I_{OUT} , it is possible to obtain the scattering cross section σ . It is difficult to experimentally change the length of the collision chamber, but the scattering cross section can be obtained by changing the density of targets and measuring the amount of change of ion strength reduction I_{OUT}/I_{IN} , even if the absolute value of the beam strength is not known.

For a collision chamber with length 1.0×10^{-2} m at 25 °C and 1.0 Pa pressure (approximately $1/10^5$ of atmospheric pressure) where the incident particles are reduced by 10 %, we have $\log_e(I_{IN}/I_{OUT}) = 0.105$. The density D of targets is obtained using the following equation of state for ideal gases:

$$D(\text{m}^{-3}) = \frac{N_A P}{RT} = \frac{6.022 \times 10^{23} (\text{mol}^{-1}) \times 1.0 (\text{Pa})}{8.3145 (\text{J K}^{-1} \text{mol}^{-1}) \times 298.15 (\text{K}^{-1})} = 2.423 \times 10^{20} \text{m}^{-3}. \quad (1.16)$$

If these values are substituted into (1.15), the scattering cross section is obtained as:

$$\sigma = \frac{\log_e(I_{IN}/I_{OUT})}{LD} = \frac{0.105}{0.01 (\text{m}) \times 2.423 \times 10^{20} (\text{m}^{-3})} = 4.34 \times 10^{-20} (\text{m}^2). \quad (1.17)$$

If the molecule radius is equal to the Bohr radius ($a_0 = 5.29 \times 10^{-11}$ m), the area seen from one direction ($\pi(2a_0)^2$) is 8.8×10^{-21} m². Considering that the diameter of the molecule is slightly larger than twice the Bohr radius, we can conclude that the scattering cross section is approximately 10^{-20} m². In fact, in many cases the scattering cross section is of the order of 10^{-20} m².

If $\sigma L D$ is small, (1.14) can be approximated by:

$$\frac{I_{OUT}}{I_{IN}} = 1 + (-\sigma LD) + \frac{1}{2!}(-\sigma LD)^2 + \dots \approx 1 - (\sigma LD) + \frac{1}{2}(\sigma LD)^2. \quad (1.18)$$

In experimental conditions where $\sigma L D$ is small, I_{OUT}/I_{IN} is linearly proportional to D , but when $\sigma L D$ is slightly larger, a large number of collisions occur.

If the collision cross section is 3×10^{-20} m² and the length of the collision chamber is 2×10^{-2} m, the numerical density of targets and the target pressure at 25 °C that result in a strength reduction of incident particles by half are related as follows:

$$D = \frac{\log_e(I_{IN}/I_{OUT})}{L\sigma} = \frac{0.693}{0.02 (\text{m}) \times 3 \times 10^{-20} (\text{m}^2)} = 1.155 \times 10^{21} (\text{m}^{-3}). \quad (1.19)$$

The above converted into pressure results in 4.76 Pa. The pressure in the ion-trap MS/MS method is of the same order, which indicates that multiple collisions are used. If the pressure is increased further, very few incident ions are detected in some cases.

When multiple collisions occur, a value called mean free path (mean free path: λ_{mean}) and mean free time (τ_{mean}) are used. The mean free path designates the average distance traveled by the particles from one collision to the next. The product between the collision cross section σ and the target density

D gives the number of collisions per unit distance. λ_{mean} is thus obtained as follows, from the inverse of the above result:

$$\lambda_{\text{mean}} = \frac{1}{\sigma D}. \quad (1.20)$$

Moreover, by dividing λ_{mean} by the velocity v of the particles, the mean free time (mean free time: τ_{mean}) from one collision to the next is given by:

$$\tau_{\text{mean}} = \frac{1}{\sigma D v}. \quad (1.21)$$

In the explanation about collision cross section, we considered a scattering cross section in which the direction of the incident particles changes to facilitate visualization. However, the concept of reaction cross section, in which the collision cross section causes a reaction, is very important. This concept includes cross sections that cause ionization, those that cause a transition to a certain state, those that cause dissociation of molecules upon collision, and those that cause electron transfer. Cross sections that originate from such a specific reaction differ from scattering cross sections and can no longer be measured from the reduction of the incident beam. For those, it is necessary to count the number of generated particles. For this reason, it is necessary to perform measurements in single-collision conditions where the effect of other reactions or multiple collisions can be avoided. The equation is similar to (1.13), but the number of generated ions I_{Formed} must be considered, resulting in a change of sign:

$$dI_{\text{Formed}}(x) = I(x)\sigma D dx. \quad (1.22)$$

In single-collision conditions, if we integrate from 0 to L considering constant $I(x)$, we obtain:

$$I_{\text{Formed}} = (\sigma L D) I_{\text{IN}}. \quad (1.23)$$

In (1.18), if we put $I_{\text{Formed}} = I_{\text{IN}} - I_{\text{OUT}}$, the first-order term becomes equal to (1.23). This equality indicates that the meaning of the collision cross section is the same no matter whether we are dealing with a scattering cross section or a generation cross section. The generation cross section and the differential cross section (explained later) are meaningful in single-collision conditions. Except for scattering collisions, the exact cross section cannot be usually obtained unless the target concentration satisfies the approximation of (1.23).

The ionization cross section for atoms and molecules is reported to be as shown in Fig. 1.5 [8]. This measuring method consists of measuring ions resulting from collisions between molecules and electrons whose energies are known. As mentioned in the Lab and CM systems of Sect. 3, since almost all the kinetic energy of the electrons is used for ionization, there is zero gap between the kinetic energy and the ionization energy. A sudden rise occurs soon after the ionization energy as a function of the collision energy. As the kinetic energy grows, the ionization cross section is gradually reduced. As shown in Fig. 1.5, in electron ionization, collisions in the range of 70–100 eV result in ionization cross sections with the highest efficiency, with little dependency on collision energy. For that reason, we use electron energies in the range of 70–100 eV for electron ionization, in which case the ionization cross section is of the order of 10^{-20} m^2 (10^{-16} cm^2 , \AA^2), depending on the molecule, matching the size of the atom and molecule mentioned.

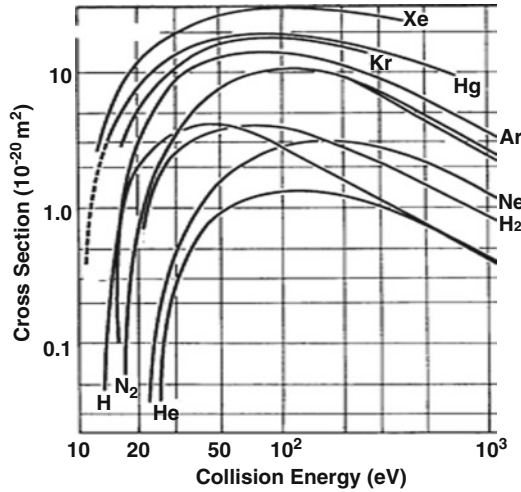


Fig. 1.5 Ionization cross section due to electron collision [8].

1.6 Intermolecular Potential

The scattering cross section of a rigid sphere according to classical theory is expressed as $\pi (R_{\text{Inc}} + R_{\text{Tar}})^2$ as mentioned in Sect. 5, and therefore does not depend upon collision velocity. Figure 1.6 shows the collision cross section for K atoms colliding with a rare gas [9]. Here, the collision cross section shows a clear dependency upon velocity. At lower velocities the effect of the attracting force causes an increase in the collision cross section. It is possible to discuss the interactions among molecules based on the dependency of the scattering cross section upon velocity.

Unlike the rigid spheres of Sect. 5, the interactions among actual molecules and ions suffer the force of $F(R)$, which depends on the distance (R) among the particles. The integral of this force yields the potential energy $V(r)$, which has the dimension of energy. Since there is no force at an infinite distance in the case of collisions, we can express the potential as follows, considering zero potential at an infinite distance:

$$V(r) = \int_{\infty}^r F(R) dR. \quad (1.24)$$

Expressed this way, the potential becomes a scalar value that depends only on the distance r between two particles. In the case of rigid bodies, no force is involved since the particles are located infinitely apart until they approach each other up to $(R_{\text{Inc}} + R_{\text{Tar}})$, and therefore the potential until $R_{\text{Inc}} + R_{\text{Tar}}$ continues to be 0. When the distance becomes $R_{\text{Inc}} + R_{\text{Tar}}$, the particles cannot approach each other any closer, and at this point, they suffer the effect of an infinite force. As shown by the two straight lines intersected at right angle in Fig. 1.7, the potential for the collision of rigid bodies is 0 at an infinite distance and jumps vertically to infinite at $R_{\text{Inc}} + R_{\text{Tar}}$.

Even if the molecules are homogeneous, if the motion of the nucleus of the atom differs from that of the electron, they exhibit an induced dipole moment. The force associated with this induced dipolar moment is called London dispersion force. The attractive potential arising from the force is proportional to r^{-6} . In Fig. 1.6, the straight line represents values calculated considering that the attractive

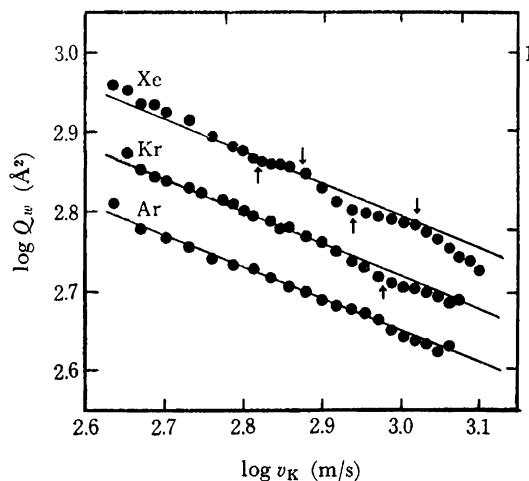


Fig. 1.6 Collision cross section between K atoms and rare gas with $\text{\AA} = 10^{-10} \text{ m}$ [9]. (Copied from ref. [9] with the permission of the Chemical Society of Japan)

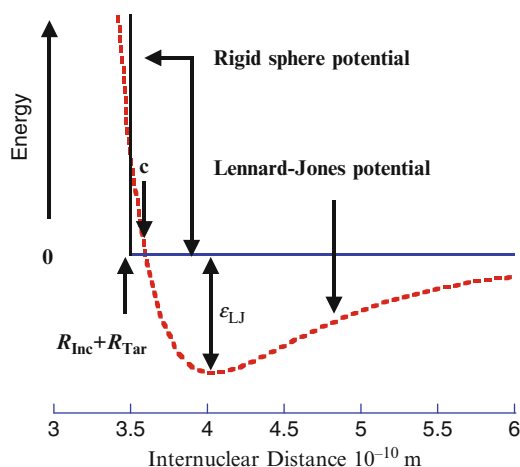


Fig. 1.7 Illustration of rigid sphere potential and Lennard-Jones potential

potential is proportional to r^{-6} , which matches experimental values. The dependency of the scattering cross section upon velocity in Fig. 1.6 can be explained in terms of the induced polarization effect¹⁶. In the case of molecules, intermolecular forces produce an attractive potential at longer distances, while for short distances Coulomb's repulsion produces a repulsive potential. The attractive potential proportional to r^{-6} prevalent at long distances is theoretically corroborated as the London dispersion force. As to the repulsive potential proportional to r^{-12} that occurs when the intermolecular distance approaches at the length of atoms, the following Lennard-Jones potential is used as an approximation of intermolecular potential:

$$V(r) = 4\epsilon_{LJ} \left[\left(\frac{c}{r} \right)^{12} - \left(\frac{c}{r} \right)^6 \right]. \quad (1.25)$$

Table 1.1 Parameters of the Lennard-Jones potential

Atom/molecule	c [10^{-10} m]	ϵ_{LJ} [meV]
He	2.57	0.93
Kr	3.59	14.9
CH ₄	3.81	12.8

Table 1.2 Parameters of the Morse potential

Diatomic molecule	r_e [10^{-10} m]	D_e [eV]
O ₂	1.21	5.18
O ₂ ⁺	1.12	6.6

There is no physicochemical corroboration for the repulsive force to be proportional to r^{-12} , but this approximation is often used because it is close to the actual potential and permits easy calculation. As shown in Fig. 1.7, c and ϵ_{LJ} are respectively the distance that yields zero potential energy and a parameter related to potential deepness. By differentiating (1.25) with respect to r and putting the result equal to 0, the intermolecular distance that yields the lowest energy can be obtained as the product of c and the 6-th root of 2. Example values for atoms and molecules are given in Table 1.1. These values show that c is of the order of 10^{-10} m, and ϵ_{LJ} is of the order of meV. These values make it possible to obtain the order of magnitude of molecular sizes and the forces involved.

The Lennard-Jones potential (12,6) relates to the potential between atoms and molecules that are neutral and stable. For the formation of stable diatomic molecules, the electrons serve to stabilize the repulsion between nuclear charges. A small internuclear distance requires a large attractive force. The Morse potential is used in this case:

$$V(r) = D_e \exp[-2a(r - r_e)] - 2D_e \exp[-a(r - r_e)]. \quad (1.26)$$

r_e and D_e are respectively the internuclear distance and energy deepness that yield the lowest potential. “ a ” is a parameter that defines the shape of the potential, and for the diatomic molecule case it is related to the vibrational force constant. In the same way as the Lennard-Jones potential, the first term refers to repulsive force and the second term refers to attractive force in a Morse potential. In the first term the dependency upon the distance ($r - r_e$) relative to the most stable internuclear distance (r_e) is squared. The Morse potential parameters for an oxygen molecule and an oxygen molecule ion are shown in Table 1.2. The Morse potential and the Lennard-Jones potential (12,6) apparently show the same shape, but the difference in distance that gives the smallest potential is about twice, and the difference in potential deepness is approximately 1,000 times. In the Morse potential parameters of Table 1.2, we considered the example of an ion, but in a collision such as one involving ions in which one of the particles is charged, the charge causes an induced dipole moment, resulting in an attractive potential proportional to r^{-4} :

$$V(r) = -\frac{\alpha q^2 e^2}{32\pi^2 \epsilon_0^2 r^4} = -\left(\frac{\alpha}{4\pi\epsilon_0}\right) \frac{q^2 e^2}{8\pi\epsilon_0 r^4} = -\alpha' \frac{q^2 e^2}{8\pi\epsilon_0 r^4}. \quad (1.27)$$

Here, α is the polarizability of the molecule, and ϵ_0 is the electric permittivity of vacuum. The SI unit of polarizability is $[\text{J}^{-1} \text{C}^2 \text{m}^2]$, but it is often provided as polarizability volume in $\alpha' \text{ m}^3$ after dividing by $4\pi\epsilon_0$. Moreover, the polarization results from Coulomb's force due to the electrical charge, and it increases as the number of loosely combined electrons increases. Therefore, especially large values can be observed for large molecules, alkali metals, and the like. Equation (1.28) shows the potential expressed in eV, r in 10^{-10} m units, and the polarizability volume α' in 10^{-30} m^3 .

$$V(r) = -\frac{7.20\alpha'q^2}{r^4}. \quad (1.28)$$

If we introduce the value $43.4 (10^{-30} \text{ m}^3)$ for potassium (K) and consider $q = 1, r = 3.0 \times 10^{-10} \text{ m}$, we obtain 3.86 eV, which differs considerably from the meV value of the Lennard-Jones potential (12,6). It is rather close to the eV value for the Morse potential. The α' value for argon is $1.64 (10^{-30} \text{ m}^3)$, which is smaller than K, but when the distance is as short as $r = 2.0 \times 10^{-10} \text{ m}$, it goes up to 0.73 eV, which is considerably larger than meV. In the ion molecule reaction, the potential deepness is large because the potential is proportional to r^{-4} and produces an effect from a large distance. We observe that the collision is largely affected by this force [10]. If there is a force that produces an effect from a large distance, the collision cross section depends on such factors as a function of the scattering angle, that is, the direction of the output particles.

1.7 Differential Cross Section and Impact Parameter

As mentioned in Sect. 3, the collision between two particles can be thought of as the scattering of a particle with reduced mass μ from its center of mass \mathbf{O} . The scattering of an incident particle due to a potential is illustrated in Fig. 1.8. At a far distance there is no effect of force and the particle continues its rectilinear movement. Consider an x axis shown by dashed line passing through \mathbf{O} parallel to the direction of movement. Since the values start from \mathbf{O} , the sign at the incidence position is negative. Considering a y -axis perpendicular to x , the value of y remains constant at long distances. The value of y at an infinitely far distance is called impact parameter and is usually referred to as b . The center of mass and the respective distance change depending on the value of b , and therefore the outgoing direction after scattering changes. In the case of b_1 , only the term related to attractive force is

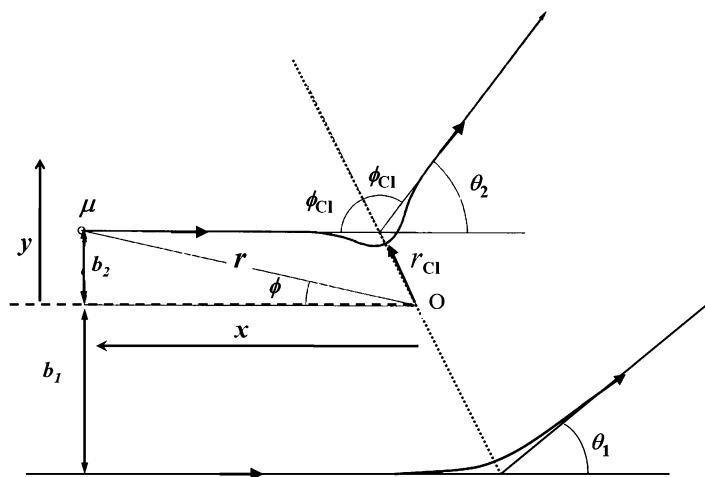


Fig. 1.8 Scattering in a center-of-mass system: collision parameter (b), nearest approaching distance (r_{CI}), and scattering angle (θ)

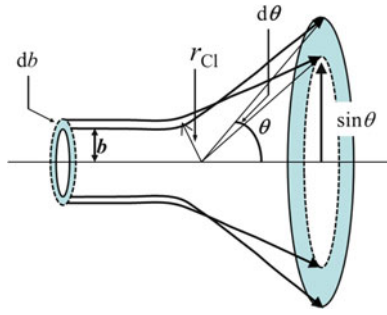


Fig. 1.9 Model illustration of differential cross section

effective, and the direction towards the center-of-mass changes. In the case of b_2 , at first it bends towards the center due to the attractive force like in b_1 . However, when the repulsive force near the center grows and the distance becomes close to the nearest approaching distance (r_{CI}), the particle is repelled. Then, it changes direction and drifts away. When a particle with reduced mass μ is scattered by a spherically symmetrical potential, the collision occurs on a flat plane, as shown in Fig. 1.8. The impact parameter b related to scattering is of the order of the size of atoms or molecules, and experiments to determine it are very difficult. However, the incident beam can be considered uniform, and therefore the differential cross section can be estimated from the angle and strength of the particles scattered by the target. In some cases, the term differential cross section refers to energy, but here the discussion is limited to differential cross section with respect to angle.

Figure 1.9 shows a 3-dimensional image of the process to determine the differential cross section. Supposing that ions that enter the impact parameter range $2\pi b db$ are scattered in the range $d\theta$, then the corresponding area is given as $2\pi r^2 \sin\theta d\theta$. Although small deviation of the position of the center of scattering exists, deviations of the order of atom size can be ignored relative to the size in actual measurements. If the number of incident molecules per unit time and unit area is I_0 , the number of molecules between b and $b + db$ per unit time is $I_0 2\pi b db$. When the differential cross section related to the scattering angle is expressed by $q(\theta)$, the number of particles per unit time detected in θ and $\theta + d\theta$ is $I_0 q(\theta) 2\pi \sin\theta d\theta$. Since both are equal, the differential cross section is obtained by the following equation, with the unit being area/angle:

$$q(\theta) = \frac{b}{\sin\theta} \left(\frac{db}{d\theta} \right). \quad (1.29)$$

The integral of (1.29) through all solid angles $d\Omega$ ($\sin\theta d\theta d\varphi$) yields the total cross section. Since the spherically symmetrical potential does not depend on the direction φ , it is possible to replace it by 2π to obtain:

$$\begin{aligned} \sigma &= \int_0^{4\pi} q(\theta, \varphi) d\Omega = \int_0^{2\pi} \int_0^\pi q(\theta, \varphi) \sin\theta d\theta d\varphi = 2\pi \int_0^\pi q(\theta) \sin\theta d\theta \\ &= 2\pi \int_0^\pi \frac{b}{\sin\theta} \left(\frac{db}{d\theta} \right) \sin\theta d\theta = 2\pi \int_0^\infty b db. \end{aligned} \quad (1.30)$$

The integral over all directions of the scattering angle results in the total cross section, which matches the total cross section obtained by integrating the impact parameter over all regions, showing

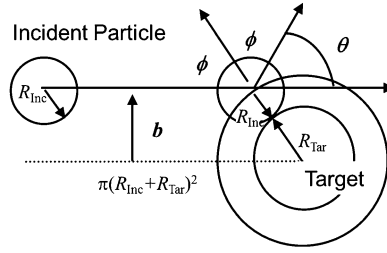


Fig. 1.10 Example of angle scattering of a rigid sphere

that there is no contradiction. The impact parameter b at the end of (1.30) refers to the value of b when the scattering is originated. Integrating this equation does not diverge but rather results in a finite value.

The angle scattering of a rigid sphere is shown in Fig. 1.10. The scattering angle θ for incident particles with impact parameter b is given by the following equation, using the angle ϕ between the center and the collision point with respect to the central line of the collision:

$$\theta = \pi - 2\phi = \pi - 2 \sin^{-1} \left(\frac{b}{R_{\text{Inc}} + R_{\text{Tar}}} \right). \quad (1.31)$$

Moreover, according to this equation, the relation between impact parameter b and scattering angle θ is given by:

$$\frac{b}{R_{\text{Inc}} + R_{\text{Tar}}} = \sin \left(\frac{\pi - \theta}{2} \right) = \sin \left(\frac{\pi}{2} - \frac{\theta}{2} \right) = \cos \left(\frac{\theta}{2} \right). \quad (1.32)$$

Since the value of $R_{\text{Inc}} + R_{\text{Tar}}$ is constant for a rigid sphere collision, the following equation can be obtained by integrating both sides of (1.32):

$$\frac{db}{R_{\text{Inc}} + R_{\text{Tar}}} = -\frac{1}{2} \sin \left(\frac{\theta}{2} \right) d\theta. \quad (1.33)$$

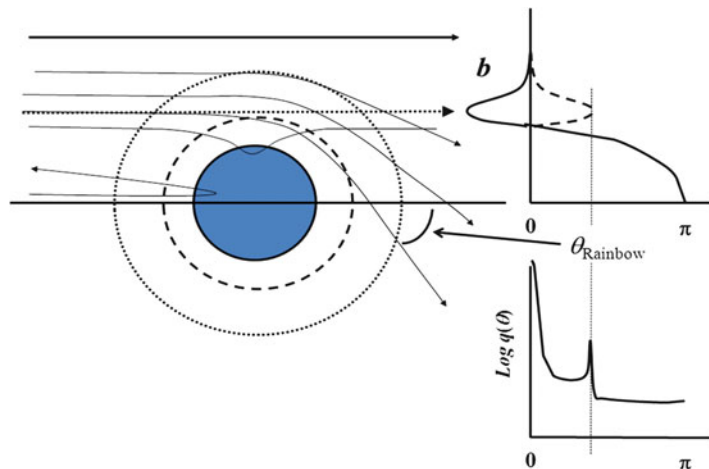
$$\frac{db}{d\theta} = -\frac{R_{\text{Inc}} + R_{\text{Tar}}}{2} \sin \left(\frac{\theta}{2} \right) = -\frac{R_{\text{Inc}} + R_{\text{Tar}}}{2} \sin \left(\frac{\pi}{2} - \phi \right) = \frac{R_{\text{Inc}} + R_{\text{Tar}}}{2} \cos \phi. \quad (1.34)$$

By substituting these equations into (1.29), the differential cross section can be obtained using:

$$q(\theta) = \frac{b}{\sin \theta} \left(\frac{db}{d\theta} \right) = \frac{(R_{\text{Inc}} + R_{\text{Tar}}) \sin \phi}{2 \sin \phi \cos \phi} \left(\frac{(R_{\text{Inc}} + R_{\text{Tar}}) \cos \phi}{2} \right) = \frac{(R_{\text{Inc}} + R_{\text{Tar}})^2}{4}. \quad (1.35)$$

As shown in (1.35), in collisions involving rigid spheres the differential cross section characterizes an isotropic scattering and does not depend on the scattering angle θ . The total cross section for a rigid sphere collision is obtained by integrating $q(\theta)$ in (1.35) over all scattering angles as in the equation below, and coincides with the total cross section previously obtained in Fig. 1.4.

Fig. 1.11 Differential cross section under the influence of attractive and repulsive force potentials



$$\begin{aligned}\sigma &= 2\pi \int_0^\pi q(\theta) \sin \theta d\theta = 2\pi \int_0^\pi \frac{(R_{\text{Inc}} + R_{\text{Tar}})^2}{4} \sin \theta d\theta = 2\pi \frac{(R_{\text{Inc}} + R_{\text{Tar}})^2}{4} \int_0^\pi \sin \theta d\theta \\ &= \frac{\pi (R_{\text{Inc}} + R_{\text{Tar}})^2}{2} [\cos \theta]_0^\pi = \frac{\pi (R_{\text{Inc}} + R_{\text{Tar}})^2}{2} [2] = \pi (R_{\text{Inc}} + R_{\text{Tar}})^2.\end{aligned}\quad (1.36)$$

In collisions involving real molecules, the scattering occurs in the outer attractive force region and the inner repulsive force region, as shown in the intermolecular potential example of Sect. 6. The relation between that kind of scattering and the differential cross section is shown in Fig. 1.11. In collisions between positive ions and molecules, an attractive force becomes effective under much larger intermolecular distances than in the case of rigid sphere collisions, resulting in deflection towards the target, where the impact parameter is large. Unlike the case of rigid spheres, the deflection occurs towards the particles in the region with large impact parameter, resulting in negative values of scattering angle. In the scattering experiment, it is possible to observe the deflection, but not the sign of the deflection angle. For this reason, in the experiment the relation between b/R and θ is measured considering only values on the positive side. This part is depicted by dotted lines in Fig. 1.11. When the effect of the repulsive force begins to be effective due to the small impact parameter, the deflection angles cancel each other, and the scattering angle does not change due to small changes of the impact parameter. Such an impact parameter causes $db/d\theta$ to become infinitely large, as well as the scattering cross section $q(\theta)$, characterizing the so-called rainbow scattering. This kind of scattering is shown in Fig. 1.11 as θ_{Rainbow} . Actually measured scattering cross sections never become infinitely large, but a pronounced peak appears in the θ_{Rainbow} region. When the impact parameter becomes smaller, the scattering angle becomes 0 in a case. In the case that collisions with different impact parameters are scattered with the same angle, the type of scattering with different overlapping waves is called glory scattering and causes the appearance of peculiar structures in the differential cross section. For even smaller impact parameters, the scattering angle changes its sign. For scatterings with the same potential, if the kinetic energies of the incident particles differ, forces with the same magnitude are felt at different times even when they have the same magnitude. Therefore, the scattering angle depends on the energy of the particles. For this reason, the scattering angle that results in rainbow scattering becomes smaller as the incident energy grows.

1.8 Centrifugal Potential

The collision between two particles expressed in a CM system can be converted to a one-body problem where a particle with reduced mass μ is scattered in a central force potential $V(r)$. In this section, we handle the case where the motion occurs in central force potential $V(r)$. Consider \mathbf{r} to be the position vector of a colliding particle seen from the center of mass. This motion occurs within a plane originated by the central force potential, and can be described by the distance r from the center of mass expressed as a scalar quantity and the angle ϕ of the particle with respect to the center of the scattering.

We considered the collision in a Lab and a CM system in Sect. 3. It is worth noting that even in a CM system, not all the kinetic energy is converted into internal energy. Considering the x and y axes, as shown in Fig. 1.12, the relation between r and ϕ is expressed as:

$$x = r \cos \phi, \quad y = r \sin \phi. \quad (1.37)$$

Deriving the equation above with respect to time results in:

$$\frac{dx}{dt} = \frac{dr}{dt} \cos \phi - r \sin \phi \frac{d\phi}{dt}, \quad \frac{dy}{dt} = \frac{dr}{dt} \sin \phi + r \cos \phi \frac{d\phi}{dt}. \quad (1.38)$$

The kinetic energy (T) in a CM system is given by (1.5) and can be converted into the equation below:

$$\begin{aligned} T &= \frac{1}{2} \mu v^2 = \frac{1}{2} \mu \left[\left(\frac{dx}{dt} \right)^2 + \left(\frac{dy}{dt} \right)^2 \right] = \frac{1}{2} \mu \left[\left(\frac{dr}{dt} \cos \phi - r \sin \phi \frac{d\phi}{dt} \right)^2 + \left(\frac{dr}{dt} \sin \phi + r \cos \phi \frac{d\phi}{dt} \right)^2 \right] \\ &= \frac{1}{2} \mu \left[\left(\frac{dr}{dt} \right)^2 + r^2 \left(\frac{d\phi}{dt} \right)^2 \right]. \end{aligned} \quad (1.39)$$

Considering potential $V(r)$ to be 0 when the particle is infinitely distant, the total energy (E) is given by the following equation, in view of the energy conservation law:

$$E = \frac{1}{2} \mu v_0^2 = T + V(r) = \frac{1}{2} \mu \left[\left(\frac{dr}{dt} \right)^2 + r^2 \left(\frac{d\phi}{dt} \right)^2 \right] + V(r). \quad (1.40)$$

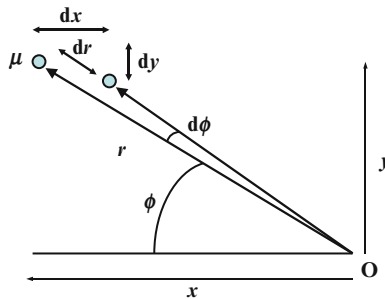


Fig. 1.12 Conversion between x, y axes and r, Φ axes

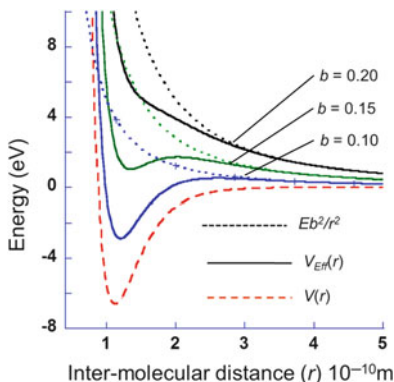


Fig. 1.13 Illustration of effective potential

For infinite distances, the energy in the left-hand term of the equation contains only kinetic energy. As r becomes smaller, the effect of $V(r)$ starts to appear in the right-hand term. Since the potential depends only on r , the motion occurs in the plane, and the angular momentum (L) is conserved. The angular momentum is given by either the vector product [distance \times momentum] or the vector product [moment of inertia (μr^2) \times angular velocity ($d\phi/dt$)], and therefore the following equation is valid:

$$\mathbf{L} = r \times \mu \mathbf{v} = b\mu v_0 = \mu r^2 \frac{d\phi}{dt}. \quad (1.41)$$

The energy is given by the following equation, using L and rewriting $d\phi/dt$ in (1.40):

$$E = \frac{1}{2}\mu \left(\frac{dr}{dt}\right)^2 + \frac{L^2}{2\mu r^2} + V(r). \quad (1.42)$$

The kinetic energy with respect to distance (r) is given as $(1/2)\mu (dr/dt)^2$, and other terms can be thought of as potentials. The following equation, resulting from the sum of terms 2 and 3 of (1.42), is called effective potential V_{Eff} (Effective):

$$V_{\text{Eff}}(r) = \frac{L^2}{2\mu r^2} + V(r) = \frac{Eb^2}{r^2} + V(r). \quad (1.43)$$

$(L^2/2\mu r^2)$ ($= (Eb^2)/r^2$) is the term derived from angular momentum, and is called the centrifugal potential. This value becomes large when the kinetic energy and the impact parameter are large. Here, the angular momentum L^2 is given by discrete values of $\hbar^2 l(l+1)$ according to quantum theory and a positive integer of l .

This effective potential is shown in Fig. 1.13. This figure depicts potential $V(r)$ of O_2^+ for $E = 500$ eV, $b = 0.1, 0.15, 0.20 \times 10^{-10}$ m. Since the centrifugal potential depends on r^{-2} , V_{Eff} related to the motion of the particles increases as the distance (r) becomes smaller. Because it grows by r^{-2} as the potential decreases by r^{-6} in intermolecular and by r^{-4} in ion–molecule reactions, a potential hill appears when the energy or the impact parameter belongs to a certain region, as shown in Fig. 1.13. This hill is called the centrifugal force barrier.

Obtaining dr/dt from (1.42) gives:

$$\frac{dr}{dt} = \pm \sqrt{\frac{2E}{\mu}} \sqrt{1 - \frac{b^2}{r^2} - \frac{V(r)}{E}}. \quad (1.44)$$

The minus sign indicates that the particle is approaching, since the distance r decreases with time. By differentiating with respect to angle instead of time using (1.41), we obtain:

$$\frac{dr}{d\phi} = \pm \frac{r^2}{b} \sqrt{1 - \frac{b^2}{r^2} - \frac{V(r)}{E}}. \quad (1.45)$$

Since the closest distance (r_{Cl} : Closest) corresponds to that when the derivative is 0, r_{Cl} satisfies the equation:

$$1 - \frac{b^2}{r_{\text{Cl}}^2} - \frac{V(r_{\text{Cl}})}{E} = 0. \quad (1.46)$$

The following equation is obtained by inverting the numerator and denominator of (1.45):

$$d\phi = \pm \frac{b}{\sqrt{1 - \frac{b^2}{r^2} - \frac{V(r)}{E}}} \frac{dr}{r^2}. \quad (1.47)$$

Since the value of ϕ for the closest distance becomes ϕ_{Cl} , the scattering angle θ is $\pi - 2\phi_{\text{Cl}}$ as can be seen in Fig. 1.8. By integrating (1.47) from infinity to the closest distance r_{Cl} , the scattering angle θ can be obtained as the following function of the impact parameter b and the total energy E :

$$\theta(b, E) = \pi - 2 \int_{r_{\text{Cl}}}^{\infty} \frac{b}{\sqrt{1 - \frac{b^2}{r^2} - \frac{V(r)}{E}}} \frac{dr}{r^2}. \quad (1.48)$$

1.9 Orbiting (Langevin) Cross Section

Mass spectrometry is a method to analyze ions, and the ion-molecule reaction, which involves ions and molecules, is the kind of molecular collision most closely related to it. The ion-molecule reaction includes several types of reactions such as proton transfer, electron transfer, ion recombination, etc. Many of such reactions are exothermic, but even so they do not occur unless the ion and the molecule approach each other closer than a certain threshold. If the centrifugal potential mentioned in Sect. 8 exists, the ion and the molecule cannot approach each other closer than a certain threshold. For such cases, Langevin proposed the concept of orbiting trajectory [11] to judge whether the reaction will occur or not, and the related cross section is called the Langevin cross section.

In many cases that involve ion-molecule reactions, the centrifugal force existing between ions and neutral molecules consists of the ion's charge and the polarizability potential due to the polarizability of the neutral molecule. Similar to (1.27), it is expressed by:

$$V_{\text{Pol}}(r) = -\frac{\alpha q^2 e^2}{32\pi^2 \epsilon_0^2 r^4}. \quad (1.49)$$

Since the potential depends on r^{-4} , the effect of the potential is felt from a farther distance than the van der Waals force, and its value is considerably larger than the usual intermolecular potential. Gioumouis and Stevenson [12] determined the orbiting trajectory related to this potential. The effective potential that includes this attractive potential is given by the following equation, which is obtained by substituting into $V(r)$ of (1.43):

$$V_{\text{Eff}}(r) = \frac{Eb^2}{r^2} + V_{\text{Pol}}(r) = \frac{Eb^2}{r^2} - \frac{\alpha q^2 e^2}{32\pi^2 \epsilon_0^2 r^4}. \quad (1.50)$$

Since the intermolecular potential is proportional to r^{-4} , its contribution grows compared to the centrifugal force potential, which is proportional to r^{-2} when the energy or the impact parameter b is small. This appears as a local maximum such as the one in the second continuous line from the bottom in Fig. 1.13 representing V_{Eff} . By exceeding the local maximum of the effective potential, the reaction may occur due to the interaction between ions and molecules.

Because the local maximum in the effective potential occurs at a far distance, the orbiting cross section can be calculated by ignoring the repulsive force at short distances. Since the maximum is reached when the incident energy of the particles becomes equal to the local maximum of the potential, the following equation is obtained by substituting E into the left-hand term of (1.50), after some manipulation:

$$r^4 - b^2 r^2 - \frac{\alpha q^2 e^2}{32\pi^2 \epsilon_0^2 E} = 0. \quad (1.51)$$

The square of r (r^2) can be obtained by this equation. As double roots occur at the local peak, the following equation is obtained by putting 0 for the square root part of the quadratic equation root formula:

$$b^4 = \frac{\alpha q^2 e^2}{8\pi^2 \epsilon_0^2 E}. \quad (1.52)$$

When the kinetic energy is E , the critical impact parameter (b_{Cr}) to reach the hill of the effective potential is obtained as the 4th-root of (1.52). Moreover, the intermolecular distance r_{Cr} as a function of the impact parameter in that situation is obtained from the equation that yields the multiple roots of (1.51) in terms of r^2 , as below:

$$r_{\text{Cr}} = \frac{b_{\text{Cr}}}{\sqrt{2}} \quad (1.53)$$

The above is illustrated in Fig. 1.14. Incident ions with an impact parameter that corresponds to that value follow the trajectory shown as a continuous line in the figure and rotate repeatedly around the impact center with radius r_{Cr} . This trajectory is called the orbiting trajectory. If the incidence occurs with the same kinetic energy but a larger impact parameter, the larger centrifugal force potential Eb^2 makes the particles follow a farther path as shown by the dashed line in the figure, and they do not reach the hill. If they approach with the same kinetic energy and an impact parameter smaller than b_{Cr} , they cross the hill and reach the region where the reaction between ions and molecules occurs, as shown by the dotted line in the figure. In case Eb^2 keeps the same value and the energy has a smaller value during the approach, it is not possible to surpass the centrifugal force

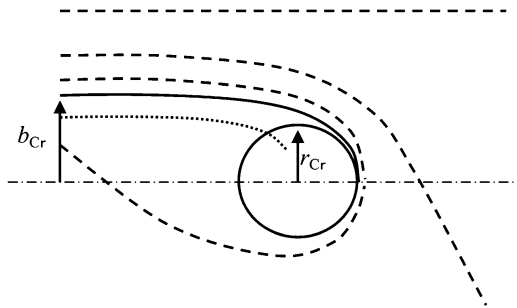


Fig. 1.14 Illustration of orbiting

potential due to lack of energy, even though two mathematical roots exist. Particles possessing the energy to overcome this hill can enter the reaction region. However, if we consider just the kinetic energy, the centrifugal force barrier decreases when the kinetic energy is reduced, and the actual value of b_{Cr} increases.

The cross section to enter the reaction region is calculated using b_{Cr} by the following equation, using the orbiting cross section (σ_{Or}) (1.52):

$$\sigma_{Or} = \pi b_{Cr}^2 = \pi \sqrt{\frac{\alpha q^2 e^2}{8\pi^2 \epsilon_0^2 E}} = \pi \sqrt{\left(\frac{\alpha}{4\pi \epsilon_0}\right) \frac{q^2 e^2}{2\pi \epsilon_0 E}} = \pi \sqrt{\alpha' \frac{q^2 e^2}{2\pi \epsilon_0 E}}. \quad (1.54)$$

As seen in (1.54), the orbiting cross section is inversely proportional to the square root of the kinetic energy. Introducing values for q , e , ϵ_0 , the cross section for the collision between one ion and a neutral particle with polarizability volume α' is given by:

$$\sigma_{Or} = 16.9 \sqrt{\frac{\alpha'}{E}} \quad (1.55)$$

where the unit for polarizability volume is 10^{-30} m^3 , that for E is eV, and that for σ_{Or} is 10^{-20} m^2 . Considering a CM system with kinetic energy 1.0 keV and target K, the value of α' is $43.4 \times 10^{-30} \text{ m}^3$, and σ_{Or} is as high as $3.5 \times 10^{-20} \text{ m}^2$. As to Ar, with $\alpha' = 1.64 \times 10^{-30} \text{ m}^3$, we have $\sigma_{Or} = 6.8 \times 10^{-21} \text{ m}^2$, which corresponds to approximately 1/5 of that with a K target. However, as we can see from (1.55), σ_{Or} increases when the energy is reduced. In the ion-molecule reaction, which is an exothermic reaction, low energies of the order of eV are expected to result in a large reaction cross section.

Exceeding the centrifugal force potential and entering the reaction region do not necessarily result in a reaction. σ_{Or} gives the cross section for entering the reaction region, and can be thought of as the maximum value of the reaction cross section. If P is the probability that a specific reaction occurs when an ion enters the reaction region, the reaction cross section is given by:

$$\sigma_{React} = P\sigma_L = P\pi \sqrt{\frac{\alpha q^2 e^2}{8\pi^2 \epsilon_0^2 E}} = 16.9P \sqrt{\frac{\alpha'}{E}} \quad (1.56)$$

In the discussion so far, we considered that it is necessary to exceed the centrifugal force barrier and enter the reaction region, but for some types of reaction it is sufficient that the intermolecular distance approaches r_{React} . As shown in Fig. 1.13, when the energy is large the ion and the molecule

can approach each other to a certain extent even when a centrifugal force barrier exists. Dividing (1.51) by r^2 gives:

$$b^2 = r_{\text{React}}^2 + \frac{\alpha q^2 e^2}{32\pi^2 \epsilon_0^2 E r_{\text{React}}^2}. \quad (1.57)$$

The reaction cross section for this case is obtained by the following equation, considering a reaction probability P :

$$\begin{aligned} \sigma_{\text{React}} &= P\pi b^2 = P\pi \left(r_{\text{React}}^2 + \frac{\alpha q^2 e^2}{32\pi^2 \epsilon_0^2 E r_{\text{React}}^2} \right) = P\pi r_{\text{React}}^2 \left(1 + \frac{b_{\text{Cl}}^4}{4r_{\text{React}}^4} \right) \\ &= P\pi r_{\text{React}}^2 \left(1 + \left(\frac{r_{\text{Cl}}}{r_{\text{React}}} \right)^4 \right). \end{aligned} \quad (1.58)$$

We suppose that the larger one out of the cross sections given by (1.56) and (1.58) yields the reaction cross section, depending on the reaction. As an example, when the cross sections for a resonant electron transfer of singly and doubly charged Kr ions with Kr targets were measured by Koizumi et al., they reported the occurrence of reversals due to changes in the magnitude of σ_{Or} and σ_{React} at the collision energy of around 0.1 eV [13]. We have just considered the r^{-4} potential for induced dipole moment, but in some cases the reacting neutral particle has a permanent induced dipole moment. Molecules show rotational distribution at room temperature, which does not produce a significant effect at far distances but does so at short distances and low energies. This is handled in averaged dipole orientation (ADO) theory [14].

1.10 Semiclassical Theory and Massey Criterion

We have handled several types of collisions so far, but not those in which the internal energy of the particles changes. Moreover, we have not used quantum theory. Except for electron ionization and electron capture, the reactions involved in mass spectrometry are collisions among atoms, molecules, and ions. In collisions handled in mass spectrometry of the order of a few eV or more, the matter wave is short for the particles involved in the collision. Until the particles get very close to each other, their motions follow the potential described in the above sections in a classically defined trajectory. The method in which the relative motion is handled in a classical framework, while the internal states of the particles at short distances are handled by quantum dynamics, is called semiclassical theory. For collisions involving enough kinetic energy to change the internal energy of the particles, the trajectories of the particles do not deflect much. In that case, it is possible to assume that the colliding particles describe a constant-velocity, linear motion in accordance with the equation:

$$\mathbf{r} = \mathbf{b} + \mathbf{v}t. \quad (1.59)$$

If \mathbf{b} is selected so as to be perpendicular to \mathbf{v} , b will be equal to the impact parameter described in Sect. 8. Since the total cross section is given by (1.30), the cross section for the reaction is given by the equation below, obtained by multiplying it with probability $P(b, v)$ that such a reaction occurs:

$$\sigma = 2\pi \int_0^\infty P(b, v) b \, db. \quad (1.60)$$

This method is called the impact parameter method.

In general, in order to find $P(b,v)$, it is necessary to solve the wave equation (1.61) dependent on time that includes the momentum and potential of all nuclei and electrons.

$$\hat{H}\Psi(\mathbf{R}, t) = \left(\sum_j \frac{\hbar^2}{2m_j} \nabla_j^2 + V(\mathbf{R}(t)) \right) \Psi(\mathbf{R}, t) = i\hbar \frac{\partial}{\partial t} \Psi(\mathbf{R}, t). \quad (1.61)$$

When the incident and target particles are far from each other and do not interact, consider that eigenstates and eigenfunctions are given for all atomic nuclei and electrons of the incident and target particles. If the coordinate is $r_{\mathbf{R}}$, the Hamiltonian is $H_{\mathbf{R}}(r_{\mathbf{R}})$, and the wave function is given by $\varphi_{\mathbf{R}}(r_{\mathbf{R}})$, then the relation among them satisfies:

$$H_{\mathbf{R}}(r_{\mathbf{R}})\varphi(r_{\mathbf{R}}) = E_{\mathbf{R}}\varphi(r_{\mathbf{R}}). \quad (1.62)$$

Using $H_{\mathbf{R}}(r_{\mathbf{R}})$ of (1.62), and expressing the potential term of $V(R(t))$ which depends on the distance between the two colliding particles in terms of $r(t)$, which changes with time, (1.61) can be rewritten to include a derivative with respect to time, as follows:

$$\{H_{\mathbf{R}}(r_{\mathbf{R}}) + V(r_{\mathbf{R}}, r(t))\}\Psi(r_{\mathbf{R}}, t) = i\hbar \frac{\partial \Psi(r_{\mathbf{R}}, t)}{\partial t}. \quad (1.63)$$

Here, the following equation is obtained by considering zero potential before the reaction:

$$H_{\mathbf{R}}(r_{\mathbf{R}})\Psi(r_{\mathbf{R}}, t) = i\hbar \frac{\partial \Psi(r_{\mathbf{R}}, t)}{\partial t}. \quad (1.64)$$

The wave function that satisfies the equation above is:

$$\Psi(r_{\alpha}, t) = \varphi_{\alpha}(r_{\mathbf{R}}) \exp\left(-\frac{E_{\alpha}t}{\hbar}\right). \quad (1.65)$$

The following linear combination of the wave equation can be used to calculate:

$$\Psi(r_{\alpha}, t) = \sum_{\alpha} c_{\alpha}(t)\varphi_{\alpha}(r_{\mathbf{R}}) \exp\left(-\frac{E_{\alpha}t}{\hbar}\right). \quad (1.66)$$

The conditions that must be fulfilled by c_{α} are expressed by:

$$i\hbar \frac{dc_{\alpha}}{dt} = \sum_{\beta} c_{\beta}(t) V_{\alpha\beta}(r(t)) \exp\left(-\frac{i}{\hbar}(E_{\beta} - E_{\alpha})t\right). \quad (1.67)$$

Here, $V_{\alpha\beta}(r(t))$ is given by:

$$V_{\alpha\beta}(r(t)) = \int \varphi_{\alpha} \times (r_{\mathbf{R}}) V(r_{\mathbf{R}}, r(t)) \varphi_{\beta}(r_{\mathbf{R}}) dr_{\mathbf{R}}. \quad (1.68)$$

Considering the wave function as φ_0 corresponding to a certain state before the collision, the initial condition of (1.67) is $c_\alpha(t) \rightarrow \delta_{\alpha 0}$ for $t = -\infty$. Under these conditions, if $c_\alpha(\infty)$ is found, the transition probability for each collision is given by:

$$P(0 \rightarrow \alpha, b, v) = |c_\alpha(\infty)|^2. \quad (1.69)$$

The reaction cross section is obtained by substituting the probability above into (1.60) and integrating it.

Solving the equation above based on perturbation theory, the 0th order equation is:

$i\hbar(dc_\alpha^{(0)}/dt) = 0$, and $c_\alpha^{(0)}(t) = \delta_{\alpha 0}$ corresponds to the case where the system returned to the previous state.

The first-order equation is as follows:

$$\begin{aligned} i\hbar \frac{dc_\alpha^{(1)}(t)}{dt} &= \sum_{\beta} c_\beta^{(0)}(t) V_{\alpha\beta}(r(t)) \exp\left(-\frac{i}{\hbar}(E_\beta - E_\alpha)t\right) \\ &= V_{\alpha 0}(r(t)) \exp\left(-\frac{i}{\hbar}(E_0 - E_\alpha)t\right). \end{aligned} \quad (1.70)$$

which can be integrated to yield:

$$c_\alpha^{(1)}(t) = \frac{1}{i\hbar} \int_{-\infty}^t V_{\alpha 0}(r(t)) \exp\left(-\frac{i}{\hbar}(E_0 - E_\alpha)t\right) dt. \quad (1.71)$$

The transition probability is determined by the value of $c_\alpha^{(1)}(t)$ for $t = \infty$. The term $\exp(-\frac{i}{\hbar}(E_0 - E_\alpha)t)$ is a function that oscillates in time. The product of the oscillating function above with $V_{\alpha 0}(r(t))$ determines the magnitude of $c_\alpha^{(1)}(\infty)$. Since $V_{\alpha 0}(r(t))$ is a matrix element corresponding to the interaction, it is reasonable to suppose that its value affects the integral of (1.71) only when the two particles approach each other to a certain extent. Let “ a ” be the distance where the two particles interact. If the relative velocity between the two particles is v , the time τ when the interaction occurs is given by a/v . As shown in Fig. 1.15a, if the term $\exp(-\frac{i}{\hbar}(E_0 - E_\alpha)t)$ that oscillates with time does so with an extremely fast period, the values of (1.71) cancel each other for a fast vibration, resulting in a small value, even inside the region where the value of $V_{\alpha 0}(r(t))$ belongs to a certain range. In other words, we can expect that:

$$\frac{a \cdot (E_0 - E_\alpha)}{\hbar v} \gg 1 \quad \text{then } P(0 \rightarrow \alpha) \ll 1. \quad (1.72)$$

Moreover, if the velocity is high and the collision time is short, the integration time becomes shorter. As a consequence, as shown in Fig. 1.15c, the value of (1.72) becomes smaller. In a very rough interpretation, we can say that for a shape such as the one in Fig. 1.15b, the transition is likely to occur if the conditions given by the equation below are satisfied. This idea is called Massey’s adiabatic criterion, borrowing the name of the person who first proposed the theory [15].

$$\frac{a \cdot (E_0 - E_\alpha)}{\hbar v} \approx 1 \quad (1.73)$$

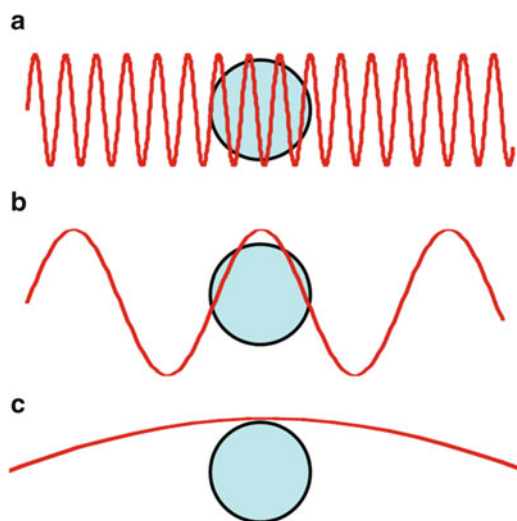


Fig. 1.15 Image of the molecule size and the number of oscillations

Table 1.3 Velocities and kinetic energies that yield the maximum cross section of a 100 u -ion in Massey criterion

Excitation energy (eV)	0.01	0.1	1	10
Velocity (m s^{-1})	4.6×10^3	4.6×10^4	4.6×10^5	4.6×10^6
Kinetic energy (keV)	0.011	1.08	108	1.08×10^4

To test the validity of the idea, Hasted plotted the cross section and energy that result in local maxima of the excitation cross section for several atomic collisions, and reported that the above relation matches very well [16], and the values match the experimental data when $a = 7 \times 10^{-10}$ m. However, Massey discussed the issue above using the term “adiabatic” based on $a\Delta E/hv$. The calculations by Hasted were compatible with that equation, and the value of a was larger by 2π . The value calculated by Hasted corresponds to $a \approx 1 \times 10^{-10}$ m, which is obtained by dividing 7×10^{-10} in (1.73) by 2π . This value is not expected to be extremely precise, but one may expect to use a slightly larger value for molecules. Here, using $a = 3 \times 10^{-10}$ m since organic molecules are larger than atoms, we estimated the collision energy that gives the largest cross section for each value of excitation energy.

As we can see in Table 1.3, when the excitation energy difference grows, the necessary velocity grows proportionally. The necessary collision energy grows with the square of velocity. For a vibrational energy difference of about 0.03 eV, the collision energy of the excitation can be about 100 eV in case of 100 u ions. However, it is necessary to cleave bonds in the molecules in order to perform structural analysis. Therefore, multiple collisions are normally necessary to cleave intramolecular bonds of the order of eV. In the case of low-energy collision used in mass spectrometry, the weakest bond is normally the one to be cleaved, due to the statistical distribution of internal energies. The local maximum that causes an excitation of 1 eV in 100 u ion is 108 keV. Collisions of the order of a few keV can cause a number of excitations of a few eV. In the case of high-energy collisions used in mass spectrometry, the excitation in a single collision causes bond dissociation, whose energy distribution differs from that of low-energy dissociation.

1.11 Probability of a Collision Causing a Specific Reaction

In mass spectrometry, it is important to know the probability of a specific reaction. It is necessary to consider how to determine the probability P for a reaction to occur in view of the collision cross section that causes a specific excitation state. In some cases, the internal energy of the excitation depends on the vibrational frequency, which may spread over several vibration modes. Thus, it is necessary to consider the excitation due to the collision and the reaction caused by that type of excitation. When the collision causes an excitation, it is necessary to consider the Franck-Condon factor. For example, if the ion shown in Table 1.3 with 100 u mass is accelerated by 1.08 keV, its velocity goes up to $4.6 \times 10^5 \text{ m s}^{-1}$. Considering the distance for interaction to be $3 \times 10^{-10} \text{ m}$, the corresponding time for the interaction will be $6.5 \times 10^{-16} \text{ s}$, which is considerably shorter than the usual vibrational frequency of a molecule, 10^{-13} s . In this process, since the internuclear distance does not change from the collision until the start of the excitation, the Franck-Condon factor can be applied similarly to the case of photon and electron excitation, and thus we can suppose that vertical transition takes place. However, in the case of the multiple collisions described by (1.19) of Sect. 5 with a mean free path of $2.9 \times 10^{-2} \text{ m}$, the mean free time for a 100 u ion with kinetic energy of 100 eV is $2.1 \times 10^{-6} \text{ s}$, which is much longer than the vibrational frequency 10^{-13} s and results in vibrational relaxation.

Another discussion related to transition probability is the transfer due to potential crossing. Transfer due to potential can be clearly observed when electron transfer occurs, and that has been a matter of extensive discussion. The reports on potential crossing published in the same year by Landau [17], Zener [18], and Stüeckelberg [19] as well as the report by Demkov [20] are famous examples of model processes related to the inelastic electron transfer.

The model by Landau–Zener–Stüeckelberg considers nonadiabatic transitions governed by pseudo-crossings among adiabatic states that belong to the same symmetry. Transition probabilities for two adiabatic potentials are calculated from matrix elements near the potential crossings. A calculation method was reported for the matrix elements and was successfully applied to many electron transfer collisions. Demkov’s model is applied in the case of perturbations in weak couplings and is based on distorted wave approximation. This model is applied when transitions occur between two potential curves that are parallel with a constant intermolecular distance. Transition probabilities for different reactions are very important and have been the subject of extensive research, but they depend on the particular reaction and cannot be explained in detail in this book. Please refer to the books and other references given in the beginning of the text.

This chapter presented several actual examples and showed how to evaluate numerical values by yourself. You are encouraged to go ahead and try to understand the order of magnitude of energies and cross sections, to deepen your understanding of the basics of mass spectrometry.

References

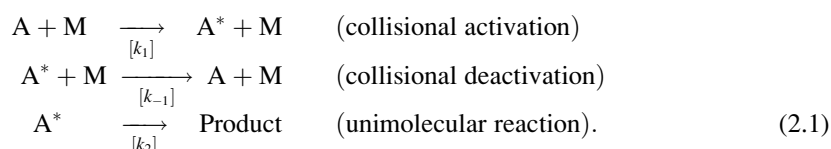
1. Cooks RG (ed), Beynon JH, Caprioli RM (1973) *Metastable ion*. Elsevier, Amstemsam
2. Cooks RG (ed) (1978) *Collision spectroscopy*. Plenum, New York
3. Busch KL, Glish GL, McLuckey SA (1988) *Mass spectrometry/mass spectrometry techniques and application of tandem mass spectrometry*. VCH, New York
4. Levine RD (2005) *Molecular reaction dynamics*. Cambridge University Press, Cambridge
5. Terwillinger DT, Beynon JH, Cooks RG (1974) *Proc R Soc A* 341:135
6. Hayakawa S (1989) *Int J Mass Spectrom Ion Process* 90:251
7. Hayakawa S, Matsumoto A, Yoshioka M, Sugiura T (1992) *Rev Sci Instrum* 63:1958
8. von Engel A (1965) *Ionized gases*, 2nd edn. Oxford University Press, London

9. Kusunoki I (1971) *Bull Chem Soc Jpn* 44:2067
10. Hayakawa S, Kitaguchi A, Kameoka S, Toyoda M, Ichihara T (2006) *J Chem Phys* 124:224320
11. Langevin P (1905) *Ann Chim Phys Ser* 8(5):245
12. Gioumousis G, Stevenson DP (1958) *J Chem Phys* 29:294
13. Koizumi T, Okuno K, Kobayashi N, Kaneko Y (1982) *J Phys Soc Jpn* 52:2650
14. Su T, Bowers MT (1973) *Int J Mass Spectrom Ion Phys* 12:347
15. Massey HSW (1949) *Rep Prog Phys* 12:248
16. Hasted JB (1964) *Physics of atomic collisions*. Butter-worths, London
17. Landau LD (1932) *Z Sov Union* 2:46
18. Zener C (1932) *Proc Roy Soc A* 137:696
19. Stuecklberg ECG (1932) *Helv Phys Acta* 5:370
20. Demkov YN (1964) *Sov Phys JETP* 18:138

Toshihide Nishimura

2.1 Statistical Theory of Unimolecular Dissociation

Gaseous reactions can be categorized as (a) thermal reactions in which activation and deactivation of a molecule proceed via molecule/molecule collisions, and (b) unimolecular reactions of highly excited molecules or ions taking place without collisions:



Thus, unimolecular reaction of a molecule A can be described by the Rice–Ramsperger–Kassel–Marcus (RRKM) theory [1–6], in which a molecule is considered as a set of harmonic oscillators which can interact with each other by exchanging energy freely. The unimolecular reaction rate $k(E)$ is derived by statistical assumptions as follows (Fig. 2.1):

1. An excited molecule A^* with internal energy E can assume all possible internal states, and A^* undergoes unimolecular reactions when it goes beyond the critical state, C. This critical state is often referred to as a transitional state.
2. The internal redistribution of the initial vibrational excitation modes to other possible vibration modes in an activated molecule A^* occurs much faster than unimolecular reaction.

In this model, it is assumed that the initial energy distribution of a reactant can be described statistically and that energy is not exchanged between molecular assemblies. Such assemblies are termed “microcanonical.” Since each state of A^* at a given energy has the same probability with respect to unimolecular reaction, the microcanonical ensemble is conserved via a unimolecular reaction. Therefore, the rate constant of a unimolecular reaction can be described merely using $k(E)$. To be comprehensive, simply replace the term unimolecular reaction with “unimolecular

T. Nishimura (✉)

Biosys Technologies Inc. & Tokyo Medical University, 2012-865 Sasagi, Tsukuba, Ibaraki 305-0043, Japan
e-mail: linne300@hotmail.co.jp

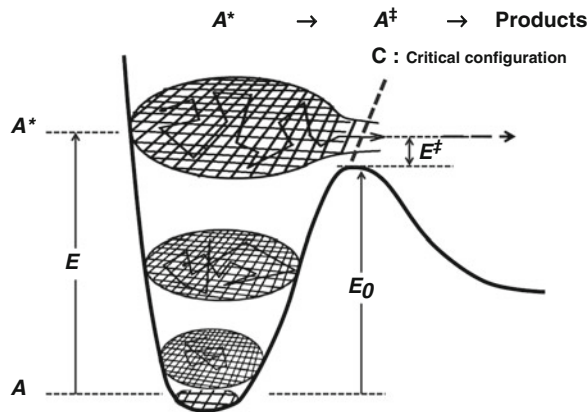


Fig. 2.1 A schematic potential surface of unimolecular reaction (dissociation) of a molecule A, where representative internal-state assemblies at several energies E is shown as a cross section comprising individual states (*squares*). A^* and A^\ddagger are the molecules at excited state and critical configuration. E_0 and E^\ddagger are, respectively, the activation and internal excess energies via unimolecular reaction

dissociation.” From the assumption of rapid redistribution of internal vibrational energy, it follows that an excited molecule A^* at a given energy E has a random lifetime distribution [6] given by

$$P(\tau) = k(E) \exp(-k(E) \tau). \quad (2.2)$$

There is no preference regarding the dissociation of any specific molecule or of its possible radioactive decay.

For a molecular state with a classical energy E , the number of states, N , with one degree of freedom for the momentum p and position q is described as

$$N = \frac{dp dq}{h}, \quad (2.3)$$

where h is Planck’s constant. That is, the phase space volume per unit state equals h , and then the total sum of state, $G(E)$, at a given energy E becomes the total phase space V divided by h :

$$G(E) = \frac{V}{h}. \quad (2.4)$$

When one harmonic oscillator with a vibrational frequency of ν is considered, its classical *Hamiltonian equation* is given as

$$H(p, q) = \frac{p^2}{2} + \frac{\lambda q^2}{2}, \quad (2.5)$$

where $\lambda = 4\pi^2 \nu^2$. Then, the phase space volume is calculated by

$$V = \int_{H=0}^{H=E} \int dp dq = \pi ab \quad (2.6)$$

which is equal to the “ellipse” area with the semimajor and semiminor axes, a and b , given as $b = (2E)^{1/2}$ and $a = (2E/\lambda)^{1/2}$. It then becomes

$$V = \frac{E}{\nu}. \quad (2.7)$$

Therefore, from (2.4) the number of classical states is expressed as

$$G(E) = \frac{E}{h\nu}. \quad (2.8)$$

For the Hamiltonian expanded to the harmonic oscillators ($n = s$)

$$H(p, q) = \sum_{i=1}^s \left(\frac{p_i^2}{2} + \frac{\lambda_i q_i^2}{2} \right), \quad (2.9)$$

its corresponding volume of phase space is similarly obtained by

$$V_s = \frac{E^s}{s! \sum_{i=1}^s \nu_i}. \quad (2.10)$$

Then, the state sum becomes

$$G(E) = \frac{V_s}{h} = \frac{E^s}{s! \sum_{i=1}^s h\nu_i}, \quad (2.11)$$

and so the state density is given as follows:

$$N(E) = \frac{dG(E)}{dE} = \frac{E^{s-1}}{(s-1)! \sum_{i=1}^s h\nu_i}. \quad (2.12)$$

For a molecule comprising harmonic oscillators ($n = s$) having a total energy E , the probability that an internal excess energy, $E - E_0$, beyond a critical energy E_0 in the vibrational modes will lead to facile dissociation is given by

$$\frac{N(E - E_0)}{N(E)} = \left(\frac{E - E_0}{E} \right)^{s-1}. \quad (2.13)$$

Therefore, the classical rate constant $k(E)$ can be expressed using this probability multiplied by the frequency ν of a specific vibrational mode along reaction coordinate [7]:

$$k(E) = \nu \left(\frac{E - E_0}{E} \right)^{s-1}, \quad (2.14)$$

which is known as the classical rate constant (Kassel's equation).

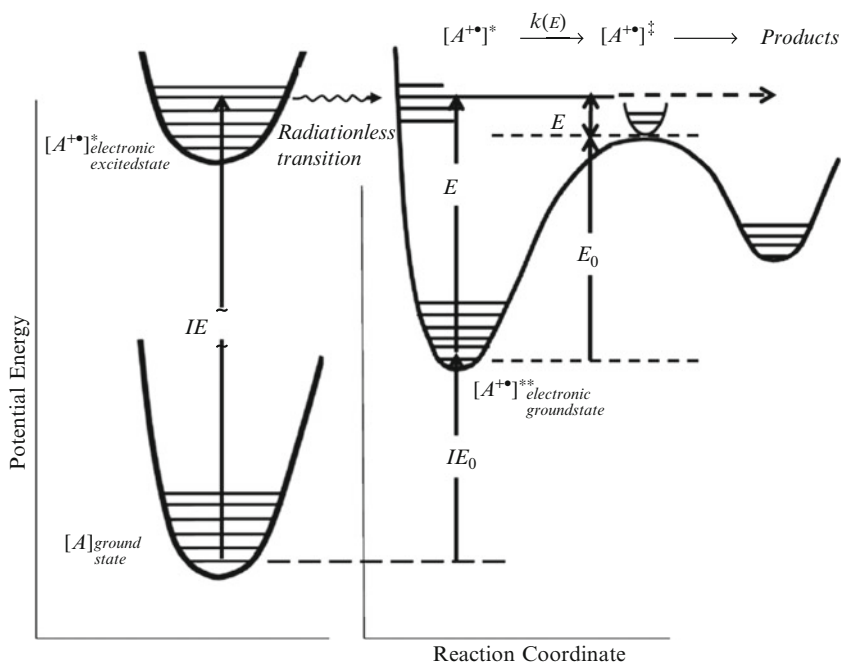


Fig. 2.2 A schematic diagram on unimolecular dissociation based on QET. Ionization of the molecule $[A]$ and internal conversion (radiationless transition) of initially excited electronic states to the ionic ground state $[A^{+\bullet}]$ is followed by unimolecular dissociation

In a mass spectrometer, molecular ions are produced via ionization and are separated according to their m/z prior to detection. In simple cases such as electron ionization (EI) and photoionization (PI), an isolated neutral molecule in the ground state, $[A]_{\text{ground}}$, is first excited to its electronically excited ionic state, $[A^{+\bullet}]^*_{\text{electronic}}$, following the so-called *Franck–Condon principle*. The Franck–Condon principle states that ionization takes place at constant internuclear distance because the removal of an electron (\bullet) occurs within 10^{-16} s and so is much faster than a vibrational oscillation, 10^{-13} – 10^{-14} s. This electronically excited molecular ion then undergoes its unimolecular reaction (dissociation) to dissipate excitation energy. The modern theory of mass spectra, the *quasi-equilibrium theory* (QET), is introduced by Rosenstock et al. [8] based on the following main hypotheses:

1. An electronically excited molecular ion is rapidly converted via radiationless transition (internal conversion) to its electronic ground state ion $[A^{+\bullet}]^{**}_{\text{ground}}$ via vibrational oscillation prior to dissociation (see Fig. 2.2).
2. The rate of dissociation is slow relative to the rate of redistribution of the initial excitation energy over all degrees of freedom.
3. Ions generated in a mass spectrometer represent isolated systems in a series of internal equilibrium.

Thus, a vibrationally excited molecular ion, $A^{+\bullet**}$, in the electronic ground state undergoes unimolecular dissociation following the RRKM scheme as described by $k(E)$ in the previous section.

The kinetic energy release (KER) distribution, $P(E, \varepsilon_t)$, via dissociation can be obtained by

$$P(E, \varepsilon_t) = \frac{G(E - E_0 - \varepsilon_t)}{G(E - E_0)} = (s - 1) \frac{(E - E_0 - \varepsilon_t)^{s-2}}{(E - E_0)^{s-1}}. \quad (2.15)$$

Herein, ε_t is the kinetic energy released via dissociation, and $P(E, \varepsilon_t)$ is the monotonically decreasing function having its maximum at $\varepsilon_t = 0$.

Then, the averaged KER is obtained as

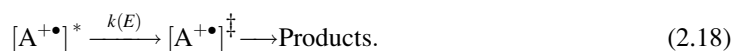
$$\bar{\varepsilon}_t = \int_0^{E-E_0} \varepsilon_t P(E, \varepsilon_t) d\varepsilon_t = \frac{(E - E_0)}{s}. \quad (2.16)$$

Equation (2.16) means that the initial internal excess energy $E - E_0$ is dispersed equally via each possible free motion. Equation (2.16) can be compared with the empirical correlation found by Haney and Franklin for numerous experiments [9]:

$$\bar{\varepsilon}_t = \frac{(E - E_0)}{0.44s} \quad (2.17)$$

in which the denominator $0.44s$ is the parameter called “effective oscillator.”

The modern RRKM theory is constructed by linking the statistical unimolecular reaction rate with its transition state, and so is also referred to as “microcanonical transition state theory” in which vibrational-rotational states are taken into account for the reaction:



The unimolecular dissociation of an activated molecule A^* occurs by passing through the transition state A^\ddagger corresponding to the unique critical configuration leading to products (see Fig. 2.1). Herein, reaction trajectory from A^* to products is assumed to pass a transition state only once. According to classical statistical mechanics, a total flux of trajectories leading to products through the transition state can be described as

$$\begin{aligned} \frac{dN}{dt} &= \frac{N \int_0^{H-E-E_0} \cdots \int dq_2 \cdots d_{3n} dp_2 \cdots dq_{3n}}{\int_{H=E} \cdots \int dp_1 \cdots dp_{3n} dp_1 \cdots dp_{3n}} = \frac{N \int_0^{H-E-E_0} \cdots \int dq_2 \cdots d_{3n} dp_2 \cdots dq_{3n} / h^{3n}}{\int_{H=E} \cdots \int dp_1 \cdots dp_{3n} dp_1 \cdots dp_{3n} / h^{3n}} \\ &= N \frac{G^\ddagger(E - E_0)}{hN(E)}. \end{aligned} \quad (2.19)$$

On the other hand, since the total flux can be written as

$$\frac{dN}{dt} = k(E)N \quad (2.20)$$

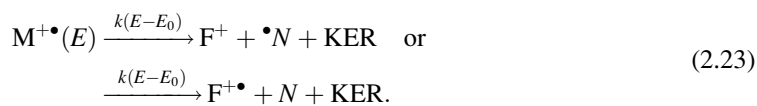
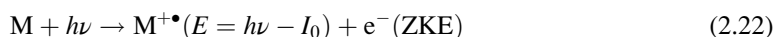
by using the unimolecular rate constant $k(E)$, the microcanonical rate constant of unimolecular reaction is then obtained as follows:

$$k(E) = S \frac{G^\ddagger(E - E_0)}{hN(E)}, \text{ or } = S \int_0^{E-E_0} \frac{N^\ddagger(\varepsilon) d\varepsilon}{hN(E)}. \quad (2.21)$$

Here, S denotes the degeneracy of reaction paths.

2.2 Threshold Photoelectron-Photoion Coincidence Mass Spectrometry

The validity of those theories can be examined experimentally by determining how an energy-selected molecular ion undergoes its unimolecular dissociation. Photoelectron-photoion coincidence (PEPICO) mass spectrometry is the most appropriate method for this purpose. PEPICO mass spectrometry is a powerful method for studying dissociation kinetics of gas-phase ions including determination of their thermochemical quantities [10]. PEPICO mass spectrometry was pioneered by Brehm and Eland more than 40 years ago; a fixed energy light source (usually a He (I) lamp) was used and electrons' energy was analyzed via a retarding grid or hemispherical analyzers [11–13]. Stockbauer and Baer introduced the use of continuum vacuum UV light sources, dispersed by a monochromator, to collect ions in coincidence with threshold photoelectrons (TPE) [11–16]. Threshold PEPICO (TPEPICO) mass spectrometry has been developed as the modern approach because of its better electron energy resolution and more readily extractable ions associated with threshold electron detection. In TPEPICO, only zero-energy (ZKE) electrons are selected for coincidence with the photoions, and the ion energy is scanned by varying the photon energy. The combined photon–electron energy resolution of these experiments approaches, and for one of these instruments has already gone beyond, 1 meV (0.1 kJ mol⁻¹):



Thus, TPEPICO mass spectrometric studies can provide the following detailed kinetic and thermodynamic information based on dissociation of energy-selected molecular ions [17,18]:

1. Appearance potentials of fragment ions (thermochemical onsets)
2. Breakdown curves (dissociation pathways)
3. Metastable dissociation rates, $k(E)$
4. KERs

A time-of-flight (TOF) mass spectrometer is typically employed with TPEPICO since it is appropriate for the measurement of dissociation rate constants corresponding to slow and metastable decay occurring within field regions, and of kinetic energy releases from the TOF distributions of fragment ions. Figure 2.3 shows a schematic of instrumentation used for TPEPICO experiments, in which both a threshold electron analyzer and TOF mass spectrometer are utilized. A threshold (ZKE) electron and fragment ions produced via a single photoionization event are detected as a coincidence signal. A photoelectron triggers a TOF measurement as the “start”; its “stop” signal is given by a fragment ion. A slow dissociation taking place in the field region (denoted by the pink-colored area in Fig. 2.3a) is reflected in its asymmetric TOF distribution of product ions.

As shown in Fig. 2.3b, true coincidences give TOF peaks although random coincidences result in exponential signal slope in the TOF mass spectrum, which can be minimized by controlling ionization events. A TOF distribution also reflects the kinetic energy release distribution accompanied by dissociation. When an ion is ejected opposite to (←) and toward (→) the detector with a larger KER, as indicated in Fig. 2.3a, the former ions reach the detector with a delay due to retardation by the electric field (E_1) and the latter reach it earlier. An example of coincidence TOF mass spectra is

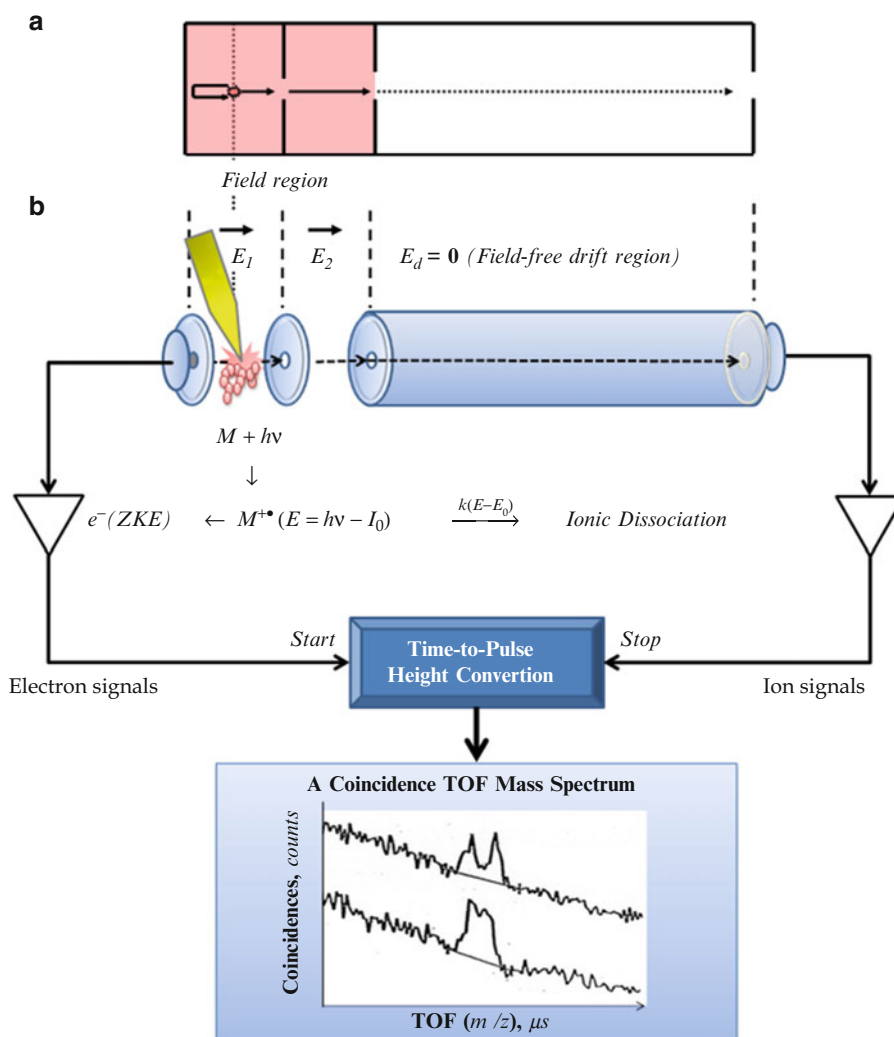
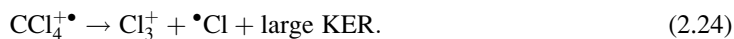


Fig. 2.3 A threshold photoelectron-photoion coincidence (TPEPICO) mass spectrometer equipped with a double-field ionization source

presented in Fig. 2.3b, where a tetrachloromethane ion rapidly decomposes to a trichloromethane ion accompanied by a large and sharp KER (unpublished data):



The dual-peak-shaped distribution observed in the coincidence TOF mass spectrum of CCl_3^+ in Fig. 2.3b is derived from the presence of defined apertures toward the detector in the ionization source.

2.3 Modeling of Dissociation Dynamics: RRKM and Phase Space Theory

The mass spectrum measured by a mass spectrometer results from an integration of the microcanonical rate constant, $k(E)$, being detected as individual ions via the following factors: (1) the initial excitation energy distribution in ionization; (2) thermal energy distribution of a molecule, P_B , prior to ionization; and (3) the reaction time, τ , specific to an apparatus [19]. When the reactant state is at constant temperature, T , and has the Boltzmann distribution, such a molecular assembly is referred to as a “canonical ensemble” and the canonical rate constant $k(T)$ can be written as

$$k(T) = \int_0^{\infty} k(E)P_B(E, T) dE, \quad (2.25)$$

where $P_B(E, T)$ is the normalized Boltzmann distribution function. However, in order to study both reaction dynamics mechanisms and the validity of statistical theories the direct measurement of the microcanonical rate constant, $k(E)$, is essential.

Modern theories of unimolecular dissociation can be classified mainly as the tight-transition RRKM model and loose transition phase space (PS) model [20,21]. However, the two types of transitions incorporated in these models can be understood to approximate a real dissociation dynamics on an intrinsically multidimensional potential supersurface along the reaction coordinates.

A schematic of a hypothetical supersurface displaying reaction coordinates is illustrated in Fig. 2.4. The theories of mass spectra, QET, and/or the RRKM model hypothesize an equilibrium between the “activated complex” and “tight” transition state along the reaction coordinates. The “tight” transition state is located as a “hump” on the potential surface determining both dissociation rate and energy dissipation of products. However, it remains difficult to determine the transition state for a specific dissociation reaction. The cases where there is no “hump” along the reaction coordinates are more difficult but the statistical phase space theory (PST) [21] addresses them in terms of the equilibration between the reactant and product states:

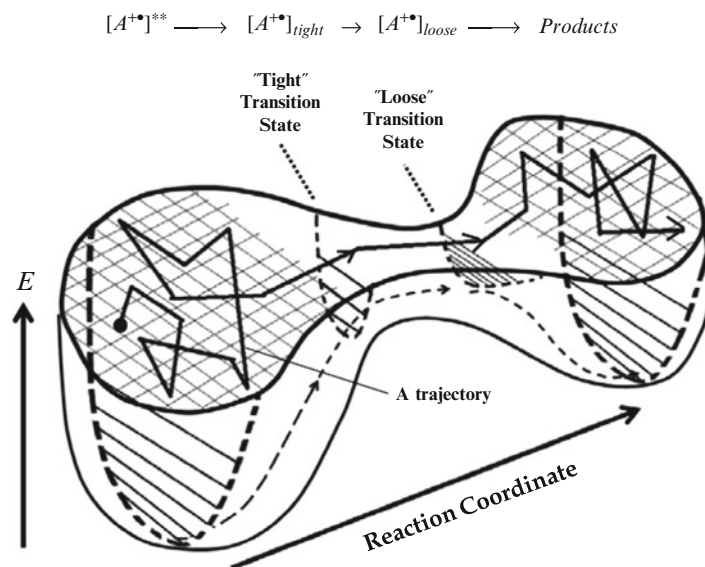
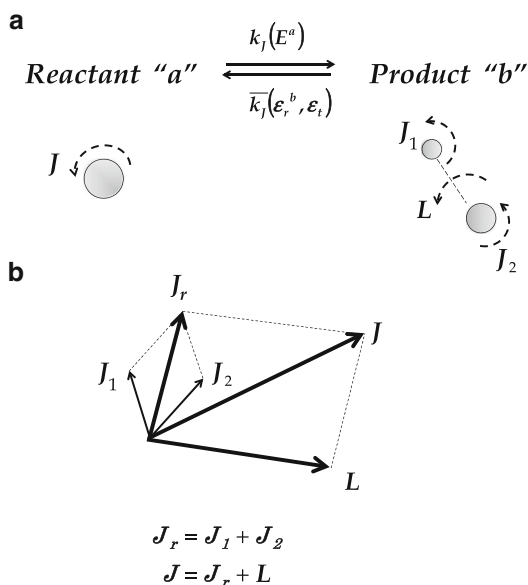


Fig. 2.4 A visualized schematic potential supersurface along a reaction coordinate. The state of a reactant molecular ion proceeds along the reaction coordinate to the states of the product passing through the rate-determining “tight” RRKM transition state and the “loose” PS transition determining the energy partitioning of the product (see [22–24] for fundamental properties of reaction potential surfaces)

Fig. 2.5 The conservation of total angular momenta and coupling of each momentum. J_1 and J_2 are the rotational angular momentum vectors of products, J_r their total momentum vector, and L the orbital angular momentum vector



Consider a system consisting of the molecular ion as the reactant “a” and the product (the fragment ion plus neutrals) “b.” In PST both the forward and reverse reaction fluxes are in detailed equilibration so that the total angular momentum J and total internal energy E^a are conserved, namely,

$$R_J(a \rightarrow b) = R_J(b \rightarrow a). \quad (2.26)$$

The coupling of angular momentum vectors between “a” and “b” is shown in Fig. 2.5.

The reverse reaction rate is given by the association reaction rate $\bar{k}_J(\epsilon_r^b, \epsilon_t)$ between an ion and neutral species with available relative translational energy ϵ_t and total rotational energy, ϵ_r^b . Assuming that *Langevin* ion-molecular reaction model [25] is applied to this association reaction, there is no need for activation energy. The only reaction barrier is the local maximum point of the effective potential that consists of long-range ion-dipole potential and centrifugal force between an ion and neutral species, and an association reaction takes place whenever the energetics of a projectile ion and neutral molecules equal or exceed the maximum of this potential barrier. Therefore, the transition state in PST is often termed an “Orbiting” transition state since it is defined as this maximum point along the association reaction [21].

A cautionary note is in order regarding the proper use of RRKM calculations. The RRKM theoretical frame calculations compare only the properties of the transition state of the fragmenting molecule (A^\ddagger) with those of the excited normal configuration of the molecule (A^*). Therefore RRKM theory is only appropriate for calculating rates or state distributions in the region of the transition state on the potential surface. RRKM theory is not appropriate for calculating properties of the system in the product region of the energy surface. Other simplifying assumptions should be kept in mind as well. There are $3n - 12$ vibrational degrees of freedom in the products versus $3n - 6$ in the normal configuration of the fragmenting molecule and $3n - 7$ in the transition state. This situation is not considered in RRKM analysis. Also in the classical RRKM theory neither conservation of angular momentum nor long-range potential of the system are taken into account.

The microcanonical dissociation rate constant of the reactant “*a*” with rotational angular momentum *J* can be expressed as

$$k_J(E^a) = \frac{\sigma_a S_r^b}{\sigma_b S_r^a} \left\{ \frac{\int \int \overline{k}_J(\varepsilon_r^b, \varepsilon_t) N_t(\varepsilon_t) N_r(\varepsilon_r^b) d\varepsilon_t N_b(E^a - E_0 - \varepsilon_r^b) d\varepsilon_r^b}{N^a(E^a - \varepsilon_r^a)} \right\}. \quad (2.27)$$

Herein, $N_t(\varepsilon_t)$, $N_r(\varepsilon_r^b)$, and $N_b(E^a - E_0 - \varepsilon_r^b)$ are, respectively, the state densities of translation, rotation, and vibration of the product “*b*”. S_r^a and S_r^b are degeneracies of spatial angular momenta of the system “*a*” and “*b*.” σ_a and σ_b are the numbers of symmetry for the forward $a \rightarrow b$ and reverse $b \rightarrow a$ reactions. Then, the rate constant to be compared to experiment can be obtained by averaging the thermal distribution $P(J)$ of *J*:

$$k(E^b) = \frac{\int_0^\infty k_J(E^b) P_J(J) dJ}{\int_0^\infty P_J(J) dJ}. \quad (2.28)$$

The probability that the reactant “*a*” decomposes with internal energy E^a and angular momentum *J*, and accompanying KER ε_t , is given as

$$P_J(E^a, \varepsilon_t) = \frac{k_J(E^a, \varepsilon_t)}{k_J(\varepsilon_t)}. \quad (2.29)$$

Dissociations can be only observed when an ion decomposes within the field region in a TOF mass spectrometer (shown in Fig. 2.3a). In general this time window is defined between an entering time τ_1 and exiting time τ_2 . The probability that the reactant “*a*” decomposes between τ_1 and τ_2 becomes

$$P_\tau(E^a, J) = \exp\{-k_J(E^a)\tau_1\} - \exp\{-k_J(E^a)\tau_2\}, \quad (2.30)$$

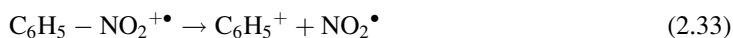
whereas τ_1 is usually 0 in a TOF mass spectrometer. Therefore, the KER distribution obtained from TPEPICO experiments is described as

$$P(\varepsilon_t) = \frac{\int_0^\infty dJ P(J) P_\tau(E^a, J) P_J(E^a, \varepsilon_t)}{\int_0^\infty dJ P(J) P_\tau(E^a, J)} \quad (2.31)$$

and the averaged KER ($\overline{\varepsilon}_t$) at a given E^b will be

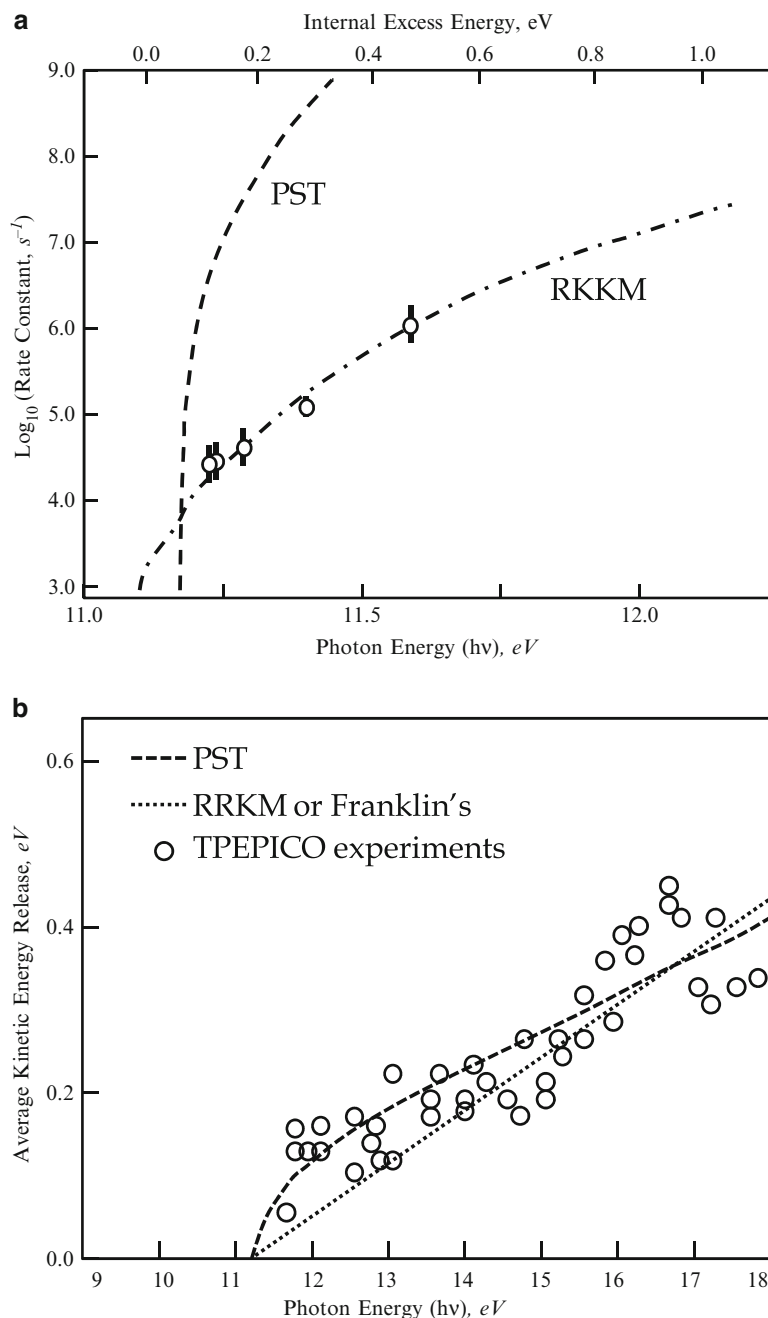
$$\overline{\varepsilon}_t(E^b) = \frac{\int_0^{E^b} \varepsilon_t P(\varepsilon_t) d\varepsilon_t}{\int_0^{E^b} P(\varepsilon_t) d\varepsilon_t}. \quad (2.32)$$

As an example, the dissociation rates and averaged KERs for the formation of phenyl cation from nitrobenzene radical cation [26]



are shown in Fig. 2.6.

Fig. 2.6 (a) The dissociation rate constants and (b) kinetic energy releases in the dissociation of $C_6H_5NO_2^{+\bullet}$ to $C_6H_5^+$ and NO_2^{\bullet} , measured by the TPEPICO experiments [26] (those figures newly redrawn)



The TPEPICO decay rates (ϕ) as a function of internal excess energy were well interpreted by the RRKM calculation whereas the PST predicted much higher rates. In contrast, the averaged KERs obtained experimentally seem to be better fitted with PST although both PST and Franklin's empirical formulae gave reasonable matches to experiment. Even in the case where a potential surface is smooth without the "rigid" transition state (which is the model of the RRKM tight transition state,

the so-called hump) from the reactant “*a*” to the product “*b*,” the rate-determining factor is the RRKM decay rate corresponding to the lowest density state perpendicular to the reaction coordinate. The “Orbital” transition state is located much closer to the product “*b*,” and so their energy partitioning including kinetic energy release is determined. Therefore, several transition states along the reaction coordinates are utilized to approximate a real reaction dynamics of dissociation. In Fig. 2.4, a rigid RRKM transition state and loose “Orbital” transition state are indicated along the reaction supersurface. As seen in the example of the phenyl cation formation from the nitrobenzene radical cation, the rate constant is supposed to fit the RRKM theory since the reaction flux of the RRKM transition state is rate limiting while the KER reflecting the final energy partitioning would be determined by the “Orbiting” state. This concept was first introduced by Miller (1976) [27] as the unified statistical theory (UST), in which at least two “transition states” are assumed on the reaction coordinate.

2.4 Breakdown Curves

The validity of statistical theories can be assessed in their comparison with experimentally constructed breakdown curves for the molecular ion and its product ions. Experimental breakdown curves are obtained by TPEPICO mass spectra measured as a function of photon energy. Breakdown curves are the plot of product-ion relative abundances with a certain reaction time contingent on the internal energy of the molecular ion. With a known internal energy distribution of the molecular ion $P_{\text{int}}(E)$ resulting from ionization, the relative abundance of a product ion $[m^+]_t$ at a reaction time t can be given as

$$[m^+]_t = \int_0^{E_{\text{max}}} P_{\text{int}}(E) B_{m^+}(E, t) dE, \quad (2.34)$$

where $B_{m^+}(E, t)$ is the breakdown curve of the product ion m^+ . The reaction time is that required for a molecular ion to travel across the field regions (\vec{E}_1 and \vec{E}_2 in Fig. 2.3).

2.4.1 Consecutive Reaction

For the following consecutive reaction

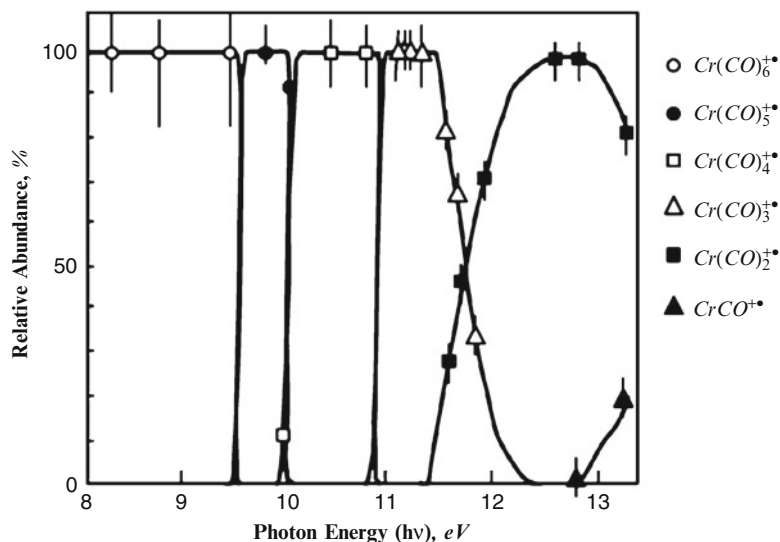


the relative abundances of product ions at the reaction time t as a function of the internal energy E are given by

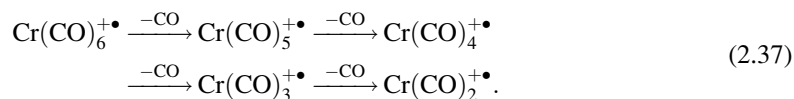
$$\begin{aligned} [A^+]_t &= \exp(-k_1 t) \\ [m_1^+]_t &= k_1 \frac{\{\exp(-k_1 t) - \exp(-k_2 t)\}}{k_2 - k_1} \\ [m_2^+]_t &= 1 - \frac{\{k_2 \exp(-k_1 t) - k_1 \exp(-k_2 t)\}}{k_2 - k_1} \end{aligned} \quad (2.36)$$

and herein $[A^+]_{t=0} = 1$.

Fig. 2.7 The TPEPICO breakdown curves of hexacarbonyl chromium ion (modified from [28])



A typical consecutive reaction can be found in the dissociation of hexacarbonyl chromium ion, $\text{Cr}(\text{CO})_6^{+\bullet}$ [28]. The experimentally elucidated breakdown curve of this molecular ion reflects its consecutive fragmentations with the successive loss of CO up to the photon energy less than 13 eV (Fig. 2.7):



As a different example, it has been known that $\text{C}_{60}^{+\bullet}$ undergoes successive loss of C_2 up to the molecular internal energy less than 80 eV (Fig. 2.8) [29]. With increasing internal energy, the fullerene radical cation changes its 3-D structure, from the so-called Solid to Floppy phase and from Floppy to Pretzel phase. Moreover, the fullerene radical cation explosively dissociates to the small carbon-cluster ions at the same internal energy which coincided with the internal energy equal to the Pretzel phase (Fig. 2.9). This dissociative behavior of $\text{C}_{60}^{+\bullet}$ has been observed from the relative cross-section measurements for the collision-induced dissociation of $\text{C}_{60}^{+\bullet}$ by varying the center-of-mass (CM) collision energy in mass-analyzed ion kinetic energy spectroscopy (MIKES) experiments.

2.4.2 Competitive Reaction

Similarly, for the simple competitive reaction



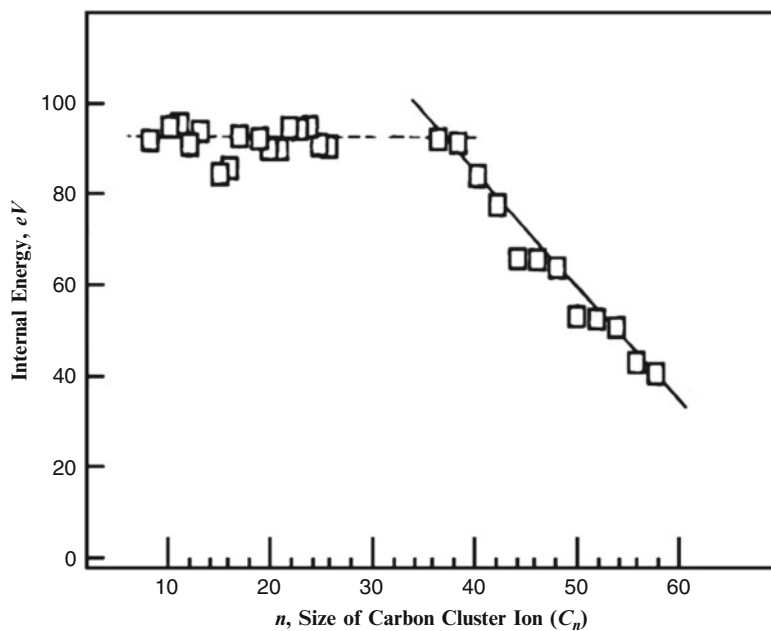


Fig. 2.8 Appearance energies of carbon-cluster ions elucidated from the CM collision energy-dependent MIKES experiments (modified from [29])

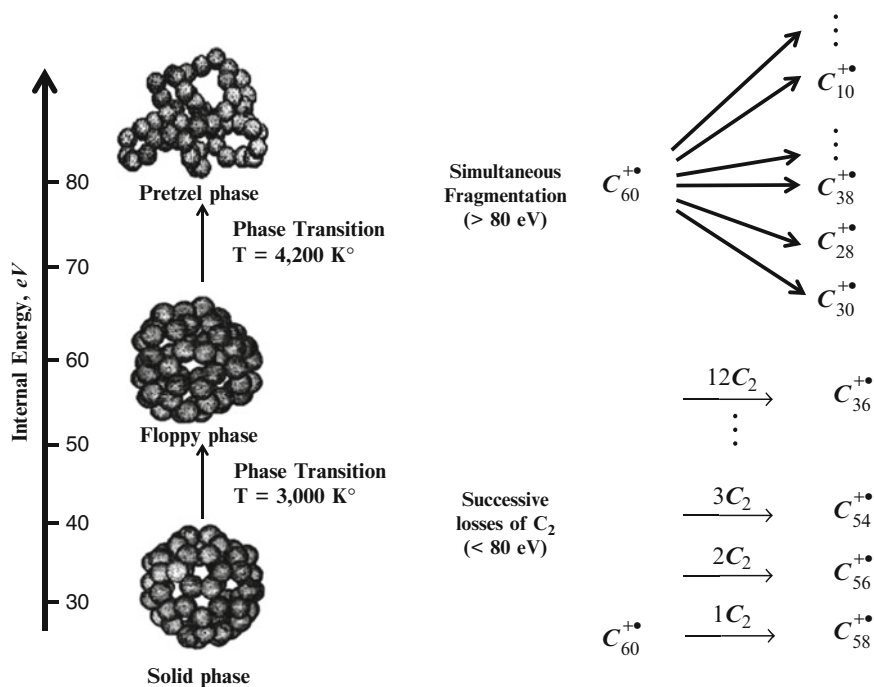


Fig. 2.9 The successive fragmentation of the fullerene radical cations $C_{60}^{+•}$ occurring at lower internal energies, and their fragmentations to the smaller carbon-cluster ions simultaneously at the Pretzel phase

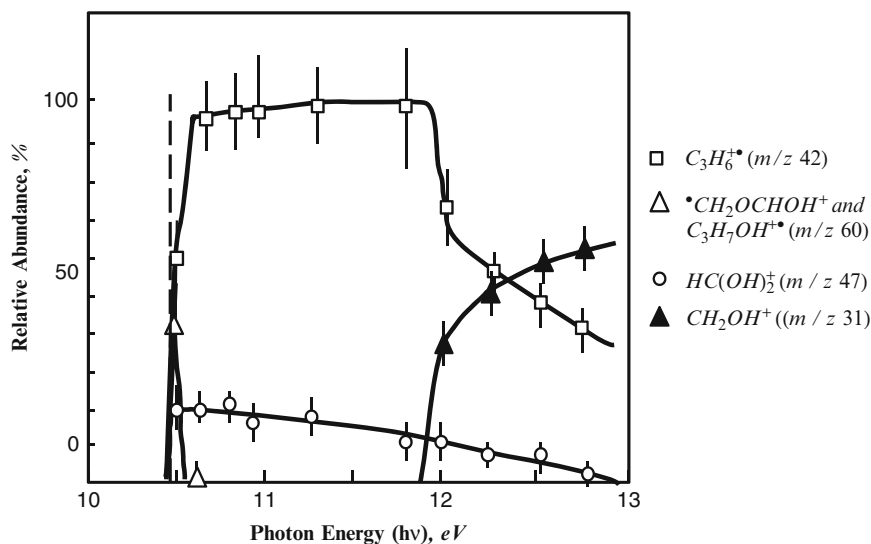


Fig. 2.10 The TPEPICO breakdown curves of propyl formate radical cation at a photon energy of 10–13 eV (modified from [30])

the relative abundance of their product ions at the reaction time t as a function of E is

$$\begin{aligned}
 [A^+]_t &= \exp(-k_{\text{total}} t) \\
 [m_i^+]_t &= k_i \frac{\{1 - \exp(-k_{\text{total}} t)\}}{k_{\text{total}}} \quad (i = 1, 2, 3).
 \end{aligned}
 \tag{2.39}$$

Here, k_{total} is the total reaction rate constant ($= k_1 + k_2 + k_3$). Their breakdown curves are given merely as the ratio among respective reaction rate constants.

Breakdown curves can determine the appearance potentials (APs) of fragment ions and give the possible fragmentation scheme of a molecular ion. Such direct comparison with statistical theories can provide insight into ionic dissociation dynamics.

The following breakdown curves are obtained for propyl formate radical cations, $\text{HCOOC}_3\text{H}_7^+\bullet$, by using TPEPICO mass spectrometry (the energy resolution of threshold photoelectrons is ca. 21 meV) [30]. Of particular significance in this breakdown curves is that the appearance energies of four fragment ions $\text{C}_3\text{H}_6^+\bullet$ (m/z 42), $\text{HC}(\text{OH})_2^+$ (m/z 47), and $\bullet\text{CH}_2\text{OCHOH}^+$ and $\text{C}_3\text{H}_7\text{OH}^+\bullet$ (m/z 60) are identical with the measured ionization energy of the propyl formate molecule (that is, 10.45 ± 0.05 eV as indicated by the dashed line in Fig. 2.10). These observations are interpreted by assuming that the propyl formate radical cation first isomerizes to the distonic intermediate (i) prior to dissociation, and then competitive fragmentations occur via this distonic intermediate (Fig. 2.11). A possible mechanism for the formation of $\text{C}_3\text{H}_6^+\bullet$ (m/z 42) is a two-step McLafferty rearrangement (Fig. 2.12), involving the intermediacy of a distonic radical cation (i). The formation of $\text{HC}(\text{OH})_2^+$ is the so-called [R–2H] loss reaction or “McLafferty +1” rearrangement. Both occur via the intermediacy of (i).

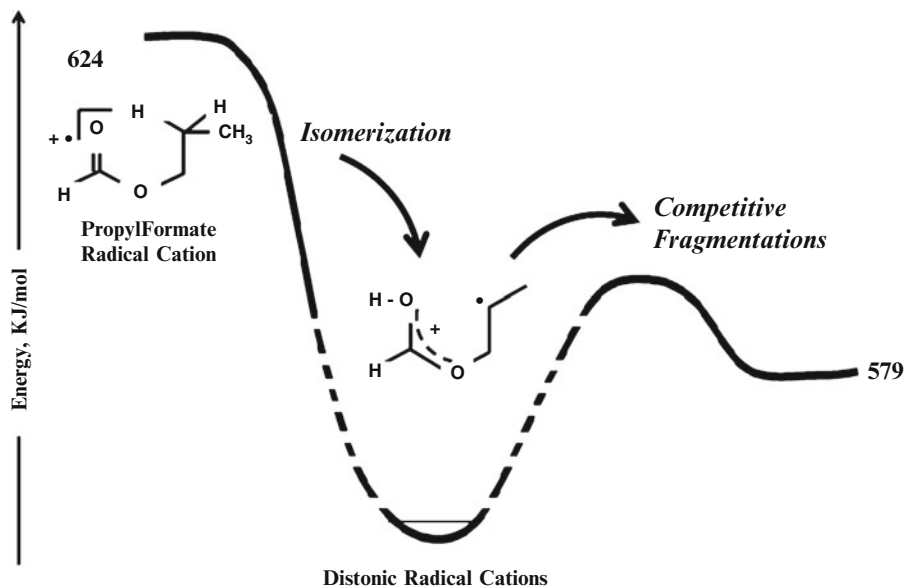


Fig. 2.11 A schematic potential energy surface for the fragmentation of the propyl formate radical cation undergoing isomerization to a distic radical cation (i)

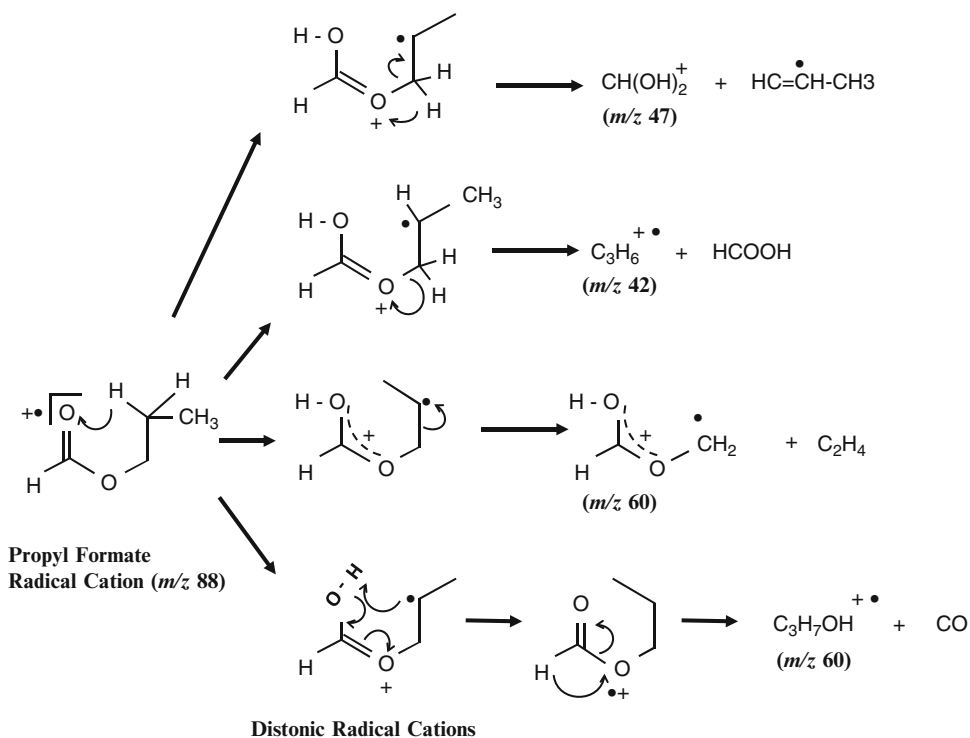


Fig. 2.12 Competitive fragmentations from a distic radical cation that is formed via *MacLafferty* rearrangement of the propyl formate radical cation prior to dissociation

2.5 TOF Distributions of Product Ions

The TOF distribution of a product ion would reflect both the dissociation rate $k(E)$ and KER in dissociation.

2.5.1 Metastable Dissociations

Metastable dissociations occurring in the field regions (indicated in pink in Fig. 2.13 and also in Fig. 2.3a) result in asymmetric TOF distributions of product ions whereas for dissociation in the field-free drift region the TOF of its product ions is the same as that of the molecular ion. Figure 2.13 illustrates the origin of asymmetric TOF distribution of product ions.

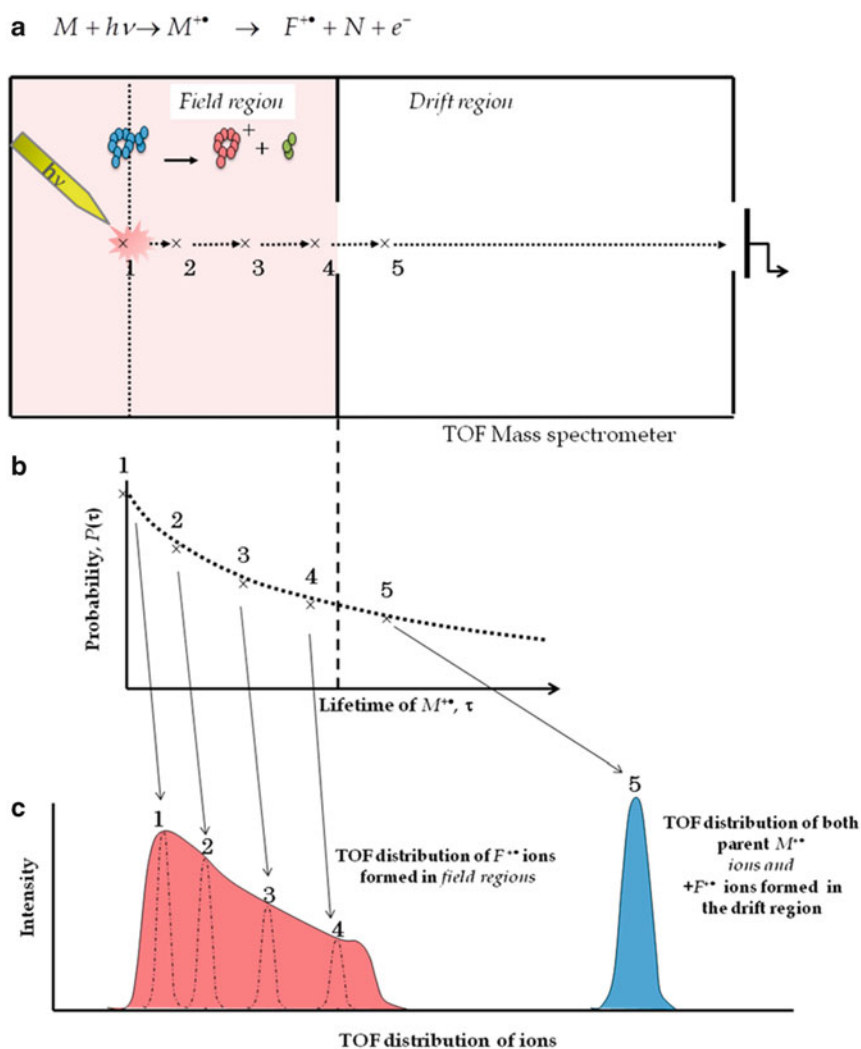


Fig. 2.13 Metastable dissociation of a parent ion (M^{**}) to a product ion (F^{**}) and their TOF distributions

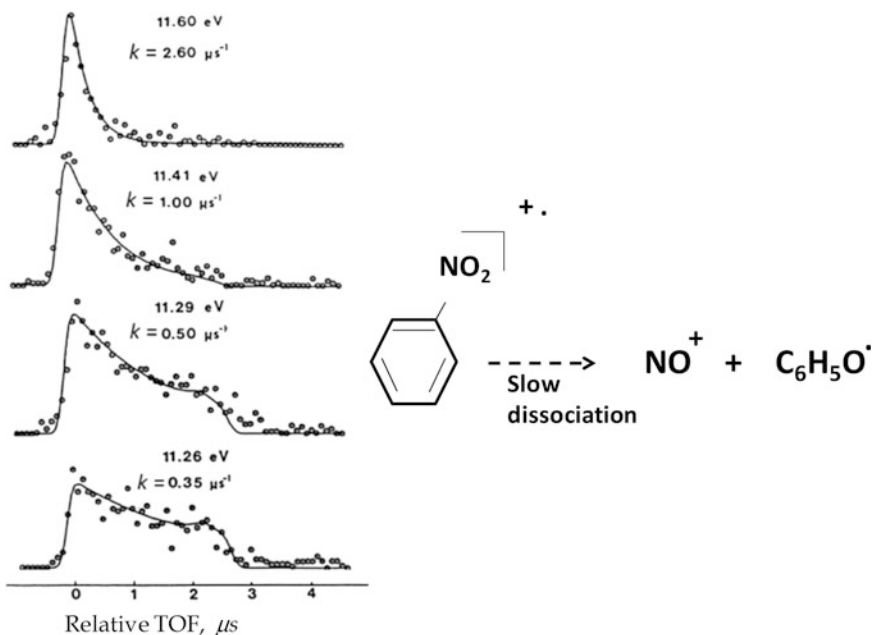


Fig. 2.14 Asymmetric TOF distributions due to metastable fragmentation (modified from [26]). The metastable formation of NO^+ from nitrobenzene radical cation. Individual dissociation rates (k) were obtained so that TOF distributions could be obtained on the basis of ion trajectory calculation assuming that lifetimes of the parent ion (solid curves) give the best fit to experiments (filled circle)

Figure 2.14 shows the examples of asymmetric TOF distributions due to metastable decay occurring in the electric field regions. Based on ion trajectory calculations, metastable decay constants can be elucidated from the best least-square fit curve with experimental TOF distributions.

2.5.2 Kinetic Energy Releases in Dissociation

When the isotropic fragmentation of the ion M^+ to the fragment ion m^+ and neutral fragment $[\text{M} - \text{m}]$ accompanies a single KER Q_i in center of mass



the TOF distribution $F(\tau; Q_i)$ of the ion m^+ can be calculated numerically. Each TOF distribution observed, $F(\tau)$, is deconvoluted by a set of the TOF distributions $F(\tau; Q_i)$ corresponding to a series of KERs defined as

$$Q_i = (2i - 1)^2 E_0. \quad (2.41)$$

Herein, $F(\tau; Q_i)$ is normalized and E_0 is chosen as the minimum KER to broaden a thermal peak by one channel width of a TOF spectrum. Then, from the coefficients $W(i)$ which give the best fit to experiment

$$F(\tau) = \sum_i W(i) F(\tau; Q_i). \quad (2.42)$$

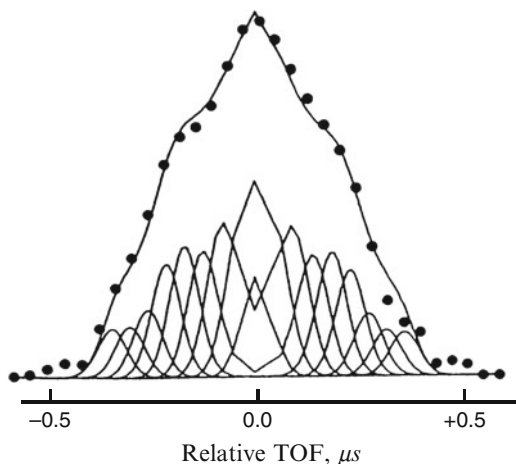


Fig. 2.15 A TPEPICO TOF distribution of m/z 29 ion produced from $\text{HCOOH}^{+\bullet}$ at the photon energy of 7.28 eV. Using $E_0 = 8.16$ meV and room temperature $T = 300$ K², the experimental $F(\tau)$ (filled circle) was deconvoluted with the calculated $F(\tau; Q_i)$ with the nine discrete KERs Q_i ($i = 1 - 9$) (solid curves) (modified from [31])

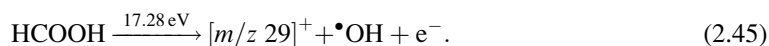
The KER distribution (KERD), $P(Q_i)$, can be formulated as

$$P(Q_i) = \frac{\left[\frac{W(i)}{\sum_i W(i)} \right]}{[4(2n - 1)E_0]}. \quad (2.43)$$

The averaged KER can then be given as

$$\langle Q \rangle = \frac{\sum_{i=1}^l Q_i P(Q_i)}{\sum_{i=1}^l P(Q_i)}. \quad (2.44)$$

Figure 2.15 shows the TOF distribution of m/z 29 ion obtained by TPEPICO experiments of the formic acid radical cation [31]:



2.6 Energy Disposal and Theoretical Expectations

The theoretical model commonly used to describe the KERD is based on statistical theory, in which the energy in excess of the dissociation limit is assumed to be distributed statistically among the product electronic, vibrational, rotational, and translational degrees of freedom, subject only to the conservation of angular momentum. The average energy deposited in the various modes can be easily calculated by

$$E^* = \langle E_t \rangle + \langle E_r \rangle + \langle E_v \rangle, \quad (2.46)$$

in which E^* is the energy in excess of the dissociation limit, and $\langle E_t \rangle$, $\langle E_r \rangle$, and $\langle E_v \rangle$ are, respectively, the average energies residing in the translational, rotational, and vibrational degrees of freedom. To assess how experiments compare with theoretical expectations, there are several approaches described below.

2.6.1 Scaling Law

The scaling law was first applied to thermodynamics of phase transition by Widom [32] and Domb and Hunter [33]. The function Γ is defined to be homogeneous when Γ has the following relation with the scaling λ :

$$\Gamma(\lambda r) = \lambda^p \Gamma(r). \quad (2.47)$$

Herein, p is the degree of homogeneity. In cases where Γ has two variables, r and q , it can be similarly expressed as

$$\Gamma(\lambda r, \lambda q) = \lambda^p \Gamma(r, q). \quad (2.48)$$

Then, by defining $\lambda = 1/r$ (2.48) can be rewritten as

$$\Gamma\left(1, \frac{q}{r}\right) = r^{-p} \Gamma(r, q). \quad (2.49)$$

This means that by conversions with $q \rightarrow q/r$ and $\Gamma \rightarrow r^{-p}\Gamma$, all points $(r; \Gamma(r, q))$ are located on one smooth curve being determined by only one variable q/r .

When this scaling law is applied to the kinetic energy distribution $P(E, \varepsilon_t)$, this distribution as a function of different internal energy E will be plotted on one distribution if $P(E, \varepsilon_t)$ is homogeneous as per the following conversion:

$$\begin{aligned} \varepsilon_t &\rightarrow \frac{\varepsilon_t}{E} \\ P &\rightarrow EP. \end{aligned} \quad (2.50)$$

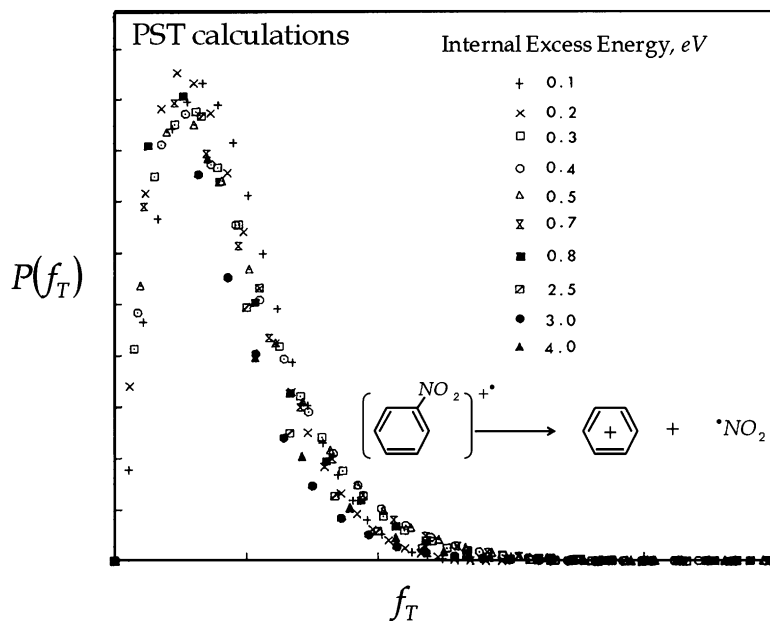
It can be demonstrated that the KERD based on RRKM theory is expressed by a single curve by the above conversion. For an example, the classical RRKM KERD is given by

$$\begin{aligned} P(E^a, \varepsilon_t) &= \frac{N^{\ddot{o}}(E^a, \varepsilon_t)}{G^{\ddot{o}}(E^a)} \\ &= s \frac{(E^a - \varepsilon_t)^{s-1}}{(E^a)^s} = s \left(\frac{E^a - \varepsilon_t}{E^a} \right)^{s-1} \frac{1}{E^a}. \end{aligned} \quad (2.51)$$

Therefore, the conversion results in

$$E^a P(E^a, \varepsilon_t) = s \left(1 - \frac{\varepsilon_t}{E^a} \right)^{s-1}. \quad (2.52)$$

Fig. 2.16 The scaling plots of KERDs for the dissociation of nitrobenzene ion $C_6H_5NO_2^{+\bullet}$ to phenyl cation $C_6H_5^+$ and $\bullet NO_2$, calculated at various internal excess energies by PST



That is, for the one variable $f_T = \epsilon_t/E^a$, $P(f_T) = E^a P(E^a, \epsilon_t)$ becomes the single distribution. This is a central feature of statistical theories in which the internal excess energy is uniformly distributed to all available degrees of freedom regardless of its value. This applies to the statistical phase space (PS) theory. Figure 2.16 shows the KERD calculated by PST and obtained by the conversion (2.52) for the dissociation of nitrobenzene molecular ion to phenyl cation (unpublished data).

In the TPEPICO experiments of ethyl bromide ions ($C_2H_5Br^{+\bullet}$) [34], the KERDs for the formation of $C_2H_5^+$ were extracted as a function of the parent-ion internal energy as described in the previous section. Those KERDs were converted using $f_T = \epsilon_t/E^a$ and $P(f_T) = E^a P(E^a, \epsilon_t)$ as plotted in Fig. 2.17. If all fragmentations to $C_2H_5^+$ occur in the same dynamic range, then the scaling plot of KERDs should be represented by a single curve. However, Fig. 2.17 features two different curves in the scaling plot of KERDs. That is, the KERDs for the ethyl bromide ion dissociation were statistical only in the region of the ground electronic state. Ions prepared in the A state have KERDs characteristic of a direct dissociation. This indicates that the direct dissociation rate is faster than the rate of radiationless transition to the ground electronic state. The QET assumes that the internal conversion of the initially excited electronic states to the ground state takes place much faster than ionic dissociation. The scaling plot for the formation of $C_2H_5^+$ from $C_2H_5Br^{+\bullet}$ [34] represents an example of a breakdown of the QET.

2.6.2 Information Theoretical Approach

Another approach to examine how the state distribution of products resulting from the reactant matches theories is based on information theory. Jaynes [35] first presented a mathematical link to statistical mechanics with the information theory, which Levine and Bernstein then applied to molecular reaction dynamics [36,37]. The central concerns are (1) “What is the prior expectation?” and “What is the measure for deviation from expectation?” To answer these questions, the “Surprisal” concept was introduced.

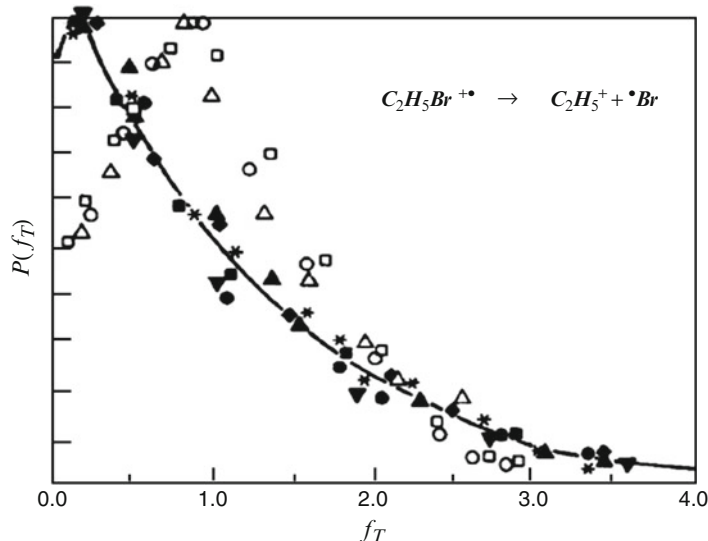


Fig. 2.17 The scaling plots of KERDs for the dissociation of ethyl bromide $C_2H_5Br^{+\bullet}$ to $C_2H_5^+$ and $\bullet Br$, revealing a distinct difference between ions with photon energies above (*open circle, open triangle, open square*) and below (*filled square, filled circle, filled triangle, asterisk, inverted triangle*) the \tilde{A} state onset near 12.0 eV (modified from [34]). The *solid line* is the result calculated by statistical theory with angular momentum conservation similar to PST

2.6.2.1 Surprisal Analysis

Consider events A, B, etc. which are independent of each other. Each surprisal $I(A)$ is defined as

$$I(A) \equiv -\ln P(A). \quad (2.53)$$

Herein, $P(A)$ is the probability of event A. Then the surprisals, $I(A)$ and $I(B)$, satisfy the following mathematical relationship. Since for the probability of event $A \cap B$ (“B takes place following A”)

$$P(A \cap B) = P(A) \times P(B), \quad (2.54)$$

the following relation between surprisals holds:

$$I(A \cap B) = I(A) + I(B). \quad (2.55)$$

When a priori probability $P^\circ(A)$ is given, the surprisal is redefined to be

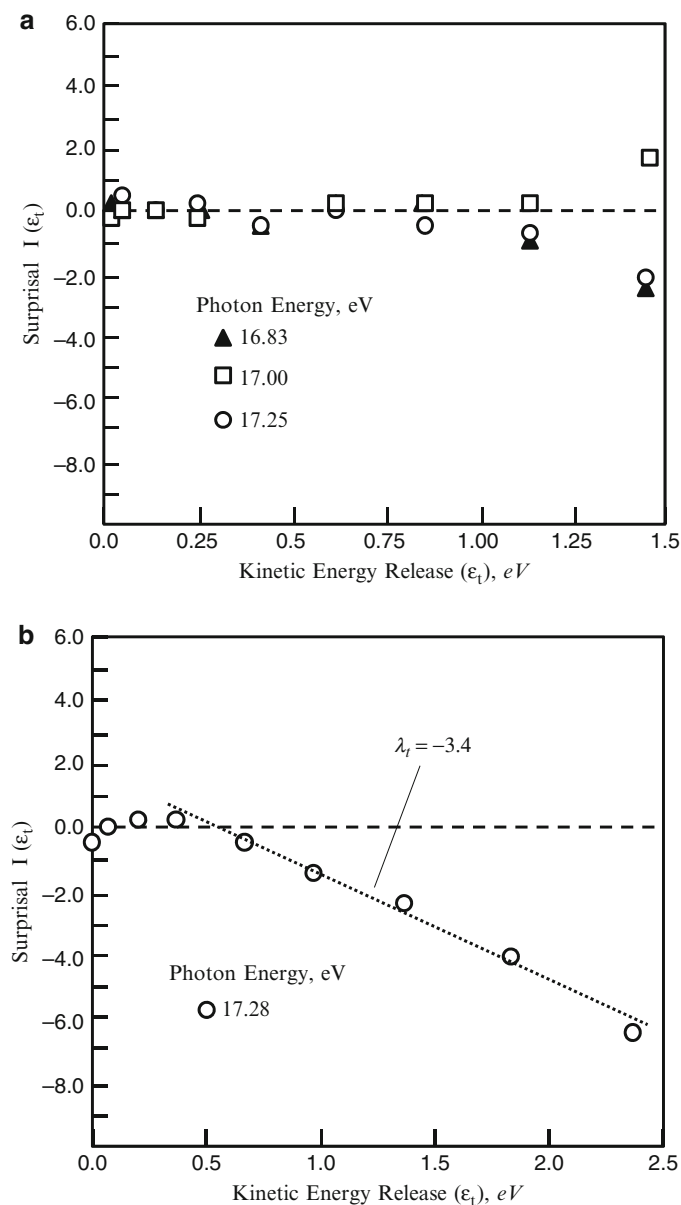
$$I(A) \equiv -\ln P(A) - \{-\ln P^\circ(A)\} = -\ln[P(A)/P^\circ(A)]. \quad (2.56)$$

In other words, $I(A)$ is the measure for deviation of observed probability $P(A)$ from $P^\circ(A)$. The kinetic energy distribution (KERD) is one of physical observations reflecting the energy disposal among final products resulting from dissociation dynamics. A priori KERD would be given by the expectation based on RRKM/PST.

Those surprisal plots clarify deviations from expected values as a function of each state variable (f) of products. Usually, the function

$$P(f) / P^\circ(f) \equiv \omega(f) \quad (2.57)$$

Fig. 2.18 The surprisal plots on KERDs: (a) The C_2H_2 -elimination from fluorobenzene ion at several photon energies (modified from [38]), and (b) the m/z 29 ion formation from formic acid radical cation $HCOOH^{+\bullet}$ (modified from [31])



is a smooth function. The so-called temperature constant (λ_f) is introduced in relation to each state quantity (vibration, rotation, and translation) to indicate deviation from an expected distribution.

Figure 2.18 shows examples of surprisal analyses on the KERDs observed for two dissociative reactions. The surprisal analysis of KERDs for the C_2H_2 -elimination from the fluorobenzene radical cation demonstrates that $I(\epsilon_t) \approx 0$ over KERs (ϵ_t) at several photon energies (Fig. 2.18a) [38]. This means that this fragmentation can be interpreted by the statistical RRKM theory. In contrast, the formation of CHO^+ (m/z 29) from formic acid radical cation showed $I(\epsilon_t) \approx 0$ with kinetic energies less than 0.5 eV but a surprisal with the linearity ($\lambda_t = -3.4$) was revealed (Fig. 2.18b) [31], most probably indicating participation of two different dissociation dynamics rather than the formation of two different ion species, HCO^+ and COH^+ .

Since the slope of the surprisal plot is given by

$$\lambda_f \equiv \frac{dI(f)}{df}, \quad (2.58)$$

an observed distribution $P(f)$ can be expressed with the distribution characterized by λ_f

$$P(f) = P^\circ(f) \frac{\exp(-\lambda_f f)}{\exp(-\lambda_0)}. \quad (2.59)$$

Herein the denominator is

$$\exp(-\lambda_0) = \sum_f P^\circ(f) \exp(-\lambda_f f) \equiv Q_f, \quad (2.60)$$

which serves as the partition function Q_f . That is, the average $\langle f \rangle$ is expressed as

$$\langle f \rangle = \sum_f f P(f) = -\frac{d \ln Q_f}{d\lambda_f}. \quad (2.61)$$

2.6.2.2 Principle of Maximum Entropy [36]

The 1st-order (“linear”) surprisal observations can be accounted for by the principle of maximum entropy that follows from statistical dynamics. That is, the most probable distribution being observed is that which has the maximum entropy, subject to the particular constraints of a system. For example, regarding the vibrational state distribution P^v , this system at least is constrained per

$$1 = \sum_j P^v(j) \quad (\text{Normalization}), \quad (2.62)$$

and

$$\langle E_j^v \rangle = \sum_j P^v(j) E_j^v \quad (\text{1st momentum term of vibrational energy}). \quad (2.63)$$

Maximizing the system entropy under the above conditions does correspond to minimizing the “information quantity” (I)

$$I = \sum_j P^v(j) \ln \left[\frac{P^v(j)}{P^\circ(j)} \right] \quad (2.64)$$

upon the averaged surprisal (P^v). Then, for its *Lagrangian* (L)

$$L = I + \alpha \langle 1 \rangle + \beta \langle E_j^v \rangle \quad (2.65)$$

$\delta L = 0$ should be calculated. That is,

$$\begin{aligned} 0 = \delta L &= \delta \left[\sum_j (P_j^v \ln P_j^v - P_j^v \ln P_j^o + \alpha P_j^v + \beta P_j^v E_j^v) \right] \\ &= \sum_j \delta P_j^v \left(1 + \ln \frac{P_j^v}{P_j^o} + \alpha + \beta E_j^v \right). \end{aligned} \quad (2.66)$$

Therefore,

$$-\ln \left(\frac{P_j^v}{P_j^o} \right) = I(j) = (1 - \alpha) + \beta E_j^v. \quad (2.67)$$

Indeed this means a 1st-order (linear) relationship for surprisal. In cases where L includes the 2nd momentum term, a surprisal would become 2nd order.

2.7 Historical Background

The TPEPICO studies on fundamentals of mass spectrometry were conducted under Drs. Gerry G. Meisels (past President, the American Society for Mass Spectrometry, ASMS), Michael L. Gross (Professor, Washington University), and active and stimulating discussions with the late Chava Lifshitz (Professor of Emeritus, Hebrew University) (she made great contributions in mass spectrometry; regretfully, she lost her decades-long struggle with cancer on March 1, 2005) and Tomas Baer (Professor, University of North Carolina) and collaborators in ASMS during the 1980s. Regarding theoretical and experimental challenges in Japan, TN had been guided under Drs. Kozo Hirota (Professor of Emeritus, Osaka University), the late Toshikazu Tsuchiya and Yoshio Niwa (AIST, Japan), and Hiroshi Matsumoto (past President, Thermo Fisher Scientific, Japan) in photoelectron spectroscopy and mass spectrometry from the early 1970s to 1990s. TN especially thanks Dr. Andrew J. Alpert (President, PolyLC Inc., USA) for his valuable suggestions in this manuscript.

References

1. Rice OK, Ramsperger HC (1928) *J Am Chem Soc* 50:617–620
2. Kassel LS (1928) *J Phys Chem* 32:1065–1079
3. Marcus RA (1951) *J Phys Colloid Chem* 55:894–908
4. Forst W (1973) *Theory of unimolecular reaction*. Academic, New York
5. Robinson PJ, Holbrook KA (1972) *Unimolecular reaction*. Wiley, New York
6. Hase WL (1976) *Unimolecular reactions*. In: Miller WH (ed) *Dynamics of molecular collisions part B*. Plenum Press, New York
7. Bunker DL (1966) *Theory of elementary gas reaction rates*. Pergamon Press, New York
8. Rosenstock HM, Wallenstein HB, Warhaftig AL, Eyring H (1952) *Proc Natl Acad Sci U S A* 38:667–678
9. Haney MA, Franklin JL (1968) *J Chem Phys* 48:4093–4097
10. Sztaray B, Bodi A, Baer T (2010) *J Mass Spectrom* 45:1233–1245
11. Brehm B, von Puttkamer E (1967) *Z Naturforsch A* 22:8
12. Eland JHD (1972) *Int J Mass Spectrom Ion Process* 8:143–151
13. Niwa Y, Nishimura T, Nozoye H, Tsuchiya T (1979) *Int J Mass Spectrom Ion Phys* 30:63–73
14. Stockbauer R (1973) *J Chem Phys* 58:3800–3815
15. Werner AS, Baer T (1975) *J Chem Phys* 62:2900–2910

16. Batten CF, Taylor JA, Tsai BP, Meisels GG (1978) *J Chem Phys* 69:2547–2552
17. Révész A, Szepes L, Baer T, Sztáray B (2010) *J Am Chem Soc* 132:17795–17803
18. Shuman NS, Johnson M, Stevens WR, Harding ME, Stanton JF, Baer T (2010) *J Phys Chem A* 114:10016–10023
19. Cooks RG, Beynon JH, Caprioli RM, Lester GR (1973) *Metastable ion*. Elsevier, Amsterdam
20. Klots C (1971) *J Chem Phys* 75:1526–1532
21. Chesnavitch WJ, Bowers MT (1977) *J Chem Phys* 66:2306–2315
22. Beynon JH, Gilbert JR (1984) *Application of transition state theory to unimolecular reactions*. Wiley, Chichester
23. Levine RD, Bernstein RB (1987) *Molecular reaction dynamics and chemical reactivity*. Oxford University Press, New York
24. Smith IWM (1976) *Kinetics and dynamics of elementary gas reactions*. Butterworths, London, p 129
25. Langevin P (1905) *Ann Chim Phys Ser* 8(5):245–288
26. Nishimura T, Das PR, Meisels GG (1986) *J Chem Phys* 84:6190–6199
27. Miller WH (1976) *J Chem Phys* 65:2216–2223
28. Das PR, Nishimura T, Meisels GG (1985) *J Phys Chem* 89:2808–2812
29. Nishimura T, Arakawa R (1999) *J Mass Spectrom* 34:175–183
30. Zha Q, Hayes RN, Nishimura T, Meisels GG, Gross ML (1990) *J Phys Chem* 94:1286–1290
31. Nishimura T, Meisels GG, Niwa Y (1989) *J Chem Phys* 91:4009–4018
32. Widom B (1965) *J Chem Phys* 43:3892–3897
33. Domb C, Hunter DL (1965) *Proc Phys Soc* 86:1147–1151
34. Miller BE, Baer T (1984) *Chem Phys* 85:39–45
35. Jaynes ET (1963) *Statistical physics, Brandeis Lectures*, vol 3. Benjamin, New York, p 81
36. Bernstein RB (1982) *Chemical dynamics via molecular beam and laser techniques*. Oxford University Press, New York, Chapter 9
37. Shannon CE, Weaver W (1949) *Mathematical theory of communication*. University of Illinois Press, Urbana
38. Nishimura T, Meisels GG, Niwa Y (1991) *Bull Chem Soc Jpn* 64:2894–2900

Kenichiro Tanaka and Inosuke Koyano

3.1 Introduction

The component techniques currently used for mass spectrometry can be divided roughly into three: ionization of a sample, mass analysis, and detection. Among these steps, ionization is the most fundamental, and various methods are used for the ionization of a sample. Historically, electron ionization (EI) was the first technique used for mass spectrometry, and is still widely used because of the abundant database of mass spectra for many molecules. In EI, an electron beam having energy of around 70 eV is usually used, since beams of this energy are easy to control, and provide a relatively high ionization efficiency. In EI, however, not only parent ions but also fragment ions are produced. Therefore, in the mass spectrometry of a complicated molecule or a mixed sample, the interpretation of the mass spectrum may become difficult.

By contrast, in photoionization (PI) mass spectrometry, first developed by Lossing and Tanaka [1] in 1956, a resonance line from a lamp (for example, the 1,236 Å (10.03 eV) or 1,165 Å (10.64 eV) lines of Kr rare gas) is used as an ionizing light source. In PI mass spectrometry, as described below, the creation of fragment ions is suppressed, and the parent ion dominates in the mass spectrum, simplifying its interpretation. In this chapter, the fundamental features of PI are described briefly, and compared to those of EI [2].

3.2 Principles and Features of PI

3.2.1 Threshold Law of Ionization

PI events result in the formation of an ion and a free electron (photoelectron) pair, and the photon which participates in the ionization disappears. As this process follows the principle of conservation of energy, the free electron receives the energy that is the difference between the photon energy ($h\nu$) and the

K. Tanaka (✉)

XFEL Utilization Division, Japan Synchrotron Radiation Research Institute, Hyogo, Japan
e-mail: kentanaka@spring8.or.jp

I. Koyano

University of Hyogo, Hyogo, Japan
e-mail: Koyano@ceres.ocn.ne.jp

ionization energy (E_i) as kinetic energy. By contrast, in EI with the electron energy of E_0 , the electron which participates in the ionization does not disappear, and the incident electron and the free electron share the excess energy ($E_0 - E_i$). These processes can be represented by the following equations:



The difference between these processes is dramatically reflected in the ionization cross section and its incident energy dependence (ionization efficiency curve). When the microscopic behavior just above the threshold of ionization for each process is considered, only one low-energy electron separates from the ion in PI, but two low-energy electrons must separate from the ion in EI. Considering the limit of infinitely small excess energy, this small excess energy will be given to one electron in PI, and the electron can separate from the ion as a threshold electron with nearly zero kinetic energy. In this case the ionization efficiency curve shows a sharp rise at the threshold. On the other hand, in the case of EI, two electrons with kinetic energies near zero will exist around the ion. If one of the two electrons separates from the ion with a small kinetic energy, the electron left behind must lose energy, and is unable to separate from the ion. This results in the formation of a highly excited Rydberg state of a neutral molecule. In other words, the ionization efficiency of EI is nearly zero at the threshold. With increasing excess energy, the second electron will be able to separate from the ion, and the ionization efficiency gradually increases.

It was a topic of interest for many years that the efficiency of EI is close to zero at the threshold and increases linearly with increasing incident electron energy. Wannier [3] argued that the ionization efficiency curve near threshold is proportional to the 1.127th power of the excess energy for EI, and proposed the following formula,

$$\sigma_i \propto (E_0 - E_C)^{1.127}, \quad (3.3)$$

where σ_i is the ionization cross section, E_0 is the incident electron energy, and E_C is the threshold energy. As stated above, the ionization efficiency is proportional to the 1.127th power and not the 1.0th power of the excess energy (3.3), meaning that it does not increase linearly with excess energy, but increases asymptotically from zero near the threshold. In fact (3.3) does not depend on the method of ionization, but can be simply generalized by the following formula, which is now called a threshold law:

$$\sigma_i \propto (E_0 - E_C)^{n-1}. \quad (3.4)$$

Here, n is the number of electrons that separate from the collision domain. This formula means that ionization efficiency is dependent only on the excess energy and the number of degrees of freedom (i.e., electrons) that share the energy. Examples of this threshold law applied to various ionization processes are summarized in Fig. 3.1. For single ionization by an electron beam (⑧), the efficiency curve will accordingly be the 1.0th power of excess energy (polygonal-line type) because n equals 2. The ionization efficiency curve for single PI (④), where n equals to 1, will be of the 0th power of excess energy (step-function), and rises sharply to a steady value at $E_0 = E_C$. The ionization efficiency is then constant for $E_0 > E_C$, until a higher threshold (excited state of the ion) is reached. In addition, the structure of ionization efficiency curves for autoionization following electron beam excitation (⑤), and autoionization following photoexcitation (②), can also be described well by a step-function ($n = 1$) and a delta-function ($n = 0$), respectively, because the first process is the excitation to a neutral state for both processes.

Fig. 3.1 Threshold laws of ionization processes


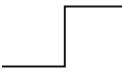
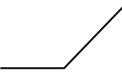

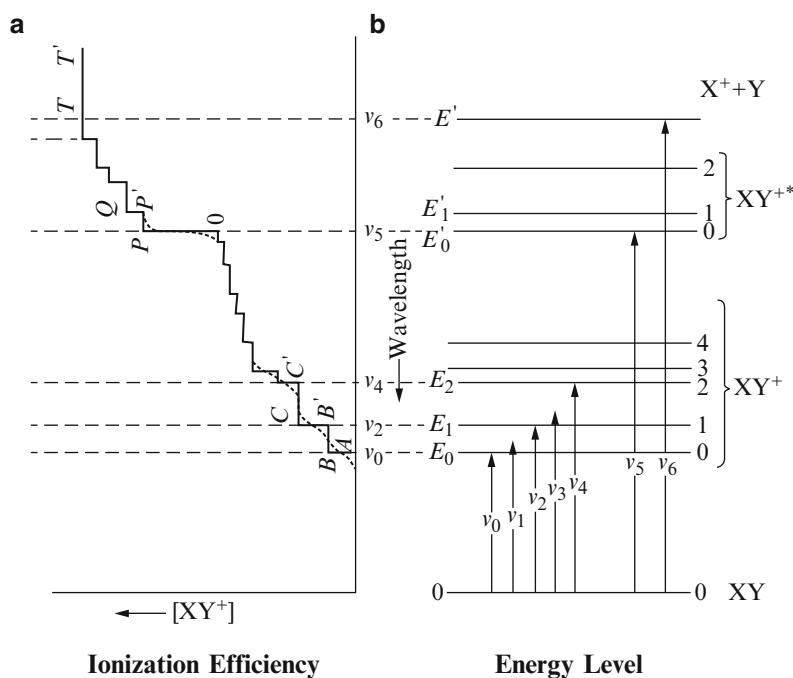
n	Type of Ionization	Shape of Efficiency
0	① $A + h\nu \rightarrow A^* \rightarrow A^+ + e$ ② $A + h\nu \rightarrow A^* \rightarrow B^+ + C^-$ ③ $A + e \rightarrow A^-$	
1	④ $A + h\nu \rightarrow A^+ + e$ ⑤ $A + e \rightarrow A^* + e \rightarrow A^+ + 2e$ ⑥ $A + e \rightarrow A^* + e \rightarrow B^+ + C^- + e$	
2	⑦ $A + h\nu \rightarrow A^{++} + 2e$ ⑧ $A + e \rightarrow A^+ + 2e$	
3	⑨ $A + e \rightarrow A^{++} + 3e$	

Fig. 3.2 Conceptual picture of PI of a molecule

3.2.2 Structure of PI Efficiency Curves

Here, PI with monochromatic light of a molecule XY (X and Y represent atoms or atomic groups) which has an energy level structure shown in Fig. 3.2b is considered. The molecule XY is considered to be in the single state XY (0) (vibrational and rotational ground state), and the light intensity is assumed not to vary with wavelength. The ions XY⁺ and XY⁺* have vibrational and rotational states

1, 2, 3 . . . Here, 1, 2, 3 . . . simply denote vibrational levels. This is because in usual experiments it is rare to use resolution of light source high enough to resolve rotation levels. Because there are many vibrational modes and these modes are mixed with each other in polyatomic molecules, the intervals between consecutive levels are generally irregular.

Naturally, ions are not generated for photon energies below E_0 ($E_0 = h\nu_0$), which is equivalent to the energy difference between $XY(0)$ and $XY^+(0)$. Ions are first created at E_0 and the ion in the state of $XY^+(0)$ is formed. E_0 is called the first adiabatic ionization energy of XY . The height A–B (Fig. 3.2a) is determined by the transition probability from $XY(0)$ to $\{XY^+(0) + e\}$. When the frequency of the incident light reaches ν_2 , $XY^+(1)$ ion appears, and the height B'–C is similarly determined by the transition probability from $XY(0)$ to $\{XY^+(1) + e\}$. Here, unless the interval between 0 and 1 is large, the intensity of ion $XY^+(0)$ is about the same as that at ν_0 (threshold law). Similar processes occur when the frequency increases from ν_2 to ν_4 and so on; thus the ionization efficiency curve can be represented with a step-functional structure, as shown in Fig. 3.2a. As mentioned above, the height of each step is proportional to the transition probability from $XY(0)$ to $\{XY^+(n) + e\}$, which is in turn proportional to the Franck–Condon factor between $XY(0)$ and $XY^+(n)$, where n represents the vibrational quantum number.

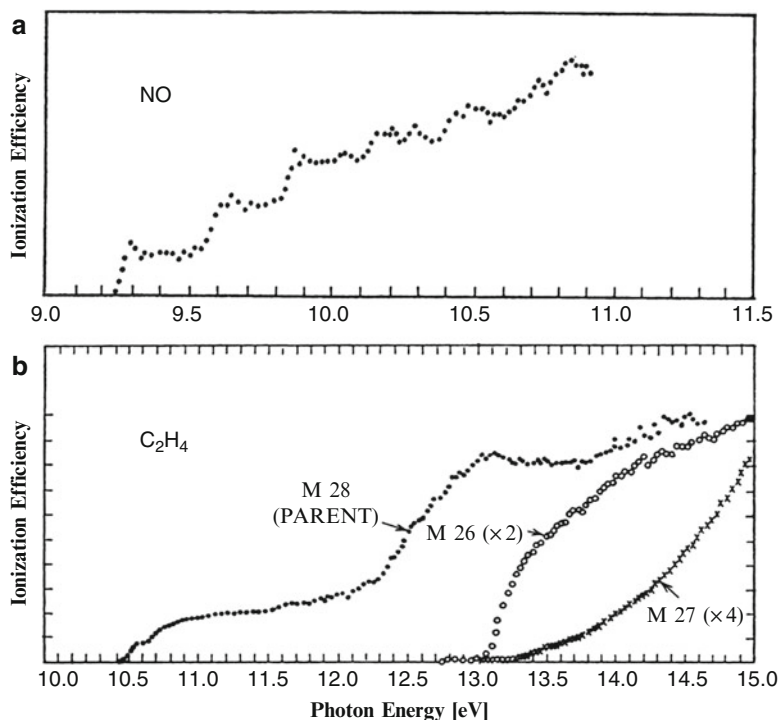
If the frequency of light increases further and reaches ν_5 , corresponding to the first electronically excited state XY^{+*} of the XY^+ ion, $XY^{+*}(0)$ ions appear newly superimposed on the $XY^+(0, 1, 2 \dots)$ ions. The height O–P in Fig. 3.2a is also determined by the transition probability from $XY(0)$ to $\{XY^{+*}(0) + e\}$, and the new step of $XY^{+*}(0, 1, 2 \dots)$ is superimposed on the step of $XY^+(0, 1, 2 \dots)$. Additional steps for the second and third excited states of ions are similarly observed. When the internal energy of the molecular ion reaches a certain value ν_6 , the dissociation reaction $XY^+ \rightarrow X^+ + Y$ can take place. Dissociation takes place not only from the electronically excited state XY^{+*} but also from the vibrationally excited $XY^+(n)$ states in the electronic ground state XY^+ . When dissociation reactions become possible, the production efficiency of the parent ion does not increase above this point ν_6 , but stays at a constant value (T–T'). The fragment ion X^+ will first appear at this frequency and increase with photon energy.

The basic structures of PI efficiency curves are shown in Fig. 3.2a. Because the monochromatized ionizing light actually has a finite energy width, each step in ionization efficiency curve for molecules that have closely spaced vibrational/rotational levels cannot be clearly resolved, but shows curvature at both ends, as shown by the dotted line in Fig. 3.2a. So far only the direct ionization denoted by (3.1) has been considered, but in PI there is another important process, which is denoted by the following equation:



Here, A^* stands for a neutral excited state (called a super-excited state), with an internal energy higher than the ionization energy. The process in which a radiationless transition takes place from this super-excited state to an ionization continuum state consisting of an ion plus an electron is termed autoionization (or pre-ionization), and competes with the neutral dissociation process (predissociation). As described above (threshold law), the efficiency curve for autoionization shows a peak structure (delta-function) because the initial process in autoionization is excitation to a neutral state. Therefore in actual PI efficiency curves, peak structure due to autoionization may be superimposed on step structure for direct ionization. However, when the interaction between a neutral super-excited state and the ionization

Fig. 3.3 (a) PI efficiency curve for NO from Hurzeler, Inghram, and Morrison (1958); (b) PI efficiency curve for ethylene from Chupka, Berkowitz, and Refaey (1969)



continuum state (configuration interaction) is large, distinction between direct ionization and autoionization becomes impossible. The ionization efficiency curve no longer shows a superposition of peaks upon steps, but consists of characteristic structures called Fano profiles [4] which extend below and above autoionization energy positions. The details of the Fano profile are not described here, but a brief summary is that the autoionization peak shows an asymmetry between the low- and high-energy sides, and the probability of the direct ionization which interacts with autoionization falls to nearly zero at one side of the peak.

Some typical PI efficiency curves are presented in Fig. 3.3. Figure 3.3a shows the PI efficiency curve for NO as observed by Hurzeler and coworkers [5]. The series of steps seen in the figure correspond to the vibrational progressions ($\nu = 0-5$) of the NO⁺ ion, and the height of each step expresses the transition probability to each vibrational state. For diatomic molecules (H₂, N₂, O₂, etc.), the curves are dominated by many autoionization peaks, which obscure the step structure for direct ionization. For NO, however, the peak structures due to autoionization are exceptionally small. Although not so clear as for NO, the PI efficiency curve for ethylene [6] in Fig. 3.3b also shows a step structure corresponding to vibrational progressions (in this case a combination of overtones of twist vibrations and C–C stretching vibrations) immediately after the appearance of parent ions (M28). After a gradual increase, a second onset is observed at around 12.4–13.0 eV. This onset corresponds to the first electronic excited state of the ion (the second ionization energy), and three steps are also seen around this energy. The efficiency curve for parent ions stops rising for energies above 13.0 eV, and becomes flat. This energy is in good agreement with the appearance energy of fragment ions C₂H₂⁺ and C₂H₃⁺ (M26 and M27).

3.3 Conclusion

When PI or EI is used as the ionization method in mass spectrometry, it is necessary to consider the principles and features of both methods, especially their different threshold laws. For PI the ionization efficiency rises steeply with a step-type shape when incident photon energy reaches the ionization threshold. By contrast, for EI, the ionization efficiency is nearly zero at the threshold, increases linearly with increasing electron beam energy, and reaches values sufficient for practical use with energies several eV above the threshold. A comparison of PI and EI for ethylene is convincing. Because the appearance energies of $C_2H_4^+$ (the parent ion), $C_2H_2^+$, and $C_2H_3^+$ ions are 10.51, 13.13, and 13.25 eV, respectively, only the parent ion is produced when a Kr resonance line (1,165 Å, 10.64 eV) or an Ar resonance line (1,048 Å, 11.84 eV) is used as the ionizing light source. In EI, however, in order to secure sufficient efficiency the electron beam energy must be at least 10 eV higher than the threshold. If ethylene is ionized using an electron beam with the energy of 20 eV, the generation of fragment ions is unavoidable. In general, the appearance energy of fragment ions from larger molecules is lower than that for ethylene, and it becomes increasingly more difficult to avoid the generation of fragment ions in EI. Furthermore, controlling the low-energy electron beam becomes more difficult with decreasing energies due to the influence of geomagnetism and the Coulomb repulsion between electrons. For these reasons, an electron beam with energy of around 70 eV that guarantees the easy control and sufficient ionization efficiency is used in mass spectrometry.

Finally, the features of PI have been often utilized in a basic study on ion–molecule reactions, especially state-selected ion–molecule reactions. The reactions of the primary ion in the selected state (vibrational and electronic state) are intensively examined by using sophisticated PI techniques [7, 8]. The features of PI have also been utilized industrially in a simple PI gas detector (photo ionization detector, PID), which was developed in the USA, Russia, and other countries, and applied to the measurement of contaminant contained in soil or groundwater. Kr lamp (10.64 eV) is incorporated as an ionizing light source, and all the chemical substances which can be ionized with this light source are detected as ion current.

References

1. Lossing FP, Tanaka I (1956) *J Chem Phys* 25:1031
2. Koyano I (1987) In: Tanaka I (ed) *Chemistry of excited molecules*, vol 11, Bunshi-Kagaku-Koza Series. Kyoritsu Publishing, Tokyo, pp 285–342, in Japanese
3. Wannier GH (1953) *Phys Rev* 90:817
4. Fano U (1961) *Phys Rev* 124:1866
5. Hurzeler H, Inghram MG, Morrison JD (1958) *J Chem Phys* 28:76
6. Chupka WA, Berkowitz J, Refaey KMA (1969) *J Chem Phys* 50:1938
7. Chupka WA (1972) In: Franklin JL (ed) *Ion-molecule reactions*. Plenum Press, New York, pp 33–76, and references therein
8. Koyano I, Tanaka K (1992) In: Ng C-Y, Baer M (eds) *State-selected ion-molecule reaction dynamics*, vol 82, *Advances Chemical Physics Series*. John Wiley & Sons, New York, pp 263–307, and references therein

Shin-ichi Wada and Kenichiro Tanaka

4.1 Introduction

Core electrons (inner shell electrons) localize within specific atoms because they are bound in core orbitals by quite high binding energy. Therefore, it is considered that, unlike valence electrons core electrons do not participate in chemical bonding. If this is the case, what phenomena take place in exciting or ionizing the core electrons by providing high energy? Does the core electron excitation/ionization indeed induce any change in chemical bonds or structural change in materials?

High-energy excitations are obtained nowadays with the remarkable recent development of the synchrotron radiation (SR) technique and have also been widely applied in atomic, molecular, and optical science, material science, bioscience, environmental science, etc. Above all, they demonstrate their strength in the field of materials and structural analysis. This chapter presents some typical studies on dissociation/desorption reactions with a focus on the most distinctive feature of core electron excitations, namely, element-selectivity, after reviewing the characteristics of core electron excitation/ionization.

4.2 Core Electron Excitation/Ionization

The following points can be described as the main characteristics of core electron excitation [1, 2].

- (1) Core electrons are localized within specific atoms, and they do not directly participate in chemical bonds.
- (2) The binding energy of core electrons strongly depends on the elements. Even for the same element, the energy differs slightly under the effect of the surrounding chemical environment. (Such a core-level energy difference of several eV is called chemical shift, as in the case of nuclear magnetic resonance (NMR).)

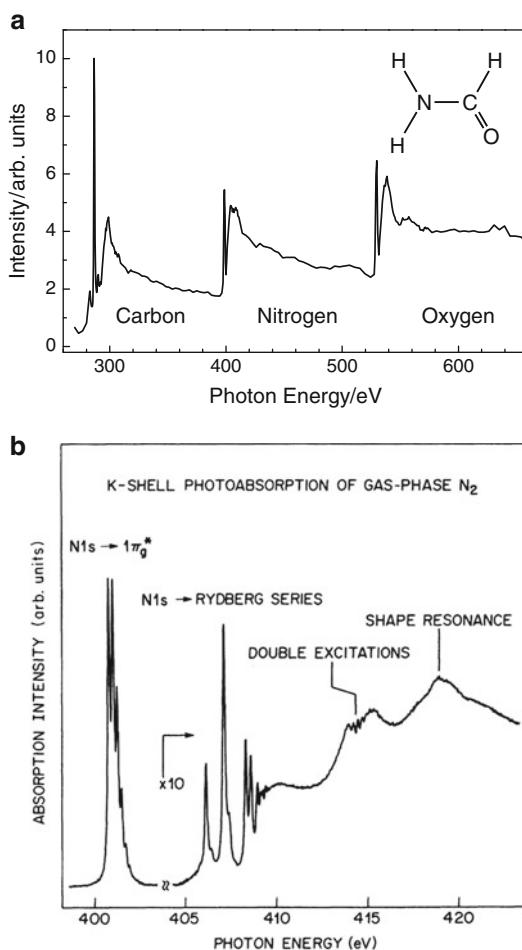
S. Wada (✉)

Department of Physical Science, Graduate School of Science, Hiroshima University, 1-3-1 Kagamiyama,
Higashi-Hiroshima, Hiroshima 739-8526, Japan
e-mail: swada@sci.hiroshima-u.ac.jp

K. Tanaka

XFEL Utilization Division, Japan Synchrotron Radiation Research Institute, 1-1-1 Kouto, Sayo,
Hyogo 679-5198, Japan

Fig. 4.1 (a) X-ray absorption spectrum for formamide thin film, which consists of one C, N, and O atom. Because of the large binding energy difference, each atom can be excited separately and selectively. (b) High-resolution absorption spectrum of gaseous N_2 molecules ($E/\Delta E = 10,000$) [3]. The various fine structure of the spectrum is attributed to resonant excitations and vibrational progression



- (3) Because of the localization of core orbitals within specific atoms as described in (1), the selection rule for core electron transitions is approximated by the atomic selection rule $\Delta l = \pm 1$ (l : orbital angular momentum), and enables dipole transitions to unoccupied or quasibound orbitals.
- (4) Core-hole states created by excitations decay immediately. In particular, in the case of atoms of light elements such as the second row elements, Auger decay processes, which are nonradiative, take place dominantly around the excited atoms, and commonly result in ionic states.

Figure 4.1 shows typical X-ray absorption spectroscopy (XAS) data for light-element molecules. Figure 4.1a presents the spectrum measured for a formamide thin film, an organic molecule consisting of one C, N, and O atom. Because each binding energy of 1s (K shell) electrons has a large energy difference (~ 290 eV for C, ~ 410 eV for N, ~ 540 eV for O), the X-ray absorption spectrum can be measured separately for each element. Thus, the element-selectivity (and therefore site-selectivity) is the main characteristic of core excitation/ionization. The spectrum in each 1s region shows several fine structures originating from resonant excitations and a steep absorption rise that decreases gradually as a function of photon energy. This absorption rise and continuous decay originate from the direct ionization of the core electron, and this feature is normally approximated by a step function with decay. The sharp step starting from the ionization threshold is called the X-ray absorption edge.

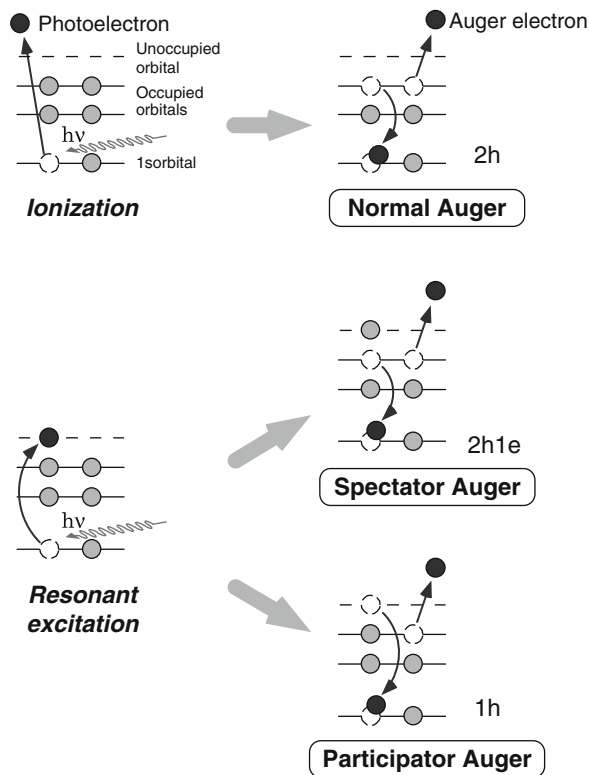
Figure 4.1b shows the high resolution spectrum of gaseous N_2 molecules measured around the N 1s absorption edge [3]. It is apparent that resonant transitions to unoccupied and quasibound orbitals like the π^* and Rydberg states have high transition probability and form the sharp fine structure of the absorption spectrum near the edge. Moreover, particular transition processes, such as two-electron excitations and shape resonance can be also observed in the spectrum, as well as the vibrational structure of the core-excited state in the π^* resonant peak. The direct ionization component is embedded in the spectrum as the shape of step function above 410 eV, where the Rydberg states converge.

Here we shall outline XAS from the viewpoint of conventional abbreviation. The fine structure can be observed around the near-edge of X-ray absorption, and for this reason it is referred to as either near-edge X-ray absorption fine structure (NEXAFS) or X-ray absorption near-edge structure (XANES) [1], which extends to ~ 50 eV around the edge. There is no distinguishing sharp line about the use of the terms NEXAFS and XANES, which are conventionally used depending on the research field. For instance, the term NEXAFS is more commonly used in chemistry, whereas XANES is used more in physics. On the other hand, the oscillation structure extending to 500 eV above the edge is also observable. This oscillation is caused by the scattering of photoelectrons emitted by core ionization with neighboring atoms, and is called extended X-ray absorption fine structure (EXAFS). The local atomic structure can be determined with high precision even for noncrystalline materials, and for this reason it is widely used as a powerful structural analysis technique [2]. Such fine structures measured in X-ray absorption spectra are collectively termed X-ray absorption fine structure (XAFS) as the technique used to determine the local geometric and electronic structure of materials. Although this chapter focuses on the inner (K) shells of the second row elements represented by organic light-element molecules, it should be noted that the L, M, etc., shells of elements after the third row are also categorized as inner-shells.

As core excitations are transition processes with extremely high energy, the core-excited states with a hole in the core orbital are quite unstable and decay within a quite short time ($< 10^{-14}$ s) by the transition of an outer valence electron to the core hole. In this situation, the process in which excess energy is emitted as radiation is X-ray fluorescence emission (radiative transitions). In contrast, when excess energy is consumed by emission of another electron in the valence orbitals, such nonradiative transitions are called Auger decay. Both radiative and nonradiative processes are competitive and their ratio strongly depends on the atomic number Z . For instance, Auger decay takes place dominantly for low- Z atoms (light elements), whereas the probabilities of both radiative and nonradiative processes at K shells become equal around $Z = 30$, and for higher- Z atoms fluorescence emission dominates inversely. In particular, the quantum yield of Auger decay is two orders of magnitude higher than that of the fluorescence yield for C, N, and O atoms.

It is convenient to describe the Auger decay processes as a two-step model: a prompt transition of an outer-valence electron to an unstable core hole created by excitation/ionization of a core electron and—to compensate the excess energy produced by this process—the simultaneous emission of another outer-valence electron. This Auger decay can be classified into three kinds of processes, as shown in Fig. 4.2. In the case of direct core electron ionization, the normal Auger decay takes place and results in the production of two-hole (2h) states, where the holes are created in valence orbitals. On the other hand, in resonant excitations, resonant Auger decay processes take place and can be distinguished by whether or not the excited electron from a core orbital to an unoccupied valence orbital participates in subsequent Auger decay. In the former case the participator Auger decay produces one-hole (1h) states, whereas the latter is called spectator Auger decay resulting in two-hole one-electron (2h1e) states. The final states after normal Auger decay are doubly ionized states and the resonant Auger decay produces singly ionized states. Namely, even though core electron transitions

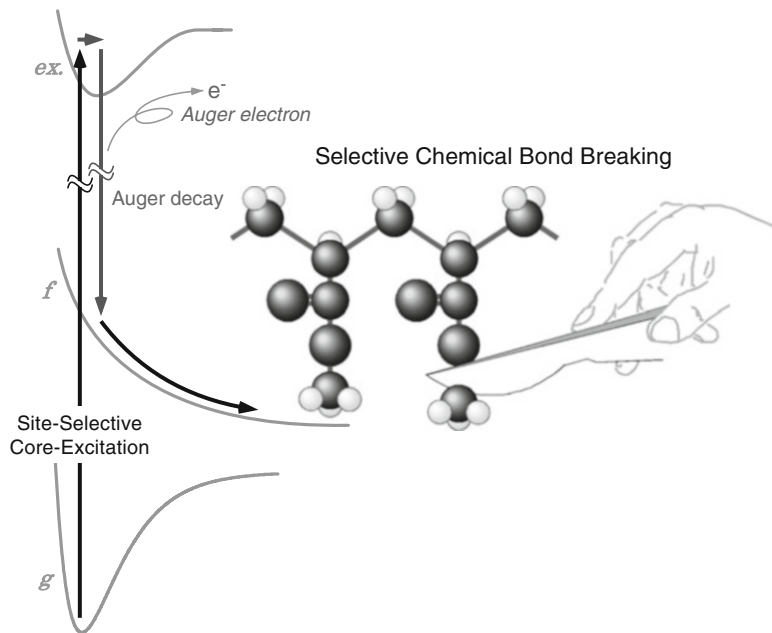
Fig. 4.2 Auger decay processes following core excitation/ionization are mainly classified into three kinds: normal Auger, spectator Auger, and participator Auger



are resonant excitations, they necessarily produce ionic states with more than one valence holes. In addition, it should be emphasized here that the spectator Auger decay leading to 2h1e final states has an important role in the characteristic reactions induced by core excitations to be mentioned later on.

The kinetic energy of emitted Auger electrons is basically determined by the combination of the orbital energies of a core electron and two concerned valence electrons. In the normal Auger decay, the kinetic energy of Auger electrons does not depend on the irradiated photon energy but remains constant, and the kinetic energy becomes highest when two electrons in the highest occupied molecular orbitals (HOMO) are involved in Auger decay. As electrons in deeper orbitals that have higher binding energies (e.g., HOMO-1, HOMO-2) are involved, the kinetic energy of Auger electrons will be lower than in HOMO. Consequently, the orbitals from which electrons are ejected, and therefore the Auger final states can be pinpointed by measuring the kinetic energy of emitted Auger electrons. Here, we will compare the normal Auger decay and the spectator one, where two electrons on the same valence orbitals are concerned (see the schematic drawing of normal and spectator Auger processes in Fig. 4.2). In such a situation, the kinetic energy of the spectator Auger decay shifts higher than the normal one when the irradiated photon energy is the same. This is basically caused by the screening effect of an electron remaining on an unoccupied outer orbital; it is also easy to understand the order of the energy levels by considering the fact that the normal and spectator Auger states are the doubly ionized and the excited state of the singly ionized ion, respectively. From this analogy, one can roughly recognize each Auger electron in a spectrum in the order of participator, spectator, and normal Auger decay from the higher kinetic energy side. As mentioned above, the participator Auger decay results in a 1h state by emission of a valence

Fig. 4.3 Conceptual illustration of the “molecular scalpel,” where a tunable soft X-ray is used as an atomic-level scalpel. A chemical bond can be selectively broken by utilizing site-selectivity of resonant core-excitations because of making a bonding power weakened by pumping a core electron into its antibonding orbital and consequently promoting Coulomb repulsion between two holes created in its bonding orbitals



electron, whereas the same $1h$ state can be also produced by direct ionization of the same valence electron. Therefore, as there is no difference between an Auger electron emitted via resonant core-excitation/participator Auger decay and a photoelectron by direct ionization with the same X-ray photon energy irradiation, both Auger and photo-electrons are measured at the same kinetic energy position on the spectrum. Distinction between the two electrons is usually difficult, but becomes possible by investigating the enhancement in electron yield (i.e., the resonant state) by scanning the photon energy.

Besides, it should be noted that other than these Auger processes, there are also phenomena that occur via more complex relaxation processes: for instance, Auger decay from a two-hole states with one hole on a core orbital and one hole on a valence orbital produced by shake-up or shake-off ionization, and multiple Auger processes caused by a deeper (higher- Z) core-hole creation (Auger cascade processes). A special Auger process, called the Coster–Kronig transition is when Auger decay occurs between subshells with the same principal quantum number.

As indicated in particular by the characteristics (1)–(4), core excitations take place within a quite local area, unlike valence excitations, because of special localization of the core electrons, and so a specific atom in a molecule can be excited selectively. The core-excited states decay within a quite short time period ($<10^{-14}$ s) by the Auger decay around the excited atoms, and commonly result in states with two holes on valence orbitals (usually excited states of a singly charged ion or doubly charged ion states). These Auger final states are also unstable, and if the holes are created on a binding molecular orbital localized within a specific chemical bond, they follow the ionic dissociation promoted by the Coulomb repulsion between two holes in the vicinity of the excited atoms within a quite short period (10^{-14} to 10^{-13} s), called the Auger stimulated desorption (dissociation) (ASD) mechanism [4, 5]. These consecutive decay processes suggest that the ionic dissociation can conserve the memory of a resonant core excitation, i.e., the local excitation, from which inner-shell orbital and to which antibonding orbital, and therefore, if using a soft X-ray of tunable SR, site-selective ionic bond breaking can be achievable in the vicinity of the excited atom. This is a very rare

phenomenon from the viewpoint of control of chemical reactions: optically selective bond breaking within a molecule, like a medical scalpel, and is termed “molecular scalpel,” as illustrated in Fig. 4.3.

4.3 Experimental Methods

In investigations of chemical reactions it is important to detect reaction products as they are, because the reaction mechanisms can be retrospectively determined from them. Thus, the main experimental strategy in the study of chemical reactions induced by core excitations is the detection of nascent electrons and ions. Nowadays, advanced measurements like neutral detection and coincidence measurement are also utilized.

4.3.1 Electron Detection

In the case of core excitations, there are three kinds of electrons: photoelectrons by initial core ionization, Auger electrons emitted in Auger decay, and secondary electrons derived from inelastic scattering of such electrons being emitted from solids. Besides, the kinetic energy of emitted photoelectrons strongly depends on the inner-shell orbital of element and the chemical environment from which the photoelectrons are emitted. In other words, one can determine the original address where the electron is bound by measuring the kinetic energy of the electrons. Photoelectrons are measured with the technique called the X-ray photoelectron spectroscopy (XPS) and a concentric hemispherical analyzer (CHA) is widely utilized. As XPS can provide unique information about the chemical composition and chemical states of materials from a measured energy shift (chemical shift), XPS is also called the electron spectroscopy for chemical analysis (ESCA). The recent development of the monochromator of SR and CHA has achieved high-resolution electron spectroscopy, for instance, vibrationally resolved photoelectron spectra even at the core levels. Auger electron spectroscopy (AES) is also a powerful electron spectroscopy technique that is widely used for surface analysis of solid samples as well as XPS.

On the other hand, a NEXAFS spectrum is obtained by measuring electrons by changing the photon energy. Typical measurement methods are the total electron yield (TEY) and the partial electron yield (PEY). The former is obtained by detecting all the emitted electrons (e.g., detection without retardation voltage or measurement of sample drain current instead of emitted electrons), while for the latter case Auger electrons with high energy are detected by applying a retarding potential of hundreds of volts in the front of a detector. These methods are chosen depending on the experimental instrument or on the sample form. As electrons are necessarily emitted after photoabsorption in the core levels in proportion to absorption intensity, the spectrum measured by each method is estimated to be equivalent to the absorption spectrum.

4.3.2 Ion Detection

The NEXAFS spectrum can be obtained even in the ion detection mode by varying the photon energy. The total ion yield (TIY) and the partial ion yield (PIY) are typical methods as well as electron detection methods. A TIY is obtained by simply detecting all fragment ions in dissociation or desorption without mass selection, and a PIY spectrum is the spectrum about each mass-selected ion, that is a so-called action spectrum. As selective dissociation reactions characteristic to core

excitations are rarely observed for gaseous samples (to be mentioned later), the TIY is often estimated to be equivalent to an absorption spectrum.

Time-of-flight mass spectrometry (TOF-MS) is widely used as a mass selection method. In measuring a gaseous sample, the origin of flight time for ions is defined by the instant detection of simultaneously emitted electrons by an electron detector facing the ion detector, and then, the traveling ions are detected by an ion analyzer equipped with acceleration electrodes, a flight tube, and a micro-channel plate (MCP) detector [6]. The mass assignment of each ion is determined from the flight time equation, $\text{TOF} \propto (m/z)^{1/2}$, where m/z is the mass-to-charge ratio.

On the other hand, it is quite difficult to detect both electrons and ions simultaneously desorbing from solid surfaces because of an instrumental restriction (see Sect. 3.4). In TOF measurements, one needs a time interval from several hundreds to more than 1,000 ns between photoirradiation (i.e., ion desorption) and ion detection, as well as a pulsed signal of SR light or another synchronized signal as a trigger. Thus, TOF measurements for surface materials can be possible by using pulsed SR light generated by a single-bunch operation of a SR storage ring [7]. For instance, at the Photon Factory at the High Energy Accelerator Research Organization (KEK-PF) in Japan, a pulsed SR with a pulse width of ~ 100 ps and 624 ns duration is utilized [8]. In this case the TOF spectrum consists of superposition of spectra triggered by several cycles of SR light. The PIY of each desorbing ion can be obtained from the TOF mass spectra as a function of photon energy.

As another detection method, the quadrupole mass spectrometer (QMS) is also used to determine desorbing ions. It is an important point that QMS not only detects ions, but is also adapted to measure neutral species under ultrahigh vacuum conditions (see the following Sect. 3.3). However, as QMS scans a mass spectrum by varying the applied voltage, in principle one cannot simultaneously detect ions with different m/z values. Therefore, this often brings about a serious disadvantage in measuring PIY spectra for various desorbing ions.

4.3.3 Neutral Detection

As opposed to the ion detection mentioned above, there are very few studies on measuring neutral species induced by core excitations, because of the experimental difficulty in detecting neutrals in comparison with ions. Attempts to detect various neutrals, however, have revealed reactions in which neutral fragments play an important role or where information is not directly obtained only by usual ion detection. QMS is one of the representative methods for neutral detection. In this case, highly sensitive detection of neutral products becomes possible by means of ultrahigh vacuum conditions. Thus, the QMS is equipped with a liquid He-cooled metal cap over the ionizer, where residual gas molecules (except H_2) are efficiently removed in the ionizer region [9–11]. Recently, a detection method combining highly sensitive laser ionization by an intense femtosecond laser and a TOF-MS has also been developed [12, 13]. The mechanism of ionization and Coulomb explosion in an intense laser field realized by focused ultrashort laser pulses is actively investigated as a new scientific subject in light–matter interactions [14], while it is expected that near-infrared pulses with intensity below $\sim 10^{14} \text{ W cm}^{-2}$ can softly ionize parent molecules without dissociation. Thus, this femtosecond laser ionization technique has attracted much attention as a new soft-ionization method, i.e., femtosecond laser mass spectrometry (FLMS) [15, 16]. Another successful detection of neutral photofragments induced by core-level excitations has also been reported by measuring UV–Visible fluorescence [17, 18] and metastable (high Rydberg) states autoionized on a MCP detector [19, 20], although in these cases the detected neutrals are limited to electronically excited ones.

4.3.4 Coincidence Spectroscopy

The correlation between two charged particles coinciding from one event can be investigated by simultaneous detection of both. In gas phase measurements, detection of an electron first and then subsequent TOF measurement of ions originating simultaneously is a popular mass analysis method called electron–ion coincidence (EICO) spectroscopy. Only detection of the electrons and ions emitted simultaneously is recorded as coincidence signals, while signals without time-correlation form a random background. It should be noted that in principle, true coincidence is proportional to the excitation-light intensity and sample vapor pressure, whereas false coincidence is proportional to their square. The lower the light intensity and sample vapor pressure are, the better the measured S/B ratio becomes. If photo- and Auger electrons are detected selectively, one can investigate the dissociation processes correlated with core-excited states and following Auger states, respectively, and these techniques are called photoelectron–photoion coincidence (PEPICO) and Auger electron–photoion coincidence (AEPICO) spectroscopy [2]. Coincidence measurements between the same kinds of charged particles are also possible. For instance, electron–electron coincidence spectroscopy enables the clarification of the correlations between core ionization and the subsequent Auger decay or between multiple ionization processes. Photoion–photoion coincidence (PIPICO) spectroscopy can reveal dissociation dynamics of multiply charged molecules. Moreover, recent multicoincidence measurements (e.g., multielectron coincidence, PEPIPICO, PEPIPIPICO) utilizing position-sensitive detectors have been actively performed to clarify even the detailed momentum correlations between emitted particles in the molecular frame [2, 6].

On the other hand, it was formerly difficult to perform coincidence measurements in surface studies because of an instrumental restriction. Recently, however, new precise instruments that combine TOF and a cylindrical mirror analyzer (CMA) coaxially have been designed, and therefore, coincidence studies are rapidly progressing even in the fields of surface analysis and surface reaction [21–23].

4.4 Chemical Reactions Induced by Core Electron Excitations

Core electron excitations essentially present selectivity of excitation sites in a different way from delocalized valence excitations. A first experiment demonstrating such characteristic selectivity was performed for photofragmentation of gaseous acetone by Eberhardt et al. in 1983 [24]. Although in an acetone molecule there are a carbonyl and two methyl groups, the resonant excitation to an unoccupied π^* orbital localized on the carbonyl group is dominated by the C 1s of the carbonyl group, and after resonant Auger decay, ionic fragmentation proceeds specifically around the carbonyl group. In consequence, it was reported that atomic ion fragments C^+ and O^+ are specifically produced only in this excitation. The authors have foreseen in their paper “the use of tunable soft X-ray as scalpel-like tools to break large organic molecules around certain selectable atoms (C, N, or O) within the molecule.” This work gave a start to numerous great studies in this field, and many experiments have since been conducted for various gaseous molecules. However, less prominent site-selectivity has been observed for many molecules other than acetone. Moreover, their finding of the site-selective ionic fragmentation for gaseous acetone has not been confirmed by later studies, and nowadays it is considered to have resulted from some impurity. Nevertheless, their pioneering work should be emphasized since it has promoted the development of this research field.

On the other hand, site-selectivity characteristic to core excitations can be clearly observed in ion desorption from surface molecules. Based on various previous studies, core excitation-induced

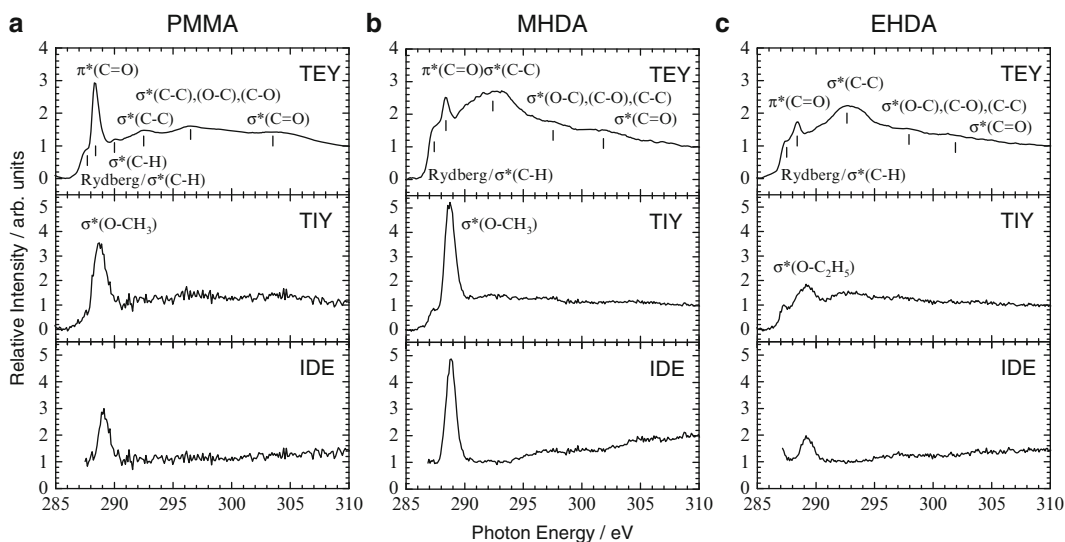


Fig. 4.4 TEY, TIY spectra and IDE spectra obtained by dividing TIY by TEY, for (a) PMMA thin film, (b) methyl ester-terminated SAM, and (c) ethyl ester-terminated SAM in the C 1s region. Assignments for typical transitions are shown in each spectrum [13]

site-selectivity is thought to be more easily expressed for surface molecules than for gaseous isolated ones [13, 25]. In this section, some representative studies that measured prominent site-selective chemical bond breaking are introduced.

4.4.1 Site-Selective Bond Breaking Measured for Ester Compounds

The first sample that demonstrated obvious site-selective bond breaking in surface molecules was for thin film of poly(methyl methacrylate) (PMMA, $-\text{[CH}_2\text{C}(\text{CH}_3)\text{COOCH}_3\text{]}_n-$) [26]. A PMMA monomer unit consists of five C and two O atoms, all of which are exactly different from each other in chemical environment, except for the eight H atoms. Therefore, PMMA is a good prototype molecule to demonstrate reaction-site dependence of reactivity. Since the selective ion desorption was measured within the functional group of its side chain ($-\text{COOCH}_3$), investigations were expanded to a series of end-functional group modified self-assembled monolayers (SAMs, here Au-S $(\text{CH}_2)_{15}\text{COOR}$, R = CH_3 , CD_3 , and C_2H_5) to clarify the reaction mechanism and to improve site-selectivity [13, 27, 28].

Figure 4.4 shows NEXAFS spectra in the TEY (upper) and TIY (middle) modes measured for (a) PMMA thin film, (b) methyl ester-terminated SAM (methyl 16-mercaptohexadecanoate; MHDA) and (c) ethyl ester-terminated SAM (ethyl 16-mercaptohexadecanoate; EHDA) in the C 1s core excitation [13]. Each spectral feature can be assigned as shown in the figures. Spectral features of the TEY spectrum for PMMA are mainly attributed to the side chain functional group, while in the case of SAMs the spectra consist of the peaks of Rydberg transitions and broad σ^* resonances around 293 eV due to long methylene chains as well as end functional groups. On the other hand, TIY spectra of PMMA and SAMs show characteristic structures around 289 eV, differently from the TEY spectra. These enhanced peaks are assigned to the transitions to the $\sigma^*(\text{O}-\text{R})$ antibonding orbitals at the methoxy group of the end sides ($\sigma^*(\text{O}-\text{R}) \leftarrow \text{C } 1s(\text{OR})$), which contribute obscurely to each TEY spectrum, and this indicates that ions desorb efficiently by this resonant excitation.

For further qualitative comparison between samples, ion desorption efficiency (IDE) spectra, which are obtained by dividing TIY by TEY, are also shown in the lower panels of Fig. 4.4. The IDE spectra of PMMA and SAMs display characteristic enhancements only at ~ 289 eV. The enhancement of the MHDA SAM is about twice that of PMMA. As the PMMA thin film is prepared by spin-casting of atactic (randomly oriented) PMMA polymer onto the Au substrate, the ester group of the side chain does not necessarily face the surface. On the other hand, the MHDA SAM orients its functional group onto the topmost surface. Therefore, the SAM has an advantage to emit its ionic fragments directly. The enhancement in the EHDA SAM, however, is four times smaller than that of MHDA. In this case, heavier $C_2H_m^+$ ($m = 1-5$) ions mainly desorb specifically from the ethyl-ester end group, which is confirmed by TOF measurement. It is considered that, although the site-specific ionic dissociation is induced by the σ^* resonant excitation even for the EHDA SAM, in the subsequent desorption process such heavier ions are easily neutralized and the yield of the ions becomes small. It should be noted here that the IDE intensities of all samples show gradual increase in the higher energy region. This phenomenon is attributed to the enhancement of ionic dissociation, since multielectron excitations such as shake-up and shake-off processes can take place above ionization thresholds (>290 eV) [29, 30], and also the kinetic energy of the emitted photoelectrons increases, which can easily contribute to the indirect dissociation process as described below.

TOF measurements are also performed to investigate photodesorbing ionic species and obtain the photon energy dependence of each ion (PIY spectra). Typical PIY spectra of PMMA and deuterated MHDA SAM (deuteride in the methoxy group of the end functional group) are depicted in Fig. 4.5. In both cases, ion desorption has a strong dependence on the initial excitations and displays structural differences. In particular, it is clearly seen that CH_n^+ (CD_n^+) ($n = 1-3$) series uniquely desorb in the resonant excitation to the antibonding orbital mainly localizing at the O-CH₃ bond, $\sigma^*(O-CH_3) \leftarrow C$ 1s(OCH₃), at 288.8 eV. On the other hand, PIY profiles of ions directly desorbing from moieties where core excitation does not directly take place, like OCH⁺ for PMMA and C₂H₅⁺ and OCD⁺ for the MHDA SAM, mostly correspond to their NEXAFS structures in TEY. Such ions only desorb in proportion to the absorption intensity. Moreover, it is clearly seen from the measurement of the deuterated MHDA SAM that the PIY spectrum of H⁺ ions desorbing from the methylene chain resembles the TEY spectrum, whereas the spectrum of D⁺ ions originating from the methoxy group shows the same characteristic feature at the $\sigma^*(O-CD_3)$ excitation as CD_{*n*}⁺ ions. This result indicates that the resonant excitation of a C 1s electron in the methoxy group to the adjacent O-C antibonding orbital takes place only within the functional group, and even after subsequent Auger decay and ionic dissociation/desorption, the initial memory of the excited site and its localization character are effectively conserved. It should be emphasized that this is a straightforward example that the characteristics of core excitations are directly reflected in reaction dynamics.

Characteristic site-selectivity in ion desorption is more obviously observed in the O 1s region. Figure 4.6 summarizes the results obtained for PMMA and the MHDA SAM. The top spectra are TEYs for both compounds, which display naturally a quite similar structure in O 1s excitation. The middle and bottom spectra show the PIY spectra of CH₃⁺ and OCH⁺ ions for both compounds, respectively. As is easily seen, the CH_{*n*}⁺ ions selectively desorb at peak A and desorption of the OCH⁺ ion is enhanced at peak B. The resonant state at peak A can be assigned to the excitation of the O 1s electron of the ether group to the antibonding orbital for the methoxy group ($\sigma^*(O-CH_3) \leftarrow O$ 1s(COCH₃)) and hence ionic elimination of the methyl group is promoted. Similarly, the $\sigma^*(C-OCH_3) \leftarrow O$ 1s(COCH₃) transition at peak B causes ion desorption of the methoxy group selectively, which thereafter results in exothermic fragmentation to the OCH⁺ ion ($OCH_3^+ \rightarrow OCH^+ + H_2$). This finding is a quite interesting phenomenon because one can cut a different chemical bond efficiently and selectively by choosing a proper irradiating soft X-ray energy with only a few eV (less than 1 %) energy difference.

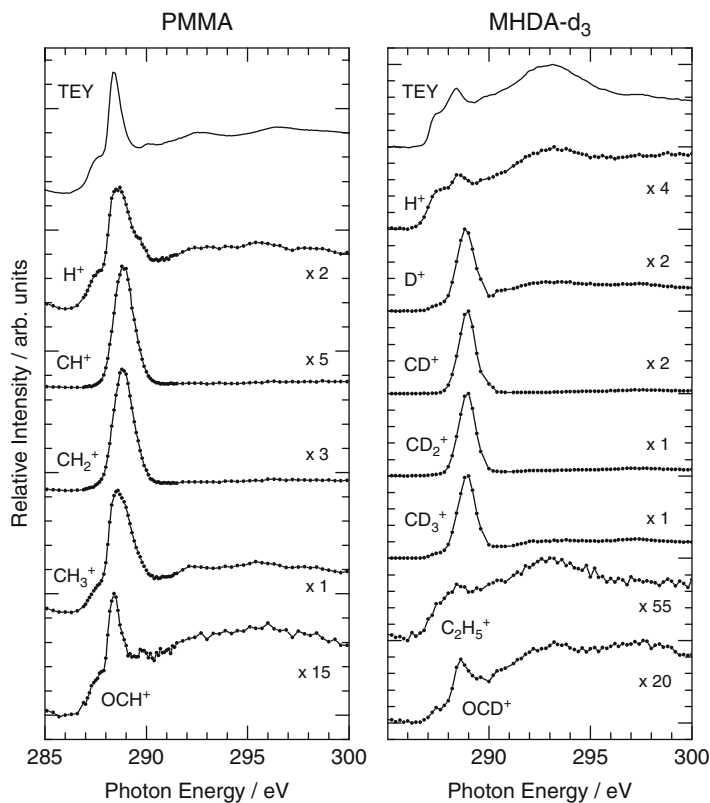
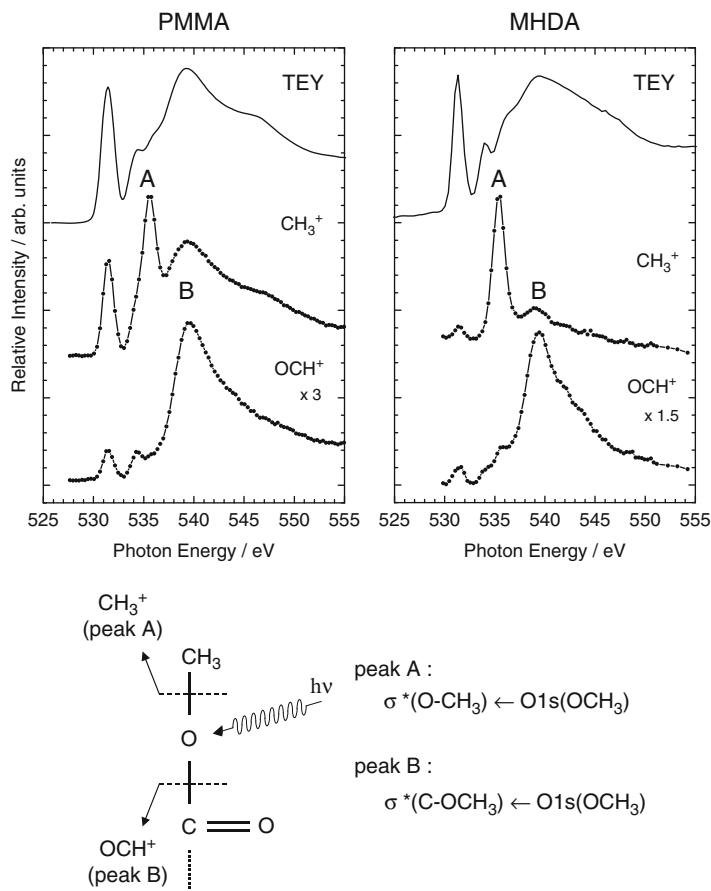


Fig. 4.5 Representative PIY spectra of (a) PMMA and (b) methyl ester-terminated SAM (deuteride) in the C 1s region. TEY spectra are also shown at the top. The intensities of the spectra are multiplied approximately by the numerical values given on the right side [13]

Moreover, the site-selectivity for desorption from the SAM becomes dramatically improved compared with PMMA thin film in the O 1s and C 1s regions.

So far, experimental demonstration was summarized for core electron excitations leading to site-selective bond breaking in ester compounds on surfaces. However, not all of the photodesorbing ions necessarily reflect the selectivity. The following two important factors disturb this characteristic phenomenon induced directly by core excitations. The core-excited states produced by soft X-ray irradiation immediately decay to Auger final states, which are also highly excited states (excited states of singly charged ions for the usual resonant Auger decay). Therefore, it may be expected that fast inter- and/or intra-charge and energy relaxation easily occurs in the final states. Such a statistical energy delocalization can give rise to ionic dissociation at every possible site in a molecule, and as a result any ion desorbs with moderate yield not influenced by the nature of the excited states, but only in proportion to the X-ray absorption intensity. The second factor is the X-ray-induced electron-stimulated desorption (XESD) process [13, 31–33]. After photoabsorption of soft X-ray, Auger and inelastically scattered electrons are emitted not only from the surface but also from the bulk. Such energetic electrons can induce electronic transition accompanied by bond dissociation. In particular, ionic fragments created on a surface can easily desorb as they are. Such indirect processes also occur at every possible site in a molecule and lose the initial memory of the element and bonding selectivity by resonant core excitations. Consequently, in many cases, these indirect processes make the ion yield signal simply a replica of the TEY spectrum originating from the bulk. In fact, the ion

Fig. 4.6 TEY and representative CH_3^+ and OCH^+ PIY spectra of (a) PMMA and (b) methyl ester-terminated SAM in the O 1s region, together with a schematic drawing of site-selective bond breaking in the methyl-ester group induced by resonant core excitations [13]



desorption via the indirect processes is a dominant process and its yield is often superior to the yield by the direct process, in particular for condensed multilayer molecules [31, 32].

Taking the above point into account, two dissociation processes causing ion desorption, a site-selective direct process and a nonselective indirect one, are quantitatively evaluated [13]. In CH_3^+ ion desorption of PMMA, the direct process in the $\sigma^*(\text{O}-\text{CH}_3)$ resonance is estimated to be 65 % and the indirect process is 35 %. Most of the ion desorption is caused by the indirect process over the other excitation and ionization region. In the case of the MHDA SAM, the direct process of 90–95 % are derived for the CH_3^+ desorption in the same $\sigma^*(\text{O}-\text{CH}_3)$ excitation, evaluating the improvement of specificity for SAM. It should be emphasized here that the SAMs are monolayers and the focused $\sigma^*(\text{O}-\text{CH}_3)$ excitation takes place locally within the ester group, so the reactions in SAMs take place only within the end functional group aligned onto the topmost surface, while the reaction parts on the side chain of PMMA occur three-dimensionally within the film. As a result, the XESD process, which dominates in bulky PMMA is strongly reduced, and this results in improvement in specificity. In other words, the small contribution of the indirect desorption measured for SAMs would be mainly caused by a statistical charge and energy delocalization.

As seen above, characteristic site-selective bond breaking is found out for core excitations of ester compounds. Besides, the following three interesting phenomena are also reported for controlling site-selective bond breaking.

1. The atomic position dependence of core excitations

The O–CH₃ bond can be selectively cut by the $\sigma^*(\text{O–CH}_3)$ resonant excitations from both end atoms, C and O. However, the fragmentation patterns of desorbing ions show different behavior in spite of the same resonant excitations. If the primary core-excited atom (C) is included in the desorbing CH₃⁺ ion, the Auger final energy is concentrated within the ion and used effectively for further fragmentation. In contrast, if the core-excited atom (O) is not included in the removing part, the deposited Auger final energy easily diffuses into the remaining part on the surface and is not effectively used for the fragmentation. From the viewpoint of controlling chemical reactions, these two different types of fragmentation are classified as bond breaking, named “hard-cut” with further fragmentation, and “soft-cut” with less fragmentation, respectively [13, 34].

2. The polarization dependence

SAM constituting molecules adsorb on the Au substrate nearly upright through van der Waals interaction between the long methylene chains, so that their end functional groups are oriented densely on the topmost surface. Accordingly, the TEY spectra of SAMs show a clear incident angle dependence of the linearly polarized SR. The polarization dependence of each desorbing ion is also measured and site-selective bond breaking is successfully controlled by simply rotating the sample holder [27, 28, 35, 36].

3. The chain-length dependence

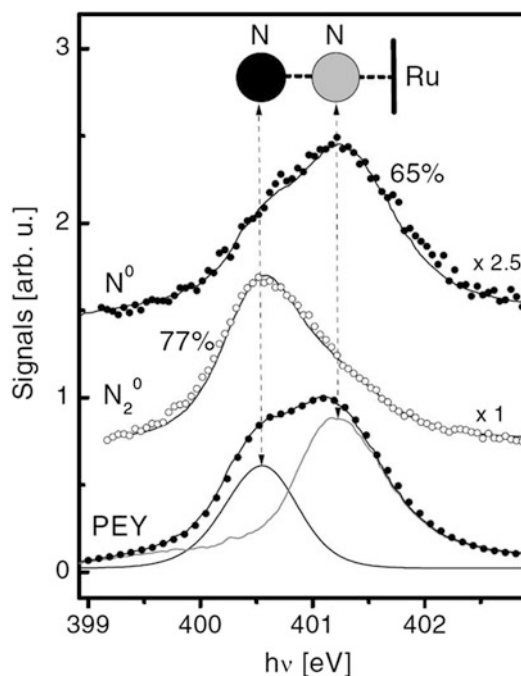
Ion desorption measurements were performed for monolayers of the ester compound HSCH₂COOCH₃, which has only one methylene group (–CH₂–), and the results were compared with MHDA SAM, which has molecules with long methylene chains [37]. Although the site-selective ion desorption of the methyl-ester site was measured even for such short monolayers, the desorption yield of CH₃⁺ was reduced by a factor of more than 10 compared with MHDA SAM. Ion desorption from monolayers usually presents an abundance of light fragments over heavier ones, because of deactivation or reneutralization resulting from the strong interaction with metal surfaces. On the other hand, as the reaction site (the end functional group) of MHDA SAM with long chains exists moderately apart from the metal surface (~20 Å), such interaction becomes weaker for SAMs.

Finally, other experimental approaches for ester compounds should be also mentioned here briefly. AEPICO spectroscopy has also contributed to this research field of site-selective ion desorption and is useful for clarifying a sequence of reactions from primary core excitations via Auger decay to ion desorption. It is proposed that the site-selective ion desorption from core-excited PMMA [38, 39] and MHDA SAM [40] is enhanced at the 2h1e final states after the spectator-type Auger decay, where one excited electron remains in the antibonding orbital and two electrons are removed from the bonding orbitals for the specific chemical bonds, which is also confirmed by theoretical calculations [41]. Measurements of photodesorbing neutrals by femtosecond laser ionization indicate that for instance, all of the neutral products desorb from core-excited PMMA nonselectively, that is almost the same photon energy dependence as the TEY spectrum, but not each PIY [12, 13]. The result suggests that ionic dissociation locally promoted by Coulomb repulsion in the ASD mechanism plays an important role in revealing site-selective dynamics.

4.4.2 Site-Selective Bond Breaking of N₂/Ru (001)

Here is another experimental example of typical site-selective chemical bond breaking. N₂ molecules adsorb perpendicularly on Ru and Ni surfaces. As this chemisorption onto the surfaces breaks the symmetry of homonuclear diatomic molecules, the inner N atom directly connected to the metal

Fig. 4.7 PEY spectrum and neutral yield spectra of N and N₂ products measured for N₂ adsorbed on a Ru (001) surface in the $\pi^*(\text{N-N}) \leftarrow \text{N } 1s$ resonant excitation [11]



surfaces and the outer N forming N–N bond shows obvious chemical shift (0.7 eV on Ru(001)). It is quite an interesting subject to study how differently site-selective bond breaking occurs by the core excitation of an outer or inner N atom. Figure 4.7 shows a typical example of yield spectra of a photodesorbing neutral N atom (N^0) and an N₂ molecule (N_2^0), together with PEY measured around the $\pi^*(\text{N-N}) \leftarrow \text{N } 1s$ resonant excitation of N₂/Ru(001) [11]. Experiments for the detection of neutrals were carried out using the QMS apparatus described in Sect. 3.3. The PEY spectrum is obviously composed of two components: the high-energy component corresponds to the excitation of the inner atom and the low-energy to the outer one. The measured yield spectra of N and N₂ evidently indicate different photon energy dependence. In the excitation of the outer atom, the desorption of the intact molecule is pronounced (77 % preferential production of N₂), whereas excitation of the inner N preferentially breaks the molecular bond (65 % of N) [10]. This result seems to be the opposite interpretation to an intuitive speculation. Nevertheless, this is a quite interesting example to reflect site-selectivity even in a neutral desorption reaction.

The two-hole configuration created by the Auger decay of the π^* core-excited state was reported to vary with the position of the excited atom, and this result is explained as follows [10]. The inner N 1s hole mainly decays into final states with $[1\pi^2]$ and $[1\pi 4\sigma]$ double holes, whereas $[5\sigma^2]$, $[4\sigma^2]$, and a manifold with the main contributions of $[4\sigma 2\pi]$ configurations dominate the outer excitation. As the 1π orbital is strongly bonding with respect to the N–N bond, the double holes efficiently dissociate the N₂ molecule and therefore the N atom is observed by the inner N excitation. On the other hand, the intramolecular bond is less weakened by 4σ and 5σ holes, which predominate in the decay states following the outer excitation, than by 1π holes. Rather, it is considered that the strength of the N–Ru bond decreased by the σ holes via some charge transfer. Although it is not shown in the figure, N⁺

desorption was also measured and its spectral profile quite resembles that of N_2 desorption. The N^+ ion is predominantly (78 %) produced by the outer N excitation, which is a reasonable result as speculated.

The experiments were later expanded to the Ni(111) surface and the isoelectronic molecule CO [11]. Both molecular systems showed Auger spectra similar to the one measured for $N_2/Ru(001)$. Although this result means that desorption takes place via the same Auger final states, different desorption results are obtained; for example, that N_2/Ni with lower binding energy shows less selectivity. From these points, the strength of interaction with metal surfaces is pointed out as a more important factor to bring about site-selectivity. Because adsorbates couple strongly to metals, Auger final states tend to be easily relaxed. Thus, only fast dissociation (site-selective, direct) processes can achieve the desorption that leads to selectivity. On the other hand, since even nonselective processes can survive in a weak interaction system, site-selective reaction is buried in them [42]. As the core-excited states of N_2 and CO molecules (NN^* and C^*O) can be regarded to be the same as the NO molecule under $Z + 1$ approximation (mentioned later), the difference in adsorption reactivity, i.e., that NO dissociatively adsorbs on Ru, whereas on Ni it adsorbs molecularly, may help in the understanding of this selective desorption.

4.4.3 Element-Selective Bond Breaking by Theoretical Calculations

With the advancement in the soft X-ray experimental techniques, nowadays the approach of theoretical calculation also shows dramatic progress. Various computational techniques were proposed for the core-level excitation processes, and their usefulness has been examined. This section introduces some of the more interesting results related with the element-selectivity of core-excitation induced reaction dynamics.

Core-excited states can be simply approximated by the equivalent core model ($Z + 1$ approximation). When the atom with atomic number Z is core-excited and a hole is created in the core orbital, i.e., a positive charge is created very close to the nucleus, it apparently can be considered that the atom Z changes to $Z + 1$. This $Z + 1$ approximation is a convenient method to qualitatively evaluate changes in chemical and physical properties by core excitations. For example, when a halogen atom of a halide is excited, since the core-excited halogen atom is replaced under the $Z + 1$ approximation with a rare gas atom, one can easily estimate that the core-excitation of a halide results in a repulsive state with completely less bonding power.

The interesting study summarizing the element-selectivity of core-excited states systematically is reported by calculating the reactivity of core-excited states about a hundred light-element compounds [43]. An example of the result is shown in Fig. 4.8. Resonant core-excited states in a molecule are calculated based on the density functional theory (DFT), and the gradients of potential energy surfaces along with the targeted chemical bonds are examined over the Franck–Condon region, which reflect the reactivity (bond breaking) of core-excited states. The figures plot the gradients of the potentials of the core-excited states as a function of the sum of atomic numbers of the bonded atomic pair ΣZ . Each point in the figure indicates the most negative one among the five low-lying core-excited states calculated for each molecule. Although the plots show broad distributions because of differences in the chemical environment, the gradient apparently becomes more negative (more repulsive) with increasing ΣZ . Furthermore, even if ΣZ is the same, the gradient is more negative when a heavier atom is core-excited, e.g., the gradient of the N^*-C bond is more negative than that of $N-C^*$.

The characteristics of core excitation-induced bond breaking obtained from the series of calculations are summarized as follows.

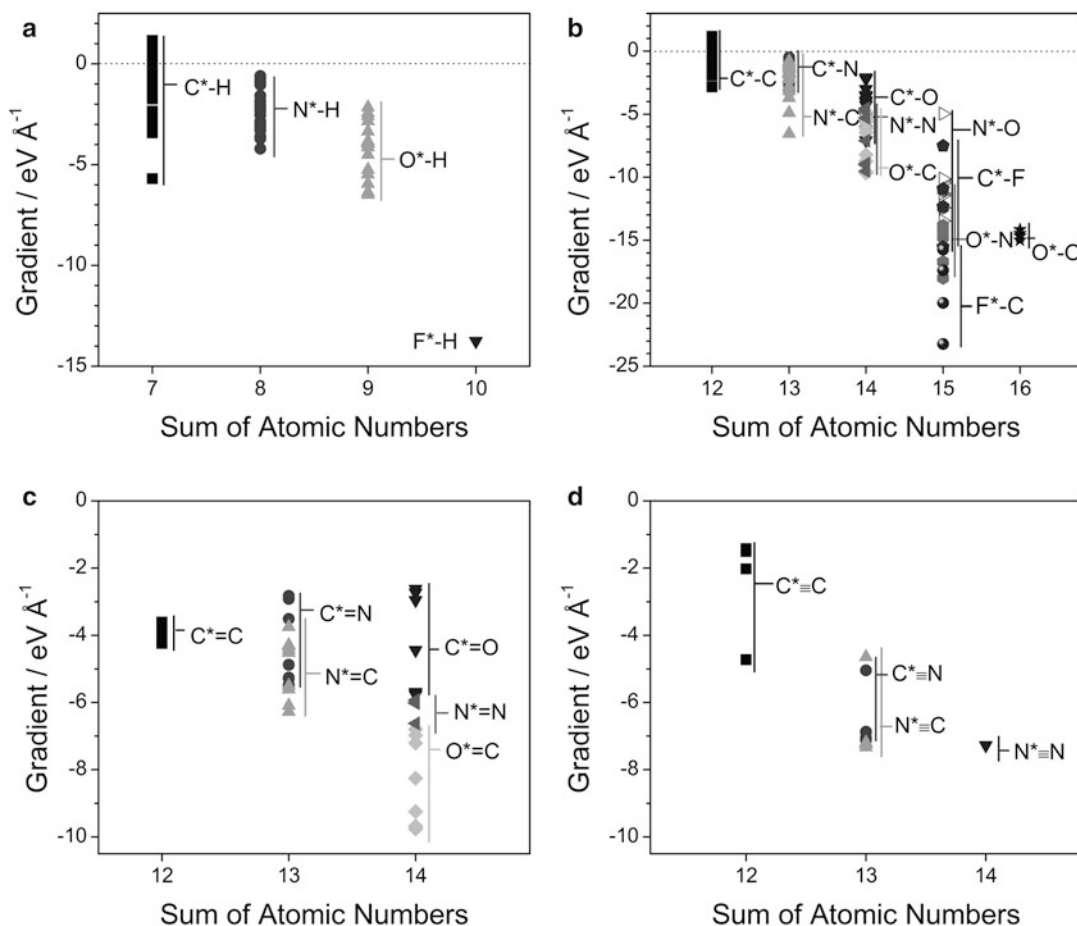


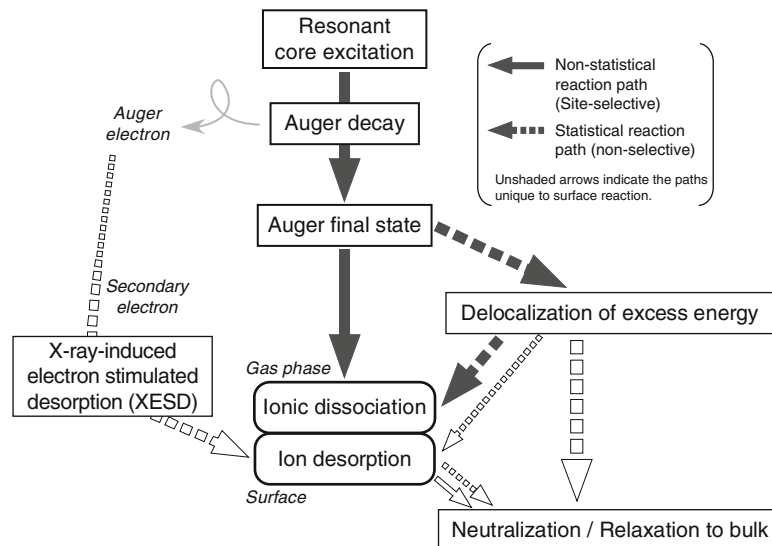
Fig. 4.8 Calculated repulsive (negative) potential gradients for the core-excited states of light-element compounds as a function of the sum of atomic numbers of bonded atomic pairs. (a) X–H bonds, (b) single bonds, (c) double bonds, and (d) triple bonds, where X indicates C, N, O, and F atoms. Asterisks indicate excited sites [43]

1. The chemical bond directly connected to an excited atom is most dissociative.
2. The chemical bond becomes more dissociative with increasing ΣZ of the bonded atomic pair.
3. The chemical bond becomes more dissociative by the core excitation of an atom with a larger atomic number.
4. The chemical bond becomes more dissociative with increased bond order.

Although point 4 seems at first glance to be an incomprehensible phenomenon, the reason is understood to be that with increased bond order, a shorter bond length enhances the nuclear–nuclear repulsion caused by the core hole.

As the lifetime of core-excited states is quite short even in comparison with molecular vibration, actual ionic dissociation takes place in the ionic states after Auger decay, except for special cases such as the ultrafast dissociation of core-excited states reported for HBr, H₂O, etc. [44, 45]. Therefore, the dissociation process strongly depends on the potential gradient of the Auger final state. However, the primary dissociative motion (elongation of chemical bonds) accelerated on the core-excited state potential may also contribute to the dissociation dynamics of the Auger state. As indicated earlier in

Fig. 4.9 Scheme of hypothetical reaction paths initiated by core excitations in the gas phase and on a solid surface. The *thickness of arrows* is indicative of relative amount on the paths



Sect. 4.1, the resonant excitations to $\sigma^*(\text{O}-\text{CH}_3)$ from both the C and O ends induce selective breaking of the O-CH₃ bond in the methyl-ester moiety. Molecular dynamics simulations of core-excited states indicate that such excited states have steep repulsive potential and therefore accelerate the O-CH₃ bond elongation [46]. The agreement of experimental and theoretical results suggests that the potential of core-excited states can effectively contribute to dissociation, even though the lifetime is quite short. In combination with the AEPICO measurements showing that selective bond breaking is enhanced via particular spectator-type Auger final states, site-selective bond breaking is promoted by dynamic synergy effects in both core-excited and Auger final states. In other words, site-selective bond breaking is considered to be promoted by two steps: the first is resonant core-excitation to an antibonding orbital at a particular chemical bond, and the second is creation of holes in bonding orbitals associated with the bond via Auger decay. From such a viewpoint, it is expected that in the future, the theoretical approach of nuclear wavepacket dynamics of the reaction chain of resonant core excitation–Auger decay–ionic dissociation, which is a time-dependent sequential reaction process, would provide a more detailed picture on the dissociation dynamics induced by core excitations.

4.5 Conclusion

Core electron excitations have attractive potential to induce selective chemical bond breaking. Compared to valence excitations, core excitations take place within a small region because of their spatial localization and atomic selectivity. Therefore, a specific atom in a molecule can be selectively excited. The core-excited states are quite unstable with an extremely high energy, so consecutive decay processes—Auger decay and ionic dissociation—can occur in the vicinity of the excited atom. From this concept, site-selective chemical bond breaking has been widely and successfully investigated in various core-excited adsorbates, polymers, and other molecular systems on surfaces (see references in [13]). On the other hand, there are very few reports that observe such site-selectivity in core excitations of gaseous molecules. The reaction scheme shown in Fig. 4.9 has been proposed to explain the difference between ionic dissociation reactions in the gas phase and on surfaces [13, 25].

The primary core excitations and the Auger decay are very fast processes of the order of less than 1 ps, so it is considered that there are essentially no differences until Auger final states between the gas phase and the surface. Generally, Auger final states have large excess energies of 10–30 eV. On the basis of these facts, one can assume that there are two reaction paths leading to ionic dissociation (fragmentation). One is the statistical reaction path, in which the excess energy delocalizes and redistribution of this energy leads to a variety of chemical reactions. The probabilities of these reaction paths can be determined by statistical considerations, and the reactions lose the memory of the site of the primary excitation. The other is the nonstatistical reaction path, in which direct and site-selective reactions occur. For isolated gaseous molecules, the excess energy that diffuses over the molecule can lead to statistical chemical reactions and thus the site-selective (nonstatistical) reaction is hidden. On the other hand, for solid surfaces, the excess energy that diffuses over the molecule rapidly flows toward the solid or toward neighboring molecules. As a result, statistical reactions are suppressed and site-selective reactions are emphasized on solid surfaces. According to this hypothesis, site-selective reactions may well be more prominent at the surface than the gas phase.

It is considered that the concept of “molecular scalpel” depicted in Fig. 4.3 can be realized in principle by using a tunable soft X-ray, although there are problems that should be overcome: a small contribution from the indirect reaction caused by a statistical delocalization still disturbs site-selectivity even in SAMs, where the XESD process is strongly reduced. This technique is expected to be applied to the future modification of atomic level surface processes. In addition, it should be emphasized that significant progress is being made in the development of light sources in the fields of X-ray free electron laser (XFEL) [47, 48] and high harmonic generation (HHG) [49]. Progress is also made in new studies using new X-ray sources, especially for XFEL (see for example, [50–52]). It is expected that new reaction dynamics induced by core excitation/ionization will be discovered by using new intense, ultrafast, and high-coherence X-ray.

References

1. Stöhr J (1992) NEXAFS spectroscopy. Springer, Berlin
2. Sham TK (ed) (2002) Chemical applications of synchrotron radiation. World Scientific, Singapore
3. Chen CT, Ma Y, Sette F (1989) *Phys Rev A* 40:6737
4. Ramaker DE, White CT, Murday JS (1981) *J Vac Sci Technol* 18:748
5. Ramaker DE, White CT, Murday JS (1982) *Phys Lett A* 89:211
6. Ueda K (2003) *J Phys B At Mol Opt Phys* 36:R1
7. Tanaka K, Tinone MCK, Ikeura H, Sekiguchi T, Sekitani T (1995) *Rev Sci Instrum* 66:1474
8. For instance, pulse duration during single-bunch operations of other SR facilities is 800 ns for BESSY-II in Berlin, Germany, and 311 ns for LNLS in Campinas, Brazil
9. Romberg R, Frigo SP, Ogurtsov A, Feulner P, Menzel D (2000) *Surf Sci* 451:116
10. Romberg R, Heckmair N, Frigo SP, Ogurtsov A, Menzel D, Feulner P (2000) *Phys Rev Lett* 84:374
11. Menzel D, Feulner P (2001) *J Phys Condens Matter* 13:11249
12. Wada S, Matsumoto Y, Kohno M, Sekitani T, Tanaka K (2004) *J Electron Spectrosc Relat Phenom* 137–140:211
13. Wada S, Kizaki H, Matsumoto Y, Sumii R, Tanaka K (2006) *J Phys Condens Matter* 18:S1629
14. Yamanouchi K (2002) *Science* 295:1659
15. Smith DJ, Ledingham KWD, Singhal RP, Kilic HS, McCanny T, Langley AJ, Taday PF, Kosmidis C (1998) *Rapid Commun Mass Spectrom* 12:813
16. Harada H, Shimizu S, Yatsuhashi T, Sakabe S, Izawa Y, Nakashima N (2001) *Chem Phys Lett* 342:563
17. Rosenberg RA, Wen C-R, Tan K, Chen J-M (1990) *J Chem Phys* 92:5196
18. Marquette A, Gisselbrecht M, Benten W, Meyer M (2000) *Phys Rev A* 62:022513
19. Hikosaka Y, Lablanquie P, Shigemasa E (2005) *J Phys B At Mol Opt Phys* 38:3597
20. Hikosaka Y, Gejo T, Tamura T, Honma K, Tamemori Y, Shigemasa E (2007) *J Phys B At Mol Opt Phys* 40:2091
21. Mase K, Nagasono M, Tanaka S, Kamada M, Urisu T, Murata Y (1997) *Rev Sci Instrum* 68:1703
22. Mase K, Nagasono M, Tanaka S, Sekitani T, Nagaoka S (2003) *S Low Temp Phys* 29:243

23. Kobayashi E, Mase K, Nambu A, Seo J, Tanaka S, Kakiuchi T, Okudaira KK, Nagaoka S, Tanaka M (2006) *J Phys Condens Matter* 18:S1389
24. Eberhardt W, Sham TK, Carr R, Krummacher S, Strongin M, Weng SL, Wesner D (1983) *Phys Rev Lett* 50:1038
25. Tanaka K, Sako EO, Ikenaga E, Isari K, Sardar SA, Wada S, Sekitani T, Mase K, Ueno N (2001) *J Electron Spectrosc Relat Phenom* 119:255
26. Tinone MCK, Tanaka K, Maruyama J, Ueno N, Imamura M, Matsubayashi N (1994) *J Chem Phys* 100:5988
27. Wada S, Sako EO, Sumii R, Waki S, Isari K, Sekiguchi T, Sekitani T, Tanaka K (2003) *Nucl Instrum Methods Phys Res B* 199:361
28. Wada S, Sumii R, Isari K, Waki S, Sako EO, Sekiguchi T, Sekitani T, Tanaka K (2003) *Surf Sci* 528:242
29. Treichler R, Riedl W, Wurth W, Feulner P, Menzel D (1985) *Phys Rev Lett* 54:462
30. Treichler R, Riedl W, Feulner P, Menzel D (1991) *Surf Sci* 243:239
31. Jaeger R, Stöhr J, Kendelewicz J (1983) *Phys Rev B* 28:1145
32. Jaeger R, Stöhr J, Kendelewicz J (1983) *Surf Sci* 134:547
33. Coulman D, Puschmann A, Höfer U, Steinrück H-P, Wurth W, Feulner P, Menzel D (1990) *J Chem Phys* 93:58
34. Tanaka K, Kizaki H, Sumii R, Matsumoto Y, Wada S (2006) *Radiat Phys Chem* 75:2076
35. Kizaki H, Wada S, Sako EO, Sumii R, Waki S, Isari K, Sekitani T, Sekiguchi T, Tanaka K (2005) *J Electron Spectrosc Relat Phenom* 144–147:447
36. Wada S, Sumii R, Kizaki H, Iizuka Y, Matsumoto Y, Sekitani T, Tanaka K (2005) *Surf Sci* 593:283
37. Kizaki H, Matsumoto Y, Ban H, Morishita K, Wada S, Tanaka K (2007) *Surf Sci* 601:3956
38. Ikenaga E, Isari K, Kudara K, Yasui Y, Sardar SA, Wada S, Sekitani T, Tanaka K, Mase K, Tanaka S (2001) *J Chem Phys* 114:2751
39. Ikenaga E, Kudara K, Kusaba K, Isari K, Sardar SA, Wada S, Mase K, Sekitani T, Tanaka K (2001) *J Electron Spectrosc Relat Phenom* 114–116:585
40. Sekitani T, Kusaba K, Morita K, Nanbu Y, Isari K, Ikenaga E, Wada S, Tanaka K (2003) *Surf Sci* 532–535:267
41. Sako EO, Kanameda Y, Ikenaga E, Mitani M, Takahashi O, Saito K, Iwata S, Wada S, Sekitani T, Tanaka K (2001) *J Electron Spectrosc Relat Phenom* 114–116:591
42. Menzel D (2006) *Surf Interface Anal* 38:1702
43. Takahashi O, Matsui T, Kawano A, Tabayashi K, Yamasaki K (2007) *J Mol Struct* 808:35
44. Morin P, Nenner I (1986) *Phys Rev Lett* 56:1913
45. Björnehholm O (2001) *J Chem Phys* 115:4139, and references therein
46. Takahashi O, Tabayashi K, Wada S, Sumii R, Tanaka K, Odelius M, Pettersson LGM (2006) *J Chem Phys* 124:124901
47. LCLS homepage. https://portal.slac.stanford.edu/sites/lcls_public/Pages/Default.aspx
48. SACLA homepage. <http://xfel.riken.jp/eng/index.html>
49. Popmintchev T, Chen M-C, Popmintchev D, Arpin P, Brown S, Ališauskas S, Andriukaitis G, Balčiūnas T, Mücke OD, Pugzlys A, Baltuška A, Shim B, Schrauth SE, Gaeta A, Hernández-García C, Plaja L, Becker A, Jaron-Becker A, Murnane MM, Kapteyn HC (2012) *Science* 336:1287
50. Young L, Kanter EP, Krässig B, Li Y, March AM, Pratt ST, Santra R, Southworth SH, Rohringer N, DiMauro LF, Doumy G, Roedig CA, Berrah N, Fang L, Hoener M, Bucksbaum PH, Cryan JP, Ghimire S, Glowia JM, Reis DA, Bozek JD, Bostedt C, Messerschmidt M (2010) *Nature* 466:56
51. Berrah N, Fang L, Murphy B, Osipov T, Ueda K, Kuk E, Feifeld R, van der Meulen P, Salen P, Schmidt HT, Thomas RD, Larsson M, Richter R, Prince KC, Bozek JD, Bostedt C, Wada S, Piancastelli MN, Tashiro M, Ehara M (2011) *Proc Nat Acad Sci* 108:16912
52. Meyer M, Radcliffe P, Tschentscher T, Costello JT, Cavalieri AL, Grguras I, Maier AR, Kienberger R, Bozek JD, Bostedt C, Schorb S, Coffee R, Messerschmidt M, Roedig C, Sistrunk E, DiMauro LF, Doumy G, Ueda K, Wada S, Dusterer S, Kazansky AK, Kabachnik NM (2012) *Phys Rev Lett* 108:063007

Noriyuki Kouchi

5.1 Introduction

The superexcited state of molecules is defined as a neutral excited state with internal energy higher than the ionization energy of the molecule. It is much different from the ordinary excited state below the ionization energy. The characteristics and dynamics of the superexcited state are discussed to substantiate that the molecule obtaining energy higher than the ionization energy does not always ionize.

5.2 What Are Superexcited States?

Ionization of atoms and molecules is essential in mass spectrometry. The energy higher than their ionization energies should be given to ionize them. A simple question arises, i.e., Are atoms and molecules always ionized when they are given energies higher than their ionization energies? Let us discuss this question since this is the origin of the superexcited state.

We consider the photoionization:



Here M denotes an atom or a molecule. The photoionization quantum yield as a function of incident photon energy E is defined as

$$\eta(E) = \frac{\sigma_i(E)}{\sigma_a(E)}, \quad (5.2)$$

where $\sigma_i(E)$ is the photoionization cross section and $\sigma_a(E)$ the photoabsorption cross section. The photoionization quantum yield, $\eta(E)$, expresses the probability of ionization when a photon with energy E is absorbed by an atom or a molecule, M . The question at issue is rewritten as follows in terms of the photoionization quantum yield, $\eta(E)$, and the ionization energy of M , I_p .

N. Kouchi (✉)

Department of Chemistry, Tokyo Institute of Technology, 2-12-1 O-okayama, Meguro-ku (Bldg.W4-4),
Tokyo 152-8551, Japan

e-mail: nkouchi@chem.titech.ac.jp

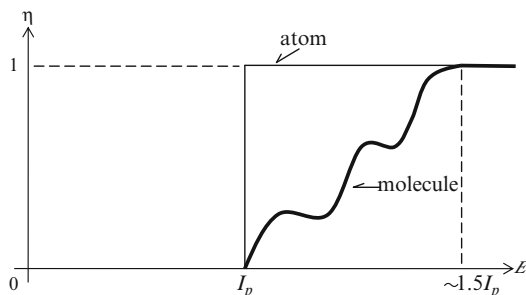


Fig. 5.1 The photoionization quantum yield η as a function of incident photon energy E for atoms and molecules. Here I_p denotes the ionization energy

Table 5.1 The hierarchical structure of internal motions of the molecule

	Electronic motion	Relative motion of nuclei	
		Vibration	Rotation
Period of motion	$\sim 10^{-16}$ s	$\sim 10^{-14}$ s	$\sim 10^{-12}$ s
Splitting of energy levels	\sim eV	~ 100 meV	\sim meV

The values are just typical ones. Translated from “Hohsyasen Kagaku no Susume” in Japanese, Gakkai Shuppan Center (2006), p. 225 with permission

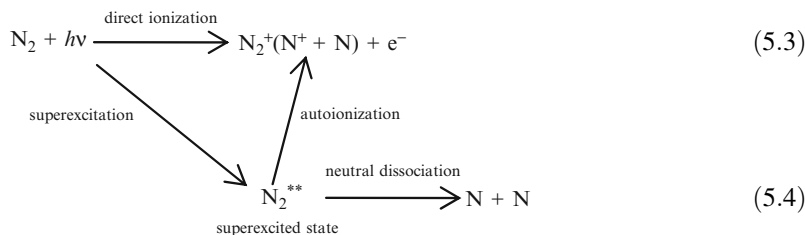
Is the photoionization quantum yield $\eta(E)$ always unity when $E \geq I_p$?

The answer is “Yes” for atoms and “No” for molecules as illustrated in Fig. 5.1, which shows that (a) Atoms or molecules are not always ionized even if they absorb a photon with energy higher than I_p . They could be excited to neutral excited states.

(b) Atoms in such excited states are spontaneously ionized to nearly 100 %.

(c) Molecules in such excited states are also ionized. However they could escape from the ionization and take non-ionization processes that do not occur for atoms.

The neutral excited states in (a) are referred to as superexcited states. They are embedded in energy continuum due to the fact that the energy of ionized electrons is not quantized since they are free. The existence and important role of superexcited states were first predicted by Platzman in the early 1960s in a pioneering theoretical work on the interaction of ionizing radiation with matter [1]. The spontaneous ionization process in (b) and (c) is referred to as autoionization. The next question is what the non-ionization process in (c) is. It competes with the autoionization. We should know the rate of the autoionization to answer this question. It is known to be larger than 10^{14} s⁻¹. The emission of fluorescence is a typical decay process. However, it cannot compete with the autoionization since the rate of the emission from valence excited states does not exceed 10^9 s⁻¹ to a large extent for isolated atoms and molecules. The only possible non-ionization process that can compete with the autoionization may be neutral dissociation. The rate of the neutral dissociation would be in the order of the reciprocal of the vibrational period, e.g., 10^{-14} s (see Table 5.1), and thus it can compete with the autoionization. This is the physics underlying Fig. 5.1, which is illustrated below for N₂.



In processes (5.3) and (5.4) N_2 is in its ground electronic state, while N , N_2^+ , and N^+ can be in their ground or excited electronic states. From now on we focus on superexcited states of molecules, not atoms.

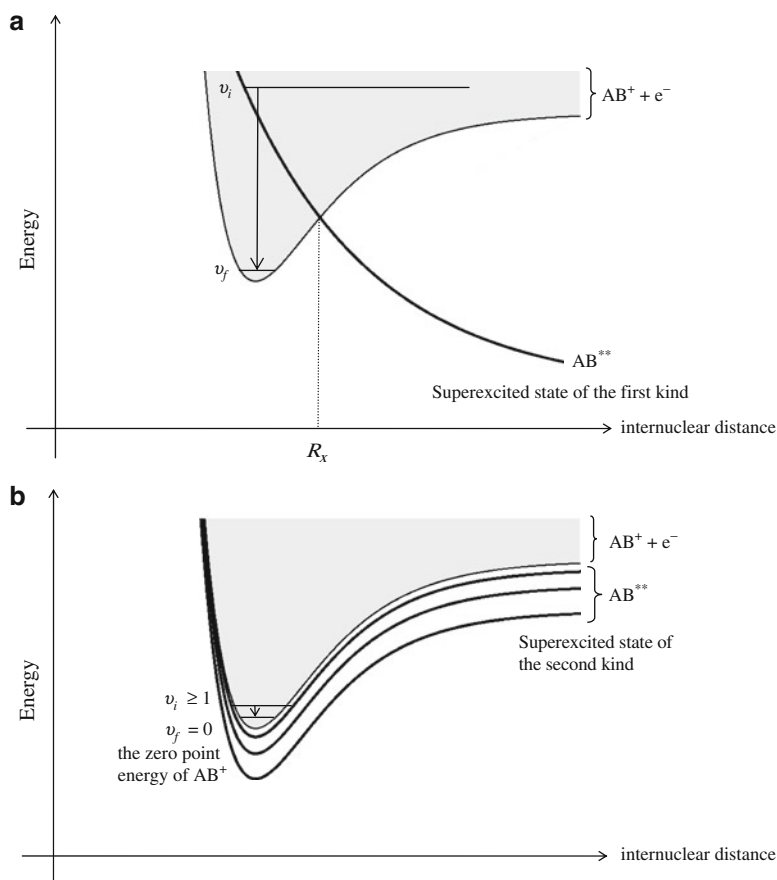
As mentioned the superexcited state is defined as a state such that its internal energy is higher than the ionization energy of the molecule. Let us substantiate how it keeps such high energy. The internal motion of molecules is divided into two parts within the Born–Oppenheimer approximation [2]: the electronic motion around the fixed nuclei and the relative motion of the nuclei. The latter motion is further divided into vibration and rotation [2]. In Table 5.1, the period and splitting of energy levels of each motion are summarized to show the hierarchical structure of internal motions of the molecule.

We take a diatomic molecule AB to show how the superexcited molecule AB^{**} keeps energy higher than the ionization energy in Fig. 5.2. The solid curves are potential energy curves of neutral electronic states of AB , and the curve with shadow represents the ensemble of the potential energy curves of $\text{AB}^+ + \text{e}^-$. The energy of the ionized electron, e^- , is not quantized and thus the potential energy curves of $\text{AB}^+ + \text{e}^-$ constitute an energy continuum, which is displayed by the shadow. The bottom edge of the continuum shows the potential energy curve of $\text{AB}^+ + \text{e}^-$ with zero kinetic energy of e^- against the fixed nuclei. It is simply referred to as a potential energy curve of AB^+ . In (a) we can readily understand that AB^{**} is a superexcited molecule even when we take only the degree of freedom of the electronic motion into account since the potential energy curve of AB^{**} is embedded in the continuum, or in other words there exists a range of internuclear distance where the potential energy curve of AB^{**} exceeds that of AB^+ , i.e., the range of the internuclear distance shorter than R_x .

In (b) the potential energy curves of AB^{**} are below the potential energy curve of AB^+ at any internuclear distance since one electron is bound by AB^+ to form AB^{**} . Thus AB^{**} could not be referred to as a superexcited molecule if we took account of only the degree of freedom of the electronic motion. However AB^{**} can vibrationally or rotationally be excited to the energy level beyond the zero point energy of AB^+ . It follows that AB^{**} in (b) is also a superexcited molecule. In (b), AB^{**} is vibrationally excited, i.e., the vibrational quantum number $v_i \geq 1$.

The superexcited state illustrated in Fig. 5.2a is called a superexcited state of the first kind and that in Fig. 5.2b is called a superexcited state of the second kind [3]. The superexcited state of the first kind is a superexcited state even when we take only the degree of freedom of the electronic motion into account. The superexcited state of the second kind, on the other hand, is a superexcited state when we take into account the degree of freedom of the nuclear motion as well as that of the electronic motion. The superexcited states of the first and second kinds keep energy higher than the ionization energy in much different ways from each other. The multiply excited state and inner-orbital excited state are superexcited states of the first kind. The rovibrationally excited Rydberg state is a superexcited state of the second kind. We note that for atoms there exists only a superexcited state of the first kind and that of the second kind does not exist.

Fig. 5.2 The potential energy curves of the superexcited states of the diatomic molecule AB (solid curves) and those of $AB^+ + e^-$ (solid curves with shadows). (a) Superexcited states of the first kind and (b) superexcited states of the second kind. Based on Fig. 19 of [3] with permission



5.3 Decay Processes of the Superexcited Molecule

In this section let us discuss decay processes of the superexcited molecule. As mentioned in Sect. 1, the autoionization is a characteristic decay process that is not seen for usual excited states with energies lower than the ionization energy. In Fig. 5.2, the autoionization is expressed by the down arrow, the length of which gives the kinetic energy of the ionized electron with respect to the center of mass of the nuclei. In the superexcited molecule of the first kind the autoionization is brought about by the energy transfer from the excited electron to the other electron, i.e., by the breakdown of the independent electron model. Such autoionization is referred to as the electronic autoionization. On the other hand in the superexcited molecule of the second kind the autoionization is brought about by the energy transfer from the degree of freedom of the vibrational or the rotational motion to that of the electronic motion, i.e., by the breakdown of the Born–Oppenheimer approximation. Such autoionization is referred to as the vibrational or the rotational autoionization.

The electronic autoionization is attributed to the energy transfer from one electron to the other electron within the degree of freedom of the electronic motion. On the other hand, the vibrational autoionization and rotational autoionization are induced by the energy transfer from the nuclear degree of freedom to the electronic degree of freedom. Hence the rate of the electronic autoionization, τ_e^{-1} , would be much larger than the rates of the vibrational autoionization, τ_v^{-1} , and the rotational

autoionization, τ_r^{-1} . To the rough approximation, the values of τ_e , τ_v , and τ_r , i.e., the lifetimes of autoionization, are in the same order of magnitude as the periods of the electronic, vibrational, and rotational motions, respectively, which are summarized in Table 5.1. It thus follows that

$$\tau_e^{-1} \gg \tau_v^{-1} \gg \tau_r^{-1}. \quad (5.5)$$

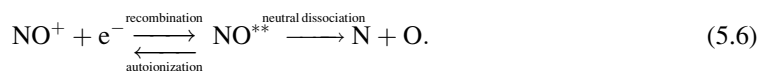
In Sect. 1, it is mentioned that the rate of the autoionization is known to be larger than 10^{14} s^{-1} . This statement in fact refers to the electronic and vibrational autoionization, but does not refer to the rotational autoionization.

As seen in processes (5.3) and (5.4), the superexcited molecule decays through the autoionization and neutral dissociation. The neutral dissociation has almost the same timescale as the vibration, and thus the rate of the neutral dissociation would be in the same order of magnitude as the reciprocal of the vibrational period. The neutral dissociation hence competes with the autoionization. It is well known that the neutral dissociation is classified into two kinds, i.e., the direct dissociation and predissociation. A typical example of the direct dissociation is shown in Fig. 5.2a, where the superexcited molecule AB^{**} dissociates down the repulsive potential energy curve. The predissociation is a transition from a discrete vibrational level to a continuous vibrational level (a dissociating level). The predissociation is hence slower than the direct dissociation. We note that the predissociation is seen for usual excited states with energies lower than the ionization energy of the molecule.

Let us explain Fig. 5.1 based on the discussion mentioned above. The superexcited molecule of the second kind, not the first kind, is produced around I_p , the ionization energy of the molecule, and thus the autoionization involved is the vibrational or the rotational one. It hence seems that the neutral dissociation dominates the decay process and most of the superexcited molecules do not autoionize. It is difficult to predict which is more likely to occur around I_p , the superexcitation or the direct ionization. The cross section of the superexcitation seems much larger than that of the direct ionization taking into account the experimental results that $\eta \approx 0$ around I_p for most of the molecules [4]. The superexcited molecule of the first kind becomes more probable with increasing the photon energy E and the autoionization becomes more an electronic one, i.e., the autoionization dominates the decay process of the superexcited molecule. It follows that the value of η approaches unity with increasing E . There would exist the range of E where no superexcited states are involved. The value of η is, of course, unity in such a range. The photoionization quantum yield as a function of incident photon energy is strongly dependent on molecule, in particular in the range between I_p and $\sim 1.5 I_p$ as shown in Fig. 5.3.

5.4 Superexcited Molecule as Reaction Intermediate

In this section let us show that the superexcited molecule plays an important role as reaction intermediate. One typical example is the Penning ionization. Another example is the dissociative recombination, which annihilates molecular ions in the ionosphere:



The transient species NO^{**} is in fact a superexcited molecule as a reaction intermediate. The neutral dissociation and autoionization compete with each other and the dissociative recombination is completed when NO^{**} dissociates into N and O atoms escaping from the autoionization.

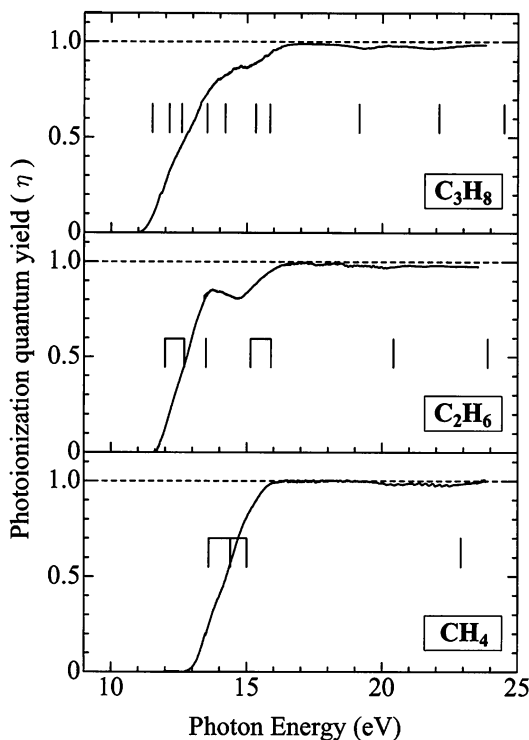


Fig. 5.3 The photoionization quantum yield of CH_4 , C_2H_6 , and C_3H_8 as a function of incident photon energy. The energies of the ionic states involved are indicated by the vertical bars. From [5] with permission

Let us consider the case in which the energy of the incident electron in process (5.6) is slightly lower than the threshold energy of an electronic excitation in the molecular ion NO^+ . The electron virtually excites NO^+ to the excited electronic state and it falls into a molecular orbital since the energy of the electron becomes negative. As a result the superexcited molecule of the first kind, NO^{**} , is produced. It is in fact the multiply excited NO molecule. Such processes occur only at certain energies of the incident electron.

Let us then consider the case in which the energy of the incident electron is slightly lower than the threshold energy of a vibrational or a rotational excitation in NO^+ . The electron virtually excites NO^+ to the vibrationally or the rotationally excited state and it falls into a molecular orbital. As a result the superexcited molecule of the second kind, NO^{**} , is produced. Such processes also occur only at certain energies of the incident electron. As seen above the superexcited molecule is considered the Feshbach resonance [6] in the collision between an electron and molecular ion.

Understanding the formation and decay processes of the superexcited molecule is a challenging subject in physical chemistry since both the independent electron model and Born–Oppenheimer approximation are much less reliable than for molecules in the ground and lower excited electronic states. From the experimental points of view the key to observing superexcited molecules is measuring cross sections free from ionization as a function of incident photon energy [see processes (5.3) and (5.4)] [7]. The experimental investigation on the dynamics of superexcited molecules was reviewed in detail in [4].

5.5 Summary

The superexcited molecule may not play a leading role in the mass spectrometry, and is always in a supporting role, but it is still essential because of the following mechanistic point of view.

1. The existence of the superexcited states of molecules suppresses the ionization. For example the photoionization quantum yield is close to zero around the ionization energy of the molecule as shown in Fig. 5.3.
2. Both electrons and molecular ions are annihilated by the dissociative recombination. The superexcited molecule plays an important role as reaction intermediate [see process (5.6)]. The competition between the neutral dissociation and autoionization from the superexcited molecule in process (5.6) governs the disappearance of charged species.

References

1. Platzman RL (1962) *Radiat Res* 17:419
2. Bransden BH, Joachain CJ (2003) *Physics of atoms and molecules*, 2nd edn, Chapters 10 and 11. Pearson Education, Harlow
3. Nakamura H (1991) *Int Rev Phys Chem* 10:123
4. Hatano Y (1999) *Phys Rep* 313:109
5. Kameta K, Kouchi N, Ukai M, Hatano Y (2002) *J Electron Spectrosc Relat Phenom* 123:225
6. McDaniel EW (1989) *Atomic collisions – electron and photon projectiles*. Wiley Interscience, New York
7. Odagiri T, Kouchi N (2011) Charged particle and photon interactions with matter. In: Hatano Y, Katsumura Y, Mozumder A (eds) *Recent advances, applications, and interfaces*, chapter 2. CRC Press, Boca Raton

Toshiki Sugai

6.1 Introduction

6.1.1 Mass Spectrometry and Ion Mobility Spectrometry

The advantages of mass spectrometry (MS) in terms of rich information, easy operation, and high throughput have been established since its invention, and they have been applied for many fields such as nanomaterials, biochemistry, and medical diagnostics. To expand the potential, the ion mobility spectrometry (IMS) combined with MS has been developed rapidly as a kind of hybrid measurement system, so called IMS/MS. IMS has close relationship with MS but also has unique properties for structural analyses and detection of intermolecular interaction [1, 2]. This IMS/MS has novel advantages originating from both systems which can be clarified by the discovery of C₆₀ which resulted in Nobel Prize in chemistry in 1996 [3] and the following structural identifications of C₆₀. The detection method of C₆₀ was MS with a laser vaporization cluster source developed by Nobel laureate R. Smalley. It would have been impossible without MS providing high sensitivity, high throughput, and high resolution for the discovery. However, the discovery also shows the limit of information obtained by MS: the final identification and structural determination were executed by NMR and X-ray diffraction, the so-called bulk measurement methods, with bulk production achieved by Krätschmer and Huffman in 1991 [4, 5, 6]. MS is powerful enough to identify “well-known materials” but is able to just show the “possibility of existence” for something new. IMS/MS, on the other hand, can tell not only the “soccer ball” structure of stable C₆₀ fullerenes without help of other measurement methods but also some new structures of unstable C₆₀ clusters [7, 8].

In this chapter, I will show the concept, the apparatus, and the potential of IMS/MS [9].

6.1.2 Concept of IMS and Difference Between MS and IMS

Figure 6.1 shows the concept of IMS. Both ions shown here consist of 60 carbon atoms but have different structures, so-called isomers. In IMS as well as in MS, ion movement under an electric field is observed. The differences are that IMS utilizes the steady movement dominated by the ion–gas

T. Sugai (✉)
Department of Chemistry, Toho University, 2-2-1 Minayama, Funabashi-shi,
Chiba 2748510, Japan
e-mail: sugai@chem.sci.toho-u.ac.jp

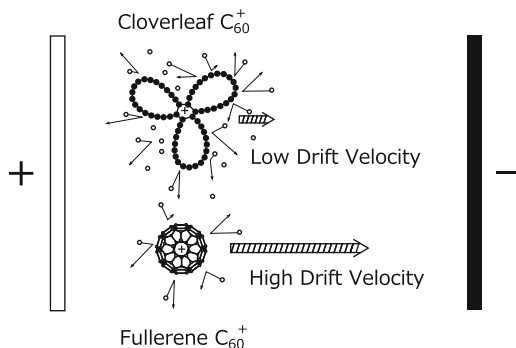


Fig. 6.1 Concept of ion mobility spectrometry. The mobility or the drift velocity of ions under electric fields reflects the structure of the ions and the interaction between the ions and the gas molecules. The *top figure* shows a cloverleaf structure of C_{60} with a small drift velocity and the *bottom figure* shows a fullerene structure with a large drift velocity. The *open circles* show the gas molecules interacting with the ion. The cloverleaf ion collides with the gas molecules more frequently or have more interaction than the fullerene ion, which results in the small mobility

interaction in a relatively high pressure gas, whereas MS utilizes the accelerated movement by the field in vacuum. The upper cloverleaf ion in the figure has more intense interaction or a larger collision cross section with the gas molecule and the lower fullerene one has less intense interaction or a smaller cross section. The consequence of those differences is the lower drift velocity of the cloverleaf isomer and the higher one of the fullerene. IMS can identify those isomers which MS cannot distinguish.

The difference between MS and IMS is shown in Fig. 6.2. Both IMS and MS are based on processes and interaction with the difference of several orders of the magnitude in energy and time. The high energy acceleration in vacuum of tens of eV to keV is utilized in MS where an ion must be stable without collision for around μs to be identified as a single species. When the ion has even single collision, the high energy collision induced dissociation (CID) is invoked and numbers of different ions are produced. It is usually difficult to investigate the weak interaction with thermal energy of several meV in MS.

On the other hand, the low energy thermal collisions in high pressure gas together with the movement by the field are utilized in IMS where very weak interaction can be observed through the drift velocity. Even if the complex between ion and gas is unstable with much shorter life time than μs , we can detect the complex and the interaction by the change of the drift velocity through many collisions. This sensitivity in terms of the weak interaction provides us the new tool to have fine information on ions like isotope effects and chiral effects suggesting the potential of IMS to explore novel scientific fields.

6.2 Kinetics in IMS

In IMS, ions obey kinetics under a static electric field as well as in MS [1, 10]. The ion movement in IMS is strongly affected by collisions with gas molecules, whereas it is dominated only by the field in MS without collision in vacuum where an ion with a mass of m and a charge of q is accelerated by the electric field of a vector \vec{E} with the magnitude $E \equiv |\vec{E}|$. Throughout this chapter a physical quantity such as an electric field is represented by E or \vec{E} where the latter one stresses the meaning of a vector. The velocity of the ion keeps increasing in MS with the acceleration of Eq/m . In IMS under the same

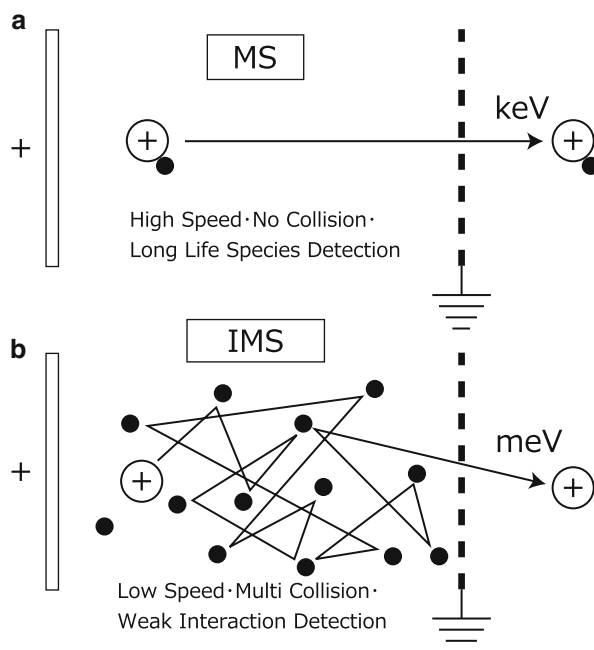


Fig. 6.2 The difference between (a) MS and (b) IMS. MS utilizes relatively high energy (tens of eV to keV) acceleration processes and the detected ion must be stable without collision during around μs in the acceleration. Even when the ion–molecule complex is unstable with short lifetime much less than μs because of the weak interaction, they can be detected with many ion–molecule collisions or many chance to form the complex in long-term observation

electric field of E , the velocity of the ion converges on a drift velocity of $v_d(E/N)$ as a function of the field of E and a molecular gas density of N . Since the obtained drift velocity reflects the interaction between the ion and the gas molecule which strongly depends on the ion structure, the structural information is deduced from the IMS measurement. This ion movement in IMS is categorized into two conditions: the low field condition and the high field condition [1, 10]. In the low field condition, it is dominated by the thermal collision with the perturbation of the field acceleration. In the latter case, on the other hand, the field acceleration is comparable to the collision, which will be discussed later.

6.2.1 Low Field Condition

The low field condition is realized by low E/N with the high pressure or the low field where the field effect is much lower than that of the collision. In this condition the velocity of the ion converges on the drift velocity which is proportional to the field E as described in Eq. (6.1).

$$v_d = KE. \quad (6.1)$$

This K is defined as an ion mobility. It has a close relationship with the structure of the ion so that we can deduce the structural information from the mobility.

Here the mobility is analyzed through the movement in gas under the static electric field. Figure 6.3 shows the collision processes of IMS, where the ion and the gas molecules are regarded as hard

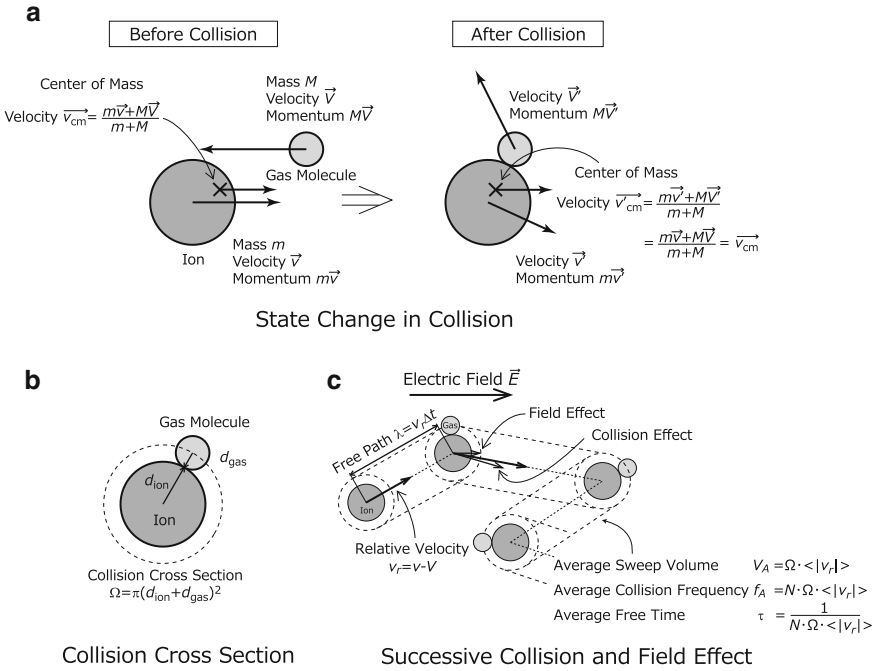


Fig. 6.3 (a) The states of an ion and a gas molecule before and after the collision. The velocities of the ion and the gas of \vec{v} and \vec{V} are changed to those of \vec{v}' and \vec{V}' , respectively. The velocity of the center of mass \vec{v}_{cm} is constant. (b) The collision cross section $\Omega = \pi(d_{ion} + d_{gas})^2$ between the ion and the gas molecule. It determines the collision frequency between the ion and the gas. The collision occurs when the distance between the ion and the gas molecule is shorter than $d_{ion} + d_{gas}$. (c) Successive collision processes. The ion is accelerated by the field during the so-called free path where no collision occurs. After these collision processes, the ion drifts in the buffer gas. The relative velocity of v_r , the average sweep volume of V_A , the average collision frequency of f_A , and the mean free time τ are described in the text

spheres with the constant collision cross section and without internal freedom like vibrations and rotations. The total collision energy is distributed only into the kinetic energy of each particle. The collision cross section is independent of the field, the temperature of the gas, and the energy. Figure 6.3a shows the kinetic processes in the collision where the masses of the ion and the gas molecules are defined as m and M , respectively. The velocities of the ion and the gas change from \vec{v} and \vec{V} to \vec{v}' and \vec{V}' , respectively, keeping the velocity of the center of mass \vec{v}_{cm} constant. As described in Fig. 6.3b, the radii of the ion and the gas molecule are defined as d_{ion} and d_{gas} , respectively. The collision cross section (Ω) is described as $\Omega = \pi(d_{ion} + d_{gas})^2$, which is independent of the temperature of the gas, the velocity, and the field. Whenever the distance between the ion and the gas molecule is less than $d_{ion} + d_{gas}$, they must collide with each other.

Figure 6.3c shows the successive collisions between the ion and the gas molecules under the field. The ion is accelerated by the field during free time Δt between the collisions where the ion moves without collision in the path of $\lambda = v_r \Delta t$, where v_r is the relative velocity defined as the difference between the velocities of the ion and the gas molecule like

$$\vec{v}_r \equiv \vec{v} - \vec{V}. \quad (6.2)$$

After these collision processes, the ion drifts in the buffer gas in macroscale and this movement is detected in IMS observation. The field effect becomes more significant with the longer Δt . The average Δt defined as τ determines the drift velocity in whole processes which is calculated as the inverse of the average collision frequency $1/f_A$. Here f_A is the average number of collisions between the ion and the gas molecules in unit time. As shown in Fig. 6.3c, f_A is deduced from the number of the gas molecules in sweep volume V_A which is defined as $\Omega \cdot \langle |\vec{v}_r| \rangle$. When the ion is assumed to move in frozen gas molecules, we have the frequency as $f_A = N \cdot \Omega \cdot \langle |\vec{v}_r| \rangle$, where N is the molecular gas density. Finally the average free time of τ is represented as [1, 10, 11]

$$\tau = 1/f_A = \frac{1}{N \langle |\vec{v}_r| \rangle \Omega}. \quad (6.3)$$

The ion has the constant drift velocity in IMS observation, the acceleration or the momentum gain by the field is lost in average by the collisions. The gain is calculated with the impulse of

$$m \langle \vec{v} - \vec{v}' \rangle = \vec{F} \times \tau = q \vec{E} \tau, \quad (6.4)$$

where \vec{F} is the field force applied to the ion. This momentum gain is converted into acceleration of the colliding gas molecule, which is represented as

$$M \langle \vec{V}' - \vec{V} \rangle = M \langle \vec{V}' \rangle - M \langle \vec{V} \rangle = q \vec{E} \tau, \quad (6.5)$$

where $\langle \rangle$ represents the average of the whole processes. Here the gas molecules do not move macroscopically, which is equivalent to the zero average velocity of the gas molecules before the collision represented as

$$\langle \vec{V} \rangle = 0. \quad (6.6)$$

From Eqs. (6.5) and (6.6) we have

$$\langle \vec{V}' \rangle = \frac{q \vec{E} \tau}{M}. \quad (6.7)$$

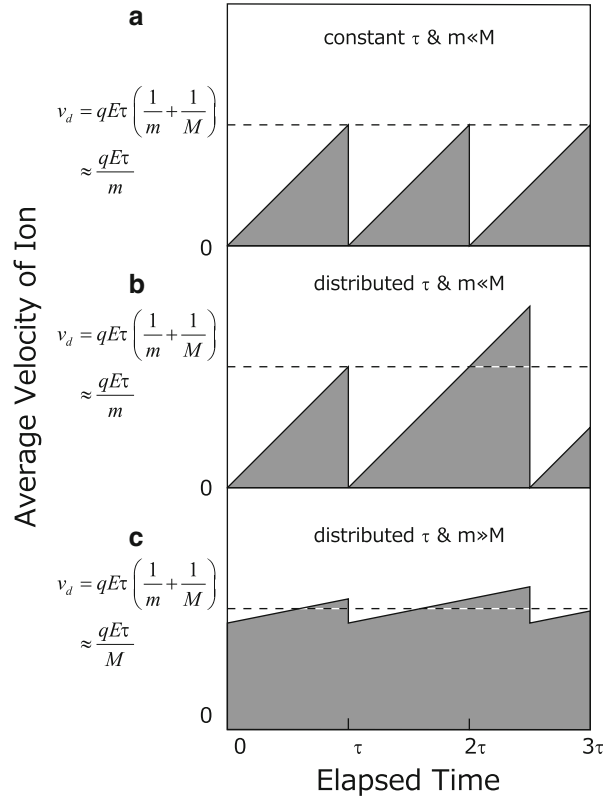
Through the collision processes, v_r randomly varies by the slight changes in positions and angles because of actual complicated structures of the ion and the gas molecule. The consequence is that the average v_r on the whole molecules is reduced to zero, which is represented as

$$\langle \vec{v}'_r \rangle \equiv \langle \vec{v}' - \vec{V}' \rangle = 0 \Leftrightarrow \langle \vec{v}' \rangle = \langle \vec{V}' \rangle. \quad (6.8)$$

The momentum conservation in the collision process tells us the following relation with $\langle \vec{v} \rangle, \langle \vec{v}' \rangle$ as

$$m \langle \vec{v} \rangle + M \langle \vec{V} \rangle = m \langle \vec{v}' \rangle + M \langle \vec{V}' \rangle. \quad (6.9)$$

Fig. 6.4 The time profile of the average velocity of an ion in IMS. The unit of horizontal line is the average free time τ . The ion is accelerated by the field in the free time and is decelerated by the collision. (a) The profile when the mass of ion is much smaller than that of the gas molecule with periodic collisions, (b) in the same mass condition as (a) with irregular collisions represented as Poisson distribution, and (c) in the condition that the mass of ion is much larger than that of the gas molecule with irregular collisions



With Eqs. (6.6)–(6.9), the average ion velocity just before the collision, which is the same as the drift velocity of v_d [1, 10], is turned out to be

$$v_d \equiv |\langle \vec{v} \rangle| = qE\tau \left(\frac{1}{m} + \frac{1}{M} \right). \quad (6.10)$$

Equation (6.10) is interpreted as follows. When the mass of ion is much smaller than that of the gas molecule, $m \ll M$, Eq. (6.10) is reduced to $v_d = qE\tau/m$ with $1/m \gg 1/M$. This case corresponds to the situation that the gas is heavy enough to stand still and the ion is reflected to random direction in the collision processes. This process results in zero average velocity of the ion after the collision which is followed by the field acceleration to $\langle \vec{v} \rangle = qE\tau/m$ until the next collision. The lighter the ion is, the higher the drift velocity we have with the larger acceleration effect.

This time dependence of the average ion velocity is shown in Fig. 6.4a, b. When the collision occurs every τ (Fig. 6.4a) the average ion velocity is represented as a periodic sawtooth wave with the average velocity of $v_d = qE\tau/(2m)$. Actually the collision does not take place periodically but randomly where the free time varies with Poisson distribution of $p(t) = \frac{1}{\tau} \exp(-t/\tau)$. Here $p(t)$ is the probability function. In this situation, the average ion velocity is represented as an irregular sawtooth wave (Fig. 6.4b) so that the time average is obtained as $v_d = qE\tau/m$ since the average of the free time between the successive collisions is 2τ [11].

When the mass of the ion is much larger than that of the gas molecule, $m \gg M$, on the other hand, Eq. (6.10) is reduced to $v_d = qE\tau/M$, where almost no velocity change occurs through the collision and the field acceleration. The profile of the velocity is shown in Fig. 6.4c where we have

$$v = v'. \quad (6.11)$$

The momentum gain of the ion by the field is transferred to the gas molecule by the collision where the average velocity of the gas molecule is changed from zero in Eq. (6.6) to

$$\langle \vec{V}' \rangle = qE\tau/M. \quad (6.12)$$

Equations (6.8), (6.11), and (6.12) show that this average velocity of the gas molecule after the collision is the same as that of the ion represented as

$$\langle \vec{v} \rangle = \langle \vec{v}' \rangle = v_d = \langle \vec{V}' \rangle = qE\tau/M. \quad (6.13)$$

The smaller the mass of the gas molecule is, the higher drift velocity we have with the lower loss of the field acceleration.

For the analysis of actual IMS measurement, v_d should be obtained as a function of a gas temperature T together with the molecular gas density N and the collision cross section Ω . When the free time τ in Eq. (6.3) is introduced to Eq. (6.10), the drift velocity is represented as

$$v_d = \frac{qE}{N \langle |\vec{v}_r| \rangle \Omega} \left(\frac{1}{m} + \frac{1}{M} \right). \quad (6.14)$$

To introduce the gas temperature T the average velocity of $\langle |\vec{v}_r| \rangle$ is approximated with root mean approximation as

$$\langle |\vec{v}_r| \rangle \approx \sqrt{\langle v_r^2 \rangle} = \sqrt{\langle (\vec{v} - \vec{V})^2 \rangle} = \sqrt{v^2 - 2\langle \vec{v} \cdot \vec{V} \rangle + V^2} = \sqrt{\frac{3k_B T}{m} + \frac{3k_B T}{M}}, \quad (6.15)$$

where $\langle \vec{v} \cdot \vec{V} \rangle$ is reduced to zero because of the independence of v and V with Eq. (6.6) [1, 10, 11].

With introduction of Eqs. (6.15) and (6.14), the drift velocity is summarized as

$$v_d = \frac{1}{\sqrt{3}} \frac{qE}{N} \left(\frac{1}{m} + \frac{1}{M} \right)^{1/2} \left(\frac{1}{k_B T} \right)^{1/2} \frac{1}{\Omega}. \quad (6.16)$$

The N and T dependence comes from the fact that τ is inverse of the collision frequency which is proportional to N and \sqrt{T} , respectively. The dependence on m and M , on the other hand, comes from two effects: the momentum effect in Eq. (6.10) and the thermal velocity effect in Eq. (6.2). The momentum transfer and the thermal velocity effects are proportional to $(\frac{1}{m} + \frac{1}{M})$ and $(\frac{1}{m} + \frac{1}{M})^{-1/2}$, respectively, so that we have the mass dependence of $(\frac{1}{m} + \frac{1}{M})^{1/2}$ in Eq. (6.16). The approximation used in Eq. (6.16) is corrected with a more precise treatment as [1, 10, 11]

$$v_d = \frac{3}{16} \frac{qE}{N} \left(\frac{1}{m} + \frac{1}{M} \right)^{1/2} \left(\frac{2\pi}{k_B T} \right)^{1/2} \frac{1}{\Omega}. \quad (6.17)$$

With Eqs. (6.1) and (6.17), the mobility K is represented as

$$K = v_d/E = \frac{3}{16} \frac{q}{N} \left(\frac{1}{m} + \frac{1}{M} \right)^{1/2} \left(\frac{2\pi}{k_B T} \right)^{1/2} \frac{1}{\Omega}, \quad (6.18)$$

Thus the mobility K observed in IMS contains the information on the structure of ions which is elucidated from the cross section Ω in Eq. (6.18).

Typical ambient pressure IMS/MS measurement [12] is performed at 300 K in 500 Torr He. The estimated cross section from the observed mobility with the analysis of Eq. (6.18) is $1.34 \times 10^{-14} \text{cm}^2$. The hard sphere model tells that the cross section of C_{60} in He is $\Omega = 1.37 \times 10^{-14} \text{cm}^2$ with $r_{C_{60}} = 3.5 \text{ \AA}$ obtained by X-ray diffraction [6] together with the van der Waals radii of helium and carbon atoms of $r_{\text{He}} = 1.4 \text{ \AA}$ and $r_C = 1.7 \text{ \AA}$. This good agreement shows that the hard sphere model describes the essence of IMS.

6.2.2 High Field Condition

The discussion so far is based on the low field model where the field acceleration is much smaller than the collision effect. Here the high field model is described in which the field effect is comparable to the collision effect [1, 10]. In this condition, the collision frequency and its effect increase as the field increases, whereas they are independent of the field in the low field condition. The field acceleration is analyzed by the collision energy distribution [1, 10], which is represented as

$$\begin{aligned} \frac{1}{2} m \langle v^2 - v'^2 \rangle &= \frac{1}{2} M \langle V'^2 - V^2 \rangle \\ &= qE v_d \tau = \left(\frac{1}{m} + \frac{1}{M} \right)^{-1} v_d^2. \end{aligned} \quad (6.19)$$

Here the first row of Eq. (6.19) shows that the energy loss of the ion is equal to the energy gain of the gas molecule in the collision since there is no internal freedom like rotations or vibrations. The second row represents the energy gain of the ion by the field acceleration with the relationship between τ and v_d in Eq. (6.10). Equation (6.19) is further represented with the relative velocity of v_r and the velocity of the center of mass of v_{cm} . The ion velocities before and after the collision v and v' are represented as [1, 10, 11]

$$\vec{v} = \vec{v}_{\text{cm}} + \frac{M}{m+M} \vec{v}_r, \quad (6.20)$$

$$\vec{v}' = \vec{v}_{\text{cm}} + \frac{M}{m+M} \vec{v}'_r, \quad (6.21)$$

where we use the conservation of the velocity of the center of mass.

The energy loss of the ion is represented with those velocities as

$$\begin{aligned}
\frac{m}{2} \{ \langle v^2 \rangle - \langle v'^2 \rangle \} &= m \left\{ \left\langle \left(\vec{v}_{\text{cm}} + \frac{M}{m+M} \vec{v}_r \right)^2 \right\rangle - \left\langle \left(\vec{v}_{\text{cm}} + \frac{M}{m+M} \vec{v}'_r \right)^2 \right\rangle \right\} \\
&= 2 \cdot \frac{m}{2} \left\langle \vec{v}_{\text{cm}} \cdot \frac{M}{m+M} \vec{v}_r \right\rangle \\
&= \frac{mM}{(m+M)^2} \langle mv^2 - MV^2 \rangle,
\end{aligned} \tag{6.22}$$

where we used the randomized relative velocity after the collision ($\langle v'_r \rangle = 0$) in Eq. (6.8), the conservation of the absolute value of the relative velocity ($|v_r| = |v'_r|$) in an elastic collision, and the average of the square of the relative velocity ($\langle v_r^2 \rangle = \langle v^2 \rangle + \langle V^2 \rangle$). Finally this equation combined with Eq. (6.19) leads to the following energy relations of

$$\begin{aligned}
\frac{m}{2} \{ \langle v^2 \rangle - \langle v'^2 \rangle \} &= \frac{mM}{(m+M)^2} (\langle mv^2 \rangle - \langle MV^2 \rangle) = \frac{mM}{m+M} v_d^2 \\
\therefore \langle mv^2 \rangle - \langle MV^2 \rangle &= (m+M)v_d^2
\end{aligned} \tag{6.23}$$

and

$$\frac{1}{2} m \langle v^2 \rangle = \frac{1}{2} M \langle V^2 \rangle + \frac{1}{2} m v_d^2 + \frac{1}{2} M v_d^2. \tag{6.24}$$

Equation (6.24) shows that the kinetic energy of the ion is the sum of the thermal energy, the kinetic energy of drift velocity, and the field acceleration energy distributed in the gas molecules [1, 10].

This high field effect results in higher v_r than that in the low field condition shown as

$$\begin{aligned}
\langle v_r^2 \rangle = \langle v^2 \rangle + \langle V^2 \rangle &= \frac{3k_B T}{m} + v_d^2 + \frac{M}{m} v_d^2 + \frac{3k_B T}{M} \\
&= \left(\frac{1}{m} + \frac{1}{M} \right) 3k_B T + \left(1 + \frac{M}{m} \right) v_d^2 \\
&= \left(\frac{1}{m} + \frac{1}{M} \right) (3k_B T + M v_d^2),
\end{aligned} \tag{6.25}$$

where $\langle V^2 \rangle = 3k_B T/M$ is held even in the high field condition. This increase of the relative velocity in Eq. (6.25) is represented by the newly introduced effective temperature of T_{eff} defined as

$$T_{\text{eff}} \equiv T + \frac{M v_d^2}{3k_B} > T. \tag{6.26}$$

The effective temperature T_{eff} is higher than the gas temperature T . The drift velocity v_d is represented with T_{eff} as

$$\begin{aligned}
v_d &= \frac{qE}{N} \left(\frac{1}{m} + \frac{1}{M} \right)^{1/2} \left(\frac{1}{3k_B T + M v_d^2} \right)^{1/2} \frac{1}{\Omega} \\
&= \frac{qE}{N} \left(\frac{1}{m} + \frac{1}{M} \right)^{1/2} \left(\frac{1}{3k_B T_{\text{eff}}} \right)^{1/2} \frac{1}{\Omega},
\end{aligned} \tag{6.27}$$

where the drift velocity is reduced with T_{eff} higher than T .

The high and the low field conditions are classified according to the index of T_{eff} with E/N as an ion acceleration parameter. The threshold for the low field is defined as the condition of $T_{\text{eff}} \approx T$, which is equivalent to

$$\frac{E}{N} \ll \frac{3k_{\text{B}}T\Omega}{q} \left(\frac{m}{m+M} \right)^{1/2}. \quad (6.28)$$

Thus E/N is an important index for IMS represented by a unit of Td ($1 \text{ Td} \equiv 10^{-17} \text{ V cm}^2$). The low field condition is realized when E/N is around 1 Td while the high field of $E/N > 100 \text{ Td}$ is utilized in high field IMS [1, 2, 13, 14, 15].

The high E/N is not just for high T_{eff} . We can identify and manipulate molecular ions by applying high E/N . Those sophisticated measurements are enabled by controlling the internal freedom and the molecular interaction with E/N [1, 2, 15]. Although the kinetics of IMS discussed so far is based on hard sphere model without the internal freedom and the interaction, those freedom and interaction play significant roles in the actual measurement [1, 2, 10]. The collision energy is distributed in the rotations and the vibrations, which affects the momentum transfer in the collision and mobility eventually. The cross section also strongly depends on the temperature and the field because those parameters affect the interaction. With the effects the observed mobility show complicated behaviors on E/N from which we can deduce fine information on the internal freedom and the interaction of the ion [13, 14, 16].

For example, the significant reduction of the mobility of diatomic molecular ions is observed at liquid He temperature, which is originated in enhancement of the momentum transfer from the ion to the gas molecules caused by excitation of a rotational mode [17]. Single atomic ion does not show these behaviors. The degree of the ion–molecule interaction is controlled by the relative velocity or the temperature in IMS [1, 18]. Both these parameters are widely investigated independently by changing T and T_{eff} . The observed phenomena are well understood as the effect of T_{eff} in wide scanning region of E , N , and T , even though T_{eff} and T should be strictly distinguished from each other. The collision processes observed in IMS is well represented as a two-body problem dominated by very local relationship between the accelerated ion and the colliding gas molecule [1].

6.3 Combination of IMS and Mass Spectrometry

6.3.1 Introduction

IMS can reveal the structural information which is hard to be deduced by MS. However the highest resolution of IMS is about 100 usually [12] or 1,000 when special combined methods are applied [19, 20]. This is much lower than that of MS up to 10^5 – 10^6 . In terms of the sensitivity and the throughput, MS with electron multipliers also has much higher ones than those of IMS with a charge collection and an electronic amplifier. To have both advantages, IMS and MS are combined into a hybrid measurement system of IMS/MS recently [2, 9]. This novel hybrid measurement system is applied to wide research areas and is creating new scientific fields. Technically ion loss in the connection between IMS and MS is a serious problem so that effective ion transfer is the key technology. Two types of IMS/MS have been widely used: differential pumping system and ion injection system.

6.3.2 Ion Injection System

The ion injection system has been widely available since late 1980s revealing the cluster structures [21]. The system, at first, is developed to study the cluster reactions and the dissociation induced by the collision with buffer gas in the cell. By increasing up the cell pressure, IMS measurement is realized. The system is quite analogous to a mass spectrometer with CID, so-called MS/CID/MS. The IMS cell is located between the mass spectrometers of the magnetic sector or the quadrupole. Ions selected by the first mass spectrometer are injected into the cell with the pressure of several Torr and their mobility is analyzed by the cell and the second mass spectrometer. The second mass spectrometer is utilized as the arrival time measurement and the product analysis when dissociation or reaction occurs in the cell. The similarity to MS/CID/MS makes it easier to introduce IMS into existing mass spectrometers. Many commercial systems of this type have been developed recently.

The system has several advantages in addition to the similarity to MS/CID/MS: the utilization of the injection process for the structural control of the ion. The ion is heated through the injection with the energy up to several 100 eV against the flow from the IMS cell where the kinetic energy is converted to the internal energy of the ion. After entering inside the cell, the heated ion is immediately cooled down by the gas in the cell. The heat up and the cool down induce the structural conversion [8, 22], which are utilized for exploring new structures or investigating thermal stabilities of nascent structures. Disadvantage arising from this system is low resolution. Since the gas flow from the cell to MS is hazardous for the vacuum of MS and the flow prevents the ions to enter the cell, it is difficult to increase the gas pressure of the cell which usually results in the low resolution. To have much higher resolution with high pressure cell, ambient IMS/MS with differential pumping systems have been developed.

6.3.3 Differential Pumping System

In IMS/MS system, ions are lost during the transport between IMS and MS because of the pressure difference. To improve the efficiency, differential pumping IMS/MS system shown in Fig. 6.5 has been developed. The system itself has long history from 1960s [23]. However this system is widely available recently because of the experimental difficulties to detect diluted ions in the IMS cell. The system in Fig. 6.5 is developed by Prof. Jarrold and co-workers which consists of a laser desorption/ionization system, a high-pressure drift cell with a differential pumping system, and a quadrupole mass filter (QMS) with an ion detection system [24]. Ions like carbon clusters are produced by the laser system and are separated according to their mobility in the drift cell. They are finally mass analyzed by QMS to have two-dimensional IMS/MS profiles. The system can also be equipped with ESI for biomolecules.

In this system, an ion bunch is introduced in the cell with the static electric field and the mobility is observed by measuring the drift time as the time difference between the start of the drift or the ion injection and its end or the ion detection. The ion bunch is created by the ion shutter from a continuous ion source like ESI or the pulsed ion source of the laser system shown in the figure. This system is analogous to the time of flight mass spectrometer. The higher mobility ion has, the shorter drift time is observed. The correlation between the detected ion intensity and the drift time is observed as an IMS spectrum (drift profile).

Two distinct characteristics are realized in this system. One is the long drift cell with ambient buffer gas and high voltage of 10 kV with the low field condition to observe cross section. The other is the small aperture of ϕ 0.1 mm and the large-scale differential pumping system with diffusion

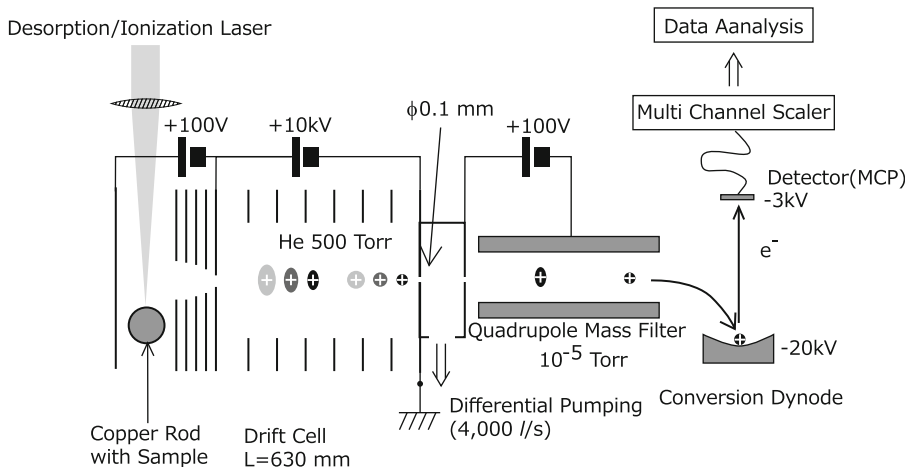


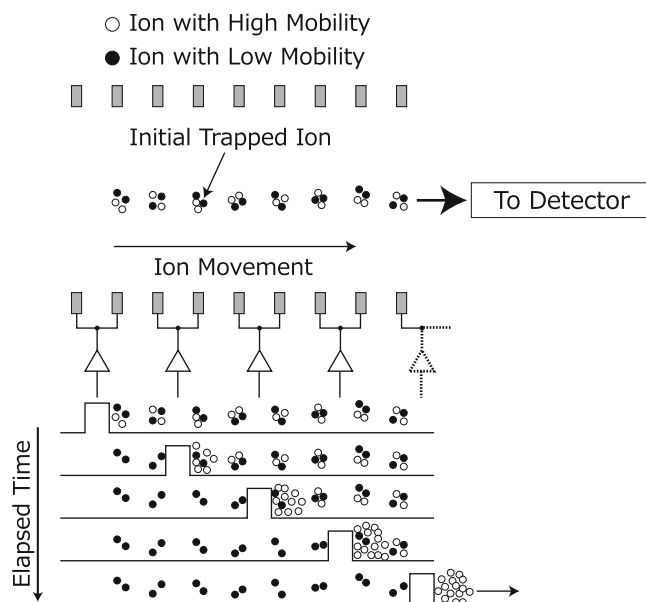
Fig. 6.5 A schematic diagram of a differential pumping high-resolution IMS/MS system. Produced ions are introduced to an IMS drift cell filled with high pressure buffer gas and they are separated according to their mobility. The ions then are passed through the differential pumping part and are introduced into a high vacuum quadrupole mass measurement system with detection and analysis functions

pumps (4,000 l/s). The ions are spatially separated in IMS and then are mass analyzed by QMS in vacuum under 10^{-5} Torr. Those kinds of differential pumping are often used in conventional MS system with an ambient ionization source like ESI. However the conventional MS system handles ions of the order of nA or 10^{10} ions/s which are directly introduced to the acceleration region of MS. The ions in this IMS/MS system, on the other hand, are spatially separated or diluted in the cell and then are transferred into MS. The experimental difficulties for the effective detection of such diluted ions are severer than the conventional MS with the ambient ion source.

The system shows still one of the highest IMS resolutions to observe the cross section. The resolution of this system is determined by the space resolution of the ion bunch [1, 9, 10]. When the ion bunch diffuses from the initial shape of a delta function to a Gaussian function, the resolution is proportional to $\sqrt{V/T}$ where V and T represent the whole voltage across the IMS cell and the gas temperature, respectively. This relation is due to the fact that the space separation increases when the drift effect exceeds the thermal diffusion. Here the thermal diffusion and the mobility compensate each other so that the drift length of the system does not affect the resolution apparently [1, 9, 10]. Many experimental results show that the resolution does not depend on the pressure and gas species indicating the universality of the resolution formula [13, 14, 25].

The higher voltage and the higher pressure with low E/N are crucial for high-resolution cross section measurements. Those measurements are realized with the cost of the detection efficiency, the system size, and complexity. Newly developed high-resolution IMS systems utilize much effective ion focusing systems with radio frequency AC high voltages (RF) [20, 26, 27]. The detection efficiency is also lowered by the low repetition frequency due to the long drift time. This problem has been solved in TOFMS by the so-called orthogonal acceleration keeping the high repetition rate to detect ions from continuous sources utilizing the fact that the ion velocities in TOFMS are much higher than those in the ion source. This method cannot be applied to this type IMS unfortunately since the drift velocity is comparable to the thermal velocity in the ion source.

Fig. 6.6 A schematic diagram of a traveling wave (TW) ion mobility measurement system. Stacked ring electrodes with high-frequency (\sim MHz) AC voltages accumulate ions at the center of each electrode. TW signals extract the ions with higher mobility (*open circles*) from those with lower mobility (*solid circles*) and eject them out of the system selectively for mass analyses



6.3.4 Traveling Wave System

IMS has serious problem in ion detection efficiency as described in Sect. 6.3.3 where the differential pumping system and the RF ion focusing system play significant roles. Here a new approach for handling the problem is shown: traveling wave ion mobility spectrometry (TWIMS) system developed by Waters Co. Ltd. [28]. Figure 6.6 shows the schematic diagram of the system. The system is equipped with a stacked ring ion guide (SRIG) where RF (\sim MHz and \sim kV) is applied to co-axial ring electrodes to trap ions. Each adjacent electrode of SRIG has opposite polarity of RF so that intense and high-frequency electric fields are applied between the nearest electrodes. The frequency is so high that the ions cannot follow the polarity change of RF moving gradually from the inner rim to the center of SRIG according to the field strength, where the highest alternative field is applied at the rim and the lowest at the center. The ions then are trapped at the center of the each electrode since the trap potential is cylindrically symmetric with sinusoidal distortion along the center axis [28]. The potential is similar to that of linear ion trap (LIT) utilized for MS frequently but is different in the distortion along the axis. The trapped ion can be easily transported by applying bias voltages along the axis in SRIG while extra electrodes and complicated procedures are required in LIT to move the ions axially [29].

This distorted potential is crucial for TWIMS where the whole ions are utilized for the mobility measurements in contrast to the differential pumping system in Sect. 6.3.3. In the differential pumping system, the ions must be sliced as a thin bunch to have high resolution with the cost of losing intensity [28]. The procedure of TWIMS is shown in Fig. 6.6, where a waveform called traveling wave (TW) is applied to the SRIG electrodes for ion mobility with the superimposed RF for ion trap. TW is continuous moving waves with the field of tens of V/cm and the speed of hundreds of m/s, which drives the trapped ions out of SRIG to be detected by MS. The ions with higher mobility represented by open circles in the figure are effectively transferred to MS whereas those with smaller ones represented by filled circles are left in SRIG. Thus the mobility is measured by the eject

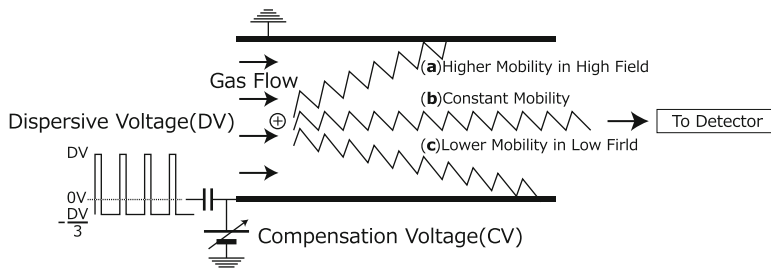


Fig. 6.7 A schematic diagram of a field asymmetric waveform ion mobility spectrometry (FAIMS) system. The system consists of two plates or coaxial cylinders between which ions are transferred to a detector or a mass spectrometer with flowing gas. Asymmetric high-frequency and high-voltage dispersion voltage (DV) and compensation voltage (CV) are applied to the electrodes. DV is asymmetric and its time average is zero. DV consists of a high positive voltage with a short period and a low negative voltage with a long period. When the ion has constant mobility, which is independent of the field, the ion can pass through the system as represented in (b) with $CV = 0$ condition. When the ion mobility increases or decreases with the increase of the field the ion movement is represented as (a) or (c) which cannot be detected. Those (a) and (c) type ions are detected by applying $CV < 0$ or $CV > 0$ for movement compensation, respectively

efficiency in TWIMS. High sensitivity with reasonable resolution is realized by tuning the voltage and the speed of TW. TWIMS is integrated as an ion injection system to observe the mobilities of mass selected ions. Since the injection system has the serious gas flow problem from IMS to MS, the cell pressure is limited to below several Torr and higher resolution is difficult to be achieved eventually [30]. TWIMS is the sensitivity-oriented measurement system.

TWIMS has achieved high sensitivity with SRIG by applying not only the DC bias but also the well-designed RF and TW waveforms. Those waveforms drive the ions with complicated trajectories and the high fields of the waveforms heat up and distort the ions [28, 31]. These effects make it difficult to convert the observed eject efficiencies or the time profile of TWIMS to the actual mobilities. For example, the linear relationship between the mobilities obtained from the TWIMS profile and the mobilities obtained by other measurement systems is fairly good for rigid and spherical molecules, whereas they are not held for asymmetric or soft molecules [32].

6.3.5 Field Asymmetric Waveform Ion Mobility Spectrometry

As described in Sect. 6.2, the low field should be applied to observe the cross section and the ion structure in IMS. In high field IMS, on the other hand, the mobility depends on the field because of the changes in the structures and the interaction leading to weak correlation between the observed mobility and the ion structure. This field dependence of mobility is sophisticatedly utilized in a field asymmetric waveform ion mobility spectrometry (FAIMS) to separate and distinguish ions [2, 15, 33].

Figure 6.7 shows the schematic diagram of FAIMS, where the system consists of two electrodes of plates or coaxial cylinders with gas flow. The observed ions transferred to a detector or a mass spectrometer by the gas flow under the fields of an asymmetric high frequency and high voltage waveform for dispersion (DV) and a static low voltage between the electrodes for compensation (CV). DV is asymmetric and its time average is zero. DV consists of a high positive voltage with a short period and a low negative voltage with a long period. The ion movement is classified in three types of (a)–(c). When the ion has a constant mobility, the ion can pass through the system as

represented in (b) with the condition of $CV = 0$. When the ion mobility increases or decreases as the field increases the ion movement are represented as (a) or (c). They collide with the electrodes and cannot be detected. Those (a) and (c) type ions are detected by applying $CV < 0$ or $CV > 0$ to compensate their movement to pass through the system like (b) condition. We can identify or separate ions of interest by tuning CV with steady DV and whole ion profiles are obtained as an intensity- CV correlation. Practically DV of several kV with frequency from several hundreds of kHz to MHz and CV of tens of V are applied to the electrodes with the gap from tens of μm to mm [15, 34].

FAIMS provides us the information not on the cross section but on the mobility dependence on the field which is difficult to interpret and is independent of most of the properties such as mass and size. This property is quite opposite to that of the cross section obtained by the low field IMS. The ion with larger cross section mostly have larger mass and size. The cross section is dependent on the mass and size, in other word, is not “orthogonal” to them. Here orthogonality means that two values are perpendicular, nonoverlapping, or uncorrelated. On the other hand, ions with similar mass and size, for example ions of proteins and metal particles, can show totally different “the field dependence of the mobility” because of their internal structures and bond strength. The field dependence of the mobility is quite independent of and orthogonal to mass and other properties.

Those independence and orthogonality, conversely, are employed to separate or to distinguish ions with similar mass and size, which is usually very difficult for MS. For this property FAIMS is mainly utilized as a filter for MS to select interest ions from background of solvents in ESI and of matrices in MALDI. There are many those kinds of pre-stage filter for MS. However FAIMS shows much higher performance especially for ions with similar mass and chemical properties. Those ions are difficult to be identified only by MS even with other chemical filtering processes such as liquid chromatography. FAIMS can select those ions with the difference in the field dependence of mobility. On the contrary, the low field IMS distinguish with the cross section which has close relationship with the size and the mass, which suggests that ions with similar size and mass are selected in the almost same condition resulting in its low performance as a filter.

With the improvement of the resolution of FAIMS, the method now begins to be utilized for more advanced purposes such as manipulation of molecules and investigation of ion–molecule interaction [2, 9, 15]. For example, amino acid molecules with hydrogen/deuterium, $^{12}\text{C}/^{13}\text{C}$, and $^{14}\text{N}/^{15}\text{N}$ exchanges show different FAIMS profiles [35]. Those isotopomer ions with the same mass constructed by the combination of these exchanges also show the different properties in FAIMS, which have not been observed by the low field IMS. It is difficult to explain the origin of the effect, but their differences in the vibrational and the rotational states and those in the long range interaction may cause the results [35].

6.4 Applications

IMS has long history especially in aerosol science and security area as described in Sect. 6.1 and has wide application fields [2]. Here structural studies on nanomaterials and detection of molecular interaction between chiral species are shown, since the main topic of this book is MS which has been a major tool for nanomaterials and biomolecules. Especially in biomolecules the interaction like chiral selectivity is one of the key issues [36]. Both of them show structural varieties and their properties are strongly dependent on the structures to which IMS clearly provides important information. Many research articles on bio-related molecules are published [36]; so chiral molecular detection is described here together with nanomaterials.

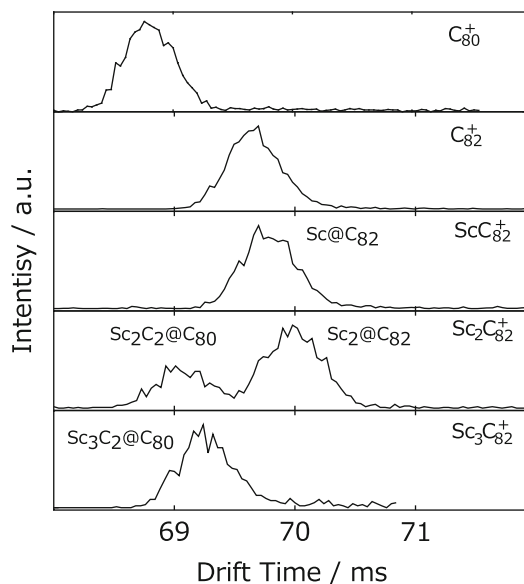


Fig. 6.8 High-resolution ion mobility profiles of C_{80}^+ , C_{82}^+ and $Sc_nC_{82}^+$ ($n = 1-3$) produced from laser desorption/ionization of solvent extractable fullerenes. $Sc_2C_{82}^+$ shows two distinct peaks (details see text)

6.4.1 Metallofullerene

Fullerene is one of the most significant nanomaterials as the first atomically identified and purified ones. Fullerene consists of around 100 carbon atoms with spherical shell structures and shows various distinct and useful properties which are determined by the structures. One of them is hollow inside space which can hold other molecules and materials resulting in modified structures and properties [37]. By changing the number of atoms inside and changing outside fullerene structures, those properties are controlled so that the structural studies on whole species are crucial. For these materials conventional structural analyses have been performed by NMR and X-ray diffraction together with isolation. Fullerenes like other nanomaterials are produced as mixtures through vapor condensation processes. Those mixtures are difficult to purify, which require several months to prepare mg order isolated samples with HPLC separation. The HPLC separation requires not only huge efforts but also dissolution in organic solvents so that some of the fullerenes cannot be studied by their low solubility. As a result, atomically resolved nanomaterials known up to now are not so rich: a part of fullerenes, noble metal clusters, and carbon nanotubes. To expand structural studies on other nanomaterials by improving efficiency and by applying comprehensive structural analyses, IMS/MS is one of the best methods in terms of direct treatment and high throughput on mixture samples without pre-purification.

Figure 6.8 shows drift time profiles for positive ions of empty fullerenes and metallofullerenes obtained from solvent extractable C_{80} , C_{82} , and Sc_nC_{82} ($n = 1-3$) using the IMS/MS apparatus shown in Fig. 6.5. C_{80}^+ and C_{82}^+ have a single peak and the drift time of C_{80}^+ is clearly shorter than that of C_{82}^+ . Simple analyses of the drift time in Eq. (6.18) show that their spherical structures exactly correspond to those obtained by X-ray [37, 38] and computational calculation [39]. Those results show that fullerene structures are not disturbed by the laser desorption/ionization, and the structural resolution of the apparatus is good enough to identify the fullerene size but is not sufficient to resolve structural isomers [39]. The ion of $Sc@C_{82}^+$ also shows a single peak which exactly corresponds

to that of C_{82}^+ and well-annealed C_{82}^+ clusters [22, 40]. These results are consistent with the endohedral structures determined by X-ray diffraction [38]. On the other hand, the di-metallofullerene $Sc_2C_{82}^+$ shows two distinct peaks. The main peak with larger drift time and larger cross section corresponds to the peaks of C_{82}^+ and $Sc@C_{82}^+$. The other peak has a substantially smaller drift time which is very similar to that of C_{80}^+ revealing that some of $Sc_2C_{82}^+$ has C_{80} cage. The tri-metallofullerene $Sc_3@C_{82}^+$ shows only one peak close to C_{80}^+ . The high-resolution ion mobility measurements enable us to detect these two structures for the first time.

One of the significant merits of IMS observation is investigation on whole species. In terms of Sc mono-metallofullerenes in the size region less than C_{100} , their cross section is almost same as those of the corresponding empty fullerenes, which indicates that Sc metallofullerenes have endohedral structures of $Sc@C_n$. In contrast, most of $Sc_2C_n^+$ ($n \leq 86$) have two cage sizes: one corresponds to that of C_n^+ and the other corresponds to that of C_{n-2}^+ . These results strongly suggest that $Sc_2C_n^+$ ions have a “carbide” structure like $(Sc_2C_2)@C_{n-2}^+$ as well as $Sc_2@C_n^+$ of the simple endohedral structure. Larger Sc di-metallofullerenes $Sc_2@C_n^+$ ($n \geq 88$) and Sc tri-metallofullerenes $Sc_3@C_n^+$ only have the smaller cage. These Sc tri-metallofullerenes may also possess carbide $(Sc_3C_2)@C_{n-2}^+$ structures. The drift time of the metallofullerenes is slightly larger than that of corresponding empty fullerenes (cf. Fig. 6.8). These differences are probably associated with the electronic properties of the metallofullerenes. Electrons are transferred from the metal atoms to the cage, which resulted in, for example, $Sc^{2+}@C_{82}^{2-}$ [38]. Since the ion mobility is mainly dominated by close interaction between the fullerene cage and He [41], $(Sc^{2+}@C_{82}^{2-})^+$ and C_{82}^+ are expected to have slightly different mobilities [42].

Since this IMS/MS measurement requires the laser desorption/ionization, the carbide structures may be generated through the processes. The laser power dependence of $Sc_2@C_{82}^+$ shows that the carbide structures are preferred in the large power condition suggesting the laser-induced reactions from the normal to the carbide. Although these new carbide structures are observed in gas phase upon desorption/ionization, we have produced and identified $(Sc_2C_2)@C_{84}$ in macroscopic quantities [43]. The other group recently has identified this carbide structures of $(Sc_3C_2)@C_{80}$ for Sc tri-metallofullerenes [44]. The results presented here show that the carbide encapsulated structure are universal in the wide size range. The results also clarified that novel structures can be identified by series of IMS/MS measurements utilizing its high sensitivity and high throughput, which is available for mixtures and wide range of materials.

6.4.2 Chiral Detection

The chiral detection has been a key issue for MS but is difficult to be realized [45]. Usually chiral molecules are identified by optical activity or chiral columns. Those methods are the so-called bulk methods requiring large amount of isolated samples. High sensitive method like MS has been waited for long term. Even though the interaction difference between chiral molecules can affect the dissociation pattern [45], the difference is usually too small to be detected in dissociation processes. However this small difference is apparently observed by IMS with a sum effect through many collisions as described in Sect. 6.1.2 [46, 47, 48].

Simple chiral molecules are investigated by a differential pumping type IMS/MS where chiral (*S*)-(+)-2-butanol and (*R*)-(-)-2-butanol are doped in the buffer gas of the IMS cell with the order of ppm [46]. When the ion and the dopant have the same chirality, a longer drift time or stronger interaction is observed indicating that the chiral interaction is intense enough to be detected with the cross section difference to the order of 10^2 – 10^3 between the chiral pairs. The origin of this chiral

dependence and the generality should be investigated, but the results show the potential and the sensitivity of IMS as a tool for molecular investigation. FAIMS also reveals this chiral dependence [48].

Other chiral dependence is found in spontaneous crystallization of proline clusters ($[\text{Pro}_x + n\text{H}]^{n+}$, $x = 40\text{--}100$, $n = 4, 5$) [47]. Pure D-proline or L-proline forms rod-like clusters, whereas racemic mixtures of proline form globular clusters. The rod-like clusters from pure D-proline and L-proline have exactly the same mobility suggesting symmetrical structures of those clusters. If we consider those clusters a type of bulk crystals, the chiral dependence of the cluster structures may be attributed to spontaneous crystallization and spontaneous optical resolution.

Those two researches show that IMS has very high sensitivity to detect fine molecular interaction which should come from many collisions and summed effects in the cell described in Sect. 6.1.2

6.5 Summary

IMS has similarity with MS as a method detecting charged particles. They are now combined as the hybrid measurement system of IMS/MS, which is now a key tool to investigate bio and medical sciences, nano and material technologies. The structural observation and utilization of low energy processes provide a new aspect to MS. The wide range applications and new sciences are realized by this method. However understanding and analysis of the observed information are not simple since the measurement is performed through the many collisions between ions and gas molecules where the interaction between them are statistically averaged. To understand the obtained results and elucidate more information, the study and analysis on the basic processes in IMS are still necessary. Computational investigation would play significant roles for further analyses. Technically relatively low resolution and low sensitivity compared to MS are ongoing problems. RF devices, vacuum technology, and fluid dynamics have been utilized to overcome those difficulties. Even with these problems and difficulties, IMS/MS has huge potential in wide range fields. This method provides not only structural information but also detection of weak molecular interaction by utilization of wide range of E/N . They have been developed to realize sophisticated chirality detection and manipulation of molecules. The measurement system has been rapidly developed by various groups to be commercialized. I hope that this measurement be more and more common globally and be applied to much wider area, which would lead us to the next stage of science and technology.

References

1. Mason EA, McDaniel EW (1988) Transport properties of ions in gases. Wiley, New York
2. Eiceman GA, Karpas Z (2005) Ion mobility spectroscopy. CRC, Boca Raton
3. Kroto HW, Heath JR, O'Brien SC, Curl RF, Smalley RE (1985) Nature 318:162
4. Krätschmer W, Lamb LD, Fostiropoulos K, Huffman DR (1990) Nature 347:354–358
5. Taylor R, Hare JP, Abdul-Sada AK, Kroto HW (1990) J Chem Soc Chem Commun 20:1423–1425
6. Hawins JM, Meyer A, Lewis TA, Loren S, Hollander FJ (1991) Science 252:312–313
7. von Helden G, Hsu MT, Kemper PR, Bowers MT (1991) J Chem Phys 95:3835–3837
8. von Helden G, Hsu MT, Gotts N, Bowers MT (1993) J Phys Chem 97:8182–8192
9. Sugai T (2010) J Mass Spectrom Soc Jpn 58:47–73
10. Revercomb HE, Mason EA (1975) Anal Chem 47:970
11. Berry RS, Rice SA, Ross J (2000) Physical chemistry. Oxford University Press, New York
12. Sugai T, Inakuma M, Hudgins R, Dugourd P, Fye JL, Jarrold MF, Shinohara H (2001) J Am Chem Soc 123:6427–6428
13. Tabrizchi M, Rouhollahnejad F (2006) Talanta 69:87–90
14. Nazarov EG, Coy SL, Krylov EV, Miller RA, Eiceman GA (2006) Anal Chem 78:7697–7706

15. Shvartsburg AA (2009) *Differential ion mobility spectrometry: nonlinear ion transport and fundamentals of FAIMS*. CRC, New York
16. Tanuma H, Sakamoto M, Fujimatsu H, Kobayashi N (2000) *Rev Sci Instrum* 71:2019–2024
17. Hidaka H, Jinno S, Tanuma H, Kobayashi N (2003) *J Phys B At Mol Opt Phys* 36:1515–1524
18. Levine RD, Bernstein RB (1987) *Molecular reaction dynamics and chemical reactivity*. Oxford University Press, New York
19. Merenbloom SI, Bohrer BC, Koeniger SL, Clemmer DE (2007) *Anal Chem* 79:515–522
20. Merenbloom SI, Glaskin RS, Henson ZB, Clemmer DE (2009) *Anal Chem* 81:1482–1487
21. Kuk Y, Jarrold MF, Silverman PJ, Bower JE, Brown WL (1989) *Phys Rev B* 39:11168
22. Shelimov KB, Jarrold MF (1996) *J Am Chem Soc* 118:1139–1147
23. McDaniel EW, Martin DW, Barnes WS (1962) *Rev Sci Instrum* 33:2–7
24. Dugourd P, Hudgins RR, Clemmer DE, Jarrold MF (1997) *Rev Sci Instrum* 68:1122–1129
25. Ruotolo BT, McLean JA, Gillig KJ, Russell DH (2004) *J Mass Spectrom* 39:361–367
26. Tang K, Shvartsburg AA, Lee H-N, Prior DC, Michael FL, Buschbach A, Tolmachev AV, Anderson GA, Smith RD (2005) *Anal Chem* 77:3330–3339
27. Merenbloom SI, Koeniger SL, Valentine SJ, Plasencia MD, Clemmer DE (2006) *Anal Chem* 78:2802–2809
28. Giles K, Pringle SD, Worthington KR, Little D, Wildgoose JL, Bateman RH (2004) *Rapid Commun Mass Spectrom* 18:2401–2414
29. Takada Y, Nagano H, Suzuki Y, Sugiyama M, Nakajima E, Hashimoto Y, Sakairi M (2011) *Rapid Commun Mass Spectrom* 2011:2448–2452
30. Williams JP, Scrivens JH (2008) *Rapid Commun Mass Spectrom* 22:187–196
31. Shvartsburg AA, Smith RD (2008) *Anal Chem* 80:9689–9699
32. Bush MF, Hall Z, Giles K, Hoyes J, Robinson CV, Ruotolo BT (2010) *Anal Chem* 82:9557–9565
33. Buryakov IA, Krylov EV, Nazarov EG, Rasulev UK (1993) *Z Phys* 128:143–148
34. Shvartsburg AA, Smith RD, Wilks A, Koehl A, Ruiz-Alonso D, Boyle B (2009) *Anal Chem* 81:6489–6495
35. Shvartsburg AA, Clemmer DE, Smith RD (2010) *Anal Chem* 82:8047–8051
36. Wyttenbach T, Bowers MT (2007) *Annu Rev Phys Chem* 58:511–533
37. Shinohara H (2000) *Rep Prog Phys* 63:843–892
38. Nishibori E, Takata M, Sakata M, Inakuma M, Shinohara H (1998) *Chem Phys Lett* 298:79–84
39. Kobayashi K, Nagase S (1998) *Chem Phys Lett* 282:325–329
40. Shvartsburg AA, Hudgins RR, Dugourd P, Gutierrez R, Frauenheim T, Jarrold MF (2000) *Phys Rev Lett* 84:2421–2424
41. Clemmer DE, Jarrold MF (1997) *Int J Mass Spectrom* 32:577–592
42. Lermé J, Dugourd P, Hudgins RR, Jarrold MF (1999) *Chem Phys Lett* 304:19–22
43. Wang CR, Kai T, Tomiyama T, Yoshida T, Kobayashi Y, Nishibori E, Takata M, Sakata M, Shinohara H (2001) *Angew Chem Int Ed* 40:397–399
44. Iiduka Y, Wakahara T, Nakahodo T, Tsuchiya T, Sakuraba A, Maeda Y, Akasaka T, Yoza K, Horn E, Kato T, Liu MTH, Mizorogi N, Kobayashi K, Nagase S (2005) *J Am Chem Soc* 127:12500–12501
45. Tao WA, Zhang D, Wang F, Thomas PD, Cooks RG (1999) *Anal Chem* 71:4427–4429
46. Dwivedi P, Wu C, Matz LM, Clowers BH, Siems WF, Herbert J, Hill H (2006) *Anal Chem* 78:8200–8206
47. Myung S, Fioroni M, Julian RR, Koeniger SL, Baik M-H, Clemmer DE (2006) *J Am Chem Soc* 128:10833–10839
48. Mie A, Jörntén-Karlsson M, Axelsson B-O, Ray A, Reimann CT (2007) *Anal Chem* 79:2850–2858

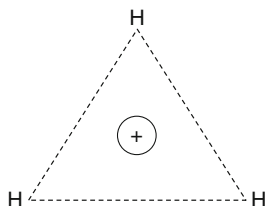
Kenzo Hiraoka

7.1 Introduction

H_3^+ was the first ion observed by the ion/molecule reaction (IMR),



In a cathode ray tube filled with hydrogen gas, J. J. Thomson (1912) [1] found the H_3^+ ion, which is the protonated hydrogen molecule, $\text{H}_2 + \text{H}^+ = \text{H}_3^+$. The determination of the structure of H_3^+ was beyond the scope of the science at that time. This was symbolized by the comment made by Eyring, “The scandal of modern chemistry” [2]. Later theoretical and experimental studies revealed that H_3^+ has a regular triangular geometry with a three-center–two-electron bond.

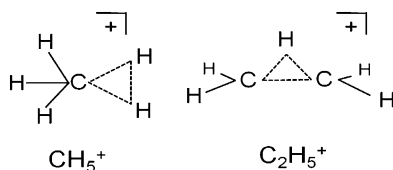


It took almost 40 years after the discovery of H_3^+ to observe the protonated methane CH_5^+ and the protonated ethylene C_2H_5^+ formed by IMRs taking place in methane (early 1950) [3, 4]. This finding triggered the explosive research work on gas-phase IMRs:

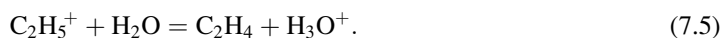


K. Hiraoka (✉)
Clean Energy Research Center, University of Yamanashi, Kofu, Japan
e-mail: hiraoka@yamanashi.ac.jp

When methane is ionized by energetic electrons, CH_4^+ and CH_3^+ are formed with approximately equal abundance. These ions react with methane to form CH_5^+ and C_2H_5^+ , respectively (reactions (7.2) and (7.3)). The ions CH_5^+ and C_2H_5^+ have three-center–two-electron bonds in their geometry.



Field and Munson found that CH_5^+ and C_2H_5^+ were annihilated quickly because of the reactive loss when methane is contaminated with some impurities such as water vapor, i.e., with the occurrence of the proton transfer reactions [5]:



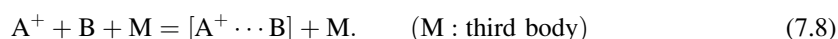
They soon noticed that IMRs like these can be used to analyze impurities contained in gas samples. In reactions (7.4) and (7.5), CH_5^+ or C_2H_5^+ is the “reactant ion” and H_3O^+ is the “product ion.”

IMRs were found to produce much fewer fragment ions than electron ionization (EI). Thus, IMR has emerged as a very versatile method for the determination of molecular masses of analyte molecules. Because the analytes are ionized through chemical reactions, this ionization method is called “chemical ionization” (CI) [6]. Chemical ionization that occurs at atmospheric pressure is called “atmospheric-pressure chemical ionization (APCI).”

Because CI is based on the chemical reactions, it is influenced by many factors (see later sections) [7]. Thus, by adjusting various experimental parameters, the optimum experimental conditions for detection in highly sensitive analyses can be achieved. In other words, for CI analysis, fundamental knowledge on IMRs is mandatory, i.e., the types of chemical reactions, reaction rates and their temperature and pressure dependence, basicity (proton affinity) and acidity of the analyte, hydride affinity, ionization energy, electron affinity, bond energy of cluster ion, thermodynamics, reaction rate theory, etc. [7, 8] have to be defined. In the 1980s, an extensive collection of the basic data on CI that are essential for the application of CI to analytical chemistry has been compiled. The fundamentals of IMRs are described in the following sections.

7.2 Rate of Ion/Molecule Reactions

Three types of IMRs are generally observed: unimolecular (first order), bimolecular (second order), and trimolecular (third order), reactions (7.6), (7.7), and (7.8), respectively.



For example, the unimolecular fragmentation of an electronically excited ion is first order; the proton transfer and charge transfer reactions (CTRs) are second order, and the ion–molecule clustering reaction is third order.

The reaction rates for reactions (7.6), (7.7), and (7.8) are represented as follows:

$$-d[A^+]/dt = k[A^+] \quad (\text{unimolecular}) \quad (7.9)$$

$$-d[A^+]/dt = k[A^+][B] \quad (\text{bimolecular}) \quad (7.10)$$

$$-d[A^+]/dt = k[A^+][B][M]. \quad (\text{trimolecular}) \quad (7.11)$$

In CI, the concentrations of analyte [B] in reactions (7.10) and (7.11) determine the reaction rates. In addition, the number of collisions of reactant and product ions with surrounding gas molecules increases with increasing gas pressure of the ion source. The high collision frequency suppresses the diffusion of reactant ions toward the walls of the ion source. Because ions are annihilated (neutralized) when they collide with the wall, the increase in pressure of the ion source gas results in the longer lifetimes of reactant ions in the ion source, resulting in higher probability for the reaction of reactant ions with analyte molecules. IMR does not take place in an electron ionization ion source because of the low pressure ($\sim 10^{-3}$ Pa), as it starts being observed at pressures higher than $\sim 10^{-1}$ Pa. As a rule of thumb, the higher the collision frequency (at higher pressure), the higher the detection sensitivity for CI. This explains why APCI is generally more sensitive than CI.

As shown in reactions (7.9)–(7.11), the rate constants (k) determine the rates of IMRs. In the following section, the rate constants for various IMRs will be described in detail. Because of the electric field induced by the charged particle, the reaction dynamics of IMR is basically different from that of neutral gas reactions because ions interact with neutral molecules much more vigorously than neutral molecules with each other.

7.2.1 Capture Limit Rate Constants

In neutral gas reactions, because reacting molecules are attracted only by the weak van der Waals short-range forces, for a reaction to take place close encounters of reactants are necessary and these can be visualized as billiard-like collisions. In contrast, an ion interacts much more strongly with molecules by the ion-induced dipole and ion–dipole interactions when the molecules have permanent dipoles. The interaction between an ion and a molecule may be compared to the orbit of a comet approaching the earth being trapped by the gravitational force.

7.2.1.1 Collisions of Ions with Nonpolar Molecules

A molecule that has no dipole moment is called as a nonpolar molecule. Molecules are composed of nuclei and a surrounding electron cloud. In nonpolar molecules, the centers of the nuclei and the electron cloud coincide, and thus the molecules do not have the dipole moments. H_2 , N_2 , O_2 , CH_4 , CO_2 , SF_6 , C_{60} , etc. are examples of such molecules. When a nonpolar molecule approaches a positive ion, the electron cloud of the molecule will be attracted to the ion but the nuclei will be repelled, causing the centers of the electron cloud and the nuclei to stop corresponding with each other, i.e., a dipole moment is induced. That is, the molecule has a temporal “induced dipole” during the interaction with the ion. Thus even if the molecule is nonpolar, it will experience an attractive force toward the ion by the ion-induced dipole interaction. The measure of “softness” of an electron

Table 7.1 Permanent dipole and polarizability of atoms and molecules

Atom, molecule	Permanent dipole, μ (Debye)	Polarizability, α (\AA^3)
Rare gas atoms		
He	0	0.21
Ne	0	0.41
Ar	0	1.64
Kr	0	2.48
Xe	0	4.02
Diatomic molecule		
H ₂	0	0.81
D ₂	0	0.8
O ₂	0	1.57
N ₂	0	1.74
CO	0.1	1.94
NO	0.16	1.7
HCl	1.03	2.58
HBr	0.79	3.49
Triatomic molecule		
CO ₂	0	2.59
CS ₂	0	8.08
H ₂ O	1.84	1.45
N ₂ O	0.17	2.92
H ₂ S	1.02	3.61
SO ₂	1.62	3.78
Polyatomic molecule		
CH ₄	0	2.56
CCl ₄	0	10.24
C ₂ H ₄	0	4.1
C ₂ H ₆	0	4.39
n-C ₄ H ₁₀	0	8
<i>i</i> -C ₄ H ₁₀	0	8
C ₆ H ₆	0	9.99
NH ₃	1.47	2.16
H ₂ CO	2.31	2.81
CH ₃ OH	1.7	3.25
(CH ₃) ₂ CO	2.85	6.11

cloud is quantitatively given by the “polarizability” (α). The α values of several atoms and molecules are summarized in Table 7.1, where α is given in volume units, i.e., \AA^3 [9–12]. For example, the values of α for rare gas atoms (in \AA^3) increase in the order He (0.21) \rightarrow Ne (0.41) \rightarrow Ar (1.64) \rightarrow Kr (2.48) \rightarrow Xe (4.02). The two electrons occupying the 1-s orbital of He are tightly bound to the nucleus, but the outer shell electrons of Xe are much more loosely bound, resulting in $\alpha(\text{He}) \ll \alpha(\text{Xe})$.

According to Langevin theory [13, 14], the “capture collision rate constant” for the bimolecular reaction, $A^+ + B$, for A^+ with mass m (u) and B with mass M (u) is given by (7.12), where μ denotes the reduced mass, $[mM/(m + M)]$. In this theory the ion is treated as a “point charge.” The capture collision means that the ion and the reactant molecule collide with each other regardless of whether IMR occurs:

$$K_L = 2.34 \times 10^{-9} (\alpha/\mu)^{1/2} \text{ cm}^3 \text{ s}^{-1}. \quad (7.12)$$

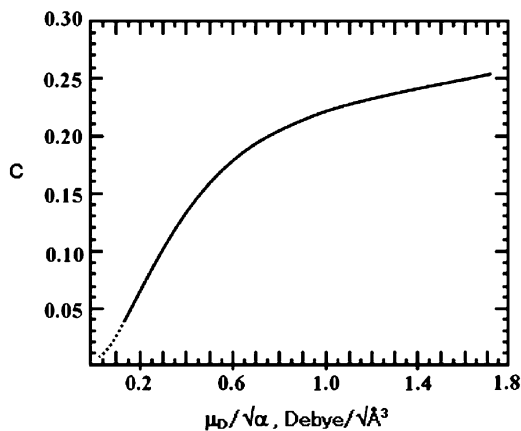


Fig. 7.1 The “locking” constant c as a function of $\mu_D \times \alpha^{-1/2}$. (Reproduced with permission from [15])

For example, in reaction (7.2), using the values of $\alpha(\text{CH}_4) = 2.56 \text{ \AA}^3$ and $\mu = 16 \times 16 / (16 + 16) = 8 \text{ u}$, k_L was calculated to be $1.32 \times 10^{-9} \text{ cm}^3 \text{ s}^{-1}$, and this is in very good agreement with the experimental value of $1.1 \times 10^{-9} \text{ cm}^3 \text{ s}^{-1}$. It is well known that the Langevin theory (k_L) predicts the rate constants correctly for many exothermic proton transfer reactions. This implicitly suggests that the ion interacts with the neutral molecule with the long-range distance and thus the ion can be regarded as a point charge.

7.2.1.2 Collisions of Ions with Polar Molecules

For a polar molecule, one side is positively charged and the other is negatively charged, i.e., the molecule has a permanent dipole. For example, H_2O is a dipolar molecule because there is an excess negative charge on the oxygen atom and a counterpart excess positive charge on the two hydrogen sites. The capture collision rates for the reactions of ions with dipolar molecules are predicted by the average dipole orientation (ADO) theory [15, 16]:

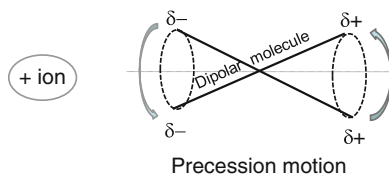
$$k_{\text{ADO}} = (2\pi e / \mu^{1/2}) [\alpha^{1/2} + c\mu_D (2/\pi kT)^{1/2}], \quad (7.13)$$

where e is the electric charge of the ion, μ the reduced mass, α the polarizability of the molecule, μ_D the permanent dipole moment of the molecule, k the Boltzmann constant, and T the temperature (K). The first term originates from the interaction of an ion with induced dipole and the second term from the interaction of an ion with a dipole. The term c is the “locking constant” determined by the value of $\mu_D/\alpha^{1/2}$ as shown in Fig. 7.1 [15, 16].

For α in Å^3 , μ in u, and μ_D in Debye ($3.3 \times 10^{-30} \text{ C m}$), (7.13) is reduced to (7.14):

$$k_{\text{ADO}} = 2.34 \times 10^{-9} (\alpha/\mu)^{1/2} + 3.016 \times 10^{-9} \times c \times \mu_D (2,780/T\mu)^{1/2} \text{ cm}^3 \text{ s}^{-1}. \quad (7.14)$$

In the ion–dipolar molecule interaction, the molecule will rotate with the motion of precession in order to preserve the angular momentum.



The ADO theory takes into account the average dipole moment of precession as a function of temperature (T). As an example, k_{ADO} will be calculated for reaction (7.15):



The k_{ADO} value at 300 K was calculated to be $2.2 \times 10^{-9} \text{ cm}^3 \text{ s}^{-1}$ by using $\alpha = 2.16 \text{ \AA}^3$ and $\mu_{\text{D}} = 1.47$ Debye for NH_3 (Table 7.1), a μ value of $17 \times 17 / (17 + 17) = 8.5$ u, and $c = 0.22$ in Fig. 7.1 with the value of $\mu_{\text{D}}/\alpha^{1/2} = 1.47 / (2.16)^{1/2} = 1$. This theoretical value is in excellent agreement with the experimental value of $2.3 \times 10^{-9} \text{ cm}^3 \text{ s}^{-1}$. The fact that there are many ion/molecule reactions with capture collision rates means that there is no apparent activation barrier for the exothermic IMR. That is, the dependence of the IMR rates on temperature is small or negligible. It is generally accepted that k_{L} and k_{ADO} predict the rate constants of exothermic proton transfer reactions within the experimental error.

Not only the polarizability and the permanent dipole moment but also the quadrupole moment of the molecule may have some small effect on the rate constant of IMR [17]. A typical molecule that has a large quadrupole moment Θ (but no permanent dipole moment) is carbon dioxide: $\text{O}^{\delta-}-\text{C}^{\delta+}-\text{O}^{\delta-}$, e.g., $\Theta(\text{CO}_2) = -4.3 \text{ esu cm}^2$ vs. $\Theta(\text{N}_2) = -1.52 \text{ esu cm}^2$ (where esu denotes electrostatic unit).

7.2.2 Types of IMRs and Their Rate Constants

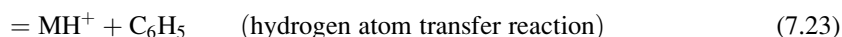
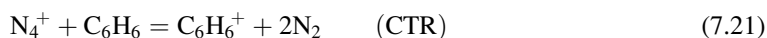
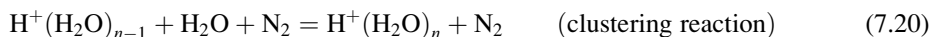
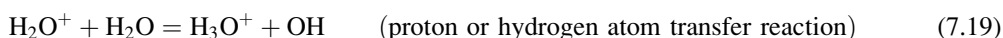
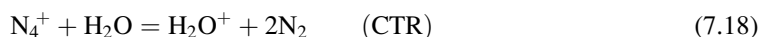
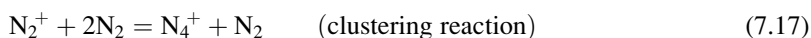
7.2.2.1 CTRs

In a CTR of type $\text{A}^+ + \text{B} \rightarrow \text{A} + \text{B}^+$, an electron is transferred from B to A^+ . That is, charge means “electron.” As the mass of one electron is much smaller than that of the nucleus ($\sim 1/1,800$ of the hydrogen atom), the momentum transfer in this type of reaction is negligible. Thus, the charge (electron) transfer reaction proceeds via the “resonant energy transfer process.” In general, the dependence of the rate constants of CTRs on temperature is small or negligible. When the reactant atoms or molecules have rather simple structures, the rate constants may become much smaller than the capture rate constants based on the Franck–Condon factors for the ionization process. However, as the size of the molecules increases (i.e., more density of rovibronic (rotational, vibrational, and electronic) states becomes available for the formed molecular ion), this restriction becomes less strict and the rate constants increase to the order of the capture collision rates or even larger [18].

When the reactant ion is a rare gas ion, $\text{Rg}^+ + \text{M} = \text{Rg} + \text{M}^+$, all of the recombination energy (RE) of Rg^+ will be imparted to the product ion, M^+ [19]. Here, RE is defined as the energy released in the reaction $\text{Rg}^+ + e^- = \text{Rg}$; that is, RE can be approximated to be the ionization energy (IE) of Rg. The rate constant of the reaction, $\text{He}^+ + \text{Ar} = \text{He} + \text{Ar}^+$, is very small, about $\sim 10^{-14} \text{ cm}^3 \text{ s}^{-1}$, because the “dissipation channel” of the excess energy imparted to Ar^+ by the amount of RE (He) – IE (Ar) = $(24.5 - 15.6) \text{ eV} = 8.9 \text{ eV}$ is virtually absent for Ar^+ . However, the rate constant for the reaction, $\text{He}^+ + \text{CH}_4 \rightarrow \text{He} + \text{CH}_4^+$, has the capture collision rate of $1.7 \times 10^{-9} \text{ cm}^3 \text{ s}^{-1}$. This is because the energy imparted to the product CH_4^+ (IE (He) – IE (CH_4)) = $24.5 - 12.5 = 12 \text{ eV}$

can be dissipated efficiently in the fragmentation of CH_4^+ to form CH_3^+ , CH_2^+ , and CH^+ . As the discrete energy is imparted to the product ion, the CTR is suitable for the study of the kinetics of unimolecular decomposition for the ion with a known amount of the internal energy.

Horning et al. first applied the CTRs to APCI using N_2 as a reagent [20, 21]:



When N_2 , He, or Ar are used as a carrier gas in gas chromatography–chemical ionization mass spectrometry (GC–CIMS), fragmentation prevails due to the high REs for the ions of N_2^+ , He^+ , or Ar^+ , and the mass spectra become similar to those obtained by EI. Contrary to CI at pressures of \sim a few torr, fragmentation is largely suppressed in the APCI method [22], in which the excess internal (electronic, vibrational, and rotational) energies imparted to the product ions have more chance to be affected by “collisional deactivation,” i.e., by collisions with the buffer gas molecules. The collision frequency of an ion at 1 atm is $\sim 10^{10} \text{ s}^{-1}$. Thus, if the lifetime of the excited ion leading to the fragmentation is longer than 10^{-10} s , this ion may have a chance to be stabilized by the collision, i.e., occurrence of the energy transfer: $\text{A}^{+*} + \text{M} (\text{buffer gas}) = \text{A}^+ + \text{M}^*$, where * denotes the excess energy. This results in the less fragmentation in APCI than in CI.

As NO^+ has a low recombination energy, $\text{RE}(\text{NO}^+) \leq 9.2 \text{ eV}$, NO^+ can be used as a reactant ion for the soft and selective ionization because only the reactants with IE below 9.2 eV are selectively ionized [23–28]. Trimethylsilyl (TMS) ether could be detected as the molecular ion M^{+*} using NO^+ as a reactant ion [25].

7.2.2.2 Proton Transfer Reactions

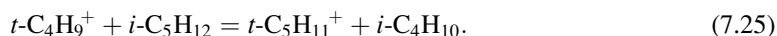
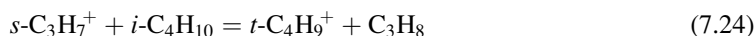
In general, exothermic proton transfer reactions (PTRs) have capture collision rates. As (7.12) does not contain a temperature term, the rate constants for ion–nonpolar molecule reactions are temperature independent. Equation (7.14) has the term of T^{-1} and thus rates of ion–permanent dipolar molecule reactions will decrease gradually with T . With increase in T , the precession motion becomes more active, resulting in weaker ion–dipole interaction [29]. Equations (7.12) and (7.14) predict the rates of many PTRs within $\pm 50 \%$ deviation. Some exception may occur when the reactive sites of the ions and/or molecules have some steric hindrance for the occurrence of PTR, namely, reactions have some “entropy barrier.” In such cases, rates become smaller than those predicted by k_L and k_{ADO} .

In matrix-assisted laser desorption ionization (MALDI), the organic acids are frequently used as matrices that act as proton donors to form the protonated analytes. In positive-mode electrospray

ionization, a number of protons enriched in the charged droplets are donated to the analytes (e.g., peptides and proteins) to form multiple protonated analytes. In any ionization method, the formation of the protonated molecules indicates the occurrence of the PTRs. The protonated molecules are most often observed in various ionization phenomena because PTRs have usually no activation barriers and proceed with capture collision rate (reaction probability of one).

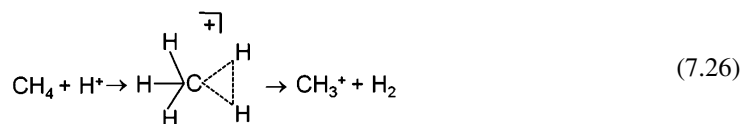
7.2.2.3 Hydride Transfer Reactions

For hydrocarbons, the so-called hydride transfer reactions are frequently observed. Reactions (7.24) and (7.25) are the typical examples:



Unfortunately, the term “hydride ion transfer” is misleading. In PTRs, such as reaction (7.15), $\text{CH}_5^+ + \text{NH}_3 = \text{CH}_4 + \text{NH}_4^+$, the proton really transfers from CH_5^+ to NH_3 . However, the reaction mechanism of hydride transfer reactions (HTR) is not that simple; the nominal H^- transfer does not take place in reactions (7.24) and (7.25).

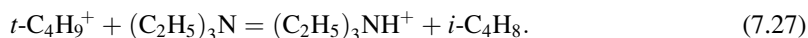
To understand the mechanism of hydride ion transfer reactions, let us consider a simple exothermic reaction, $\text{CH}_4 + \text{H}^+ = \text{CH}_3^+ + \text{H}_2$ (exothermic by 299 kJ mol^{-1}).



In reaction (7.26), H^+ inserts itself into one of the C–H σ bonds in CH_4 to form the three-center–two-electron bond as an intermediate complex. As shown above, hydrides play no role in the reaction. Instead, an H atom transfer reaction may be more appropriate for the interpretation of this reaction [30].

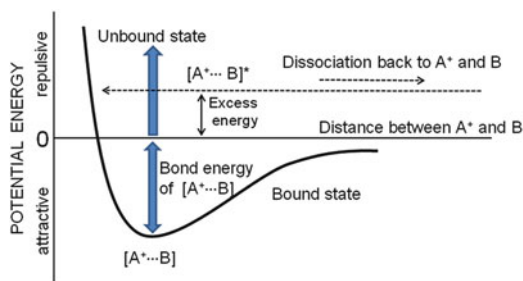
The HTR takes place via the formation of the tight intermediate complex shown above [29, 31, 32]. This is accompanied by a decrease in entropy (from a loose complex to a tight complex), i.e., there is an “entropy barrier” for the reaction. As a certain time is necessary to form the tight complex, the reaction rates of HTR decrease drastically with increasing temperature, because at higher temperature the loose complex has a shorter lifetime and it dissociates to the original reactants in this limited lifetime before the formation of the tight complex. For example, the rate constants k for reaction (7.25) are 1.7×10^{-12} , 1.4×10^{-11} , and $1.1 \times 10^{-9} \text{ cm}^3 \text{ s}^{-1}$ at 640, 300, and 200 K, respectively. Below 200 K, k becomes constant with the value of the capture collision rate constant. That is, below 200 K all the loose complexes lead to the formation of the tight complex. As such, the rates of HTR change orders of magnitude depending on the ion source temperature. Thus, for the observation of HTR appropriate control of the ion source temperature is required.

Contrary to HTR, the rates of PTR are affected very little by temperature. For example, the rate constant for reaction (7.27) is $1.6 \times 10^{-9} \text{ cm}^3 \text{ s}^{-1}$ at 300 K and $1.5 \times 10^{-9} \text{ cm}^3 \text{ s}^{-1}$ at 640 K:



The hydride ion is the negative hydrogen ion, H^- . The hydrogen atom has a positive electron affinity (EA) of 0.7 eV, i.e., the reaction, $\text{H} + \text{e}^- = \text{H}^-$, is exothermic by 0.7 eV. The ions H^- and Li^+

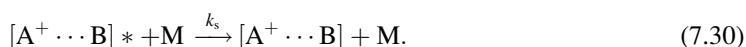
Fig. 7.2 Potential energy diagram for the interaction of A^+ and B



are isoelectronic with He, in which the 1 s electronic shell is occupied by the electron pair $(1s)^2$. The halide ions, F^- , Cl^- , Br^- , and I^- , and also the alkaline ions, Na^+ , K^+ , Rb^+ , and Cs^+ , are isoelectronic with Ne, Ar, Kr, and Xe, respectively. The formation of closed electronic shells for these ions explains the high EA value of halogen atoms and the relatively low ionization energies of alkaline atoms.

7.2.2.4 Clustering Reactions

The ion–molecule clustering reaction (7.28) may proceed through the two elementary processes as shown in reactions (7.29) and (7.30):



When A^+ and B have an encounter, they form the intermediate complex, $[A^+ \cdots B]^*$, where * denotes the excess energy. This excess energy is the sum of the bond energy between A^+ and B and the original internal and translational energies of A^+ and B. That is, the energy of $[A^+ \cdots B]^*$ is larger than the bond energy of $[A^+ \cdots B]$, i.e., $[A^+ \cdots B]^*$ in the “unbound state.” Thus $[A^+ \cdots B]^*$ dissociates to the original species A^+ and B within a finite time (Fig. 7.2).

This is similar to the fact that even if two H atoms collide with each other, a hydrogen molecule will not be formed in the high-vacuum interstellar medium. In order to form the stable bound state of $[A^+ \cdots B]$, the excess energy of $[A^+ \cdots B]^*$ has to be dissipated by collision with a third body, M. The cooling process of $[A^+ \cdots B]^*$ by M is called “collisional cooling” (reaction (7.30)). Thus the rate of the clustering reaction is highly dependent on and increases with the pressure of M. In addition, the rate of the clustering reaction is highly dependent on temperature and increases at lower temperature because of longer lifetime of $[A^+ \cdots B]^*$ (less excess energy at lower temperature).

The kinetics of the clustering reaction is considered by the energy transfer mechanism expressed as reactions (7.29) and (7.30), where k_c is the capture collision rate constant of A^+ and B, k_b is the rate constant of unimolecular back dissociation of $[A^+ \cdots B]^*$, and k_s is the rate constant of collisional stabilization of $[A^+ \cdots B]^*$ by M. k_c and k_s can be approximated to be the capture collision rate constants k_L or k_{ADO} .

If a “steady-state concentration” is established for reactions (7.29) and (7.30) (i.e., $d[A^+ \cdots B]^*/dt = 0$), the rate constant k_f for reaction (7.28) is derived as (7.31):

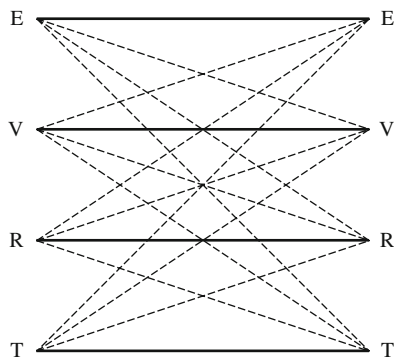


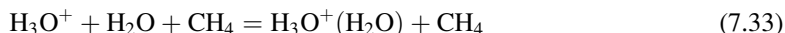
Fig. 7.3 Energy transfer between electronic (E), vibrational (V), rotational (R), and translational (T) modes

$$k_f = \frac{k_c k_s}{k_b + k_s [\text{M}]} \quad (7.31)$$

First, let us consider reaction (7.28) with low pressure of the buffer gas M. In this case, a greater part of $[\text{A}^+\cdots\text{B}]^*$ dissociates back to A^+ and B before being stabilized by the third-body collision, and (7.31) is reduced to (7.32) by the relation of $k_b \gg k_s [\text{M}]$:

$$k_f = \frac{k_c k_s}{k_b} = k_t \quad (7.32)$$

Equation (7.32) indicates that reaction (7.28) is third order with respect to $[\text{A}^+]$, $[\text{B}]$, and $[\text{M}]$. Namely, the reaction rate is proportional to the pressure of the buffer gas M. It should be noted that the third-order rate constant k_t shows a large negative temperature dependence [33]. For example, the clustering reaction (7.33) is inversely proportional to T^4 [34]:



$$k_t = 3.7 \times 10^{-17} / T^4 \text{ cm}^6 \text{ s}^{-1} \quad (7.34)$$

The large “negative” temperature dependence of k_t is apparently caused by the longer lifetime of $[\text{A}^+\cdots\text{B}]^*$ at lower temperature, i.e., decrease of the back dissociation rate k_b in (7.29). The lower the temperature, the smaller the excess internal energy in $[\text{A}^+\cdots\text{B}]^*$, and $[\text{A}^+\cdots\text{B}]^*$ has more chance to be stabilized by the third-body collision (7.30).

In reaction (7.30), the vibrational, rotational, and translational energy transfers take place from $[\text{A}^+\cdots\text{B}]^*$ to M. The deactivation rate constant k_s is highly affected by the nature of M. When M is a rare gas atom, the internal energy of $[\text{A}^+\cdots\text{B}]^*$ must be dissipated as the translational (kinetic) energy of a rare gas atom, because the atom does not have any vibrational and rotational modes. In contrast, if M is a polyatomic molecule, the internal energy can be dissipated as vibrational, rotational, and also translational energies of M. Thus the value of k_t when M is a molecule would be much larger than that if M is a rare gas atom [35, 36].

Figure 7.3 shows the conceptual idea for the energy transfer between electronic (E), vibrational (V), rotational (R), and translational (T) energies. The efficiency of energy transfer is largest between the same energy modes (solid line) and smaller between different modes (broken line).

With decrease in temperature and/or increase of buffer gas pressure, the relation of $k_b \ll k_s[M]$ holds and (7.31) reduces to (7.35):

$$k_f = \frac{k_c}{[M]}. \quad (7.35)$$

That is, reaction (7.28) becomes second order with respect to $[A^+]$ and $[B]$, but is independent of $[M]$,

$$-d[A^+]/dt = k_f[A^+][B][M] \approx k_c[A^+][B], \quad (7.36)$$

and the apparent order of reaction (7.28) becomes “pseudo second order” although A^+ , B , and M take part in the reaction.

In the discussion above, two extreme cases of $k_b \gg k_s[M]$ and $k_b \ll k_s[M]$ were presented. For the reactions $N_2^+ + N_2 = N_4^+$ [37], $NH_4^+ + NH_3 = NH_4^+(NH_3)$, and $(CH_3)_2NH_2^+ + (CH_3)_2NH = (CH_3)_2NH_2^+((CH_3)_2NH)$, an order transition from three to pseudo second was observed in a certain temperature region, confirming that (7.31) correctly predicts the pressure dependence of rate constants for clustering reactions [38–40], i.e., the sequential occurrence of reactions (7.29) and (7.30) for reaction (7.28).

7.2.2.5 Negative Ion Formation

Electron attachment to an atom or a molecule with positive EA value leads to the formation of a stable negative ion. The elementary processes for negative ion formation of the molecule AB is summarized in the following.

Electron capture:



Ion pair formation:



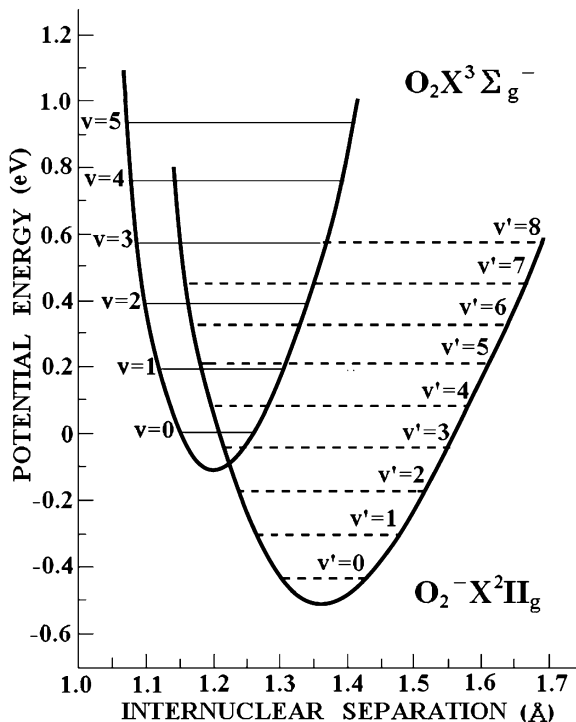
Charge transfer:



Reactions (7.42)–(7.46) are some examples of electron capture reactions frequently used for CI:



Fig. 7.4 Potential energy curves for O_2 and O_2^- . (Reproduced with permission from [41])



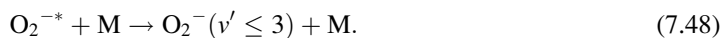
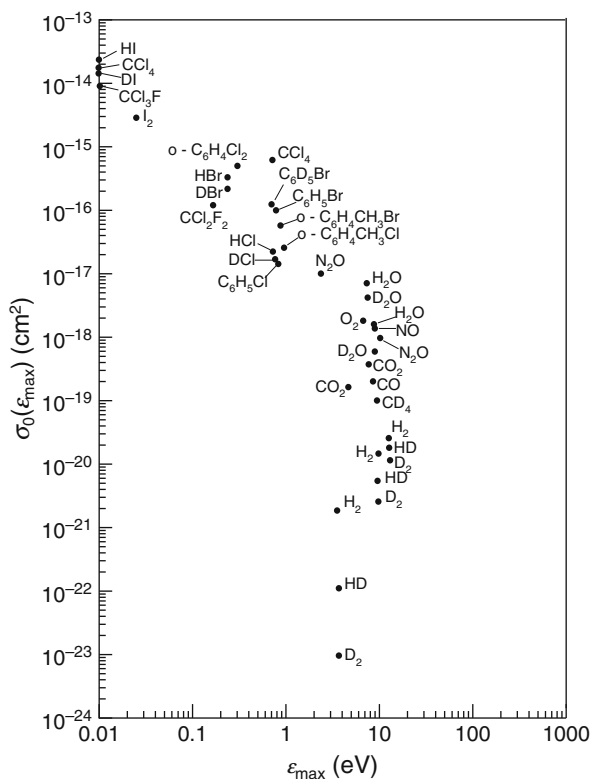
Under CI conditions, it is mainly the thermalized electrons that react with molecules. The high-energy electrons injected into the CI ion source are thermalized by multiple collisions with buffer gas molecules and ultimately the electron temperature equals the buffer gas temperature. Since a number of thermalized electrons can participate in negative ion formation, the negative-mode CI is in some cases much more sensitive than the positive-mode CI.

The electron capture process by O_2 is a good example for understanding the resonant electron capture. Figure 7.4 shows the potential energy curves for O_2 and O_2^- [41]. The v and v' stand for the vibrational quantum numbers of O_2 and O_2^- , respectively.

At room temperature, the O_2 molecule is mainly in the ground vibrational state with $v = 0$. As shown in Fig. 7.4, the energy level of O_2^- with $v' = 4$ is higher than that of O_2 with $v = 0$ by 0.08 eV. The average thermal energy of an electron at 300 K is about 0.04 eV. Thus, only a small part of thermal electrons that happen to have the kinetic energy of 0.08 eV can form O_2^- by the “resonant process,” in which the kinetic energy of an electron is transferred to the internal energy of O_2^- ($v' = 4$). In a finite lifetime, the electron with kinetic energy of 0.08 eV will detach from O_2^- ($v' = 4$) and return to O_2 ($v = 0$). When the vibrational energy of O_2^- ($v' = 4$) is deactivated by a third-body collision (reaction 7.48), a stable O_2^- ($v' \leq 3$) can form:



Fig. 7.5 Maximum values of cross sections of the dissociative electron attachment reactions $\sigma_d(\epsilon_{MAX})$ (cm^2) as a function of electron energy (eV). (Reproduced with permission from [42])



With increase in the electron energy in the reaction $\text{O}_2 + e^-$, “dissociative electron attachment” (reaction 7.43) starts taking place when the internal energy of O_2^{-*} exceeds the dissociation limit of O_2^- . Figure 7.5 shows the maximum values of the cross sections ($\sigma_d(\epsilon_{MAX}) \text{ cm}^2$) of dissociative electron attachment, $\text{AB} + e^- \rightarrow \text{A} + \text{B}^-$, as a function of electron energy for several molecules [42].

As shown in Fig. 7.5, the cross sections $\sigma_d(\epsilon_{MAX})$ for negative ion formation vary by orders of magnitude depending on the molecule. The molecules of HI, CCl_4 , DI, and CCl_3F react with thermal electrons with very large cross sections, $\sim 10^{-14} \text{ cm}^2$. CCl_4 and CCl_3F are the very useful reagents for the formation of the chloride ion, Cl^- , in CI.

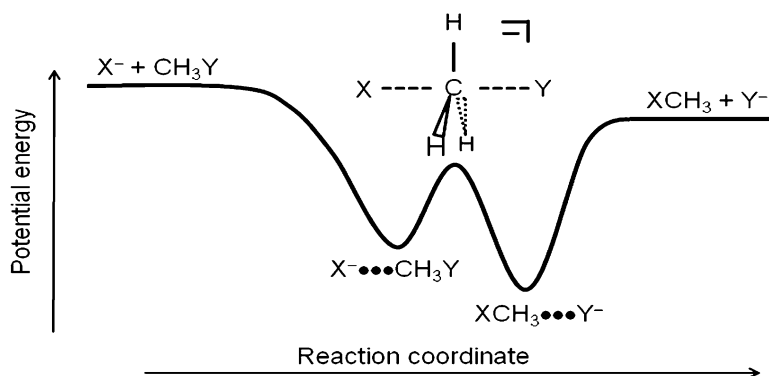
EA is defined as the energy difference between the negative ions and neutral molecules with their ground states for all modes of the internal energies, i.e., electronic, vibrational, and rotational modes. For O_2 in Fig. 7.4, the energy difference between $\text{O}_2(v=0)$ and $\text{O}_2^{-}(v'=0)$ gives the EA value of 0.5 eV for O_2 . In Fig. 7.4, the equilibrium interatomic distance for O_2^{-} ($\sim 1.36 \text{ \AA}$) is longer than for O_2 ($\sim 1.19 \text{ \AA}$), because the extra electron in O_2^{-} is occupied in the “antibonding π^* orbital” of O_2 . The EA values for some atoms and molecules are summarized in Table 7.2 (in eV) [43].

In general, the negative-mode CI and APCI are much softer (less fragmentation) than the positive-mode ones. Thus, the former is more suitable for the determination of the molecular masses of analytes (see Sect. 4.2).

Table 7.2 Electron affinity (eV)

Chemical species	Electron affinity
H	0.75
O	1.46
F	3.4
Cl	3.62
Br	3.37
I	3.07
NO	0.024
NO ₂	2.43
NO ₃	3.7
N ₂ O	0.22
O ₂	0.5
O ₃	2.05
OH	1.83
SCN	2.17
SF ₆	0.6
SF ₅	2.8
7,7',8,8'-tetracyanoquinodimethane (TCNQ)	2.83
Nitrobenzene	0.98
Tetracene	0.88
Azulene	0.66
Anthracene	0.55
Naphthalene	0.14

Fig. 7.6 Conceptual idea of the potential energy curve for the S_N2 displacement reaction, $X^- + CH_3Y \rightarrow [X \cdots CH_3 \cdots Y]^- \rightarrow XCH_3 + Y^-$



7.2.2.6 Other IMRs

In addition to several IMRs described above (CTR, PTR, HTR, clustering reactions), S_N2 reactions (called “nucleophilic 2nd order”) [44–46] and additional examples are H, H₂, and H₂⁻ transfer reactions [47]. A typical example of S_N2 reaction is the halide ion displacement reaction, $Cl^- + CH_3Br = ClCH_3 + Br^-$, in which Cl⁻ attacks the positively charged carbon atom of CH₃Br (“methyl pocket attack”). The rate constants for S_N2 reactions are generally smaller than the capture collision rates because S_N2 reactions proceed through the formation of the intermediate complex, $Cl^- + CH_3Br \rightarrow [Cl \cdots CH_3 \cdots Br]^- \rightarrow ClCH_3 + Br^-$. The potential energy curve for the S_N2 reaction

has a double-minimum potential (or double-well potential). The $X^- \cdots CH_3Y$ and $XCH_3 \cdots Y^-$ represent the cluster ions of X^- and Y^- with CH_3Y and XCH_3 , respectively.

The formation of the intermediate complex $[Cl \cdots CH_3 \cdots Br]^-$ accompanies the entropy barrier. Thus, the rate decreases with increasing temperature as is the case for HTR described in Sect. 2.2.3. The H, H_2 , and H_2^- transfer reactions are mainly observed for hydrocarbons [47].

7.2.2.7 Compilation of Rate Constants

Because matter is composed of charged particles (electrons and nuclei), IMRs always play major roles in nature, making the fundamental knowledge about these reactions a must for understanding processes in natural science. Needless to say in CI and APCI, IMRs also take place in MALDI, secondary ion mass spectrometry (SIMS), electrospray ionization (ESI), and in many other ionization methods. As described, there are numerous types of IMRs with their own characteristic rate constant and dependence on temperature. For the last several decades, a large number of gas-phase ion/molecule reaction rates have been accumulated. These data are compiled in [48–51]. Reference [51] is also available on the home page of the Japanese Mass spectrometry Society of Japan (<http://www.mssj.jp/index-jp.html>), and the reader is strongly encouraged to survey the many types of IMRs listed and their rate constants, as a good practice to understand what are the IMRs.

7.3 Thermochemical Data for Ion Chemistry

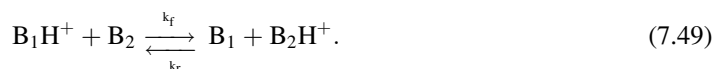
In the study of the energetics of IMRs, gas-phase thermochemical data such as the heat of formation of ions and molecules, proton affinity, acidity, hydride ion affinity, electron affinity, and standard entropy values will provide the right answers. This chapter discusses the thermochemical data and the energetics of IMRs.

7.3.1 Standard Heat of Formation

Many exothermic IMRs have capture collision rate constants. The enthalpy changes of the exothermic reactions are negative ($\Delta H^\circ < 0$). The enthalpy change (ΔH°) of reaction $A^+ + B = C^+ + D$ can be calculated by the heats of formation (ΔH_f°) of A^+ , B, C^+ , and D as follows: $\Delta H^\circ = [\Delta H_f^\circ(C^+) + \Delta H_f^\circ(D)] - [\Delta H_f^\circ(A^+) + \Delta H_f^\circ(B)]$. The ΔH° values are negative for exothermic reactions and positive for endothermic reactions. Critically evaluated data on heats of formation of positive and negative ions in the gas phase are compiled in [52]. Heats of formation, proton affinities, gas-phase basicities, EA values, and ionization energies are also available on the Web site of the National Institute of Standards (NIST) Chemistry WebBook, <http://webbook.nist.gov/chemistry/>.

7.3.2 Determination of Enthalpy and Entropy Changes in IMRs

When the rates of the forward and reverse reactions, k_f and k_r , respectively, become equal, reaction equilibrium is established. As an example, let us consider the proton transfer reaction (7.49) between B_1 and B_2 :



At equilibrium, the relation (7.50) holds:

$$k_f[B_1H^+][B_2] = k_r[B_1][B_2H^+]. \quad (7.50)$$

Equation (7.50) leads to (7.51):

$$[B_1][B_2H^+]/[B_1H^+][B_2] = k_f/k_r = K. \quad (7.51)$$

The value of $[B_1][B_2H^+]/[B_1H^+][B_2]$ corresponds to the equilibrium constant K for reaction (7.49), i.e., K for reaction (7.49) is given by the ratio of the forward and reverse rate constants, k_f/k_r . The equilibrium constant K can be obtained by measuring the ion intensities of B_1H^+ and B_2H^+ by mass spectrometry.

The equilibrium constant K is related to the thermochemical values of enthalpy change (ΔH°) and entropy changes (ΔS°) via van't Hoff equation (7.52), or (7.53):

$$-RT \ln K = \Delta G^\circ = \Delta H^\circ - T\Delta S^\circ \quad (7.52)$$

$$\ln K = -\frac{\Delta H^\circ}{RT} + \frac{\Delta S^\circ}{R}. \quad (7.53)$$

In (7.53) the natural logarithm of K ($\ln K$) is in a linear relation with $1/T$, like in a linear equation of the type $y = ax + b$, where y is $\ln K$ and x is $1/T$. From the straight line of the van't Hoff plots, $\ln K$ vs. $1/T$, the slope ($-\Delta H^\circ/R$) and the intersect extrapolated to $1/T \rightarrow 0$ (i.e., $\Delta S^\circ/R$) lead to the determination of the enthalpy and entropy changes (ΔH°) and (ΔS°), respectively, for the reaction. The equilibrium is established faster at higher pressure. Thus high-pressure mass spectrometer is mainly used to determine thermochemical data [53, 54].

7.3.3 Determination of Proton Affinities: Gas-Phase Basicities of Molecules

Protonated molecules are the most frequently observed ions in mass spectrometry. They are observed not only in CI and APCI but also in MALDI, SIMS, electrospray, etc. For this reason, for the analysis of IMRs taking place in a variety of ionization methods, knowledge about the gas-phase proton affinities (PA) is essential. PA is defined as the heat evolved in the process, $H^+ + B = BH^+$, and thus PA has the positive sign.

For the proton transfer reaction (7.54), the equilibrium constant K is given by (7.51):



When K is experimentally available, the free energy change ΔG° of the reaction is given by (7.52). Almost all the PA values were experimentally determined at only one temperature. The difference between the PA values of B_1 and B_2 (i.e., $PA(B_1) - PA(B_2)$) corresponds to the heat of reaction ΔH° :

$$\Delta H^\circ = PA(B_1) - PA(B_2). \quad (7.55)$$

If $PA(B_2)$ is larger than $PA(B_1)$, the reaction becomes exothermic ($\Delta H^\circ < 0$).

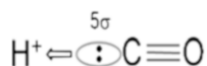
Equation (7.52) gives only the free energy change ΔG° , but not the enthalpy change ΔH° . To obtain ΔH° without measuring the temperature dependence of K as the van't Hoff plots, the values of ΔS° , i.e., $\Delta H^\circ = \Delta G^\circ + T\Delta S^\circ$, need to be estimated. Lau et al. estimated ΔS° by (7.56) that takes into account the rotational symmetry numbers σ [55]:

$$\Delta S^\circ_{\text{rotsym}} = R \times \ln \frac{\sigma(\text{B}_1\text{H}^+)\sigma(\text{B}_2)}{\sigma(\text{B}_2\text{H}^+)\sigma(\text{B}_1)}. \quad (7.56)$$

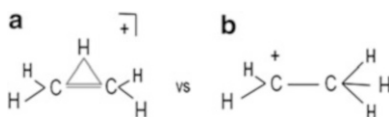
The symmetry number σ indicates the number of different (but indistinguishable, or equivalent) arrangements of the object, i.e., the order of its symmetry group. They found that the theoretical ΔS° values derived from (7.56) are in very good agreement with the experimental results [55]. One can find a comprehensive compilation of gas-phase basicities ($-\Delta G^\circ$) and PA values ($-\Delta H^\circ$) of molecules in Ref. [56]. These values are mainly obtained by using (7.52) and (7.56). For the proton transfer reaction (7.49), the entropy changes are generally small (ΔS° may be within $\pm 10 \text{ J mol}^{-1} \text{ K}^{-1}$) because the nature of chemical bonds before and after the reactions does not change drastically. Thus, the assumption of $\Delta G^\circ \approx \Delta H^\circ$ is often a good approximation for many PTRs, namely, $\Delta G^\circ \approx \Delta H^\circ = \text{PA}(\text{B}_1) - \text{PA}(\text{B}_2)$. Molecules may be categorized into three groups with their PA values:

1. Molecules with PA values lower than $\text{PA}(\text{H}_2\text{O})$: Examples are σ electron donor bases (e.g., rare gas atoms, diatomic molecules, simple hydrocarbons, etc.).
2. Molecules with PA values between $\text{PA}(\text{H}_2\text{O})$ and $\text{PA}(\text{NH}_3)$: Examples are alcohols, carbonyls, sulfur compounds, aromatic hydrocarbons, etc.
3. Molecules with PA values higher than $\text{PA}(\text{NH}_3)$: Examples are amines, pyridines, etc.

PA values for some molecules are listed in Table 7.3 [56]. From the table, very interesting characteristics of the atoms and molecules are envisaged. For example, the PA values of rare gas atoms increase steeply in the order $\text{He} \rightarrow \text{Ne} \rightarrow \text{Ar} \rightarrow \text{Kr} \rightarrow \text{Xe}$. The protonated hydrogen molecule, H_3^+ , has the equilateral triangular geometry, indicating that two σ electrons of H_2 are equally shared with three H atoms in H_3^+ . The PA values of CO at the C and O atoms are 594 and 426.3 kJ mol^{-1} , respectively. That is, HCO^+ is much more stable than COH^+ , in spite of the fact that oxygen is more electronegative than carbon. The CO molecule has a dipole moment with negative charge on the carbon atom, $\text{C}^{\delta-} \equiv \text{O}^{\delta+}$ (dipole moment of CO is 0.1 Debye). This arises from the fact that the 5σ orbital (the highest occupied molecular orbital, HOMO) of CO is extended outside of the carbon atom along the molecular axis. This results in the much stronger interaction of H^+ with the C atom than the O atom of CO.



When the ethylene molecule is protonated, the proton interacts with the π orbital electrons (HOMO) to form the three-center–two-electron bond, $\text{H}_2\text{CH}^+\text{CH}_2$, with the isosceles triangle geometry (a) [57].



The classical structure of $\text{H}_2\text{C}^+\text{CH}_3$ (b) is an unstable intermediate.

Protonated water, H_3O^+ , has an almost flat regular triangular pyramid shape. Three O–H bonds in H_3O^+ are equivalent and the positive charge is equally distributed in three H atoms. In the protonation

Table 7.3 Proton Affinity

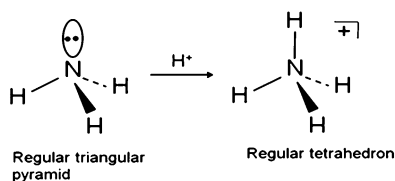
chemical species	base	proton affinity (kJ/mol)
rare gas		
He	He	177.8
Ne	Ne	198.8
Ar	Ar	369.2
Kr	Kr	424.6
Xe	Xe	499.6
simple molecule		
H ₂	H ₂	422.3
O ₂	O ₂	421.0
N ₂	N ₂	493.8
CO	CO at C	594.0
CO	CO at O	426.3
CO ₂	CO ₂	540.5
CS ₂	CS ₂	681.9
NO	NO	531.8
N ₂ O	N ₂ O at N	549.8
N ₂ O	N ₂ O at O	575.2
NO ₂	NO ₂	591.0
SO ₂	SO ₂	672.3
O ₃	O ₃	625.5
H ₂ S	H ₂ S	705.0
hydrocarbon		
CH ₄	CH ₄	543.5
C ₂ H ₆	C ₂ H ₆	596.3
C ₂ H ₄	CH ₂ =CH ₂	680.5
C ₂ H ₂	C ₂ H ₂	641.4
C ₃ H ₈	C ₃ H ₈	625.7
C ₃ H ₆	CH ₃ CH=CH ₂	751.6
C ₃ H ₄	H ₂ C=C=CH ₂	775.3
C ₃ H ₄	H ₃ CC≡CH	748.0
C ₄ H ₁₀	i-C ₄ H ₁₀	677.8
C ₆ H ₆	C ₆ H ₆	750.4
C ₇ H ₈	C ₆ H ₅ CH ₃	784.0
C ₁₀ H ₈	o-xylene	796.0
C ₁₀ H ₈	p-xylene	794.4
C ₁₂ H ₁₀	biphenyl	813.6
C ₁₄ H ₁₀	anthracene	877.3
C ₂₄ H ₁₂	coronene	861.3
oxygen-containing molecule		
H ₂ O	H ₂ O	691.0
H ₂ O ₂	H ₂ O ₂	674.5
CH ₂ O	H ₂ CO	712.9
CH ₄ O	CH ₃ OH	754.3
CH ₂ O ₂	HCOOH	742.0
C ₂ H ₆ O	C ₂ H ₅ OH	776.4
C ₂ H ₆ O	CH ₃ OCH ₃	792.0
C ₂ H ₄ O ₂	CH ₃ COOH	783.7
C ₃ H ₆ O	(CH ₃) ₂ CO	823.0
C ₃ H ₈ O	n-C ₃ H ₇ OH	786.5
C ₃ H ₈ O	i-C ₃ H ₇ OH	793.0
C ₄ H ₄ O	furan	803.4
C ₄ H ₈ O	tetrahydrofuran	822.1
C ₄ H ₁₀ O	n-C ₄ H ₉ OH	789.2
C ₄ H ₁₀ O	i-C ₄ H ₉ OH	793.7
C ₄ H ₁₀ O	(C ₂ H ₅) ₂ O	828.4
C ₆ H ₆ O	C ₆ H ₅ OH	817.3
C ₁₂ H ₂₄ O ₆	18-crown-6	967.0

(continued)

Table 7.3 (continued)

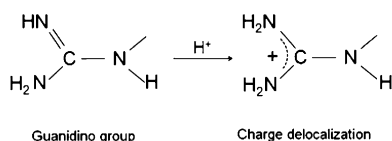
chemical species	base	proton affinity (kJ/mol)
nitrogen-containing molecule		
NH ₃	NH ₃	853.6
CH ₅ N	CH ₃ NH ₂	899.0
C ₂ H ₇ N	(CH ₃) ₂ NH	929.5
C ₃ H ₉ N	(CH ₃) ₃ N	948.9
C ₂ H ₃ N	CH ₃ CN	779.2
C ₂ H ₇ N	C ₂ H ₅ NH ₂	912.0
C ₄ H ₅ N	pyrrole	875.4
C ₄ H ₉ N	pyrrolidine	948.3
C ₅ H ₅ N	pyridine	930.0
C ₅ H ₁₁ N	piperidine	954.0
C ₆ H ₇ N	C ₆ H ₅ NH ₂	882.5
C ₉ H ₇ N	quinoline	953.2
amono acid, nucleic acid, etc.		
CH ₅ N ₃	guanidine	986.3
C ₂ H ₅ NO ₂	glycine	886.5
C ₃ H ₇ NO ₂	L-alanine	901.6
C ₃ H ₇ NO ₂ S	L-cysteine	903.2
C ₃ H ₇ NO ₃	L-serine	914.6
C ₄ H ₄ N ₂ O ₂	uracil	872.7
C ₄ H ₅ N ₃ O	cytosine	949.9
C ₄ H ₇ NO ₄	L-aspartic acid	908.9
C ₄ H ₈ N ₂ O ₃	L-asparagine	929.0
C ₄ H ₉ NO ₃	L-threonine	922.5
C ₅ H ₅ N ₅	adenine	942.8
C ₅ H ₅ N ₅ O	guanine	959.5
C ₅ H ₆ N ₂ O ₂	thymine	880.9
C ₅ H ₉ NO ₂	L-proline	920.5
C ₅ H ₉ N ₃	histamine	999.8
C ₅ H ₁₀ N ₂ O ₃	L-glutamine	937.8
C ₅ H ₁₁ NO ₂	L-valine	910.6
C ₅ H ₁₁ NO ₂ S	L-methionine	935.4
C ₆ H ₆ N ₂ O	nicotinamide	918.3
C ₆ H ₉ N ₃ O ₂	L-histidine	988.0
C ₆ H ₁₃ NO ₂	L-leucine	914.6
C ₆ H ₁₃ NO ₂	L-isoleucine	917.4
C ₆ H ₁₄ N ₂ O ₂	L-lysine	996.0
C ₆ H ₁₄ N ₄ O ₂	L-arginine	1051.0
C ₉ H ₁₁ NO ₂	L-phenylalanine	922.9
C ₉ H ₁₁ NO ₃	L-tyrosine	926.0
C ₉ H ₁₂ N ₂ O ₆	uridine	947.6
C ₉ H ₁₃ N ₃ O ₅	cytidine	982.5
C ₁₀ H ₁₃ N ₅ O ₂	guanosine	993.4
C ₁₀ H ₁₃ N ₅ O ₄	adenosine	989.3
C ₁₁ H ₁₂ N ₂ O ₂	L-tryptophan	948.9

of NH₃, the proton will attack the nonbonding lone-pair electrons of NH₃ to form NH₄⁺. The protonated ammonia, NH₄⁺, has the regular tetrahedral structure like CH₄, namely, four N–H bonds in NH₄⁺ are all equivalent.



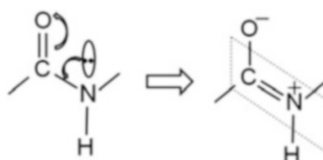
With the successive methyl substitution of the H atoms in NH_3 , PA values (in kJ mol^{-1}) increase steeply in the order NH_3 (853.6) \rightarrow CH_3NH_2 (899) \rightarrow $(\text{CH}_3)_2\text{NH}$ (929.5) \rightarrow $(\text{CH}_3)_3\text{N}$ (948.9) (Table 7.1). By the displacement of the H atoms with the methyl groups, the positive charge in the protonated amines is increasingly delocalized because of the inductive effect of the methyl groups, resulting in the stabilization of the protonated species.

In Table 7.3, three basic amino acids, arginine, histidine, and lysine, have relatively high PA values, with arginine having the highest ($1,051 \text{ kJ mol}^{-1}$). The high PA of arginine is due to the charge delocalization for the protonated arginine in its guanidino group.



Naturally, guanidine also has a high PA.

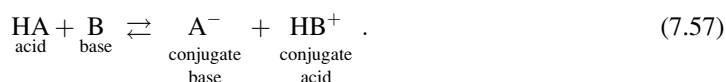
The number of charges of multiple protonated peptides and proteins observed by ESI are closely related to the number of basic amino acid residues in these molecules. The basic amino acid residues and acidic amino acid residues are the protonation and deprotonation sites for the positive and negative modes of ESI operation, respectively. The PA value of the N sites of the peptide bonds in peptides and proteins is much lower than the basic amino acid residues. The N atoms in the peptide bonds are seldom protonated in ESI, because the nonbonding lone-pair electrons on the N atom in the peptide bond are delocalized to form the semi-double bond between the C and the N atom, resulting in a decrease in the basicity of the N atom.



The double bond formation explains the planar geometry of the peptide bond moiety in peptides and proteins.

7.3.4 PTRs of Negative Ions: Gas-Phase Acidities of Molecules

The concept of the Bronsted–Lowry classification for the definition of acids and bases is useful in the interpretation of the energetics of PTRs. It defines an acid as a proton donor and a base as a proton acceptor:



This concept holds for all compounds that have H atoms. Acetic acid is known to be a weak acid, but it behaves also as a base:

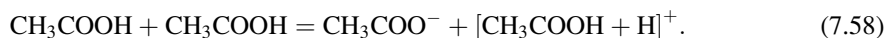


Table 7.4 [D–EA]

Molecule	[D–EA] (kJ mol ⁻¹)
H ₂	361
H ₂ O	322
CH ₃ OH	264
C ₂ H ₅ OH	256
DMSO	255
CH ₃ CN	250
(CH ₃) ₂ CO	236
HF	235
H ₂ S	161
C ₆ H ₅ OH	151
CH ₃ COOH	146
HCOOH	132
C ₆ H ₅ COOH	112
HCl	84
CF ₃ COOH	38
HBr	42
HI	3

The electrolytic dissociation of water is another example:



In general, the negative-mode PTRs are much softer than the positive-mode ones. Thus, negative-mode CI is suitable for the determination of the molecular masses of the analytes.

In the negative-mode proton transfer reaction (7.60),



the enthalpy change of the reaction, ΔH_{60}° , is given by (7.61), where $\text{PA}(\text{A}^-)$ is the PA of A^- , which is given by (7.62), where $\text{D}(\text{A}-\text{H})$ is the bond dissociation energy of the acid $\text{A}-\text{H}$, $\text{EA}(\text{A}^\bullet)$ is the EA value of the radical A^\bullet , and $\text{IE}(\text{H})$ is the IE of the H atom (13.6 eV or 1,311 kJ mol⁻¹):

$$\Delta H_{60}^\circ = \text{PA}(\text{A}_2^-) - \text{PA}(\text{A}_1^-) \quad (7.61)$$

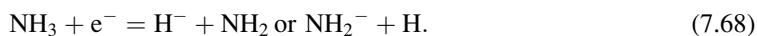
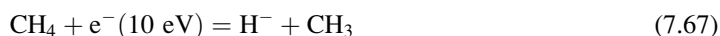
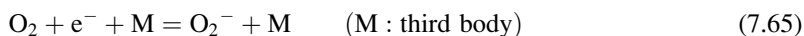
$$\text{PA}(\text{A}^-) = \text{D}(\text{A}-\text{H}) - \text{EA}(\text{A}^\bullet) + \text{IE}(\text{H}). \quad (7.62)$$

This means that

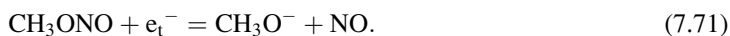
$$\Delta H_{60}^\circ = [\text{D}(\text{A}_2-\text{H}) - \text{EA}(\text{A}_2^\bullet)] - [\text{D}(\text{A}_1-\text{H}) - \text{EA}(\text{A}_1^\bullet)]. \quad (7.63)$$

The value $\text{PA}(\text{A}^-)$ corresponds to the energy released for the protonation of A^- , $\text{A}^- + \text{H}^+ = \text{AH}$. Since $\text{IE}(\text{H})$ in (7.62) is constant, the measure of the gas-phase acidities can be given by the values of $[\text{D}(\text{A}-\text{H}) - \text{EA}(\text{A}^\bullet)]$. The smaller the term $[\text{D} - \text{EA}]$, the higher is the acidity of the acid AH . The $[\text{D} - \text{EA}]$ values for aliphatic carboxylic acids, benzoic acid, phenols, and alcohols were measured using high-pressure mass spectrometry and ion cyclotron resonance mass spectrometry [58–68]. Table 7.4 shows the values of the acidity $[\text{D} - \text{EA}]$ for some typical molecules. These values were determined by measuring the enthalpy changes for reactions (7.60).

In reaction (7.60), A_1^- with higher PA is more efficient for the formation of A_2^- for the analytes A_2H . The reagent negative ions for CI can be formed by the electron irradiation of some reagent molecules as follows:



The reactions above take place through the resonant processes in the narrow electron energy regions and thus the electron capture cross sections are rather small (see Fig. 7.5). For the application of CI, the thermal electron capture reactions are much more preferable because the high-energy electrons injected into the CI ion source are quickly thermalized by the multiple collisions with the buffer gas molecules. The typical reagent molecules are CCl_4 , NF_3 , and CH_3ONO that capture thermal electrons (e_t^-) by the resonant process to produce the negative ions, Cl^- , F^- , and CH_3O^- , respectively:



All of these reactions are exothermic because the bond energies of CCl_3-Cl , NF_2-F , and CH_3O-NO are smaller than the EA values of Cl , F , and CH_3O , respectively. For example, the bond dissociation energy of CCl_3-Cl (297 kJ mol^{-1}) is smaller than the EA value of Cl (349 kJ mol^{-1}), i.e., reaction (7.69) is exothermic by 52 kJ mol^{-1} (enthalpy change of reaction (7.69): $\Delta H_{60^\circ} = 297 - 349 = -52 \text{ kJ mol}^{-1}$).

In Table 7.4, the strongest acid is HI . If the ion source is contaminated by HI , I^- will persistently appear, because the PTRs of I^- with all the molecules shown in Table 7.4 become endothermic. In contrast, the negative ions H^- , OH^- , and CH_3O^- can ionize analyte molecules that have larger acidities than H_2 , H_2O , and CH_3OH , respectively. Therefore, these reagent gases are frequently used for the negative-mode CI.

Since the value of $[D - EA]$ for H_2O is very high, as shown in Table 7.4, OH^- is one of the best reactant ions for CI. The ion OH^- can be generated efficiently by electron irradiation of H_2 and CH_4 major gas containing N_2O . The O^- ion produced by the dissociative electron attachment of N_2O abstracts the hydrogen atom from H_2 or CH_4 to produce OH^- , e.g., $O^- + CH_4 \rightarrow OH^- + CH_3$. This system was found to be versatile for negative-mode CI [69–71].

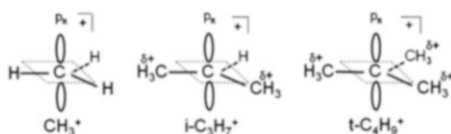
The acidity of HF is rather low and thus NF_3 is frequently used in CI to form F^- (Table 7.4). Although HCl is a strong acid in aqueous solution, the gas-phase acidity of HCl is comparatively low and Cl^- is not suitable as the reactant ion for reaction (7.60). However, Cl^- is sometimes very useful for the formation of cluster ions with the analyte molecule M , $Cl^- \cdots M$. The stability and reactivity of cluster ions are discussed in Sect. 3.6.

7.3.5 Stabilities and Reactivities of Carbenium Ions

The carbenium ion is defined as an even-electron positive ion formed by the σ bond cleavage of a hydrocarbon, e.g., CH_3^+ , C_2H_5^+ , C_3H_7^+ , and C_4H_9^+ . The thermochemical stability of the carbenium ion can be determined by measuring the equilibrium of the HTR (7.72):

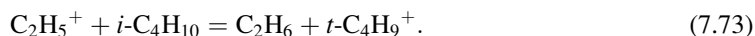


A complete survey of the thermochemical data for carbenium ions is available in Ref. [52] and can be found at URL <http://webbook.nist.gov/chemistry/>. For example, the heats of formation (ΔH_f°) of CH_3^+ , C_2H_5^+ , $i\text{-C}_3\text{H}_7^+$, and $t\text{-C}_4\text{H}_9^+$ are listed as 1,093, 902, 799, and 694 kJ mol⁻¹, respectively, in Ref. [52]. The rapid decrease in the values of ΔH_f° in the order of $\text{CH}_3^+ \rightarrow \dots \rightarrow t\text{-C}_4\text{H}_9^+$ is caused by the inductive effect of methyl groups, i.e., the energy stabilization due to the positive charge delocalization in the cations.



The vacant p_π orbitals are perpendicular to the triangular σ bond orbitals (the central carbon atoms have the sp^2 hybridization orbitals).

For a better understanding of the energetics of HTR, let us consider the heat of reaction ΔH° for reaction (7.73):



To obtain ΔH° for reaction (7.73), the ΔH_f° values of C_2H_6 , $t\text{-C}_4\text{H}_9^+$, C_2H_5^+ , and $i\text{-C}_4\text{H}_{10}$ are used, as described in (7.74):

$$\Delta H^\circ = [\Delta H_f^\circ(\text{C}_2\text{H}_6) + \Delta H_f^\circ(t\text{-C}_4\text{H}_9^+)] - [\Delta H_f^\circ(\text{C}_2\text{H}_5^+) + \Delta H_f^\circ(i\text{-C}_4\text{H}_{10})]. \quad (7.74)$$

Using the data for ΔH_f° cited in [52], we obtain $\Delta H^\circ = [(-84) + (693)] - [(902) + (-134)] = -159$ kJ mol⁻¹. That is, reaction (7.73) is “exothermic” by 159 kJ mol⁻¹. The high exothermicity of this reaction means that C_2H_5^+ can be a universal reagent ion for ionization of hydrocarbons. The great benefit of C_2H_5^+ is that this ion is readily formed by the electron irradiation of methane. Thus methane is frequently used for CI as a reagent gas for the analysis of hydrocarbons.

As an example for the detection of impurities in methane, let us consider contamination by propane. Electron irradiation of the bulk of methane leads to the formation of approximately equal amounts of CH_3^+ and CH_4^+ as primary ions, which react with methane to produce C_2H_5^+ and CH_5^+ as shown in reactions (7.2) and (7.3). As $\text{PA}(\text{CH}_4)$ (543.5 kJ mol⁻¹) is lower than $\text{PA}(\text{C}_3\text{H}_8)$, the PTR $\text{CH}_5^+ + \text{C}_3\text{H}_8 = \text{CH}_4 + \text{C}_3\text{H}_9^+$ takes place with capture collision rate. The protonated propane C_3H_9^+ is unstable and C_3H_7^+ is formed by the following unimolecular dissociation reaction, $\text{C}_3\text{H}_9^+ = i\text{-C}_3\text{H}_7^+ + \text{H}_2$. In contrast, the proton transfer reaction $\text{C}_2\text{H}_5^+ + \text{C}_3\text{H}_8 = \text{C}_2\text{H}_4 + \text{C}_3\text{H}_9^+$ does not take place because $\text{PA}(\text{C}_3\text{H}_8)$ (625.7 kJ mol⁻¹) is smaller than $\text{PA}(\text{C}_2\text{H}_4)$ (680.5 kJ mol⁻¹). However, the hydride ion transfer reaction, $\text{C}_2\text{H}_5^+ + \text{C}_3\text{H}_8 = \text{C}_2\text{H}_6 + i\text{-C}_3\text{H}_7^+$, readily takes place. Thus, $i\text{-C}_3\text{H}_7^+$ is only the terminal product ion for methane-containing propane. As described above, the thermochemical values are indispensable for the analysis of any types of ion/molecule reactions.

7.3.6 Thermochemical Stabilities of Cluster Ions

Cluster ions may be regarded as the intermediate states between isolated ions in the gas phase and solvated ions in solution. Therefore, they give us the information that bridges the gap between the gas and condensed phases. When the number of solvent molecules in the cluster ion is increased to infinity, this corresponds to the ions solvated in solution.

Regardless of whether the clusters are neutral or ionic, clustering reactions are always exothermic ($\Delta H^\circ \leq 0$). This originates from the ion–molecule or neutral–neutral attractive interactions (e.g., ion–dipole, ion-induced dipole, hydrogen-bond, and van der Waals interactions). As shown in (7.28)–(7.30), the clustering reactions are observed only at relatively high pressure where the third-body collisions become efficient. If the pressure in the ion source is below mTorr (0.1 Pa), the rates of the clustering reactions become too small to be observed because they are proportional to the pressure of the third body M (7.11). CI and APCI reactions occur at ion source pressure higher than a few Torr, and the clustering reaction (7.75) is generally observed in these processes:



Here, M is a third body, and S is the solvent molecule. Reaction (7.77) is a displacement reaction, in which a solvent molecule S is exchanged with a reactant molecule B. This reaction proceeds without the third-body collision (i.e., second-order reaction) and can thus take place even at low-pressure in the ion source. Because the heat of reaction (7.77) can dissipate as translational energy of each of the products $A^\pm S_{n-1} B$ and S, the reactions take place with capture collision rates.

Some thermodynamic data for the typical clustering reactions are listed in Table 7.5 (for more comprehensive data, see URL <http://webbook.nist.gov/chemistry/>). The values shown in the upper and lower columns correspond to the enthalpy changes ($-\Delta H^\circ$ (kJ mol⁻¹)) and entropy changes ($-\Delta S^\circ$ (J mol⁻¹ K⁻¹)), respectively, for the clustering reactions. From these values, detailed information on the structures and the stabilities of cluster ions is obtained. The following list presents a number of examples.

- The ions H_3^+ [72–74], CH_5^+ [75], and $C_2H_5^+$ [57] have the nonclassical three-center–two-electron bonds.
- The cluster ion of H_3^+ with eight H_2 molecules, $H_3^+(H_2)_8$, has the shell structure described as $H_3^+(H_2)_3(H_2)_3(H_2)_2$, namely, the three apexes and three sides of the core triangular H_3^+ ion interact with three H_2 molecules each and the other two H_2 molecules interact with the H_3^+ core ion from upper and lower sides [72].
- The cluster ion of N_2^+ with N_2 molecules, $N_2^+(N_2)_n$, has the core ion N_4^+ , which has the covalent bond with the linear D_{2h} symmetry [76].
- The cluster ions of O_2^+ and O_2^- ions with O_2 molecules form the shell structures represented as $(O_2)_3^+(O_2)_n$ and $(O_2)_2^-(O_2)_n$, respectively [77].
- The cluster ions of O_2^+ with N_2 molecules have the shell structures of the type $O_2^+(N_2)_4(N_2)_n$, in which the four π^* lobes of O_2^+ interact with four N_2 ligands [78].
- Rare gas (Rg) cluster ions have the shell structure of $Rg_3^+(Rg)_n$, and the positive charge in core ion Rg_3^+ is delocalized in the linear Rg_3^+ [79, 80].

Table 7.5 Thermochemical value for cluster ion

Cluster ion	$n = 1$	$n = 2$	$n = 3$	$n = 4$	$n = 5$	$n = 6$	$n = 7$	$n = 8$	$n = 9$
$\text{H}_3^+(\text{H}_2)_n$	28.8 72.7	13.8 72.7	13.2 77.3	7.2 74.8	6.9 79	6.4 83.6	3.7 69	3.3 74.8	2.5 79.8
$\text{N}_2^+(\text{N}_2)_n$	107.8 87.8	11.5 62.7	11.3 66.0	10.6 69.4	10.3 85.7	9.5 90.7	8.5 85.3	7.8 80.7	7.4 86.5
$\text{O}_2^+(\text{N}_2)_n$	20.9 72.7	18.8 79.8	17.6 81.9	16.7 94.1	11.3 67.7	10.2 67.3	9.4 77.3	8.8 80.6	7.8 79.8
$\text{He}^+(\text{He})_n$	227.8 –	15.6 74	2.7 53.5	2.0 45.1					
$\text{NO}^+(\text{NO})_n$	59.4 96.1	53.5 154.7	15.9 79.4	23.8 133.8	14.6 104.5	17.1 125.4	12.5 96.1	15.5 112.9	12.1 83.6
$\text{H}_3\text{O}^+(\text{H}_2\text{O})_n$	146.3 126.2	84.4 98.6	74.8 118.7	53.1 97.8	48.5 104.5	44.7 109.1			
$\text{CH}_3\text{OH}_2^+(\text{CH}_3\text{OH})_n$	115.4 122.9	82.8 114.1	58.9 104.9	48.5 96.1	41.0 86.5	37.2 84.4			
$\text{H}^+(\text{CH}_3\text{COCH}_3)$ $(\text{CH}_3\text{COCH}_3)_n$	123.7 122.5	51.0 96.1	35.5 71.1						
$\text{H}^+(\text{C}_2\text{H}_5\text{OH})(\text{H}_2\text{O})_n$	100.0 109	80.3 117	59.4 109	52.3 109	– –	54.8 117			
$t\text{-C}_4\text{H}_9^+(\text{H}_2\text{O})_n$	46.8 92	– –	74.0 121	58.0 120					
$\text{Li}^+(\text{H}_2\text{O})_n$	142 96	109 88	88 105	67 125	59 130	50 134			
$\text{Na}^+(\text{H}_2\text{O})_n$	100 92	84 92	67 92	59 105	50 117	46 109			
$\text{K}^+(\text{H}_2\text{O})_n$	71 83	67 100	54 96	50 105	46 105	42 109			
$\text{Rb}^+(\text{H}_2\text{O})_n$	67 88	59 92	50 100	46 105	42 105				
$\text{Cs}^+(\text{H}_2\text{O})_n$	59 81	50 92	46 100	44 105					
$\text{F}^-(\text{H}_2\text{O})_n$	97.4 76	80.2 93	64.0 96	58.1 111	51.4 109	45.6 104	43.5 109	46.8 130	46.4 137
$\text{Cl}^-(\text{H}_2\text{O})_n$	61.4 82	54.3 89	49.3 93	44.3 95	39.7 91	36.8 88			
$\text{Br}^-(\text{H}_2\text{O})_n$	48.9 61	48.5 75	47.7 94	46 110	45 119	43 118			
$\text{I}^-(\text{H}_2\text{O})_n$	43.1 64	39.7 74	38.5 85	38.5 99					
$\text{F}^-(\text{CO}_2)_n$	135.0 111.6	30.5 76.1	30.1 94.5	24.2 84.9	23.4 93.2	22.2 94.1	16.3 –		

Upper column, $-\Delta H^\circ(\text{kJ mol}^{-1})$; lower column, $-\Delta S^\circ(\text{J mol}^{-1} \text{K}^{-1})$

- (g) The cluster ions $\text{NO}^+(\text{NO})_n$ with even values of n are more stable than those with odd values of n , originating from the fact that the NO molecule has an unpaired electron, $\text{NO}\uparrow$ or $\text{NO}\downarrow$ (i.e., with the even-number ligands $(\text{NO})_{2n}$, unit pairs of $(\text{NO})_2$ are formed that are bound with the up and down spin electron pair formation, $(\text{NO}\uparrow\cdots\downarrow\text{NO})$; however, $(\text{NO})_{2n+1}$ has a single NO molecule with an unpaired electron and it is less stable than $\text{NO}^+(\text{NO})_{2n+2}$ [81]).
- (h) In the solvation reaction of protons, the protic solvents (e.g., H_2O and alcohols) form hydrogen bonds with the core proton and the bond energies for the cluster ions $\text{H}^+(\text{S})_n$ decrease only gradually with n . In contrast, the cluster ions of aprotic solvents (e.g., acetone, acetonitrile,

and dimethyl sulfoxide) form the stable proton-sandwich dimers $S \cdots H^+ \cdots S$, such as $H_3C-C \equiv N \cdots H^+ \cdots N \equiv C-CH_3$, and the bond energies of $H^+(S)_n$ show a sudden decrease in the value of n from 2 to 3 [82, 83].

- (i) The cluster ion $F^-(CO_2)_n$ forms a covalent bond at $n = 1$ to form the fluoroformate ion $FCOO^-$, and weak electrostatic bonds are formed with $n \geq 2$. In contrast, no covalent bond but only weak electrostatic bonds are formed in $Cl^-(CO_2)_n$ [84].

These are the only examples for the characteristic nature of the cluster ions [54].

The entropy change for the reaction, ΔS , is determined by the translational (ΔS_{tr}), rotational (ΔS_{rot}), and vibrational (ΔS_{vib}) terms, i.e.,

$$\Delta S = \Delta S_{tr} + \Delta S_{rot} + \Delta S_{vib}. \quad (7.78)$$

The electronic term ΔS_{el} is usually negligible. In ion–molecule clustering reactions, the translational entropy change has the largest contribution because the number of species changes from two to one in the clustering reaction, $A^+ + B \rightarrow [A^+ \cdots B]$, i.e., a large loss of the translational freedoms of motion occurs. The translational entropy S_{tr} ($J \text{ mol}^{-1} \text{ K}^{-1}$) for a molecule with the molecular mass M is given by the Sackur–Tetrode equation (7.79) derived from statistical mechanics,

$$S_{tr} = (R/2)(5 \ln T + 3 \ln M) - 9.66. \quad (7.79)$$

From (7.79), the entropy change ΔS_{tr} for the clustering reaction can be derived as (7.80), where M_i , M_s , and M_c are the molecular masses of the ion, the solvent molecule, and the cluster ion, respectively:

$$\Delta S_{tr} = \frac{3}{2}R \ln \frac{M_c}{M_i M_s} - \frac{5}{2}R \ln T + 9.66. \quad (7.80)$$

For example, by using (7.80), the ΔS_{tr} ($J \text{ mol}^{-1} \text{ K}^{-1}$) value for reaction $H_3^+ + H_2 = H_5^+$ at 300 K is calculated to be $-111 J \text{ mol}^{-1} \text{ K}^{-1}$. From Table 7.3, the value determined experimentally for ΔS is $-72.7 J \text{ mol}^{-1} \text{ K}^{-1}$. Therefore, $[\Delta S - \Delta S_{tr}] = [(-72.7) - (-111.0)] = +38.3 J \text{ mol}^{-1} \text{ K}^{-1}$ arises from $[\Delta S_{rot} + \Delta S_{vib}]$. The increase in entropy shown by the positive value for $[\Delta S_{rot} + \Delta S_{vib}]$ is caused by the newly formed weak bonds in the cluster ion, $H_3^+ \cdots H_2$. The weakly bound moieties in H_5^+ have several vibrational and rotational degrees of freedom of motion that contribute toward increasing the entropy change. When the strong bond is formed in the cluster ion, the ΔS values would have relatively large negative values in the range between -80 and $-120 J \text{ mol}^{-1} \text{ K}^{-1}$. In addition, when the cluster ions have geometries with high symmetry, the entropy changes also become more negative. The enthalpy and entropy changes in the formation of cluster ions reflect the thermochemical stabilities and structures of the cluster ions [54].

7.3.6.1 Water as a Solvent

Water has the highest solvation energy for protons among other solvents, that is, water is the best solvent for acids. However, the PA value of H_2O vapor is the smallest among all gas-phase oxygen- and nitrogen-containing organic compounds. How can we interpret this apparent contradiction? The small value of $PA(H_2O)$ in gas phase is caused by the “localization” of the positive charge in the three equivalent H atoms in H_3O^+ . When the H atom in H_2O is substituted by an alkyl group, the positive charge can be delocalized in the alkyl moiety (inductive effect) resulting in a drastic increase in PA values, e.g., $PA(H_2O) = 691 \text{ kJ mol}^{-1} \rightarrow PA(CH_3OH) = 754 \text{ kJ mol}^{-1}$ (see Table 7.3). The highly localized positive charge in H_3O^+ is closely related to the high hydration energy of proton in water

solvent. Because of the strong localization of the positive charge in the three H atoms, H_3O^+ can form strong hydrogen bonds with a very large number of H_2O molecules, resulting in an extended hydrogen bond network in $\text{H}_3\text{O}^+(\text{H}_2\text{O})_n$. The hydrogen bond energies in $\text{H}_3\text{O}^+(\text{H}_2\text{O})_n$ decrease only gradually with increasing n , resulting in high hydration energy for the proton in an aqueous H_2O . In fact, as shown in Table 7.5, the enthalpy changes (ΔH_n°) for $\text{H}_3\text{O}^+(\text{H}_2\text{O})_n$ are larger than those for $\text{CH}_3\text{OH}_2^+(\text{CH}_3\text{OH})_n$ for all n measured.

The gas-phase hydration reaction of protonated alcohol is one of the best examples to demonstrate that water is the best solvent for protons. In the gas-phase hydration reaction of protonated ethanol, $\text{C}_2\text{H}_5\text{OH}_2^+$ (see Table 7.5), the $\Delta H_{n-1,n}^\circ$ values reach minimum at $n = 4$ and the equilibrium could not be observed with $n = 4 \rightarrow 5$ [82] because of the occurrence of the intramolecular PTR at $n = 5$, $\text{C}_2\text{H}_5\text{OH}_2^+(\text{H}_2\text{O})_5 \rightarrow \text{H}_3\text{O}^+(\text{H}_2\text{O})_4(\text{C}_2\text{H}_5\text{OH})$. Although the value of $\text{PA}(\text{C}_2\text{H}_5\text{OH})$ ($776.4 \text{ kJ mol}^{-1}$) in the gas phase is considerably higher than $\text{PA}(\text{H}_2\text{O})$ (691 kJ mol^{-1}), the proton attached to the $\text{C}_2\text{H}_5\text{OH}$ in $\text{C}_2\text{H}_5\text{OH}_2^+(\text{H}_2\text{O})_5$ is transferred to the H_2O moieties because the PA value of $(\text{H}_2\text{O})_5$ ($1,050 \text{ kJ mol}^{-1}$) becomes higher than the $\text{PA}(\text{C}_2\text{H}_5\text{OH})$ ($776.4 \text{ kJ mol}^{-1}$).

Another example is the hydration of the protonated $t\text{-C}_4\text{H}_9\text{OH}$ [85]. As shown in Table 7.5, the bond energy of $t\text{-C}_4\text{H}_9^+\cdots\text{OH}_2$ is relatively small ($-\Delta H_{0,1}^\circ = 46.8 \text{ kJ mol}^{-1}$) because of the delocalization of the positive charge in $t\text{-C}_4\text{H}_9^+$. For the first step of the hydration of $t\text{-C}_4\text{H}_9\text{OH}_2^+$, the isomerization already takes place, $t\text{-C}_4\text{H}_9\text{OH}_2^+ + \text{H}_2\text{O} \rightarrow \text{H}_3\text{O}^+(\text{H}_2\text{O})(i\text{-C}_4\text{H}_8)$. This reaction is an example of acid-catalyzed dehydration reactions for alcohols to form alkenes, which are well known in organic chemistry.

7.3.6.2 Reactions of Cluster Ions

In CI and APCI experiments, the cluster ions $\text{A}^\pm(\text{S})_n$ frequently appear in the mass spectra, in particular when polar gases are used as reagent gases. For example, when the selected reagent gas is H_2O or NH_3 , the reactant ions that participate in CI or APCI are usually the cluster ions $\text{H}_3\text{O}^+(\text{H}_2\text{O})_n$ or $\text{NH}_4^+(\text{NH}_3)_n$, but not the nonsolvated reactant ion, H_3O^+ or NH_4^+ . In the following, the roles of the cluster ions in CI and APCI are described.

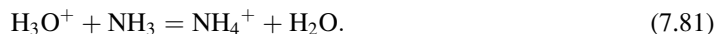
The data in Table 7.5 show the cluster ions $\text{H}_3\text{O}^+(\text{H}_2\text{O})_n$ gaining in bond energy with increasing n , e.g., the PA values of $(\text{H}_2\text{O})_n$ increase for $n = 1, 2, 3, 4$, and 5 as $691.0, 691.0 + 146.3 = 837.3, 837.3 + 84.4 = 921.7, 921.7 + 74.8 = 996.5$, and $996.5 + 53.1 = 1,049.6 \text{ kJ mol}^{-1}$. The value of $\text{PA}[(\text{H}_2\text{O})_2]$ is $837.3 \text{ kJ mol}^{-1}$, which is only slightly smaller than that of $\text{PA}[\text{NH}_3]$, $854.6 \text{ kJ mol}^{-1}$. However, this does not necessarily mean that $\text{H}_3\text{O}^+(\text{H}_2\text{O})$ cannot protonate the oxygen-containing organic compounds like alcohols and acetone (see Table 7.3). The cluster ions $\text{H}_3\text{O}^+(\text{H}_2\text{O})_n$ can ionize these analyte molecules indirectly by a substitution reaction (7.77). For example, a trace amount of acetone can be ionized by the substitution reaction, $\text{H}_3\text{O}^+(\text{H}_2\text{O}) + (\text{CH}_3)_2\text{CO} = (\text{CH}_3)_2\text{COH}^+(\text{H}_2\text{O}) + \text{H}_2\text{O}$. Since the heat of the substitution reaction is dissipated as translational (i.e., kinetic) energies of the products, reaction (7.77) occurs without fragmentation. In addition, the analyte with the molecular mass of M_A is observed as the mass of the cluster ion plus M_A , and thus the clustering reactions are useful for determination of the molecular masses of the analytes.

All the clustering reactions are exothermic and accompany the decrease in the number of reacting species from two to one. Therefore, according to Le Chatelier's law, the equilibrium conversion should increase at lower temperature and at higher pressure. In fact, the relative intensities of cluster ions $\text{A}^\pm(\text{S})_n$ observed in CI and APCI are highly dependent on the ion source temperature. Let us assume that the carrier gas (e.g., CH_4 , N_2 , etc.) containing water vapor at 1 mTorr is used as the reagent gas; the water vapor will then produce the reactant ions $\text{H}_3\text{O}^+(\text{H}_2\text{O})_n$. The n distribution of $\text{H}_3\text{O}^+(\text{H}_2\text{O})_n$ at equilibrium can be calculated using the thermodynamic values listed in Table 7.5. The n distribution of $\text{H}_3\text{O}^+(\text{H}_2\text{O})_n$ at 100°C will be calculated as an example. The values of $-\Delta H^\circ$

and $-\Delta S^\circ$ are $146.3 \text{ kJ mol}^{-1}$ and $126.2 \text{ J mol}^{-1} \text{ K}^{-1}$, respectively, for the equilibrium reaction, $\text{H}_3\text{O}^+ + \text{H}_2\text{O} \rightleftharpoons \text{H}_3\text{O}^+(\text{H}_2\text{O})$ (see Table 7.5). Thus, $-\Delta G^\circ = -\Delta H^\circ + T\Delta S^\circ = 146,300 - 373 \times 126.2 = 99,227 \text{ J mol}^{-1} = RT \times \ln K = 8.31 \times 373 \times \ln K$. From this relation, $K = 8.0 \times 10^{13}$ is obtained. The gas-phase equilibrium constant K is defined as the “pressure equilibrium constant.” By substituting the value of the $P(\text{H}_2\text{O}) = 10^{-3}/760 \text{ atm}$ in $K = \{I[\text{H}_3\text{O}^+]/I[\text{H}_3\text{O}^+(\text{H}_2\text{O})]\}/P(\text{H}_2\text{O})$, the ratio of $I[\text{H}_3\text{O}^+]:I[\text{H}_3\text{O}^+(\text{H}_2\text{O})_1]$ is obtained as $1:1.1 \times 10^8$. In the same way, the ratios of $\text{H}_3\text{O}^+(\text{H}_2\text{O})_n$ at 100°C are calculated as $[\text{H}_3\text{O}^+]:[\text{H}_3\text{O}^+(\text{H}_2\text{O})]:[\text{H}_3\text{O}^+(\text{H}_2\text{O})_2]:[\text{H}_3\text{O}^+(\text{H}_2\text{O})_3]:[\text{H}_3\text{O}^+(\text{H}_2\text{O})_4] = 1:1.1 \times 10^8:3.4 \times 10^{13}:8.5 \times 10^{11}:2.4 \times 10^8$. Namely, the cluster ion $\text{H}_3\text{O}^+(\text{H}_2\text{O})_2$ is by far the most abundant and acts as a major reactant ion in CI and APCI at 100°C .

By increasing the ion source temperature from 100 to 300°C , the ratio changes drastically as $[\text{H}_3\text{O}^+]:[\text{H}_3\text{O}^+(\text{H}_2\text{O})]:[\text{H}_3\text{O}^+(\text{H}_2\text{O})_2]:[\text{H}_3\text{O}^+(\text{H}_2\text{O})_3]:[\text{H}_3\text{O}^+(\text{H}_2\text{O})_4] = 1:7.4:3.41 \times 10^{-3}:1.9 \times 10^{-8}:4.6 \times 10^{-14}$. Thus, the major reactant ions are H_3O^+ and $\text{H}_3\text{O}^+(\text{H}_2\text{O})$ at 300°C . This marked temperature dependence in clustering reaction originates from the term of $T\Delta S^\circ$ in equation, $-\Delta G^\circ = RT \ln K = -\Delta H^\circ + T\Delta S^\circ$. As described above, the ion source temperature is one of the most important experimental parameters in CI and APCI.

Reaction (7.81) is exothermic by 163 kJ mol^{-1} and it proceeds by the capture collision rate:



The H_2O molecule has a large dipole moment of 1.84 D , and for this reason it often combines with NH_4^+ to form the cluster ion $\text{NH}_4^+(\text{H}_2\text{O})$ at m/z 36. The chloride ion Cl^- can be also used as a useful reactant ion because it forms cluster ions with various analyte molecules [54].

The reactant ion NO^+ abstracts the hydride ions from hydrocarbons to form $[\text{M}-\text{H}]^+$ and also adds to the olefins followed by elimination of small neutral alkene molecules to give the series of ions $\text{C}_n\text{H}_{2n}\text{NO}^+$ [27, 28].

When the reagent gas containing water vapor is ionized under the ambient conditions and introduced into the vacuum through a fine orifice, a series of cluster ions $\text{H}_3\text{O}^+(\text{H}_2\text{O})_n$ with a broad n distribution are often observed. This originates from the formation of a gas jet stream when the high-pressure gas expands into vacuum. In the gas jet stream, the faster molecules hit the slower ones and they ultimately have about the same velocity during the multiple collisions occurring in the jet stream. The convergence of the relative velocities results in cooling of the gas temperature, down to about $\sim 10 \text{ K}$, which in turn causes large-size cluster ions to readily form. The various types of the nozzles for the formation of large clusters such as the Laval nozzle were developed.

7.4 The Practice of CI and APCI

7.4.1 Trace Analysis

By using PTRs with rather small values of heat of reaction (i.e., less exothermic), CI with little fragmentation can be achieved. However, trace analysis requires the selection of more exothermic reactions.

Let us consider the detection of 1 ppm B in the reagent gas A , i.e., $([\text{B}]/[\text{A}] = 10^6)$. When 1% AH^+ is converted to BH^+ at equilibrium $([\text{BH}^+]/[\text{AH}^+] = 0.01)$ in a PTR such as $\text{AH}^+ + \text{B} \rightleftharpoons \text{BH}^+ + \text{A}$, the free energy change obtained at 200°C is $-\Delta G^\circ (\approx -\Delta H^\circ) = RT \times \ln K = 8.31 \times 473 \times \ln(10^{-2} \times 10^6) = 36.2 \text{ kJ mol}^{-1}$ (ΔS° is assumed to be negligible in this reaction).

This indicates that to form abundant BH^+ , the exothermicity of the reaction should not be less than 36 kJ mol^{-1} . In other words, a more exothermic PTR should be selected for the ultra-trace analysis, at the ppb and ppt levels.

7.4.2 Positive- and Negative-Mode PTRs for CI and APCI

In the positive-mode PTR (7.54), the fragmentation of the product ion B_2H^+ becomes dominant with increasing reaction exothermicity. In contrast, the negative-mode PTR (7.60) is much milder than the one in positive mode (7.54) and the fragmentation of the product A_2^- is seldom observed even if the reaction is highly exothermic:



When an exothermic PTR proceeds through a short-lived ion–molecule intermediate complex, the energy liberated remains largely in the product containing the newly formed bond [86]. In reactions (7.54) and (7.60), the bonds in B_2H^+ and A_1H are newly formed, and therefore, B_2H^+ in reaction (7.54) is vibrationally excited and fragmentation takes place. In reaction (7.60), however, the neutral A_1H is excited, but the product ion A_2^- is not. This is the reason that soft ionization takes place in negative-mode PTRs. By selecting highly reactive reactant ions such as OH^- , many compounds can be ionized as deprotonated ions of the type $(\text{M}-\text{H})^-$ without any fragmentation (see Sect. 3.4).

7.4.3 Collision Frequencies and Half-Lives of Reactant Ions

The average number of ion collisions with neutral gas molecules per unit time (collision frequency $\nu(\text{s}^{-1})$) is given by the product of the rate constant of the ion/molecule reaction $k(\text{cm}^3/\text{s})$ and the number density of the gas molecules $n(\text{cm}^{-3})$:

$$\nu(\text{s}^{-1}) = k \times n \quad (7.82)$$

Here, the number density of gas molecules at temperature $T(\text{K})$ is given by (7.83):

$$n(\text{cm}^{-3}) = 9.659 \times 10^{18} P(\text{Torr})/T(\text{K}) \quad (7.83)$$

For example, the values of $\nu(\text{s}^{-1})$ for the ion at 5 and 760 Torr (1 atm) buffer gases at 300 K are calculated to be about 10^8 and 10^{10} s^{-1} , respectively.

When the number density of the reactant ion is much lower than that of analyte molecules, reactions can be regarded as pseudo-first order with respect to the reactant ion concentration. In such a case, the half-life of reaction ($\tau_{1/2}$, the time for the reactant ion to fall to half its initial concentration) can be expressed as (7.84)

$$\tau_{1/2}(\text{s}) = \ln 2/k \times n = 0.693/k \times n \quad (7.84)$$

For example, for 1 ppm sample gas analyte in 5 and 760 Torr, the $\tau_{1/2}$ values are, respectively, calculated to be 4×10^{-3} and $3 \times 10^{-5} \text{ s}$. For the CI experiments with sample gas at 5 Torr,

the residence time of ions in the standard-size ion source is about a few ms with no electric field applied (only diffusive loss to the wall), meaning that only about a half of the reactant ions are available to participate in the ionization of the analyte. Moreover, if an electric field is applied in the ion source, the ion residence time becomes much shorter, resulting in a decrease in ionization efficiency.

On the other hand, in APCI, the diffusion of the reactant ions to the wall of the ion source becomes much slower than in CI and the reactant ions can react with the 1 ppm analytes with probability of ~ 1 . Thus in general APCI is more sensitive than CI and analytes at ppb or even ppt level can be detected by APCI.

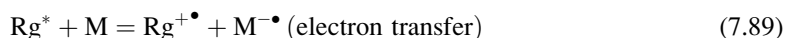
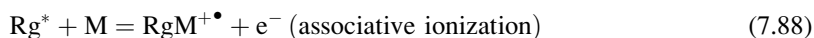
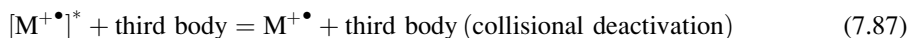
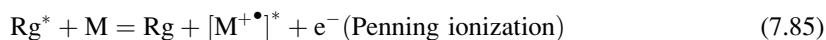
If the sample gas is composed of several components with different PA values, the analyte with the highest PA value is likely to be the final product ion, meaning that the ion intensities observed in the CI and APCI mass spectra do not reflect the relative concentrations of the analytes. For a quantitative analysis by means of CI and APCI, the use of internal standards is recommended.

In EI, dealing with the sample gas pressure of $\sim 10^{-5}$ Torr, the ions produced are directly detected without any collisions with neutral gas molecules. Therefore, the ion abundance observed in EI reflects the partial pressure of the sample gas, making EI the most reliable ionization method for quantitative as well as qualitative analysis. The drawback of EI is that it is restricted to vaporizable samples and that multicomponent sample gases are difficult to deal with. In this respect, the coupling of EI with gas chromatography (i.e., GC/MS) is a very good solution.

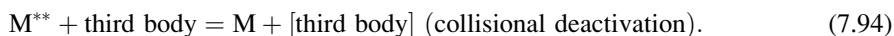
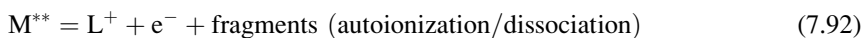
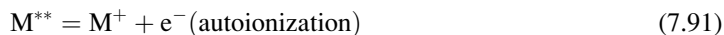
7.4.4 Penning Ionization and Related Ionization Methods

The Penning ionization refers to the interaction between a gas atom in an electronically excited state and a target molecule M. In analytical chemistry, electronically excited Rg atoms are often used for Penning ionization. The excitation energies for Rg* are He* (3S_1 : 19.8 eV), Ne* (3P_0 : 16.7 eV, 3P_2 : 16.6 eV), Ar* (3P_0 : 11.7 eV, 3P_2 : 11.6 eV), and Kr* (3P_0 : 10.6 eV, 3P_2 : 9.9 eV). All of these electronic states have long lifetimes for the optical transition because they are optically forbidden and the radiative lifetimes of Rg* are tens of seconds [87]. Because of their long lifetimes, the Rg* atoms can accumulate in the plasma source and reach high concentration, and this can lead to the very high ionization efficiencies using Penning ionization.

When the excitation energy of a metastable Rg* atom is higher than the ionization energy of the analyte molecule, various Rg*-quenching processes can take place [88] as follows:



where $[M^{+}]^*$ denotes the nascent rovibronically (i.e., rotationally, vibrationally, and electronically) excited state formed by the direct Penning ionization. The excited state M^{**} formed by reaction (7.90) is called “superexcited state” because the internal energy of M^{**} is higher than the ionization energy of M . The superexcited M^{**} has several quenching channels, as follows:



The branching ratios of reactions (7.91)–(7.94) are largely unexplored. The Penning ionization (7.85) is a Franck–Condon-controlled ionization processes, in which the electron can remove excess energy as kinetic energy [89], whereas reactions (7.86), (7.89), and (7.90) have the characteristic feature of the interaction of long-range, diabatic crossing of the covalent entrance channel and the intermediate complexes with the nature of ion-pair formation, making it very difficult to determine the individual fractions of various Rg^* -quenching processes. The fractions of these reaction channels are strongly dependent on the specific excited states of Rg^* , as well as on the target molecules [90].

Investigation on superexcited states dates back to 1962 when Platzman considered theoretically the interactions of ionizing radiation with atoms and molecules [91–93].

He pointed out the following important features, although very few experimental data were available at that time [93].

- (a) The values of an oscillator strength distribution show generally its maximum at the energy of 10–30 eV, which is larger than the first ionization energy.
- (b) Quantum yield for ionization values of molecules (η)

$$\eta(E) = \sigma_i(E)/\sigma_t(E) \quad (7.95)$$

is much smaller than unity in the energy range just above IE, where $\sigma_i(E)$ and $\sigma_t(E)$ are, respectively, the photoionization cross section and photoabsorption cross section.

- (c) There exists a hydrogen isotope effect in η values.

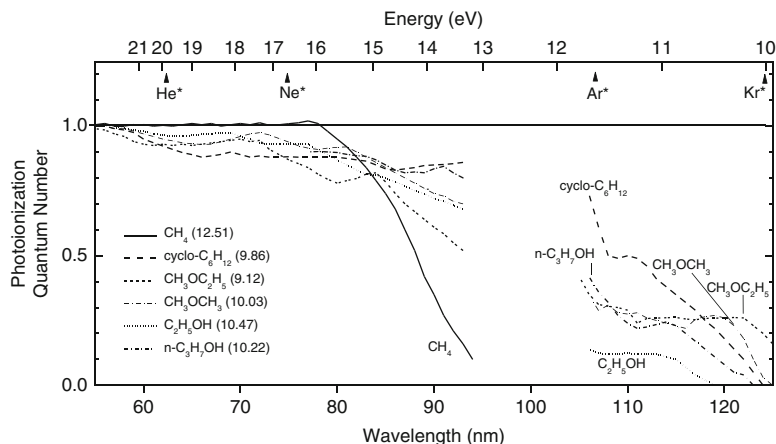
By combining all available information, (a)–(c), Platzman indicated an important role of superexcited states in reactions (7.91), (7.92), and (7.93).

When a molecule M receives energy which is larger than its IE, M may be directly ionized (7.85) and may also be excited (7.90) to form M^{**} which was named by Platzman a “superexcited” molecule. The superexcited M^{**} can ionize (7.91, 7.92) or dissociate into neutral fragments (7.93). Since η is defined by $(\eta - 95)$, the value of $[1 - \eta]$ shows the importance of the neutral dissociation processes in the total decay channels of M^{**} . The Platzman’s concept of the superexcited state has made a profound influence on the science of excited states and motivated researches in a wide field, such as radiation chemistry, photochemistry, upper-atmospheric phenomena, astronautical science, nuclear fusion, plasma science and technology, etc.

Figure 7.7 shows the ionization quantum yields of some molecules measured in the photon wavelength region of 54–92 nm together with those in the wavelength region longer than 105 nm measured by Hatano et al. [93]. No data are shown in the wavelength region between the two because appropriate optical windows were not available.

The results shown in Fig. 7.7 may be summarized as follows [93].

Fig. 7.7 Photoionization quantum yields of several molecules in the wavelength regions shorter and longer than the LiF window cutoff at 105 nm. Data were obtained by using synchrotron orbit radiation. The numbers in brackets are ionization energies (IEs) of molecules. (Reproduced with permission from [93])



1. η -Values in the region above, but close to, the first ionization energies are much less than unity, which means that most molecules, at least the molecules shown in Fig. 7.7, are not easily ionized even they have just sufficient amounts of their internal energies. In this region, therefore, neutral fragmentation of M^{**} is of great importance in the total decay channels expressed by process (7.93).
2. η -Values do not reach unity even in the energy range more than about 10 eV above the first ionization energy.
3. η -Values increase with increasing photon energy and reach unity in the absolute scale at the energy range above about 23 eV (or 54 nm).

It is apparent that nonionizing processes of M^{**} play very important roles in their decay channels.

Reactions (7.88) and (7.89) also play important roles when M is electronegative [89]. For example, the reactive quenching that produces the rare gas halide molecules RgX^* (or excited halogen atoms from predissociation of RgX^*) can be a major exit channel for halogen-containing molecules [89]. The contribution of each reaction channel to the total quenching often differs characteristically for different processes, as is the particular role of each excited atom.

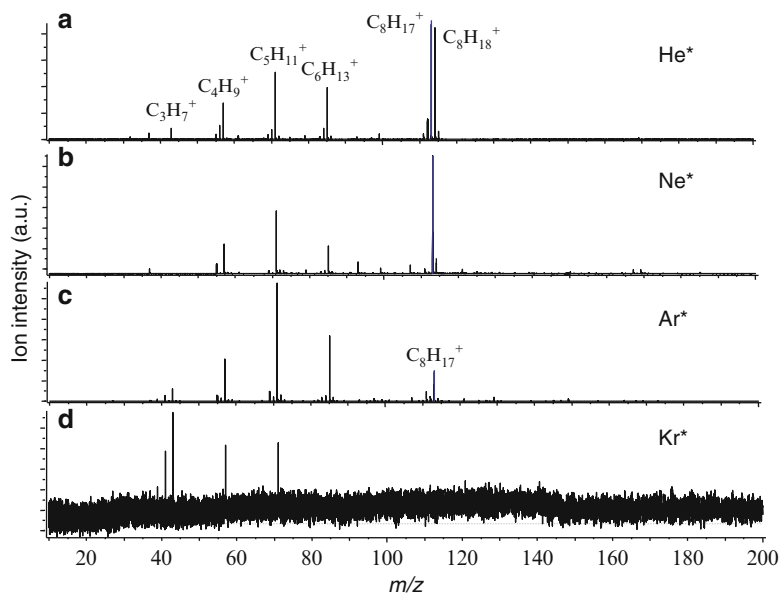
In 1993, Bertrand et al. developed the metastable atom bombardment (MAB) method [94]. They applied Penning ionization at reduced pressure ($\sim 5 \times 10^{-4}$ Torr) for an “energy-tunable rare gas metastable beam source generated by a corona discharge as an ion source for mass spectrometry.” This beam source was found to provide sensitivities of the same order as those obtained by EI.

Ionization methods that operate under atmospheric pressure, such as ESI and atmospheric-pressure-MALDI, are now indispensable techniques for measuring nonvolatile organic compounds. These methods, however, have the disadvantage of being less sensitive to less polar compounds (e.g., hydrocarbons). In 1984, Tsuchiya et al. first applied atmospheric-pressure Penning ionization in the study of liquid ionization mass spectrometry [95, 96]. This method utilizes Ar^* to ionize liquid films on the tip of a metal needle at atmospheric pressure. It is also applicable to the analysis of the samples that contain either polar or even nonpolar organic compounds.

Figure 7.8 shows the atmospheric-pressure Penning ionization mass spectra [88] for n-octane using He^* , Ne^* , Ar^* , and Kr^* as ionizing reagents [88].

In this experiment, a 0.2 μ L n-octane was injected into a gas chromatograph with a 30 m long DB-5MS column at 200 $^{\circ}$ C using He carrier gas at a flow rate of 1 mL min^{-1} . The sample vapor flowing out of the gas chromatograph was introduced into the APCI ion source in which the dc-corona discharge excited reagent Rg (He , Ne , Ar , and Kr) was supplied with 500 mL min^{-1} . In Fig. 7.8, the molecular ion $C_8H_{18}^+$ was only observed as a major ion for He^* . This clearly indicates that the

Fig. 7.8 Atmospheric-pressure Penning ionization mass spectra obtained by using He*, Ne*, Ar*, and Kr* as ionizing reagents. The excitation energies for Rg* are He* (3S_1 : 19.8 eV), Ne* (3P_0 : 16.7 eV, 3P_2 : 16.6 eV), Ar* (3P_0 : 11.7 eV, 3P_2 : 11.6 eV), and Kr* (3P_0 : 10.6 eV, 3P_2 : 9.9 eV). IE of n-octane is 9.8 eV. (Reproduced with permission from [88])

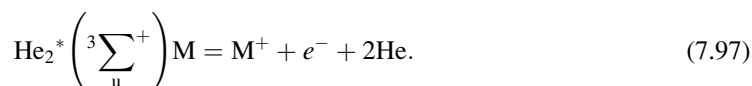


process of the direct Penning ionization (7.85) prevails for He*. In contrast, the ion $C_8H_{17}^+$ is much stronger than $C_8H_{18}^+$ for Ne* and Ar*. This suggests that processes (7.86) and/or (7.92) become more likely for Ne* and Ar*. In addition, the total ion intensities (relative η -values) were found to be in the order He > Ne \approx Ar > Kr [88]. This clearly indicates that the role of superexcited states (i.e., the neutral fragmentation processes (7.93)) becomes more important with decreasing internal energies of Rg*. The same trend is observed in Fig. 7.7.

For Penning ionization mass spectrometry at atmospheric pressure and ambient [97–103], a rare gas plasma source is generally used. In general, Rg* species are thought to be the ionizing reagent in Penning ionization, as shown in reaction (7.85). However, the long-life Rg* atom generated in plasma at atmospheric pressure collides with neutral Rg atoms ($\sim 10^{10} \text{ s}^{-1}$) and therefore there should be an ample chance to form the excited dimer (excimer) via three-body collisional deactivation processes of the type described in (7.96) [104]:



The binding energy of the strongly bound excited dimer $He_2^*(^3\Sigma_u^+)$ (triplet excimer) is reported to be 2.0 eV [87], and it should have sufficient stability in Rg at atmospheric pressure. However, the internal energy of this excimer, which is available for Penning ionization, equals the internal energy of He* 2^3S_1 (19.5 eV) less the bond energy of $He_2^*(^3\Sigma_u^+)$, i.e., $19.5 - 2.0 = 17.5$ eV. This value is still much higher than the ionization energies of all the atoms and molecules, making it possible to ionize them readily:



In the case of Ar, the bond energy of the triplet excimer Ar_2^* is about 0.7 eV [87]. Thus, the internal energy of Ar_2^* is lower than that of $Ar^*(^3P)$ (11.5 eV): $11.5 - 0.7 = 10.8$ eV. Under typical

experimental conditions, e.g., 1 atm Ar pressure, and 400 K plasma source temperature, the ratio of $[\text{Ar}_2^*]/[\text{Ar}^*]$ is estimated thermochemically to be $\sim 7,000$ [104]. This suggests that Ar_2^* as well as Ar^* must play a major role in Ar Penning ionization. For Ar_2^* , the internal energy of 10.8 eV is available for the Penning ionization of the species that have ionization energies lower than 10.8 eV. A comprehensive survey of the recent ambient ionization methods is available in [105].

References

1. Thomson JJ (1912) *Phil Mag* 24:209
2. Eyring H (1957) as quoted by Handler GS, Arnold JR, *J Chem Phys* 27:144
3. Tal'rose VL, Lyubimova AK (1952) *Dokl Akad Nauk SSSR* 88:909
4. Stevenson DP, Schissler DO (1955) *J Chem Phys* 23:1353
5. Munson MSB, Field FH (1965) *J Am Chem Soc* 87:3294
6. Munson MSB, Field FH (1966) *J Am Chem Soc* 88:2621
7. Gross JH (2011) *Mass spectrometry, a textbook*, 2nd edn. Springer, Berlin
8. Kebarle P (1977) *Ann Rev Phys Chem* 28:445
9. Rothe EW, Bernstein RB (1959) *J Chem Phys* 31:1619
10. LeFevre RJW (1959) *Advan Phys Org Chem* 3:1
11. Nelson RD Jr, Lide DR Jr, Maryott AA (1967) *NSRDS-NBS* 10
12. McLellan AL (1963) *Tables of experimental dipole moment*. Freeman WH, San Francisco, CA
13. Langevin P (1905) *Ann Chim Phys* 5:276
14. Gioumousis GG, Stevenson DP (1958) *J Chem Phys* 29:294
15. Su T, Bowers MT (1973) *Int J Mass Spectrom Ion Phys* 12:347
16. Bass L, Su T, Chesnavich WJ, Bowers MT (1975) *Chem Phys Lett* 34:119
17. Su T, Bowers MT (1975) *Int J Mass Spectrom Ion Phys* 17:309
18. Chau M, Bowers MT (1977) *Int J Mass Spectrom Ion Phys* 24:191
19. Lindholm E (1972) In Franklin JL (ed) *Ion-molecule reactions*, vol 2, Plenum Press, New York, p 457.
20. Horning EC, Horning MG, Carroll DI, Dzidic I, Stillwell RN (1973) *Anal Chem* 45:936
21. Horning EC, Horning MG, Carroll DI, Stillwell RN, Dzidic I (1973) *Life Sci* 13:1331
22. Munson B (1977) *Anal Chem* 49:772A
23. Einolf N, Munson B (1972) *Int J Mass Spectrom Ion Phys* 9:141
24. Hunter DF, Ryan JF (1972) *J Chem Soc Chem Commun* 620.
25. Jelus BL, Munson B, Fenslau C (1974) *Biomed Mass Spectrom* 1:96
26. Hunt DF, McEwen CN, Harvey TM (1975) *Anal Chem* 47:1730
27. Hunt DF, Harvey TM (1975) *Anal Chem* 47:1965
28. Hunt DF, Harvey TM (1975) *Anal Chem* 47:2136
29. Meot-Ner M, Field FH (1975) *J Am Chem Soc* 97:2014
30. Olah GA (1973) *Carbocations and electrophilic reactions*. Wiley, New York
31. Meot-Ner M, Field FH (1976) *J Chem Phys* 64:277
32. Meot-Ner M, Field FH (1978) *J Am Chem Soc* 100:1356
33. Cunningham AJ, Payzant JD, Kebarle P (1972) *J Am Chem Soc* 94:7627
34. Lau YK, Ikuta S, Kebarle P (1982) *J Am Chem Soc* 104:1462
35. Harrison AG (1975) In Ausloos P (ed) *Interactions between ions and molecules*, Plenum Press, New York, p 263
36. Good A (1975) *Chem Rev* 75:561
37. Bohme DK, Dunkin DB, Fehsenfeld FC, Ferguson EE (1968) *J Chem Phys* 49:5201
38. Meot-Ner M, Field FH (1975) *J Am Chem Soc* 97:5339
39. Olmstead WN, Lev-On M, Golden DM, Brauman JI (1977) *J Am Chem Soc* 99:992
40. Neilson PV, Bowers MT, Chau M, Davidson WR, Aue DH (1978) *J Am Chem Soc* 100:3649
41. Hatano Y (1986) In Lorents DC, Meyerhof WE, Peterson JR (ed) *Electronic and atomic collisions*, Elsevier Science Publications, p 153
42. Christophorou LG (1971) *Atomic and molecular radiation physics*, Wiley, New York, p 491
43. Smirnov BM (1982) *Negative ions*. McGraw-Hill, New York
44. Bohme DK, Mackay GI, Payzant JD (1974) *J Am Chem Soc* 96:4027
45. Payzant JD, Tanaka K, Betowsky LD, Bohme DK (1976) *J Am Chem Soc* 98:894
46. Olmstead WN, Brauman JI (1977) *J Am Chem Soc* 99:4219
47. Lias SG, Ausloos P (1975) *Ion-molecule reactions*, Am Chem Soc, Washington, DC

48. Ferguson EE (1973) *Atom Data Nucl Data Tables* 12:159
49. Sieck LW, Lias SG (1976) *J Phys Chem Ref. Data* 5:1123
50. Albritton DL (1978) *Atom Data Nucl Data Tables* 22:1
51. Ikezoe Y, Matsuo S, Takebe M, Viggiano A (1987) Gas phase ion-molecule reaction rate constants through 1986, Maruzen
52. Lias S, Bartmess JE, Liebman JF, Holmes JL, Levin RD, Mallard G (1988) Gas-phase ion and neutral thermochemistry. *J Phys Chem Ref Data* 17(Suppl 1): 1–861
53. Kebarle P (1988) Pulsed electron high pressure mass spectrometer, In Farrar JM, Saunders WH Jr (eds) *Techniques for the study of ion-molecule reactions, techniques of chemistry volume XX*, Wiley, New York
54. Hiraoka K, Yamabe S (1994) Gas-phase cluster ions: stability, structure, and solvation. In: Kuchitsu K (ed) *Dynamics of excited molecules*. Elsevier, Amsterdam
55. Lau YK, Kebarle P (1976) *J Am Chem Soc* 98:7452
56. Hunter EP, Lias SG (1998) Evaluated gas phase basicities and proton affinities of molecules: an update. *J Phys Chem Ref Data* 27:413
57. Hiraoka K, Shoda T, Kudaka I, Fujimaki S, Mizuse S, Yamabe S, Wasada H, Wasada-Tsutsui Y (2003) *J Phys Chem* 107:775
58. Yamdagni R, Kebarle P (1973) *J Am Chem Soc* 95:4050
59. Hiraoka K, Yamdagni R, Kebarle P (1973) *J Am Chem Soc* 95:6833
60. McMahon TB, Kebarle P (1974) *J Am Chem Soc* 96:5940
61. McMahon TB, Kebarle P (1976) *J Am Chem Soc* 98:3399
62. McMahon TB, Kebarle P (1974) *J Am Chem Soc* 96:4035
63. McMahon TB, Kebarle P (1977) *J Am Chem Soc* 99:2222
64. Cumming JB, Kebarle P (1977) *Can J Chem* 55:3474
65. Yamdagni R, Kebarle P (1974) *Can J Chem* 52:861
66. McIver RT Jr, Silvers JT (1973) *J Am Chem Soc* 95:8462
67. McIver RT Jr, Miller JS (1974) *J Am Chem Soc* 96:4323
68. Arnett EM, Small RT, McIver RT Jr, Miller JS (1974) *J Am Chem Soc* 96:5640
69. Smit ALC, Field FH (1977) *J Am Chem Soc* 99:6471
70. Hunt DF, Crow FW (1978) *Anal Chem* 50:1781
71. Roy TA, Field FH, Lin YY, Smith LL (1979) *Anal Chem* 51:272
72. Hiraoka K (1987) *J Chem Phys* 87:4048
73. Hiraoka K, Mori T (1989) *Chem Phys Lett* 157:467
74. Hiraoka K, Mori T (1989) *J Chem Phys* 91:4821
75. Hiraoka K, Mori T (1989) *Chem Phys Lett* 161:111
76. Hiraoka K, Nakajima G (1988) *J Chem Phys* 88:7709
77. Hiraoka K (1988) *J Chem Phys* 89:3190
78. Hiraoka K, Nakajima G (1988) *J Chem Phys* 88:7709
79. Hiraoka K, Mori T (1989) *J Chem Phys* 90:7143
80. Hiraoka K, Mori T (1990) *J Chem Phys* 92:4408
81. Hiraoka K, Nasu M, Oomori D, Minamitsu A (1996) *J Chem Phys* 105:9068
82. Hiraoka K, Takimoto H, Morise K (1986) *J Am Chem Soc* 108:5683
83. Hiraoka K, Takimoto H, Yamabe S (1986) *J Phys Chem* 90:5910
84. Hiraoka K, Mizuse S, Yamabe S (1987) *J Chem Phys* 87:3647
85. Hiraoka K, Kebarle P (1977) *J Am Chem Soc* 99:360
86. Hunt DF, Stafford GC Jr, Crow FW, Russel JW (1976) *Anal Chem* 48:49
87. Radzig AA, Smirnov BM (eds) (1985) *Reference data on atoms, molecules, and ions*, Springer series in chemical physics 31, vol 2. Springer, Berlin
88. Hiraoka K, Furuya H, Kambara S, Suzuki S, Hashimoto Y, Takamizawa A (2006) *Rapid Commun Mass Spectrom* 20:3213
89. Jones MT, Dreiling TD, Setser DW, McDonald RN (1985) *J Phys Chem* 89:4501
90. Ukai M, Hatano Y (1991) In Crompton RW, Hayashi M, Boyd DE, Makabe T (eds) *Gaseous electronics and its applications*, Kluwer Academic, Tokyo, p 51
91. Platzman RL (1962) *Rad Res* 17:419
92. Platzman RL (1962) *Vortex* 23:372
93. Hatano Y (1999) *Phys Rep* 313:109
94. Faubert D, Paul GJC, Giroux J, Bertrand ML (1993) *Int J Mass Spectrom Ion Process* 124:69
95. Tsuchiya M, Kuwabara H (1984) *Anal Chem* 56:337
96. Tsuchiya M (1998) *Mass Spectrom Rev* 17:51
97. Hiraoka K, Fujimaki S, Kambara S, Furuya H, Okazaki S (2004) *Rapid Commun Mass Spectrom* 18:2323

98. Cody RB, Laramée JA, Durst HD (2005) *Anal Chem* 77:2297
99. Na N, Zhao M, Zhang S, Yang C, Zhang X (2007) *J Am Soc Mass Spectrom* 18:1859
100. Andrade FJ, Shelley JT, Wetzel WC, Web MR, Gamez G, Ray SJ, Hieftje GM (2008) *Anal Chem* 80:2646
101. Garcia-Reyes JF, Harper JD, Salazar GA, Charipar NA, Ouyang Z, Cooks RG (2011) *Anal Chem* 83:1084
102. Hiraoka K, Ninomiya S, Chen LC, Iwama T, Mandal MK, Suzuki H, Ariyada O, Furuya H, Takekawa K (2011) *Analyst* 136:1210
103. Hiraoka K, Chen LC, Iwama T, Mandal MK, Ninomiya S, Suzuki H, Ariyada O, Furuya H, Takekawa K (2010) *J Mass Spectrom Soc Jpn* 58:215
104. Furuya H, Kambara S, Nishidate K, Fujimaki S, Hashimoto Y, Suzuki S, Iwama T, Hiraoka K (2010) *J Mass Spectrom Soc Jpn* 58:211
105. Harris GA, Galhena AS, Fernández FM (2011) *Anal Chem* 83:4508

Kenzo Hiraoka

8.1 Introduction

The electrospray (ES) process is the action of liquid dispersion into a fine aerosol, a phenomenon that takes place when a strong electric field is exerted on the liquid. The electrical atomization of liquids was first observed by George Bose in 1745 [1, 2]. Rayleigh determined an instability criterion for charged liquid droplets in 1882 [3]. In 1917, Zeleny established a criterion for the instability of an electrified liquid at the end of a capillary tube [4].

Since the pioneering works by Fenn and coworkers [5–7], ESI-MS has been one of the main tools for analyzing biological compounds in many applied fields. In order to fully exploit ES in analytical science and technology, it is essential to understand the mechanisms for the formation of charged droplets and the subsequent formation of gaseous ions. This chapter deals with the fundamentals of ES from various points of view, namely, (a) electrochemical reactions in ES, (b) the Taylor cone, (c) disintegration of the charged liquid droplet, (d) formation of gaseous ions from the charged droplet, (e) the effect of the surface tension on ES, (f) electrical breakdown and ES, (g) the suppression effect by the presence of salts, (h) downsizing of ES: conventional ESI → nano-ESI → probe electrospray ionization (PESI), (i) application of PESI to real-world samples, (j) field desorption (FD), and (k) field ionization (FI).

This chapter focuses mainly on the fundamentals of ES, but not on its applications. A recent comprehensive review on fundamentals, instrumentation, practicalities, and biological application of ES and MALDI mass spectrometry can be found in reference [8].

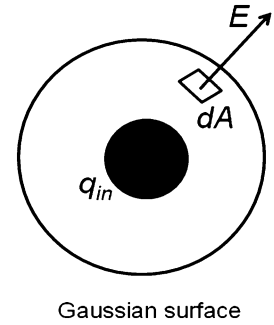
8.2 Electrochemical Reactions in ES

ES is known to be the best method for the formation of highly charged droplets with the smallest sizes and the narrowest size distribution.

To better understand ES, the electric field E is defined first. The electric field E is generated when a voltage V is applied between two electrodes. For instance, when V is applied between a metal

K. Hiraoka (✉)
Clean Energy Research Center, University of Yamanashi, Takeda-4-3-11, Kofu 400-8511,
Yamanashi, Japan
e-mail: hiraoka@yamanashi.ac.jp

Fig. 8.1 A Gaussian surface with charge q_{in} enclosed



capillary and a counter-electrode that is at ground potential (i.e., 0 V), an electric field is generated between the two electrodes. Because the metal is a conductor, no electric field is generated inside the metal. That is, the potential of the metal capillary is V at all positions of the capillary. However, the electric field depends on the shape, and therefore, the value of E is highest at the tip of the capillary [9].

The value of electric field E generated on the surface of the sphere, the tip of the needle, and the wire at potential V with respect to a counter-electrode at ground potential are expressed as (8.1), where r represents the radius of curvature of the sphere, tip, and wire and d the distance to the counter-electrode [10–12].

$$E = K \left(\frac{V}{r} \right). \quad (8.1)$$

The values of K for various shapes are given below:

For a sphere: $K = 1$

For a needle electrode: $K = 2/\ln(2d/r)$ (r : radius of curvature of the capillary tip)

For sharp knife edge: $K = 1/(2d/r)^{1/2}$ (r : radius of curvature of the knife edge)

For wire: $K = 1/\ln(d/r)$ (r : radius of the wire)

In an ES experiment using a capillary, E is expressed as in (8.2).

$$E = \frac{2V}{r \ln(2d/r)}. \quad (8.2)$$

According to (8.2), E increases with higher V , smaller r and smaller distance d .

According to Gauss's law [9], the total electric flux Φ out of a closed surface is equal to the charge enclosed (q_{in}) divided by the vacuum permittivity ϵ_0 , as follows.

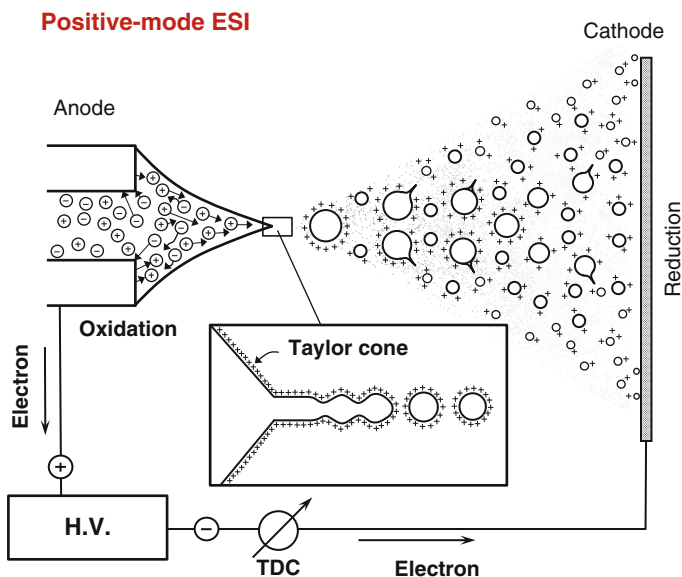
$$\Phi = \oint E \cdot dA = \frac{q_{in}}{\epsilon_0}, \quad (8.3)$$

where $\oint E \cdot dA$ is the surface integral of the electric field (Fig. 8.1).

The meaning of (8.3) is that the electric field E is generated only when a net charge q_{in} exists in the enclosed surface. On a surface with the surface charge density σ (C/m^2), the electric field E can be derived from (8.3) and is given in (8.4) [9].

$$E = \frac{\sigma}{\epsilon_0}. \quad (8.4)$$

Fig. 8.2 Schematic representation for positive ion mode. ES consisting of two half-cells: one is the capillary electrode and the other is the counter-electrode separated by an air gap (TDC means total direct current; H.V. means high voltage power supply) (reproduced with permission from [13])



Equation (8.4) shows that E is proportional to the surface charge density σ and is generated only when there is an excess charge on the surface.

Figure 8.2 [13] displays a schematic diagram of an ES ion source and the electric circuit involved for the positive ion mode.

In the ES plume, finer charged droplets and gaseous ions are distributed mainly in the peripheral region, while coarse droplets are found in the center, as shown in Fig. 8.2 [14–16].

In conventional ES, the electric field generated at a ~ 0.2 mm-diameter capillary tip is about 10^7 V/m. The liquid emerging from the capillary is exposed to the high electric field, and electrophoretic charge separation takes place, i.e., positive ions in solution migrate to the meniscus of the liquid and negative ions migrate backwards toward the metal surface. Thus, the surface of the liquid droplet becomes positively charged. However, this electrophoretic charge separation does not lead to continuous ES. The charge separation is regarded as the charging of a liquid capacitor, and thus, no direct current will flow through the electric circuit described in Fig. 8.2. When electrochemical reactions take place at the tip of the capillary, i.e., oxidation reactions in the positive ion mode and reduction reactions in the negative ion mode, excess charges accumulate on the liquid droplet. At certain critical conditions, the electric forces arising from the Coulomb repulsion between excess surface charges, which are directed outward the liquid surface, overcome the surface tension of the liquid, which is directed inward, and emission of the charged droplets from the tip of the liquid cone begins. The electrons generated by the oxidation reactions in the positive ion mode flow through the electric circuit and neutralize the positive ions arriving at the surface of the counter-electrode (and the electric circuit is closed) (Fig. 8.2). In brief, the ES phenomenon is solely ascribed to the electrochemical oxidation (positive ion mode) and reduction (negative ion mode) reactions taking place at the tip of the metal capillary. The ES current (TDC in Fig. 8.2) corresponds to the net excess charges generated by the electrochemical reactions per unit time [13].

The ES system in Fig. 8.2 may be regarded as a capacitor and (8.5) applies.

$$Q = C \times V, \quad (8.5)$$

where Q is the charge collected in the capacitor, C the capacitance, and V the applied voltage. The ES is regarded as a leak of the excess charge condensed in the liquid toward the counter-electrode.

Table 8.1 Standard electrode potentials for some oxidation and reduction reactions anticipated to take place at the interface between the metal electrode and the sample liquid

Reaction	E^0 (V vs. $2\text{H}^+/\text{H}_2$)
Oxidation(positive-ion mode)	
<i>Solvent system reactions</i>	
$4\text{OH}^- = 2\text{H}_2\text{O} + \text{O}_2 + 4\text{e}^-$	0.42
$2\text{OH}^- = \text{H}_2\text{O}_2 + 2\text{e}^-$	0.29
$2\text{H}_2\text{O} = \text{O}_2 + 4\text{H}^+ + 4\text{e}^-$	1.25
$2\text{NH}_4^+ = \text{N}_2\text{H}_5^+ + 3\text{H}^+ + 2\text{e}^-$	1.30
$\text{NH}_4^+ + \text{H}_2\text{O} = \text{NH}_3\text{OH}^+ + 2\text{H}^+ + 2\text{e}^-$	1.37
$2\text{H}_2\text{O} = \text{H}_2\text{O}_2 + 2\text{H}^+ + 2\text{e}^-$	1.79
$\text{OH}^- = \text{OH} + \text{e}^-$	2.02
$2\text{Cl}^- = \text{Cl}_2(\text{g}) + 2\text{e}^-$	1.36
<i>Electrode reaction</i>	
$\text{Fe} + 2\text{OH}^- = \text{Fe}(\text{OH})_2 + 2\text{e}^-$	-0.85
$\text{Fe} = \text{Fe}^{2+} + 2\text{e}^-$	-0.42
$\text{Fe} = \text{Fe}^{3+} + 3\text{e}^-$	-0.01
$\text{Pt} + 2\text{OH}^- = \text{Pt}(\text{OH})_2 + 2\text{e}^-$	0.18
$\text{Pt} + 2\text{H}_2\text{O} = \text{Pt}(\text{OH})_2 + 2\text{H}^+ + 2\text{e}^-$	1.00
Reduction(negative-ion mode)	
<i>Solvent system reactions</i>	
$\text{CH}_3\text{OH} + 2\text{H}^+ + 2\text{e}^- = \text{CH}_4 + \text{H}_2\text{O}$	0.60
$2\text{H}_2\text{O} + \text{O}_2 + 4\text{e}^- = 4\text{OH}^-$	0.42
$2\text{H}^+ + 2\text{e}^- = \text{H}_2$	0.00
$\text{CH}_3\text{COOH} + 2\text{H}^+ + 2\text{e}^- = \text{CH}_3\text{CHO} + \text{H}_2\text{O}$	0.11
$\text{CH}_3\text{OH} + \text{H}_2\text{O} + 2\text{e}^- = \text{CH}_4 + 2\text{OH}^-$	-0.23
$2\text{NH}_4^+ + 2\text{e}^- = 2\text{NH}_3 + \text{H}_2$	-0.53
$2\text{H}_2\text{O} + 2\text{e}^- = \text{H}_2 + 2\text{OH}^-$	-0.80
$\text{Na}^+ + \text{e}^- = \text{Na}$	-2.71
<i>Electrode reaction</i>	
$\text{Pt}(\text{OH})_2 + 2\text{e}^- = \text{Pt} + 2\text{OH}^-$	0.18
$\text{Fe}(\text{OH})_3 + \text{e}^- = \text{Fe}(\text{OH})_2 + \text{OH}^-$	-0.54
$\text{Fe}(\text{OH})_2 + 2\text{e}^- = \text{Fe} + 2\text{OH}^-$	-0.85

The standard electrode potentials are summarized in Table 8.1 for some of the oxidation and reduction reactions that are supposed to take place at the interface between the metal electrode and the sample liquid.

Oxidation of the hydroxide ion ($4\text{OH}^- = 2\text{H}_2\text{O} + \text{O}_2 + 4\text{e}^-$), or the water solvent ($2\text{H}_2\text{O} = 4\text{H}^+ + \text{O}_2 + 4\text{e}^-$), or others from the relevant list in Table 8.1 are likely to occur in the positive ion mode; reduction of methanol in acidic condition ($\text{CH}_3\text{OH} + 2\text{H}^+ + 2\text{e}^- = \text{CH}_4 + \text{H}_2\text{O}$) and the formation of hydroxide ion OH^- in oxygen-containing water solvent ($2\text{H}_2\text{O} + \text{O}_2 + 4\text{e}^- = 4\text{OH}^-$), etc., are likely to occur in the negative mode. Here, e^- represents the electron exchanged at the surface of the metal electrode in contact with the liquid. When a stainless steel capillary is used in the ESI system, oxidation of iron to give Fe^{2+} or even Fe^{3+} may occur. The use of noncorrosive metals such as gold, platinum, and titanium in the ESI system may solve the contamination of the liquid by metal ions and improve the quality of ESI mass spectra. The electrochemical reactions taking place at the tip of the capillary are difficult to predict because of the complexity of the electrospray conditions.

By knowing i (A)—the TDC value—and the flow rate of the sample solution F (L/s), the concentration of excess charge [Q (mol/L)] can be evaluated [17] from (8.6), where F is Faraday's constant (96,500 C).

$$[Q] = \frac{i}{FT}. \quad (8.6)$$

Note on units: The coulomb (C) is the SI-derived unit of electric charge. The unit of one ampere is the number of electric charges (C) passing through a point per second (i.e., $1 \text{ C/s} = 1 \text{ A}$).

In conventional and nano-ESI, the TDC is usually in the order of 10^{-7} A . For example, if TDC is $1 \times 10^{-7} \text{ A}$ and the flow rate is $5 \mu\text{L/min}$ for conventional ESI and 20 nL/min for nano-ESI, the $[Q]$ values are calculated to be 10^{-5} and $3 \times 10^{-3} \text{ M}$, respectively. Reducing the ES size drastically increases the values of $[Q]$, resulting in higher detection sensitivity (see Sect. 8.9). It should be noted that the excess charges are distributed mainly on the surface of the droplet but not in the bulk, and therefore, expressing $[Q]$ in units of mol/L is somewhat misleading (see following section).

8.3 The Taylor Cone

When a potential V is applied to an electrical conductor such as a metal or electrolyte solution, excess charges are induced on the surface (8.4), but not inside the conductor. This is because potential difference in the conductor is instantly nullified by the current flow, and thus, the neutrality of the conductor is maintained. Anywhere beneath the surface of a charged conductor the electric field is zero, meaning that the potential of a charged conductor is the same at all its positions. However, unless the conductor is spherical, the electric field strength varies depending on the shape of the conductor. Roughly speaking, the electric field is inversely proportional to the radius of curvature (8.1). For a sphere, the electric field on the surface is inversely proportional to the radius r ($K = 1$ in (8.1)) [9].

In capillary-based ES, the liquid flowing out of the capillary is exposed to a strong electric field at the tip of the capillary, and because of this high electric field, electrochemical reactions take place on the surface of the metal electrode and the excess charges are supplied to the liquid droplet. Overall, this is regarded as transfer of the excess charges induced on the tip of the metal capillary to the liquid because of electrochemical reactions (Fig. 8.3).

With the excess charges in the droplet increasing, the shape of the liquid becomes conical because of the Coulomb's repulsive forces acting normal to the liquid surface in the outward direction. On the other hand, to minimize the surface area of the liquid, the liquid surface tension acts normal to the surface as the inward force. At the Rayleigh limit, the outward and inward forces balance each other at all positions in the liquid and a cone with the whole angle of 99° is formed. This describes the formation of the Taylor cone [18]. When the electrostatic outward force overcomes the surface tension, the Taylor cone is elongated and the charged droplets are ejected from the tip toward the counter-electrode (Fig. 8.2).

The theoretical treatment of ES is as follows. The pressure P_γ originating from the surface tension of the liquid (inward pressure normal to the surface) is proportional to the product of the surface tension γ and the curvature (reciprocal of the radius, or $1/r$) κ .

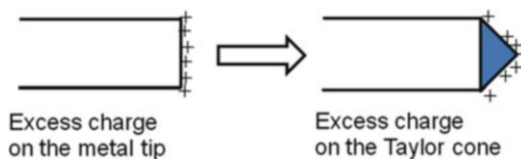
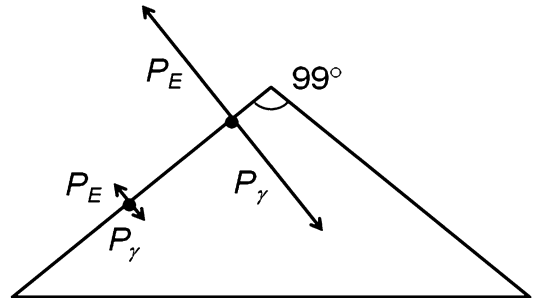


Fig. 8.3 Excess charge on the metal tip and on the Taylor cone

Fig. 8.4 Taylor cone with the whole angle of 99°



$$P_\gamma = \gamma \times \kappa. \quad (8.7)$$

The electrostatic pressure P_E induced on the surface of the conductor by the excess charges is proportional to E^2 [19].

$$P_E = 0.5\epsilon_0 E^2. \quad (8.8)$$

P_E can be derived from the Poisson's equation (8.9) for a conical equipotential plane for the electroconductive liquid [19]:

$$\nabla^2 V = \frac{-\rho}{\epsilon_0}, \quad (8.9)$$

where ∇^2 is the second partial derivative of the Cartesian coordinates, V is the potential, and ρ is the net charge density. The electrostatic pressure P_E pushes the liquid out of the capillary toward the counter-electrode, resulting in deformation of the liquid into a cone shape. A static Taylor cone is formed when P_E and P_γ are equal for all points on the surface of the cone, i.e., $P_E = P_\gamma$. The values of P_E and P_γ increase toward the tip of the cone. In other words, the tip has the highest excess charge density, and thus, the highest electric field is exerted at the apex (Fig. 8.4).

The critical voltage V_c for the formation of the Taylor cone with $P_E = P_\gamma$ is given by (8.10) [19].

$$V_c = 0.863 \left(\frac{\gamma d}{\epsilon_0} \right)^{0.5}. \quad (8.10)$$

That is, V_c is proportional to the root of the product of the surface tension γ and the distance to the counter-electrode, d . With further increase in voltage, P_E becomes larger than P_γ , and the Taylor cone elongates to the counter-electrode. With emission of the charged droplets, the excess charges in the liquid droplet at the tip of the capillary decrease suddenly and the loss of charge causes the ES to stop. The excess charges accumulate again by electrochemical reactions after some time, resulting in successive ES. As such, ES is a repetitive transient phenomenon of charged droplets emission.

In the time-lapse images shown in Fig. 8.5, it can be observed that the cone is pulsating, i.e., ES is called "electric sneeze" because of the periodical pulsating phenomenon. The period of one cycle, from (a) to (e) was measured to be hundreds of microseconds (i.e., frequency of a few kHz) [20, 21]. This means that about hundreds of microseconds are needed for the charging of the liquid by electrochemical reactions.

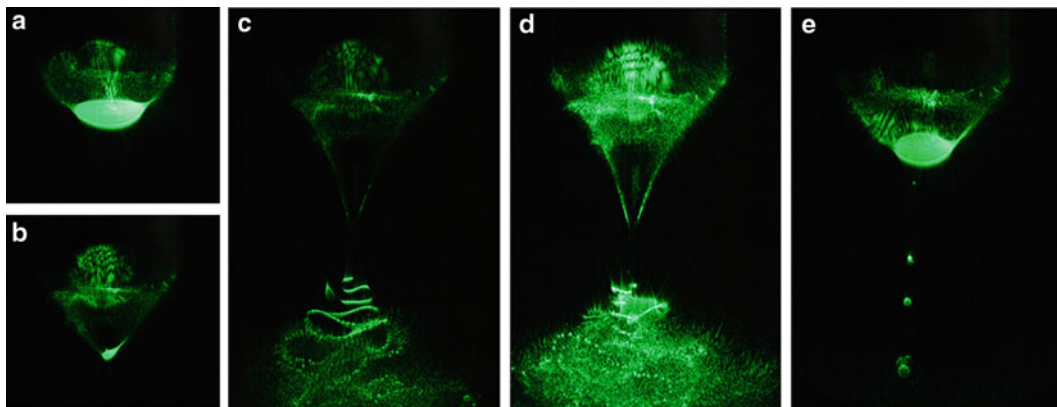


Fig. 8.5 Electrospray as an “electric sneeze.” Backlight illumination photographs and ES images taken by using pulsed laser microscopy of ES generated using a capillary with 100 μm inner diameter for a sample of 0.1 % acetic acid in methanol–water (1:1) with a flow rate of 1 $\mu\text{L}/\text{min}$ [20]; (a) liquid accumulation on the tip of the capillary; (b) the Taylor cone formation, (c) and (d) ejection of the jet of charged microdroplets, and (e) relaxation (reproduced with permission from [20])

Electric phenomena that take place at sharp edges are observed ubiquitously in nature. A typical example is the liquid metal ion source operated in high vacuum. Metal ions are emitted from the sharp tip of a metal electrode. This “point ion emission source” is used in secondary ion mass spectrometry (SIMS). In a liquid metal ion source, metals (Ga, Cs, Bi, etc.) or metal alloys that are liquid at room temperature or slightly above, cover a sharp tungsten needle electrode. When an intense electric field is applied, the metal ions (e.g., Ga^+ , Cs^+ , Bi^+) are desorbed from the tip of the tungsten tip, and this phenomenon is called as the field desorption (FD, see Sect. 8.11). The primary ion beam can be focused to tens of nanometers and imaging of the nanomaterials with this space resolution can be realized.

In field ion microscopy (FIM), He atoms are ionized via the tunneling ionization process induced by a high electric field, and the arrangement of atoms at the surface of a sharp metal tip can be observed. In scanning tunneling microscopy (STM), the tunneling current between an atomic-scale sharp needle tip and a conductive sample is measured with 0.1 nm lateral resolution and 0.01 nm depth resolution. All these techniques utilize the strong electric field generated at the tip of sharp electrodes.

Other examples are the dc corona discharge used for APCI, the lightning rod used for lightning protection, St. Elmo’s fire.

8.4 Disintegration of the Charged Droplet

The excess charges in the droplets emitted from the Taylor cone constitute 70–80 % of the Rayleigh limit [22, 23]. This is due to the dynamic fluid fluctuation and nonequilibrium fission processes. The charged droplet detached from the Taylor cone disintegrates by losing its weight through evaporation of the solvent. Right after the disintegration, the excess charges in both the parent charged droplets and the spawned secondary droplets are close to the Rayleigh limit. Figure 8.6 shows the sequential droplet fission processes of the charged parent droplet (N is the number of excess charges, r : the radius of the droplet) [13].

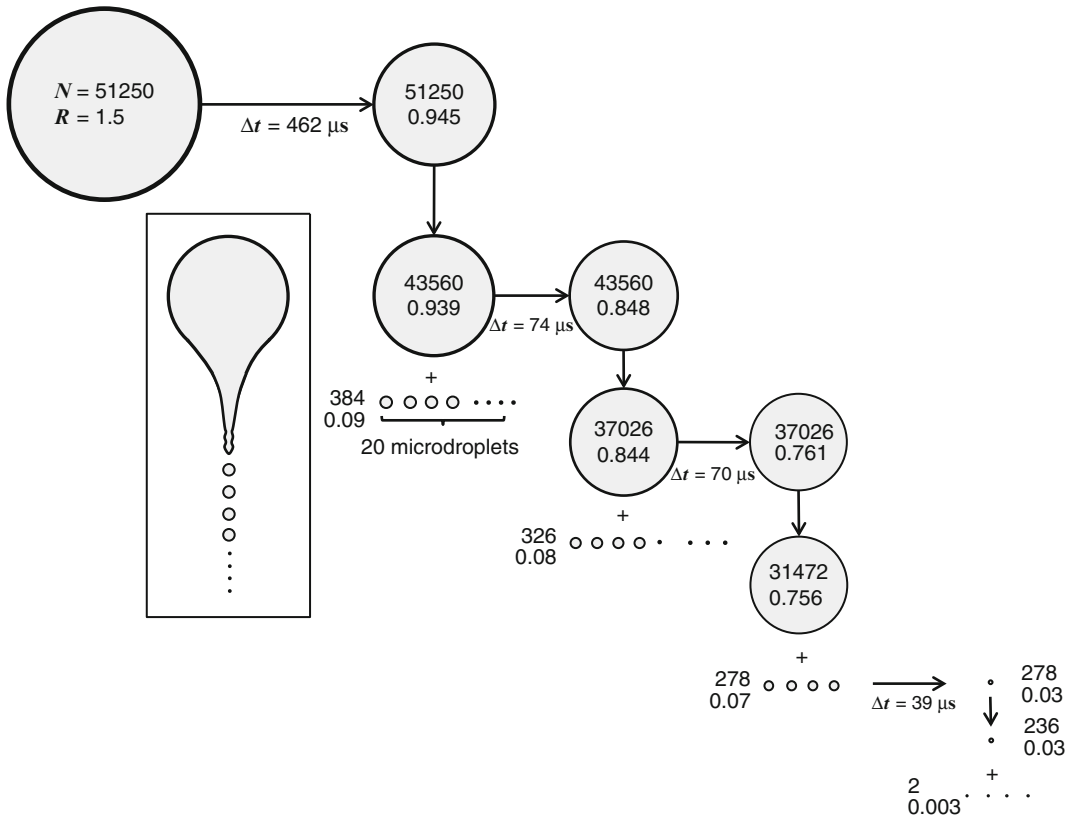


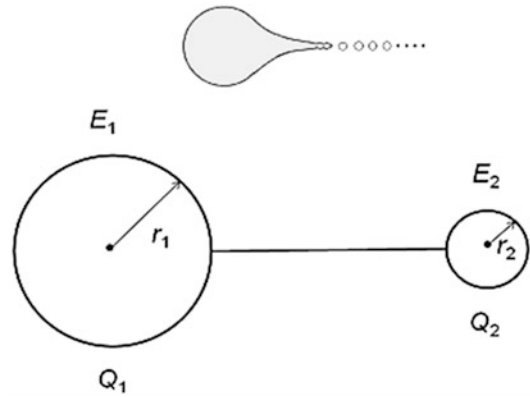
Fig. 8.6 Fission processes of the charged droplet due to the decrease in the volume by evaporation of solvent. The heat for solvent evaporation is supplied from the ambient gas that acts as a heat bath. N : the number of excess charges; r : radius, and Δt : time required for the droplet to shrink to a size suitable for droplet fission (reproduced with permission from [13])

In the figure, the parent droplet with the radius r of 1.5 μm holds the excess charges N of 51,250 (near the Rayleigh limit). At the moment of droplet fission, the parent droplet changes to a fig-like shape, as shown in the inset and the jet fission produces fine secondary droplets. This uneven fission process is similar to the formation of charged droplets from the Taylor cone shown in Figs. 8.2 and 8.5.

In droplet fission, about 20 secondary droplets with r of about 1/10 of that of the parent droplet are formed (about 1/1,000 in volume). In this fission event, about 15 % of the charge and 2 % of the mass are lost from the parent droplet [24, 25], meaning that the charge density increases significantly in the secondary off-spring droplets. The increase in excess charge density in the secondary droplets originates from the fact that the larger-size parent droplet and smaller off-spring droplets are both near the Rayleigh limit during and after the fission. To understand the relationship between the radius of curvature and surface charge density, two electrically conductive spheres with radii r_1 and r_2 , ($r_1 \neq r_2$) connected by a fine conductive wire were considered as a simplified model (Q : net charge, E : electric field) (Fig. 8.7).

To a very crude approximation, we can envisage the system at the moment of the fission of the secondary droplet from the parent droplet. Although these two spheres are at the same potential, because of the size difference the electric fields are different. With the respective excess charges Q_1

Fig. 8.7 Two conductive spheres connected with a fine wire



and Q_2 , the potentials of the spheres 1 and 2 are approximated to be $k(Q_1/r_1)$ and $k(Q_2/r_2)$, respectively (where k is Coulomb's constant) [9]. Equation (8.11) is derived from (8.4) and $\sigma = Q/4\pi r^2$.

$$\frac{r_1}{r_2} = \frac{\sigma_2}{\sigma_1} = \frac{E_2}{E_1}. \quad (8.11)$$

The meaning of (8.11) is that the excess surface charge density σ is inversely proportional to r , and this explains why second-generation droplets can have a higher surface charge density than the parent droplet.

The relation between the excess charge Q and the radius r for the spherical droplet at the Coulomb instability (the Rayleigh equation) is given in (8.12).

$$Q = (\gamma\epsilon_0 r^3)^{1/2} \times 8\pi. \quad (8.12)$$

The volume or mass of the droplet is proportional to r^3 , and thus, the mass of the droplet m is proportional to Q^2 . That is, with increasing excess charge Q , the mass of the droplet increases with Q^2 , or in other words, the excess charge density decreases with increasing droplet size.

Since the excess charges exist only on the surface of electrical conductors, the surface charge density of the spherical droplet at the Rayleigh limit is given as (8.13).

$$\sigma = \frac{Q}{4\pi r^2} = \frac{2(\gamma\epsilon_0)^{1/2}}{r^{1/2}}. \quad (8.13)$$

This indicates that the smaller the droplet size, the higher the surface charge density. This is related to the fact that nano-ESI has better performance than the conventional ESI.

8.5 Formation of Gaseous Ions from the Charged Droplet

As shown in Fig. 8.6, uneven fission takes place during droplet disintegration. This figure implicitly assumes that the droplet is composed of excess charges with the same sign and no opposite charge ions are present. In such an ideal case, all excess charges may ultimately disintegrate into single gaseous ions without the formation of charged solid salt particulates. However, real-world samples

always contain several components, such as salts, detergents, nonvolatile contaminants. When the sample is contaminated by some surface-active ions, the off-spring droplets carry them preferentially and less surface-active analytes remain in the primary droplet, leading to the suppression of analyte molecules [26]. To minimize the suppression effect and increase ion detection sensitivity, it is important to understand the formation mechanism of gaseous ions from the charged droplets.

So far, two models have been proposed for the formation of gaseous ions from the charged droplets: the charged residue mechanism (CRM) [27, 28], and the ion evaporation mechanism (IEM) [29, 30].

CRM assumes the formation of single gaseous analyte ions when only one analyte molecule is contained in the ultimate charged droplet. This situation may occur when the off-spring droplets become so small that the only one analyte molecule is contained in the charged droplet.

In IEM, ion evaporation is assumed to take place when the size of the droplet reaches ~ 20 nm in diameter [31], at which the field strength reaches the order of 10^8 V/m, i.e., the threshold value for ion evaporation. IEM plays an important role in gas-phase ion formation from ultrafine off-spring droplets [31].

When the solution contains analytes with different surface activities, the surface of the primary charged droplets will be enriched with more surface-active ions and they have more chance to be transferred to the off-spring droplets. The fractionation of the analytes with different surface activities is inevitable in the droplet disintegration processes. Ions with lower surface activity values left in the parent droplet have less chance of being detected as single gaseous ions, but may ultimately form charged residues. The best way to minimize the suppression effect is to reduce the size of the primary droplet to be as small as possible. Based on this concept, several methods have been developed, such as pneumatically assisted ES [32], infrared laser-assisted ES [33–38], nano-ES [19, 39], and probe ES [40–47].

As shown in Fig. 8.6, the size of the droplet formed by conventional ES using a capillary with an inner diameter (i.d.) of ~ 0.1 mm is about a few micrometers. The excess charge number N is about 5×10^4 near the Rayleigh limit. When the concentration of the sample is 10^{-5} M, the number of analyte molecules in the droplet is about 10^5 . This number is close to that of the excess charges ($N = 5 \times 10^4$). Thus, the 10^{-5} M analyte is rather easy to detect by conventional ES if the concentrations of other contaminants are relatively low. With the same concentration of analytes, but containing 150 mM NaCl (e.g., physiological saline solution), about 10^9 Na^+ and Cl^- ions are present in the droplet. That is, the concentration of NaCl is $\sim 10^4$ times that of the analyte. For such a multicomponent sample, it is not easy to detect the analyte with high efficiency because of the suppression effect and some sample pretreatment may be necessary to remove salt. The suppression effect can be minimized by downsizing the ES in the order $\text{ESI} \rightarrow \text{nano-ESI} \rightarrow \text{PESI}$ (see Sect. 8.9).

8.6 Effect of the Surface Tension on ES

The internal pressure P_γ forces liquid surfaces to contract to the minimal area. In ES, liquid disintegration is accompanied by a tremendous increase in surface area (Fig. 8.5). Thus, the smaller the surface tension γ , the easier it is to generate finer charged droplets (see (8.10), (8.12), and (8.13)). The aqueous solution is the most difficult solvent to electrospray, mainly because of the high surface tension of water ($\gamma = 72 \times 10^{-3}$ N/m). When methanol ($\gamma = 22 \times 10^{-3}$ N/m) or acetonitrile ($\gamma = 28 \times 10^{-3}$ N/m) is mixed in the aqueous solution, the solution becomes much easier to electrospray. Because organic solvents are more hydrophobic than water, their concentration in the

interfacial layer is enriched, resulting in marked decrease in the surface tension. The ratio of concentrations [organic solvent]/[water] in the interfacial layer becomes considerably higher than for the bulk [48].

For a solute–solvent system, the surface concentration of the solute becomes higher or lower than the bulk because of enrichment (positive adsorption) or depletion (negative adsorption) of the solute in the interfacial layer. Positive adsorption takes place for surface-active ions. One typical example is the Langmuir–Blodgett film formation of amphiphilic molecules on the water solvent surface. In contrast, salts get depleted in the interfacial layer as they do not have any surface activities. This explains why salts are suppressed by the presence of surface-active ions in ESI [17, 26]. While the surface-active ions are detected more favorably by IEM, ions with no surface activities, such as salts, are more likely to be detected by CRM.

8.7 Electrical Breakdown and ES

With increase in applied voltage, ES is sometimes disturbed by electrical breakdown leading to the formation of corona discharge at the tip of the needle. Corona discharge usually involves two asymmetric electrodes, one highly curved, such as a sharp needle, and one with low curvature. The high curvature ensures a high potential gradient of the highly curved electrode. The onset voltages of ES are roughly the same for positive and negative ion modes (8.10). However, the onset voltage of corona discharge in the negative mode is usually lower than in the positive ion mode, and for this reason it is more difficult to maintain a stable ES in the negative than in the positive ion mode of operation.

In the positive ion mode ES, electrons that are accidentally produced by the stimulation of cosmic rays or other radiation near the tip of the needle can be scavenged by the needle held at high positive voltage, and this results in suppression of the electrical breakdown. On the other hand, in the negative ion mode, electrons will drift out and induce successive ionization leading to electron avalanche.

In the negative mode corona discharge, initial electrons are supplied from the metal electrode. The photoelectric effect is one possible mechanism for the electron emission. The photoelectron emission may also be assisted by the electron tunneling process.

Figure 8.8 shows the potential near the metal tip. The electrons in the metal occupy the conduction band up to the Fermi level. With no electric field applied (Fig. 8.8a), electrons with energy greater than Φ (work function) can only escape into the gas phase. In photoelectron emission, photons with energy greater than Φ (i.e., $h\nu \geq \Phi$) can liberate electrons in the conduction band.

The application of high negative voltage results high potential gradient, as shown in Fig. 8.8b. Because of the small mass of the electron ($\sim 1/1,800$ of proton), it can have a large de Broglie wavelength λ , as shown in (8.14).

$$\lambda = \frac{h}{mv} = \frac{h}{p}, \quad (8.14)$$

where h is Planck's constant, and m , v , and p are the mass, velocity and momentum of the electron, respectively.

With increase in the negative voltage, the width of the potential barrier Δx becomes thinner. When Δx reached the order of λ , electrons near the Fermi level can tunnel through the potential barrier without surmounting the energy barrier with the value of Φ . A rough surface or burr of the metal tip might induce the tunneling emission of electrons. The tunneling electron emission from the

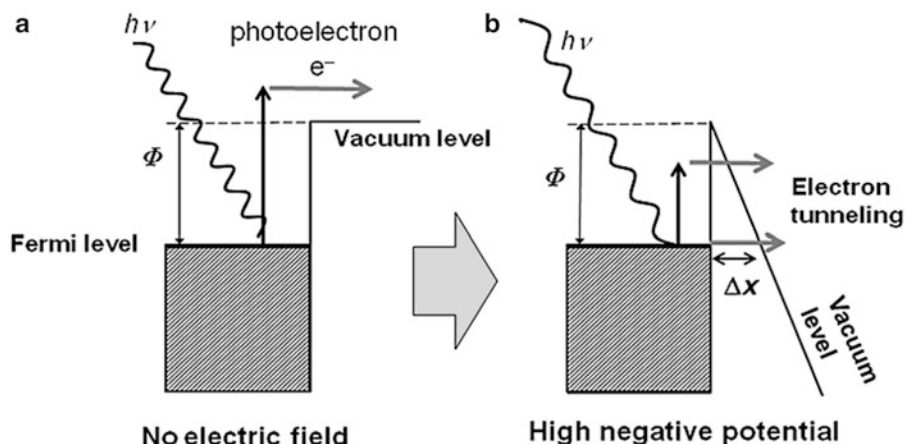
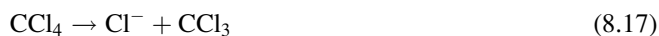


Fig. 8.8 Potentials near the tip of the electrode. Φ : work function, h : Planck's constant, ν : frequency of the photon

nanometer-size sharp tungsten tip is used as a point electron source for the electron microscope (field-emission type cold cathode).

With the start of dc corona discharge, the electric field at the tip decreases sharply because the plasma is an electrical conductor. With the gas breaking down, electrochemical reactions are almost totally suppressed and gaseous ions produced in the dc corona plasma become predominant. The supply of electron-scavenging SF_6 sheath gas to the capillary or addition of CCl_4 or CCl_3H in the sample solution suppresses the gas breakdown to some extent.



The threshold voltage for gas breakdown increases with gas pressure because of the reduction in the mean free path of electrons. This phenomenon is referred to as Paschen's law in the high pressure regime. By raising the ion source pressure to ~ 7 bar, Chen et al. verified that beside maintaining a stable cone-jet mode, the electric field at the ESI emitter could be increased up to the formation of a multiple-jet mode in both the positive and negative ion modes without triggering a corona discharge [49, 50]. Figure 8.9 is a diagram of the high-pressure ESI ion source.

This method was used to achieve stable ESI with high detection sensitivity in both positive and negative ion modes for aqueous solutions with high surface tension. This method is especially suitable to study native protein structures because an aqueous solution containing no organic solvent can be dealt with in both positive and negative ion modes of operation.

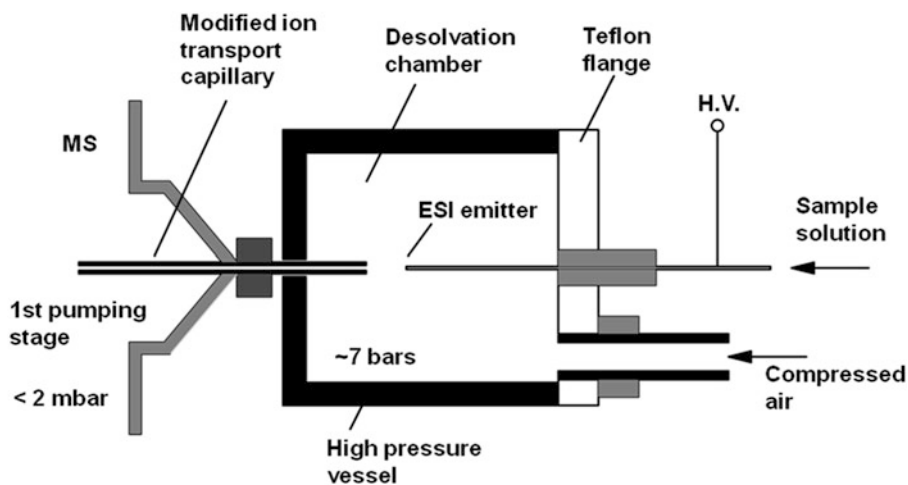


Fig. 8.9 Schematic of the high pressure ion source. The pressure in the ESI ion source is ~ 7 bar (reproduced with permission from [49])

8.8 Suppression Effect by the Presence of Salts

The ES current (TDC in Fig. 8.2) is dependent on the conductivity K of the solution [25] in the following manner.

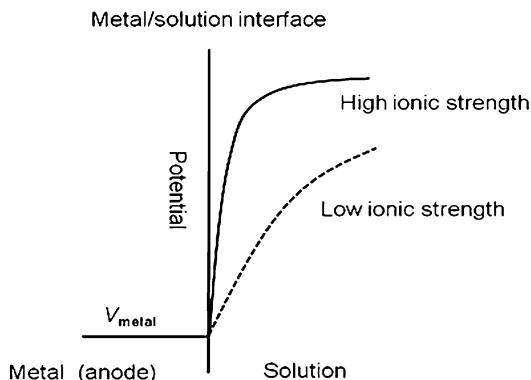
$$\text{TDC} \propto K^n \quad n = 0.2 - 0.4 \quad (8.19)$$

The rates of the electrochemical reactions increase with K , resulting in an increase in TDC. To increase K , supporting electrolytes are often added to the electrolyte solutions in the electrochemical cells. It is important to note that the electrochemical reactions are markedly enhanced by addition of the supporting electrolytes, although the supporting electrolytes are not electroactive, i.e., they do not take part in the electrochemical reactions. When a voltage is applied between the anode and the cathode for electrolysis, because of the formation of electric double layers near the anode and cathode, the potential gradient near the electrodes becomes much steeper than that in the medium between the two electrodes. The electrical double layer near the anode (positive electrode) is rich in anions, and that near the cathode (negative electrode) is rich in cations. These monopolar charge-enriched regions induce the space-charge field (see (8.9)). The potential differences applied to the two electrodes are mainly localized in these thin electric double layers. The thickness of the electric double layers is of the order of a few times of the Debye length λ_D , where C_0 is molar concentration of the electrolyte [51] (8.20).

$$\lambda_D(\text{nm}) = \frac{0.305}{C_0^{1/2}} \quad (8.20)$$

In an electrolyte solution, cations and anions attract each other by Coulomb attraction forces. That is, cations are surrounded by anions and vice versa. As a result of the Coulomb attractive interaction, the fields induced by the cations and anions are shielded by each other. That is, the region larger than $\sim \lambda_D$ can be regarded as electrically neutral (i.e., the electric field in the region larger than λ_D is roughly

Fig. 8.10 Electric potential near a surface



negligible). With increase in C_0 , the electric double layer [17] becomes thinner. Because the potential difference is mainly localized in this thin layer, the electric field increases with an increase in C_0 (Fig. 8.10).

In the high electric field applied in the thinner layer, the ions that take part in the electrical chemical reaction drift faster, and this leads to an increase in the electrochemical reaction rates.

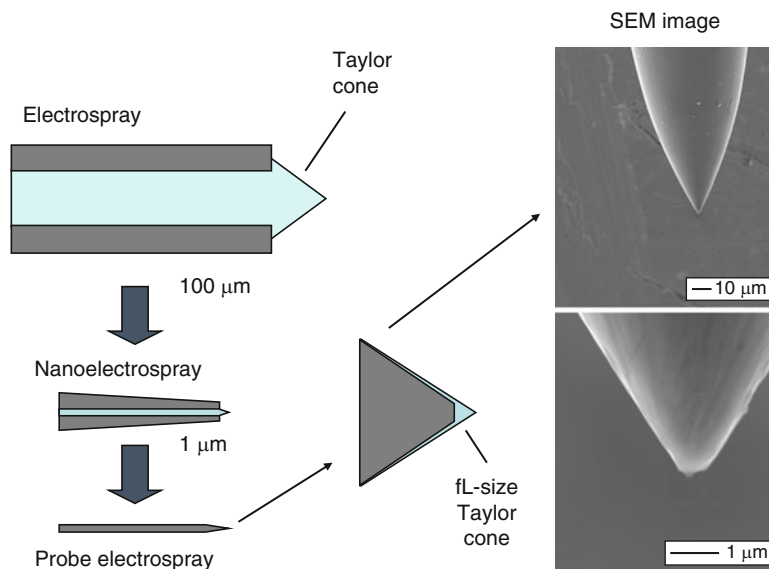
As with electrochemical cells, the reactions taking place at the tip of the capillary in ES are also enhanced with increase in C_0 (8.19). Due to the increase in the rate of excess charge supply to the liquid, the Taylor cone is formed in shorter time and TDC increases (8.19). However, ES becomes unstable with C_0 higher than $\sim 10^{-2}$ M. In such a case, higher voltage is necessary to generate ES, but dc corona discharge often occurs instead. Why does the onset voltage V_c increase at higher C_0 ? At high electrolyte concentration, the enriched excess charges on the surface of the Taylor cone are closely neighbored by the opposite-sign charges, resulting in a decrease in the electrostatic pressure P_E . For example, the Debye length for a 150 mM NaCl solution calculated from (8.20) is only 1 nm. At this high salt concentration, a higher voltage has to be applied to establish the Rayleigh limit, $P_\gamma = P_E$. For conventional ES, this criterion is not easily satisfied due to the electrical breakdown. However, nano-ESI and in particular PESI can moderate this problem (see Sect. 8.9).

8.9 Reducing ES Size: Conventional ES → Nano-ESI → PESI

ES is known to be concentration-sensitive and not flow rate-sensitive [52, 53]. Operation at low flow rates even improves the detection limit of the technique. One explanation for this phenomenon is that with decreasing liquid flow rate the ratio of the liquid volume that comes in contact with the metal surface at the tip of the metal capillary to the total liquid volume flowing out from the capillary per unit time increases. With the increase in this ratio, the rate of excess charge supplied to the liquid increases. In fact, by reducing the size of the ES, Wahl et al. [54] were able to detect subfemtomole concentration of protein. The combined use of low flow rates and small i.d. capillaries of fused-silica significantly increases sample ionization efficiency and results in high sensitivity

Wilm and Mann [19] theoretically predicted the radius of the emission region for droplets at the tip of the Taylor cone, r_c (8.21), by solving Poisson's equation (8.9) and assuming that the solution is a conductor (i.e., all points of the liquid cone are at the same potential).

Fig. 8.11 Downsizing of electrospray; ESI → nano-ESI → PESI (reproduced with permission from [20])



$$r_e = \left(\frac{dV}{dt} \right)^{2/3} \times \frac{\rho^{1/3}}{[\{4\pi^2\gamma \tan(\pi/2 - \theta)\}\{(U_a/U_t)^2 - 1\}]^{1/3}}, \quad (8.21)$$

where dV/dt is the flow rate, ρ is the density of liquid, γ is the surface tension, θ is half the Taylor cone angle, U_a is the applied voltage, and U_t is the threshold voltage for ES. Equation (8.21) predicts that a smaller flow rate generates a smaller droplet.

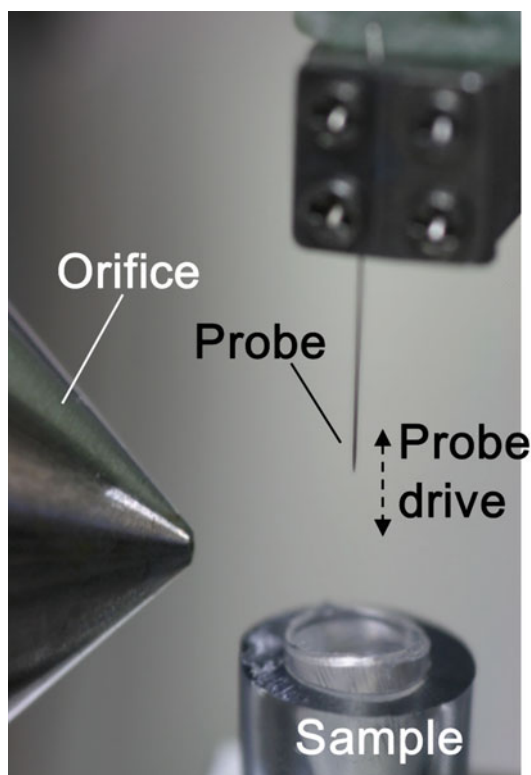
Wilm and Mann [19, 39] developed a low-flow sprayer for the analysis of small volumes of peptide solution at a flow rate in the low tens of nanoliters per minute. In general, aqueous solutions are more difficult to electrospray than those containing organic solvents such as methanol or acetonitrile. Low-flow ES (nano-ESI) was found to be more tolerant of 100 % water and small concentration of trifluoroacetic acid. Emmenett and Caprioli [55] applied a low-flow ES ion source for peptides and obtained sensitivity of the order of zeptomole/attomole per microliter.

In recent years, nano-ESI using glass capillaries seems to have reached the technical limit with the inner diameter of $\sim 1 \mu\text{m}$ because of problems with fragility and clogging. To circumvent these problems, the author and coworkers [40] developed PESI that uses a fine needle instead of a capillary. Figure 8.11 shows the history of the downsizing of ES, i.e., conventional ESI → nano-ESI → PESI [20].

The conceptual idea for PESI is displayed in Fig. 8.12 [20].

In Fig. 8.12, as one example, a disposable stainless steel acupuncture needle with a submicrometer tip diameter of $\sim 700 \text{ nm}$ was used as an electrospray emitter. Any other kinds of needles such as micro-needles for scanning tunneling microscopy, sewing needles, W/Ni/Ti/Au/Pt wires can also be used. The needle (i.e., the probe) was moved up and down along the vertical axis using a linear motor-actuated system. The bottom position of the needle tip was adjusted to just touch the surface of the biological or liquid sample that was mounted on the xyz manipulation stage. The amount of liquid adhered to the tip depends on the size of the needle, viscosity and surface tension of the sample [56]. When an acupuncture needle with sub-micrometer diameter tip is used, the sample volume is about a few picoliters. When the needle comes in contact with the sample, both needle and sample are kept at ground or floating potential. To generate ES, a high voltage of about 3 kV is applied to the needle when it is moved to the highest position.

Fig. 8.12 The probe electrospray system (PESI) (reproduced with permission from [20])



In general, a single sample loading on the tip of the needle with the volume of a few picoliters is enough for strong ion signal abundance in PESI [40]. One reason for the high performance of PESI is that the ratio of contact area between the liquid and the metal surface to the liquid volume on the tip is high compared with conventional or nano-ESI. In particular, the rate of charging of the liquid per unit volume is higher in PESI than in capillary-based ESI.

The electric field generated at the tip of the needle can be evaluated by (8.2). The combination of $V = 3,000$ V, $r = 0.35$ μm (Fig. 8.11), and $d = 5$ mm leads to $E = \sim 10^9$ V/m for PESI, which is about two orders of magnitude stronger than the conventional ES field (i.e., $E = 10^7$ V/m), and about the same order of magnitude for the estimated electric field necessary for ion evaporation from highly charged droplets [29, 30, 57]. Gas breakdown is suppressed by PESI because the liquid sample wets the tip of the probe, where the field strength is highest. Gas breakdown is prevented because the breakdown voltage in liquid is a number of orders of magnitude greater than in the gas phase.

The difference in appearance between three ES methods is shown in Fig. 8.13. Figure 8.13a, b shows images of conventional and nano-ESI, for 0.1 % acetic acid in methanol–water (1:1) solvent.

In Fig. 8.13a, a stainless steel capillary with 0.1 mm i.d. and 0.2 mm outer diameter (o.d) was used. The flow rate of the solution was 1 $\mu\text{L}/\text{min}$. The distance from the capillary tip to the counter-electrode (i.e., the ion sampling orifice of the mass spectrometer) was 10 mm. One can see the formation of the Taylor cone with the whole angle of $\sim 90^\circ$ from which emission of rather coarse droplets is observed. Figure 8.13b shows the ES using a gold-coated fused silica nano-ESI capillary with 5 μm i.d. for the same solution as the one used in Fig. 8.13a. The voltage applied to the capillary

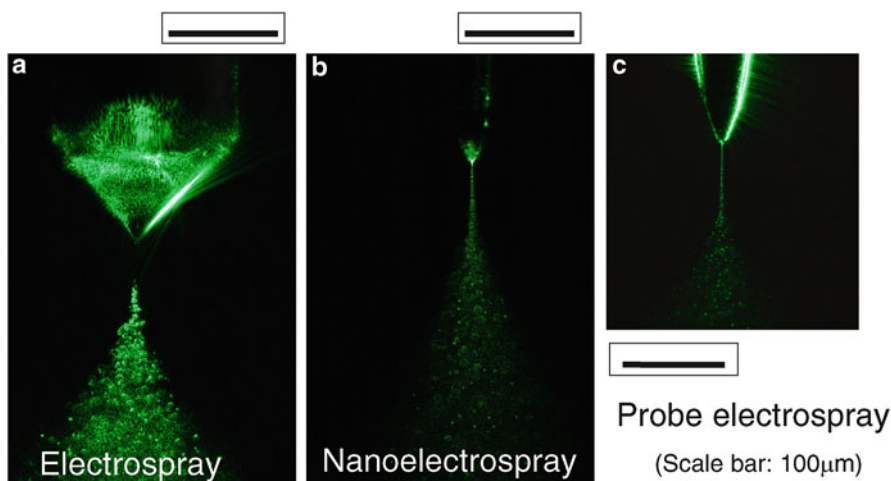


Fig. 8.13 Electrospray generated by (a) conventional ESI, (b) nano-ESI, and (c) PESI. The pictures were observed using 4 ns 532 nm YAG laser pulse

was 1.5 kV and the distance between the tip of the capillary and the counter-electrode was 3 mm. The sizes of the liquid droplets formed are much finer than those observed in Fig. 8.13a.

Figure 8.13c shows the ES generated by PESI. The sample was 10^{-5} M gramicidin S in 100 mM NaCl aqueous solution. The droplets may be smaller in size than the wavelength of the laser used for the observation (532 nm), but they can be recognized by laser light scattering. The curvature diameter of the apex of the needle was ~ 700 nm. It was confirmed that for this liquid sample no ES could be generated by conventional ES. The great advantage of PESI is that it is widely applicable to real-world samples with the presence of hundred mM salts, e.g., urine, cerebrospinal fluid, serum, blood, biological tissues.

PESI uses discontinuous sample loading. The time evolution of the ES emitted from the tip of the needle after the application of high voltage is shown in Fig. 8.14 [42].

At only 1 ms after the application of high voltage, a small ~ 1 μm -diameter droplet appeared at the tip of the needle and ES started. The ES lasted for tens of milliseconds, depending on the sample amounts picked up by the needle. The induction period for ES generation of a few milliseconds clearly indicates that the electrochemical reactions leading to the excess charge accumulation play a role in the process.

8.10 Application of PESI to Real-World Samples

Direct analysis of biological samples by conventional ES is basically difficult. Multistep sample preparations are normally necessary to achieve satisfactory performance of ES. On the other hand, PESI can be readily applicable to various biological samples (e.g., plants, animal organs, physiological fluids) without any special preparation. To show the versatility of the technique, PESI mass spectra for human and bovine milk are shown in Fig. 8.15 [41].

The human milk was analyzed directly without dilution. The bovine milk was prepared at 0.11 g/mL, as recommended on the product label. Besides sodiated and potassiated disaccharide ions, $[\text{diSac} + \text{Na}]^+$ and $[\text{diSac} + \text{K}]^+$, there are also Gaussian distributions of lipid ions at around the m/z values of 800 and 1,600. The peaks from the human milk appeared to be more densely spaced because of the nearly equal contribution from sodiated and potassiated molecules, where the

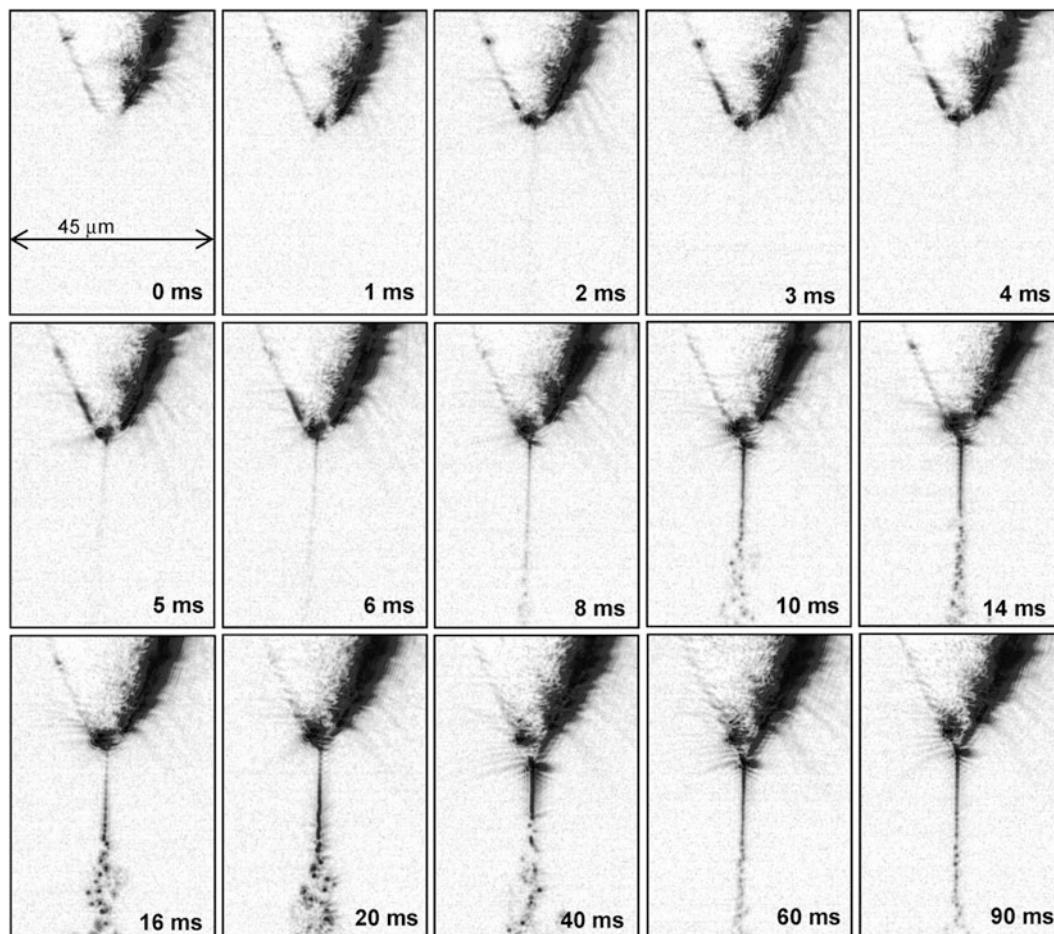


Fig. 8.14 Time-lapse images on the formation of electro spray from the solid needle probe. The needle tip was illuminated with a pulsed laser (pulse width: 4 ns) at a delay time measured from the application of the high voltage. The liquid sample was 10^{-5} M gramicidin S in 10^{-2} M ammonium acetate aqueous solution (reproduced with permission from [42])

potassiated molecules in the bovine milk appeared to be stronger due to the higher concentration of potassium.

Molecular imaging by mass spectrometry is a challenging subject. In view of its high sensitivity and small-size probe tip, PESI may be a promising technique for molecular imaging with a spatial resolution of less than tens of micrometers for biological samples. Figure 8.16 shows the depth profile of a mouse brain analyzed by PESI [43].

In this measurement, the penetration depth of the needle probe inserted in the mouse brain surface was increased gradually with 2.5 μm intervals. The mass spectra shown in Fig. 8.16 are highly dependent on the depth of penetration of the needle. For example, protonated phosphatidylcholine [PC34:1 + H]⁺ was observed as a base peak at the surface of the sample. With increased penetration depth, the intensity of potassiated phosphatidylcholine [PC34:1 + K]⁺ increases and eventually becomes stronger than that of [PC34:1 + H]⁺ (Fig. 8.16, left panel). The reason for the intensity inversion for [PC34:1 + H]⁺ and [PC34:1 + K]⁺ is ascribed to the high concentration of K⁺ in the cells than the surface membrane.

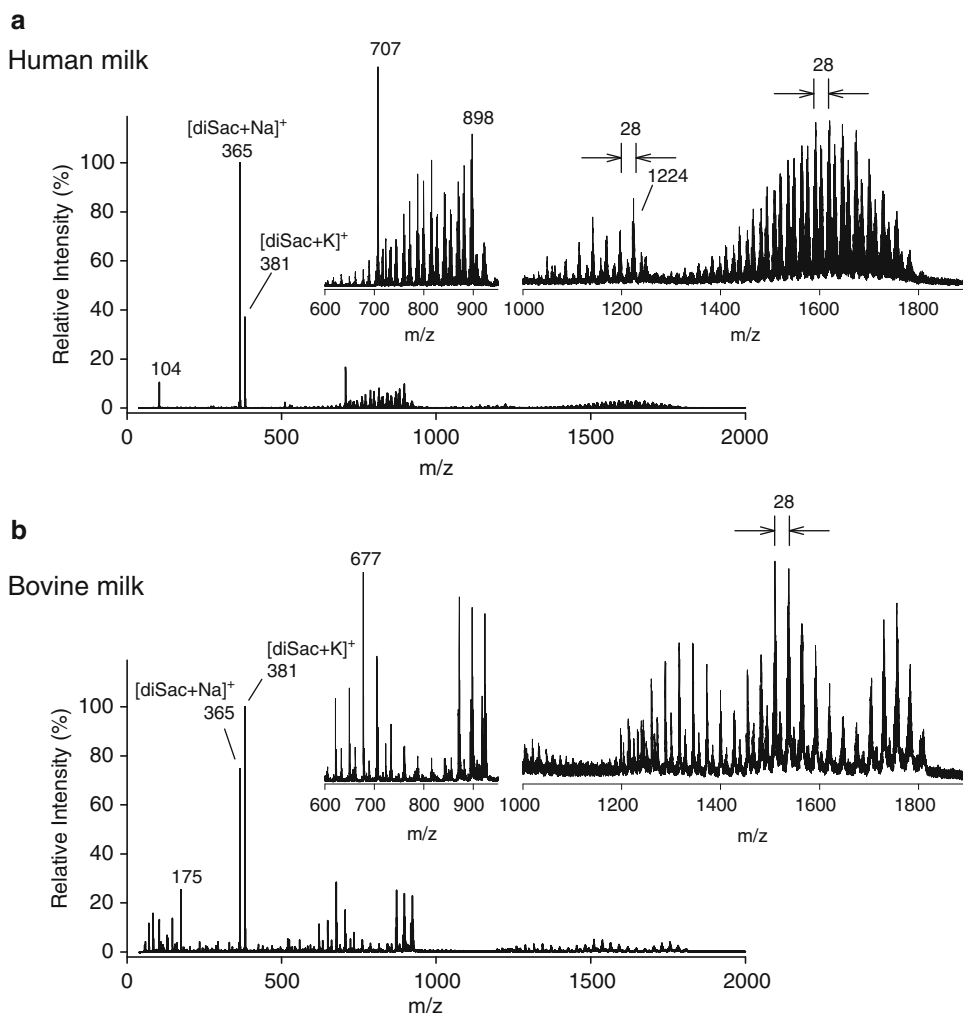


Fig. 8.15 PESI mass spectra for (a) human milk, and (b) local brand bovine milk formulated for new-born infants. Insets show the magnified mass spectra for each sample. Both samples were analyzed directly without pretreatment (reproduced with permission from [41])

Ambient imaging mass spectrometry was also applied to a mouse brain by PESI [44]. The mice were deeply anesthetized and fixed by cardiac perfusion with 2 % paraformaldehyde (PFA) in tris buffered saline (TBS: 25 mM Tris, 137 mM NaCl, 2.68 mM KCl, pH 7.2). The brain was extirpated and washed three times with TBS. It was then sliced using a razor blade to a size of about $7 \times 5 \times 2$ mm and the samples were stored in 0.9 % NaCl saline solution prior to the measurement.

The PESI-imaging-MS was performed in the positive ion mode. PESI mass spectrometric images (30×25 pixels) for the distribution of selected ion peaks on the mouse brain section are shown in Fig. 8.17 [44].

Some of the observed peaks originated from the sodiated/potassiated ions of phosphatidylcholines (PC). These observed phosphatidylcholines peaks have also been reported by MALDI and their distributions agree reasonably well with the results of MALDI-imaging-MS using a DHB (dihydroxybenzoic acid) matrix [58].

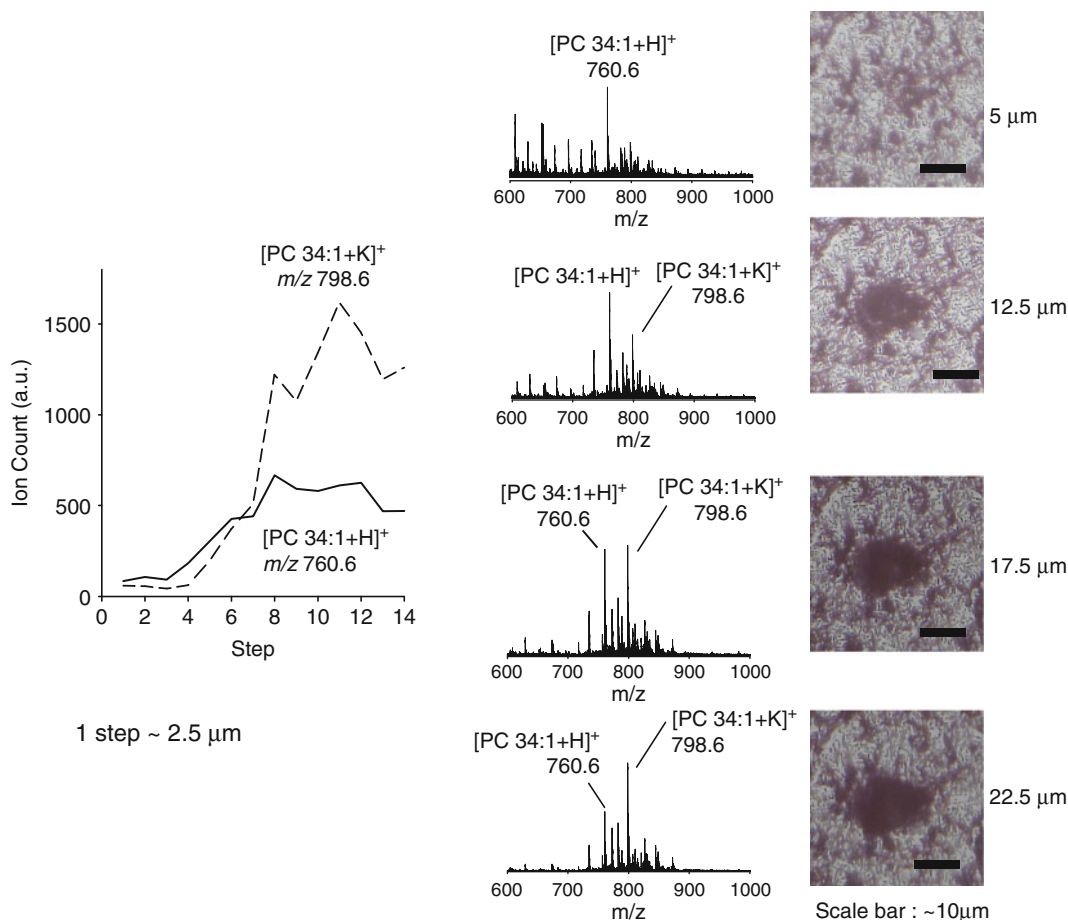


Fig. 8.16 Depth profile of a mouse brain analyzed by PESI (reproduced with permission from [43])

The MS images with most distinctive contrast are those of m/z at 822.7, 850.7, and 934.7. The peak at m/z 850.7 had been verified by the nanoparticle-MALDI to be the one of the sodiated species of galactosylceramide ($[\text{GalCer } 24 \text{ h:0} + \text{Na}]^+$) [59]. The peaks at m/z values of 822.7 and 934.7 are likely due to the $[\text{GalCer } 22 \text{ h:0} + \text{Na}]^+$ and $[\text{GalCer } 30 \text{ h:0} + \text{Na}]^+$ ions. In contrast to MALDI-imaging-MS, where the mapping of phosphatidylcholines and galactosylceramides needs to be conducted separately using different matrices (e.g., DHB for PC, and nanoparticles for GalCer) [50, 59], both lipids could be readily detected by PESI. The ability to detect analytes nonselectively means that the suppression effect is largely moderated in PESI. In fact, PESI can be applied to samples containing high concentrations of salts, surface-active agents, or urea that are difficult to deal with by the capillary-based ES [45–47].

When a 0.1 mm-diameter acupuncture needle was used, the amount of sample caught on the tip of this needle was about a few picoliters or less, which was electrosprayed within ~ 0.1 s [42]. This duration was too short for the measurement of time-dependent PESI mass spectra. To increase the spraying time, a tangentially cut titanium wire with the larger diameter of 0.5 mm was used [47]. This enabled holding a liquid droplet with tens of nanoliters, and the spray time could be increased to tens of seconds, which was sufficient for measuring time-dependent PESI mass spectra.

Figure 8.18a shows the total ion chromatogram (TIC) for 10^{-3} M Triton X-100 and 10^{-5} M cytochrome c in H_2O – MeOH – HOAc (74:25:1) obtained by using 0.5 mm titanium wire [47].

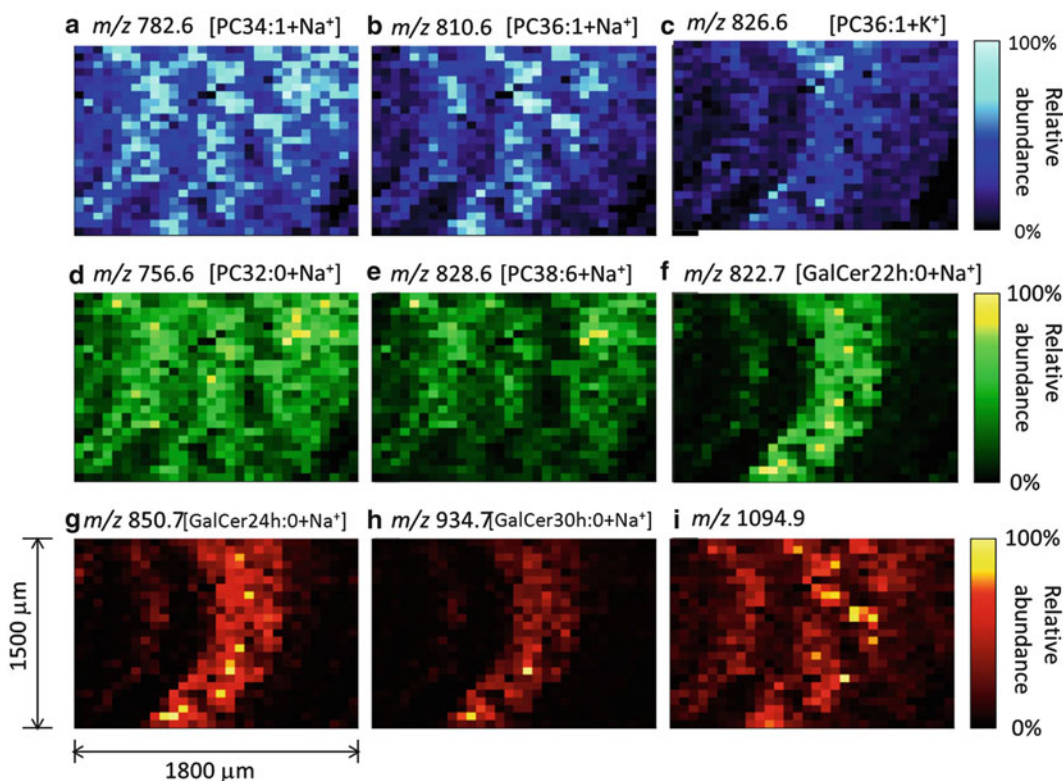


Fig. 8.17 PESI mass spectrometric images of a mouse brain (reproduced with permission from [44])

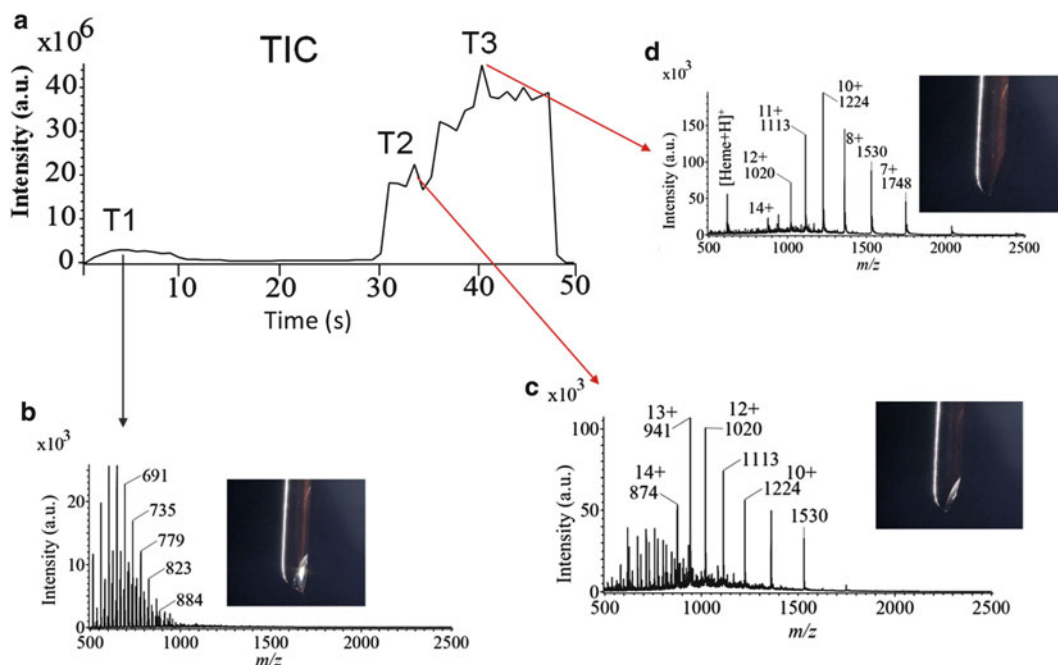


Fig. 8.18 Experimental results for 10^{-3} M Triton X-100 and 10^{-5} M cytochrome c in H_2O -MeOH-HOAc (74:25:1) obtained with 0.5 mm-diameter titanium wire. (a) Total ion chromatogram (TIC); (b) Mass spectrum measured at T1. (c) Mass spectrum measured at T2. (d) Mass spectrum measured at T3. *Insets* in (b), (c), and (d) display optical microscope images of the tip of the Ti needle measured at T1, T2, and T3, respectively (reproduced with permission from [47])

Time 0 is the moment the high voltage of 3.5 kV was applied to the needle. TIC shows an initial small increase followed by low ion current, up to 30 s. Then, TIC shows a steep increase. It is evident that ES conditions are changing during the process. Figure 8.18b–d displays the mass spectra measured at the times T1, T2, and T3 denoted in Fig. 8.18a, respectively. The insets in Fig. 8.18b–d show optical microscope images of the liquid sample attached on the titanium needle at T1, T2, and T3, respectively.

At T1, only protonated and sodiated Triton X-100, but no cytochrome c was detected in the mass spectrum (Fig. 8.18b). This trend continued just before the steep increase in TIC shown in Fig. 8.18a. The appearance of Triton X-100 only in the time interval of 0–30 s suggested that Triton X-100 was electrosprayed mainly during this period most probably because surface-active Triton X-100 was enriched on the liquid droplet surface and cytochrome c was almost totally suppressed by the presence of Triton X-100 up to 30 s.

At 30 s, sudden appearance of cytochrome c was observed (Fig. 8.18c). Apparently the electrospray condition changed at ~30 s, and this may be attributed to the decrease in the concentration of the surface-active Triton X, resulting in the availability of the liquid surface for the enrichment of the less-surface-active cytochrome c. That is, the surface excess components are being replaced from the most surface-active Triton X-100 to the less surface-active cytochrome c. This dynamic change in the constituents present on the droplet surface is reflected in the total ion chromatogram in Fig. 8.18a. The start of enrichment of cytochrome c on the liquid surface enhanced the efficiency of ES. For a comparative study of PESI with capillary-based ESI, the same solution was analyzed by nano-ESI using a 1 μm i.d. capillary. The obtained nano-ESI mass spectrum was almost similar to the PESI mass spectrum measured at T1 (Fig. 8.18b) and cytochrome c was totally suppressed by Triton X-100.

To examine the applicability of PESI to biological samples, a tissue of human breast cancer was examined [47]. The PESI mass spectra were measured after 10 μL of mixed solvent of H_2O – MeOH – HOAc (50:50:1) was dropped on the surface of a tumor tissue (Fig. 8.19).

Figure 8.19a shows the TIC that has three peaks. Figure 8.19b–d displays the mass spectra at T1, T2, and T3 denoted in Fig. 8.19a, respectively. At the initial stage of ES (T1), heme and α and β chains of hemoglobin were observed as the major ions with weaker phosphatidylcholines (PC) and triacylglycerides (TAG) signals. As time progresses (T1 \rightarrow T2), the intensities of ion signals due to hemoglobin weaken and these signals are taken over by those of PC and TAG. Ion signals of PC are observed at T1 and T2, but they decrease to the noise level at T3. Instead, sodiated TAGs become predominant at the latest stage of ES. That is, separation of components takes place in the order of hemoglobin \rightarrow PC \rightarrow TAG.

In capillary-based ES, the main part of the droplet is charge-depleted by spawning the highly charged microdroplets. In contrast, the main part of the droplet remains attached to the electrode in PESI, and thus, it is not charge-limited. Because the droplet can be electrosprayed to depletion, PESI may be the way to analyze virtually all ionizable components in the sample. In summary, analytes with different surface activities were detected sequentially in the order of their surface activity. That is, the suppression effect that is inevitable in capillary-based ESI can be minimized by PESI. Because PESI does not need any special sample pretreatment, it may be applied to perform a quick survey of wide-range real-world biological samples.

8.11 Field Desorption

When a high electric field of $\sim 10^{10}$ V/m is applied to the tip of the sharp metal needle under high vacuum, atoms or molecules approaching the tip are ionized without touching the metal surface [60]. This is the field ionization (FI) principle, on which the field ion microscope is based.

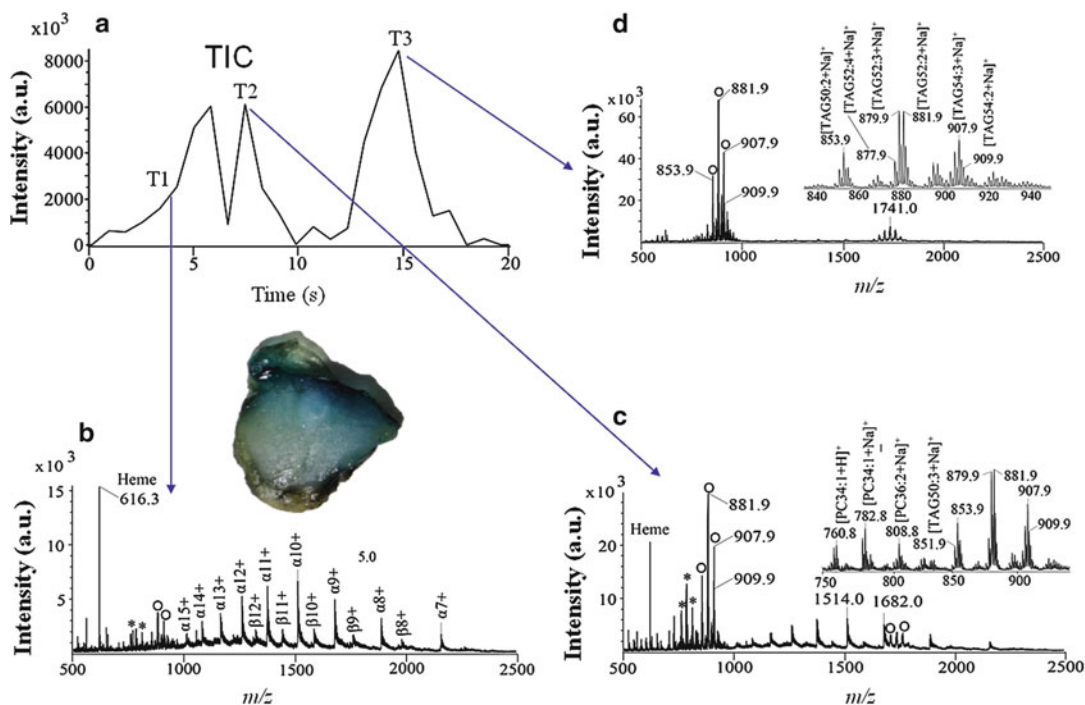


Fig. 8.19 Mass spectra for a human breast cancer tissue. (a) Total ion chromatogram; (b) mass spectrum measured at T1; (c) mass spectrum measured at T2; *Inset*: Expanded mass spectrum at m/z 750–950; (d) mass spectrum measured at T3; *Inset*: Expanded mass spectrum at m/z 840–940. Asterisks and open circles stand for peaks from phosphatidylcholines (PC) and sodiated triacylglycerides (TAG) (reproduced with permission from [47])

The ionization method for molecules deposited on fine metal needles was developed subsequently. This method is called field desorption (FD) [61]. Both of these ionization methods utilize sharp needles under high vacuum and thus are frequently discussed on the same context. However, the ionization mechanisms for these methods are basically different, and are described in the following sections.

FD operated under high vacuum may be regarded as the ultimate ES method, because single ions desorb from the sharp electrode such as a liquid metal ion source (see Sect. 8.3), making FD an excellent model to better understand ES.

Giessmann and Röllgen [62] observed the direct desorption of ions from a mixture of sucrose and NaCl under high vacuum. Figure 8.20 shows a conceptual idea of microscope images of the behavior of droplets from a concentrated aqueous solution of sucrose–NaCl (2:1).

With increasing wire temperature to ~ 100 °C, the sample was elongated toward the counter-electrode and the sample was almost completely carried away. After the major loss of the sample, residual samples formed. The effect of temperature on the sample droplet is to decrease the surface tension and viscosity of the sample. The latter also leads to an increase in the mobility of solvated ions, causing charging of the droplets in the high electric field. The field causes migration of the Na^+ and Cl^- ions in opposite directions. The Cl^- ions reaching the metal electrode surface are neutralized ($2\text{Cl}^- \rightarrow \text{Cl}_2$), and thus, the droplets are enriched by the accumulation of excess charges of Na^+ leading to the Rayleigh limit and droplet disintegration. At the stage of Fig. 8.20e, $[\text{sucrose} + \text{Na}]^+$ is generated as the major ion from the tip of the tiny cones. It should be noted that sodiated single molecules $[\text{sucrose} + \text{Na}]^+$, but not microdroplets are formed at the later stage of FD. Thus, FD may be regarded as the ultimate ES that realizes the direct evaporation of single ions from the Taylor cone. This is similar to the liquid metal ion source. The electric field necessary for single ion evaporation is

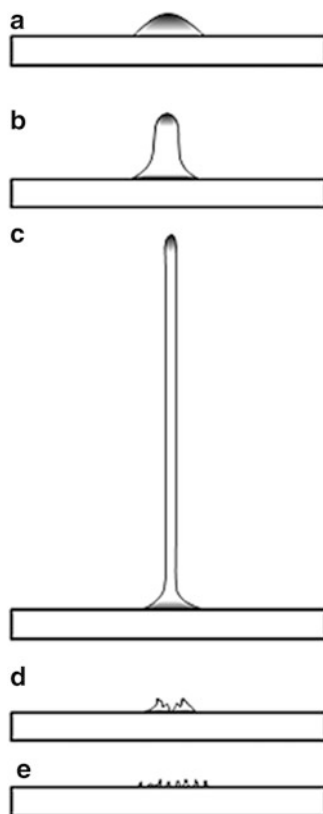


Fig. 8.20 Conceptual idea of behavior for a concentrated aqueous solution of sucrose–NaCl (2:1) deposited on a 10 μm -tungsten wire anode under the condition of FD. The anode–counter-electrode distance was 3 mm, the applied potential difference was 8 kV. The emitter heating current was slowly increased; (a) 0 mA, no change in size of the droplet, (b)–(e) current was increased from 6 to 18 mA, rupture of lamellae and formation of jets are observed. In (e) $[\text{M} + \text{Na}]^+$ was formed from the micro-cones (Taylor cones) (reproduced with permission from [62])

estimated to be 10^8 – 10^9 V/m. The species that desorb from the cone are, of course, not neutral but ionic. In this sense, FD is more appropriately defined as “field-induced ion desorption.” In contrast to FD, FI accompanies the electron tunneling in the ionization process, as described in the next section.

The electric fields generated for the conventional ESI using a 0.1 mm-diameter capillary, the nano-ESI using a few μm -diameter capillary, and PESI using a needle with 700 nm tip diameter are calculated to be $\sim 10^7$, $\sim 10^8$, and $\sim 10^9$ V/m, respectively, using (8.2). The value for PESI, $\sim 10^9$ V/m, is close to that for the ion evaporation regime. In this respect, PESI may be able to realize direct single ion desorption from the Taylor cone. However, this is not usually the case for the liquid samples, namely, fine microdroplets are formed but not the single ions (see Fig. 8.13c), because ES for solutions is a dynamic process and is far from the equilibrium, i.e., there is a voltage drop over the liquid cone and the cone angle becomes smaller than 99° [19, 54, 63]. However, in PESI, the liquid amount held on the tip becomes increasingly smaller. Actually, the liquid film becomes too thin to be recognized by the optical microscope at the last stage of spray. At this stage, strong ion signals are frequently observed (Figs. 8.18a and 8.19a). Because PESI does not adopt a continuous sample supply but the droplet trapped on the needle tip is electro-sprayed until total depletion of the sample, a phenomenon similar to FD could take place at the last stage of ES. With the depletion of the sample, the sample gets thinner. This situation must result in an increase of the electric field exerted on the liquid film. At the final stage, the sample containing nonvolatile components may become viscous by

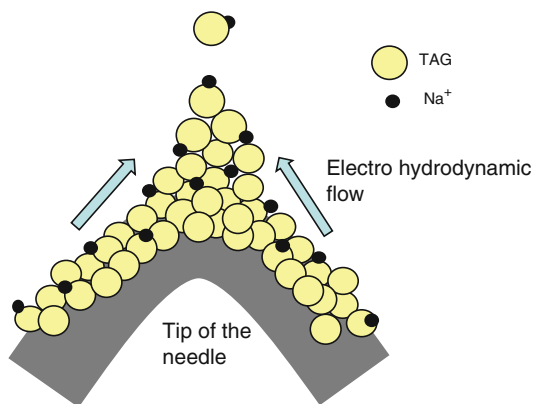


Fig. 8.21 Illustration of the desorption of ions

solvent evaporation. The thin sample film could be enriched by the excess charges with the electric field applied to the metal needle ($\sim 10^9$ V/m with the tip diameter of ~ 700 nm, see Fig. 8.21), and this value is close to the ion evaporation regime. In Fig. 8.19d, the abundant sodiated single TAG molecules were observed as dominant ions, suggesting that the ion evaporation regime, i.e., the ambient FD, is realized at the last stage of PESI (Fig. 8.21). The appearance of $[\text{TAG} + \text{Na}]^+$ in Fig. 8.19d is similar to the result that $[\text{sucrose} + \text{Na}]^+$ is the predominant ion at the last stage of FD (Fig. 8.20d) [62].

8.12 Field Ionization

In FI, atoms or molecules approaching the surface of the metal electrode are ionized by the electron tunneling process induced by the strong electric field ($\geq 10^{10}$ V/m).

Figure 8.22a shows the potential for a molecule approaching the metal surface when no electric field is applied. The ionization energy IE of the molecule is the potential difference between the highest occupied molecular orbital (HOMO) and the vacuum level; Φ is the work function of the metal and is the minimum energy necessary to remove an electron from the Fermi level into vacuum. The IE value of molecules (~ 10 eV) is usually much larger than Φ .

When a high positive voltage is applied to the metal, the potential close to the metal surface increases and the level of HOMO is lifted up. The Fermi level and the level of HOMO become the same at the critical distance x_c between the metal surface and the molecule. At x_c , (8.22) holds.

$$e[x_c \times E] = \text{IE} - \Phi. \quad (8.22)$$

Because all the energy levels of the metal above the Fermi level are vacant, an electron from the HOMO can penetrate through the energy barrier by a tunneling process when $e[x_c \times E]$ becomes larger than $[\text{IE} - \Phi]$, i.e., when FI occurs, $\text{M} \rightarrow \text{M}^{++} + \text{e}^-$. Due to the high positive electric field near the metal, the produced ion M^{++} will be repelled toward the counter-electrode. The value of x_c depends on E , IE, and Φ . Under the typical conditions of FI with $E = \sim 10^{10}$ V/m, x_c will have the values of a few to ~ 10 Å ($1 \text{ \AA} = 10^{-10}$ m), close enough for electron tunneling to occur with some probability (8.14). The ions produced by the tunneling effect are radical cations. Because the electron is lost from HOMO, M^{++} has little chance to be electronically excited and fragmentation does not take place. That is, FI is an extremely soft ionization method.

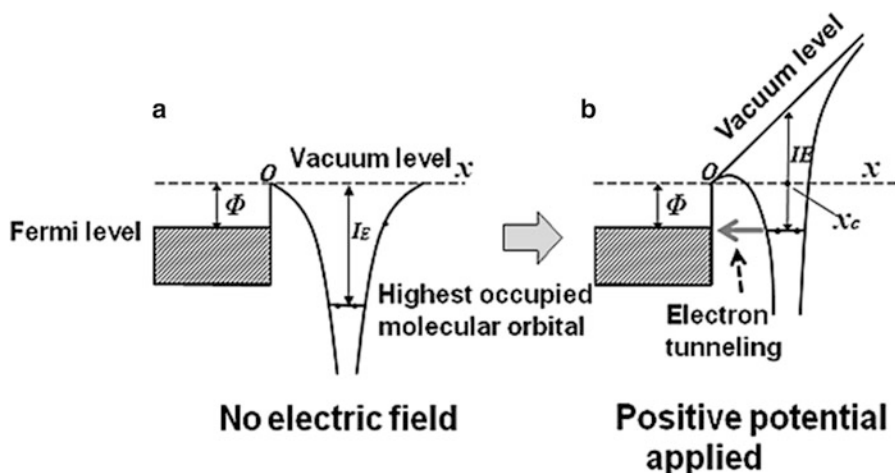


Fig. 8.22 Mechanism for FI. (a) No electric field applied. (b) A strong positive electric field is applied to the sharp metal needle. Φ : work function of the metal, x : distance of the molecule to the metal surface, x_c : critical distance where the relation $e[x_c \times E] = [I_E - \Phi]$ holds

Atoms or molecules approaching the sharp metal needle in the high electric field are attracted toward the tip. The attractive forces originate from the induced and permanent dipoles of the nonpolar/polar molecules in the high electric field. With distance smaller than x_c , FI does not take place. When molecules are not ionized by the tunneling effect with the distance of $\geq x_c$, they will enter the region within x_c , and collide with the surface. This may result in the adsorption of molecules on the metal surface. This is called “field adsorption,” and is the main cause for the contamination of FI probe tips for organic sample vapors. The contamination can be minimized by heating the FI probes. When the molecules are field-ionized, electrons produced in the gas phase bombard the metal surface and the adsorbed molecules decompose, resulting in the accumulation of insulating polymeric film. When the insulating film becomes thicker than x_c , molecules adsorbed on the surface of the insulating film can be ionized by tunneling. Because this ionization takes place on the solid surface, some ion–molecule reactions may take place, and in such a case, not only the radical cations $M^{+\bullet}$, but also the protonated molecules and other ions may be formed (e.g., $M^{+\bullet} + M \rightarrow [M + H]^+ + [M-H]^{\bullet}$), resulting in FI mass spectra that are complicated with secondary product ions.

References

1. Hogan JJ, Hendricks CD (1965) *AIAA J* 3:296
2. Drozin VDJ (1955) *J Colloid Sci* 10:158
3. Rayleigh L (1882) *Phil Mag* 14:184
4. Zeleny J (1917) *Phys Rev* 10:1
5. Fenn J, Mann M, Meng C, Wong S, Whitehouse C (1989) *Science* 246:64
6. Fenn JB, Mann M, Meng CK, Wong SF, Whitehouse CM (1990) *Mass Spectrom Rev* 9:37
7. Mann M (1990) *Org Mass Spectrom* 25:575
8. Cole RB (ed) (2010) *Electrospray and MALDI mass spectrometry*. Wiley, New York
9. Serway RA (1992) *Physics for scientists and engineers*, 3rd edn. Saunders College Publishing, Philadelphia
10. Eyring CF, Mackeown SS, Millikan RA (1928) *Phys Rev* 31:900
11. Loeb LB, Kip AF, Hudson GG, Bennett WH (1941) *Phys Rev* 60:714
12. Pfeifer RJ, Hendricks CD (1968) *AIAA J* 6:496
13. Kebarle P, Tang L (1993) *Anal Chem* 65:972A

14. Hiraoka K (1992) *Rapid Commun Mass Spectrom* 6:463
15. Hiraoka K, Fukasawa H, Aizawa K (1995) *Rapid Commun Mass Spectrom* 9:1349
16. Niessen WMA (1998) *J Chromatogr A* 794:407
17. Constantopoulos TL, Jackson GS, Enke CG (1999) *J Am Soc Mass Spectrom* 10:625
18. Taylor G (1964) *Proc Roy Soc Lond Ser A* 280:392
19. Wilm MS, Mann M (1994) *Int J Mass Spectrom Ion Processes* 136:167
20. Chen LC, Yu Z, Nonami H, Hashimoto Y, Hiraoka K (2009) *Environ Control Biol* 47:73
21. Marginean I, Parvin L, Hefferman L, Vertes A (2004) *Anal Chem* 76:4202
22. Fernandez de la Mora J, Locertales IG (1994) *J Fluid Mech* 243:561
23. Rossel J, Leiompart IG, Fernandez de la Mora J (1994) *J Aerosol Sci* 25:1093
24. Gomez A, Tang K (1994) *Phys Fluids* 6:404
25. Kebarle P, Ho Y (1997) In: Cole RB (ed) *Electrospray ionization mass spectrometry*. Wiley, New York
26. Cech NB, Enke CG (2010) In: Cole RB (ed) *Electrospray and MALDI mass spectrometry*. Wiley, New York
27. Dole M, Mack LL, Hines RL, Mobley RC, Ferguson LD, Alice MB (1968) *J Chem Phys* 49:2240
28. Schmelzeisen-Redeker Butfering GL, Röllgen FW (1989) *Int J Mass Spectrom Ion Processes* 90:139
29. Iribarne JV, Thomson BA (1976) *J Chem Phys* 64:2287
30. Thomson BA, Iribarne JV (1979) *J Phys Chem* 71:4451
31. Kebarle P, Verkerk UH (2010) In: Cole RB (ed) *Electrospray and MALDI mass spectrometry*. Wiley, New York
32. Bruins AP, Covey TR, Henion JD (1987) *Anal Chem* 59:2642
33. Takamizawa A, Fujimaki S, Sunner J, Hiraoka K (2005) *J Am Soc Mass Spectrom* 16:860
34. Takamizawa A, Maeda H, Kambara S, Furuya H, Hiraoka K (2008) *Rapid Commun Mass Spectrom* 22:2453
35. Shi X, Takamizawa A, Nishimura Y, Hiraoka K, Akashi S (2008) *Rapid Commun Mass Spectrom* 22:1430
36. Shi X, Nishimura Y, Akashi S, Takamizawa A, Hiraoka K (2006) *J Am Soc Mass Spectrom* 17:611
37. Shi X, Takamizawa A, Nishimura Y, Hiraoka K, Akashi S (2006) *J Mass Spectrom* 41:1086
38. Akashi S, Shi X, Takamizawa A, Nishimura Y, Hiraoka K (2008) *J Mass Spectrom Soc Jpn* 56:155
39. Wilm M, Mann M (1996) *Anal Chem* 68:1
40. Hiraoka K, Nishidate K, Mori K, Asakawa D, Suzuki S (2007) *Rapid Commun Mass Spectrom* 21:3139
41. Chen LC, Nishidate K, Saito Y, Mori K, Asakawa D, Takeda S, Kubota T, Terada N, Hashimoto Y, Hori H, Hiraoka K (2008) *Rapid Commun Mass Spectrom* 22:2366
42. Chen LC, Nishidate K, Saito Y, Mori K, Asakawa D, Takeda S, Kubota T, Hori H, Hiraoka K (2008) *J Phys Chem B* 112:11164
43. Hiraoka K, Chen LC, Asakawa D, Takeda S, Kubota T (2009) *J Surf Anal* 15:279
44. Chen LC, Yoshimura K, Yu Z, Iwata R, Itoh H, Suzuki H, Mori K, Ariyada O, Takeda S, Kubota T, Hiraoka K (2009) *J Mass Spectrom* 44:1469
45. Mandal MK, Chen LC, Hashimoto Y, Yu Z, Hiraoka K (2010) *Anal Methods* 2:1905
46. Mandal MK, Chen LC, Yu Z, Nonami H, Erra-Balsells R, Hiraoka K (2011) *J Mass Spectrom* 46:967
47. Mandal MK, Chen LC, Hiraoka K (2011) *J Am Soc Mass Spectrom* 22:1493
48. Adamson AW (1990) *Physical chemistry of surfaces*, 5th edn. Wiley, New York
49. Chen LC, Mandal MK, Hiraoka K (2011) *J Am Soc Mass Spectrom* 22:539
50. Chen LC, Mandal MK, Hiraoka K (2011) *J Am Soc Mass Spectrom* 22:2108
51. Atkins PW (1986) *Physical chemistry*, 3rd edn. Oxford University Press, Oxford
52. McEwen CN, Larsen BS (1997) In: Cole RB (ed) *Electrospray ionization mass spectrometry*. Wiley, New York
53. Gross JH (2011) *Mass spectrometry, a textbook*, 2nd edn. Springer, Berlin
54. Wahl JH, Goodlet DR, Udseth HR, Smith RD (1992) *Anal Chem* 64:3194
55. Emmenett MR, Caprioli RM (1994) *J Am Soc Mass Spectrom* 5:605
56. Yoshimura K, Chen LC, Asakawa D, Hiraoka K, Takeda S (2009) *J Mass Spectrom* 44:978
57. Loscertales IG, Fernandez de la Mora J (1995) *J Chem Phys* 103:5041
58. Jackson SN, Ugarov M, Egan T, Post JD, Langlais D, Schultz JA, Woods AS (2007) *J Mass Spectrom* 42:1093
59. Taira S, Sugiura Y, Moritake S, Shimma S, Ichiyanagi Y, Setou M (2008) *Anal Chem* 80:4761
60. Müller EW (1953) *Ergebnisse der Exakten Naturwissenschaften* 27:290
61. Beckey HD (1977) *Principles of field ionization and field desorption mass spectrometry*. Pergamon Press, Oxford
62. Wong SS, Giessmann U, Karas M, Röllgen FW (1984) *Int J Mass Spectrom Ion Processes* 56:139
63. Sen AK, Darabi J, Knapp DR, Liu J (2006) *J Micromech Microeng* 16:620

MALDI: A Very Useful UV Light-Induced Process . . . That Still Remains Quite Obscure

9

Rosa Erra-Balsells

9.1 Introduction

The matrix-assisted laser desorption ionization (MALDI) process constitutes a complex mixture of events, involving optical and mechanical phenomena, as well as thermodynamic and physicochemical processes of phase transition and ionization. The experiment is based on irradiation of the surface of a solid sample that is a mixture of a photosensitizer material (the matrix) and analyte(s) with a short-pulse UV laser. A successful MALDI analysis involves a number of crucial steps, namely, sample preparation, UV excitation of the matrix (photosensitizer)–analyte sample and disintegration of the condensed phase, generation and separation of charges and ionization of analyte and matrix molecules, and, finally, in the analysis step, ion separation according to the mass-to-charge ratio in the mass spectrometer, and detection (Fig. 9.1).

Despite the rapid adoption of the technique in various areas of science (i.e., chemistry, biology, physics, biomedicine, synthetic polymers, etc.) after its introduction almost 25 years ago [1, 2], for a long time its mechanisms have not been fully understood, and a more comprehensive picture has only recently begun to emerge.

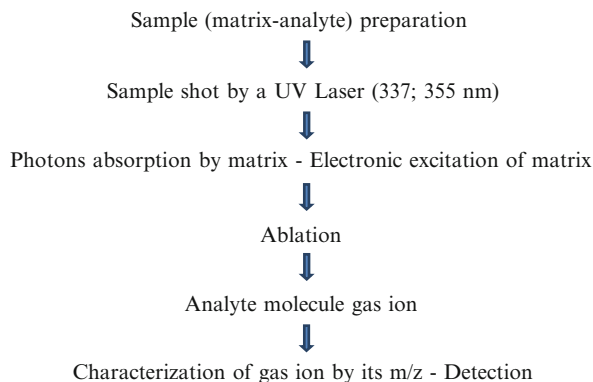
One of the most straightforward experimental tools for gaining insight into mechanisms is the systematic variation of one or more of the relevant input parameters and consequently a large number of fundamental studies into MALDI have followed this method. The roles of the different relevant irradiation (laser) parameters in the desorption/ionization process, as well as those of the matrix and the preparation protocol, have been addressed in these investigations. These included, for example, the roles of the laser parameters, such as wavelength, pulse duration, and fluence (laser energy per pulse and unit area), the nature of materials, the type of (co-)crystallization, and the incorporation of analyte molecules into matrix crystals [3, 4 and references therein]. Other works have addressed the dynamical parameters of the expanding MALDI particle “plume”: the initial kinetic energies and energy distributions of molecules and ions, and the composition of the plume (ion-to-neutral ratio and ejection of particles and clusters versus the emission of molecular constituents) [3, 4 and references therein].

R. Erra-Balsells (✉)

Organic Photochemistry and UV-MALDI MS Laboratory, CIHIDECAR (CONICET), Organic Chemistry Department, Faculty of Exact and Natural Sciences, University of Buenos Aires, Pabellón II, 3er P., Ciudad Universitaria, Buenos Aires 1428, Argentina

e-mail: erra@qo.fcen.uba.ar

Fig. 9.1 Schematic diagram of an ideal MALDI mass spectrometry experiment



Several researchers have developed theoretical models for the desorption–ablation, as well as for the ionization processes. By far the largest part of experimental investigations has naturally been focused on the MALDI ions as detected in a mass spectrometer. In interpreting these data, it should be kept in mind that ion formation is generally the combined result of three processes, i.e., electronic excitation, desorption–ablation and ionization, and this fact may easily conceal relevant details of any of the three processes [3–5].

The present chapter deals with the fundamental principles for understanding the basics of the electronic excitation process, its deactivation pathways, and the current knowledge on desorption–ablation.

9.2 Electronic Excitation of Molecules

Photochemical activation differs from thermal activation because of its selectivity. The absorption of a photon (quantum of energy) of light can selectively excite (activate) a specific bond or group in a given molecule. The use of exciting light with the proper wavelength allows activation of a solute molecule (minor component in a mixture) in the presence of a large excess of nonabsorbent (transparent) solvent–environment (mixture bulk) [6, 7].

Energies: Any photochemical process sequence includes the initial act of absorption and other processes that involve an electronically excited state of the absorbing molecule. The energy required to create an excited state is obtained from the absorption or emission spectrum of the particular molecule [6, 7], and the application of the equation:

$$E_2 - E_1 = h\nu = hc/\lambda, \quad (9.1)$$

where h is the Planck constant, ν is the frequency (s^{-1}) at which absorption occurs, and E_1 and E_2 are the energies of the molecule in the final and initial electronic states respectively (in kcal/mol). The position of an absorption band is often expressed by its wavelength (λ) in nanometers or its wavenumber ($\nu' = 1/\lambda$) in cm^{-1} . The amount of energy produced through the absorption of one mole of photons (6.02×10^{23} photons) by a compound at a given wavelength is called an Einstein. Thus, the 200 nm wavelength ($\nu' = 50,000 \text{ cm}^{-1}$) is equivalent to $E_2 - E_1 = 143.0 \text{ kcal/mol} = 6.20 \text{ eV}$, and the 700 nm ($\nu' = 14,286 \text{ cm}^{-1}$) wavelength is equivalent to $E_2 - E_1 = 40.8 \text{ kcal/mol} = 1.77 \text{ eV}$ [8, 9].

Photochemical laws: Four important photochemical rules or laws have evolved over the years that apply quite generally to molecular photochemistry. These may be stated as follows.

(1) Only the light absorbed by a system is effective in producing a photophysical–photochemical change. (2) Each photon or quantum absorbed activates one molecule in the primary excitation step of a photophysical–photochemical sequence. (3) Each photon or quantum absorbed by a molecule has a certain probability of populating either the lowest excited singlet state, S_1 or the lowest triplet state, T_1 , and (4) the states of S_1 and T_1 are in general the starting points of most molecular photophysical–photochemical processes [8, 9].

A photochemical reaction requires activation by light. The quantitative relationship between the number of molecules that react or are formed and the number of photons absorbed in a unit of time is called quantum yield (ϕ).

Electronic excitation in molecules: The discrete energy states that a molecule can reach–populate are expressed by molecular wave functions that are the solutions of the Schrödinger equation

$$H\Psi_n = E_n\Psi_n, \quad (9.2)$$

where H is the quantum mechanical Hamiltonian, the operator whose eigenvalues or solutions E_n are the possible energy levels of the molecule [8, 9]. The molecular wave functions determine the value of physically observable properties of the molecule. The mean value of the observable in the state described by Ψ_n is given by the integral

$$P = \int \Psi_n^* \Pi \Psi_n dr = (\Psi_n / \Pi / \Psi_n), \quad (9.3)$$

where Ψ_n^* is the complex conjugate of Ψ_n , Π is the operator corresponding to the observable property P , and the integration is over the spin and space coordinates of all the electrons of the molecule. The form of the quantum mechanical operator that corresponds to a particular observable is usually obtained from the corresponding classical expression. The correctness of an operator is verified if it gives parameter matching with the experimental data.

Electronic orbitals (EOs) and electronic spin in molecules: The molecular wave function Ψ defines the orbitals and properties of electrons in molecules. From the energetic point of view (values of energy of the electrons) the square wave function Ψ^2 defines the probability density in a region of space that electrons can occupy with the corresponding Eigen value of energy associated to this state. For each electron, a boundary surface can be defined that confines most of the electronic charge (>95 %) and is the pictorial representation of an EO. A complex molecule has a large number of such orbitals, which may be described by a family of primary functions ψ_n , and then the molecular wave function Ψ is expressed as a linear combination of atomic orbitals (LCAO) for the molecular orbital (MO),

$$\Psi \sim c_1\psi_1 + c_2\psi_2 + c_3\psi_3 + c_4\psi_4 + c_5\psi_5. \quad (9.4)$$

The orbitals ψ_n may be essentially localized on one nucleus, i.e., an unperturbed atomic orbital, AO, or delocalized over two or more nuclei, i.e., MO. Each ψ_n may describe an unperturbed AO essentially localized in one nucleus, or an MO delocalized over two or more nuclei. Each ψ_n is approximately the product of a space ϕ part and a spin part α or β . As a consequence of the mathematical model used for the description of the electronic structure of atoms and molecules, each AO or MO may accommodate no more than two electrons, and they must have opposite spin functions, which means that the spins must be paired as follows:

$$\psi_n = \phi_n(\alpha) \phi_n(\beta), \quad (9.5)$$

where α represents an electron in ψ_n with spin $+1/2$, and β represents a second electron in ψ_n , with spin $-1/2$ (the Pauli principle) [8, 9]. The orbitals ϕ_n are generally approximated by one-electron orbitals (the Hückel theory), which have the form of the solution of the equation $H\Psi_n = E_n\Psi_n$, for the hydrogen atom (H^*), which can be solved rigorously by the quantum mechanics theory. To find the mathematical solution of this equation, some approximations are taken into account, as follows: (a) the one-electron Hamiltonian (H) approximation is usually used, which ignores electrostatic interactions between electrons; (b) it is assumed that the nuclei are in their equilibrium positions; (c) the spin functions are factored out, then the molecular wave function is expressed as

$$\Psi \sim \phi(\text{electronic})\chi(\text{vibration})\delta(\text{spin}), \quad (9.6)$$

where ϕ is the electronic part of the wave function, χ is the nuclear wave function (vibration), and δ is the spin wave function. Furthermore, an electron wave function ψ_n may be expressed as

$$\psi_n = c_1\phi_1 + c_2\phi_2 + c_3\phi_3, \quad (9.7)$$

where the eigenfunctions or orbitals ϕ_n ($n = 1, 2, 3, \dots$) are the AO eigenfunctions. These orbitals are filled with a maximum of two electrons in accordance with the Aufbau principle (which states that the lowest energy orbitals are filled first), and the Pauli principle [8, 9]. In summary, each ψ_n describes an electronic configuration.

MOs: Five types of MOs should be taken into account to describe the photo-processes of molecules. As previously mentioned, “five types of molecular orbitals” means five types of electrons located in five different molecular orbitals (or five types of electrons) ψ_n . These entities are; pi-bonding (π), pi-antibonding (π^*), nonbonding (n), sigma-bonding (σ), and sigma-antibonding (σ^*) orbitals [8–10]. Single or covalent bonds (i.e., C–C) between two atoms involve σ orbitals and the electrons located in these orbitals are called σ electrons. These electrons form strong and quite localized bonds in the spatial image of the chemical bonds in a molecule. As a consequence, these electrons require higher excitation energy to yield an electronic excited state with σ^* populated than the π electrons that occupy the π orbital of a simple two-atoms double-bond (i.e., C=C; N=N; C=O, C=N) or multiple-bond orbitals shared by several even-number atoms (i.e., C=C–C=C–C=O; C=C–C=C–C=C; C=C–N=C–C=C). According to the MO theory, each MO is mathematically constructed as described, by two orbitals with quite different values of energy associated: for each σ and π orbital there are the corresponding σ^* and π^* orbitals, called antibonding orbitals, because of the higher respective energy content ($\sigma^* > \sigma$ and $\pi^* > \pi$). The so-called heteroatoms (i.e., O, N, S, halogen atoms, etc.) in hydrocarbons have nonbonding (n) orbitals whose electrons do not take part in the covalent bond formation. These n orbitals are essentially localized on one particular heteroatom. The counterpart vacant AO, or n^* , is not taken into account because the energy level is so high that commonly available light sources are not enough to excite the n – n^* transition, i.e., the wavelengths are beyond the orders of magnitude of the source energy used in the field of photochemistry, and analytical techniques such as electronic spectroscopy (UV–Visible absorption spectroscopy, luminescence spectroscopy, fluorescence and phosphorescence emission spectroscopy, optoacoustic spectroscopy, steady state techniques, or time-resolved spectroscopies that use lamps, flash lamps, and pulse UV-laser as sources) [11–13].

Examples of the n orbital in molecules. The n electrons and orbitals play a key role in the interaction between the UV–Visible radiation and material. They are quite important because they are often involved in the lowest energy electronic transition for molecules containing heteroatoms such as N and/or O. These orbitals are called nonbonding because they take little part in the bond of the

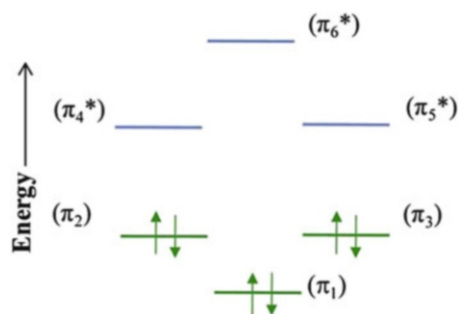


Fig. 9.2 Relative energy content of the π molecular orbitals of benzene (C_6H_6) and distribution of the 6π electrons in the ground state (S_0)

molecule and concentrate its mathematical probability-density description near heteroatoms and are almost absent in between nuclei (chemical bond) [8–10]. For example, in the case of the carbonyl group $C=O$, the n orbital is essentially a localized atomic p orbital of the oxygen atom, whereas in amine (N-containing) compounds it can be an atomic p orbital of a primary, secondary or tertiary aliphatic amines (NH_3 , CH_3NH_2 ; $(CH_3)_2NH$; $(CH_3)_3N$, etc.) or a hybrid orbital sp^2 in pyridine species $(HC)_5N$. The n electrons show atomic character when they are located in orbitals perpendicular to π orbitals present in the surrounding molecular structure. This nonbonding character disappears when—because of the structure of the chemicals groups and the molecule—lone-pair n electrons occupy an orbital parallel to or coplanar with π orbitals, and the so-called conjugation effect takes place. In this situation the n electrons become more delocalized and as a result the quantum of energy required to raise the energy level to the excited state is quite different than that for atomic-like localized n electrons.

Examples of π orbital present in molecules: The ligand (bonding) π and antiligand (nonbonding) π^* MO are delocalized over two (i.e., $C=C$; $C=O$) or a higher number of nuclei (i.e., $C=C-C=O$; $C=C-C=C$) [10]. These orbitals are described as a linear combination of atomic p orbitals. For each π orbital the MO theory generates a corresponding π^* orbital, which has one additional node between the constituents atoms compared with the corresponding π , and thus a higher energy content. The higher number of electronic transitions in molecules involve π and π^* and n orbitals. The $n-\pi^*$ and $\pi-\pi^*$ transitions are very important in photochemistry because these orbitals are present in the functional groups that absorb photons from UV light sources. The molecule of benzene is a good example to introduce another concept of MO theory. The π MOs in this example are three ligands, and three antibonding and six π electrons need to be distributed among them. The lowest MO π_1 is unique in energy and is called nondegenerate, but the next two bonding orbitals, π_2 and π_3 are of equal energy and for this reason are called degenerate. This degeneration property is also shown by the next antibonding orbitals, π_4^* and π_5^* . Finally, the highest energy anitboding π^* orbital, π_6^* is again unique in energy and is a nondegenerate orbital (Fig. 9.2).

Examples of the σ orbital in molecules: The σ bonding orbitals are of lower energy than the bonding π orbital and the nonbonding n orbitals. Correspondingly, the σ^* orbitals are of higher energy than the π^* . Although the σ bonds are common to all structures (all molecules have occupied σ and empty σ^* orbitals), the electronic transitions involving σ and σ^* orbitals are in general not used, because the amount of energy involved populates electronic excited states that are extremely reactive (nonstable) and the σ bond is easily broken. Furthermore, as it is not experimentally easy to manipulate energy sources with such high-energy photons, these transitions are in general not explored from the practical

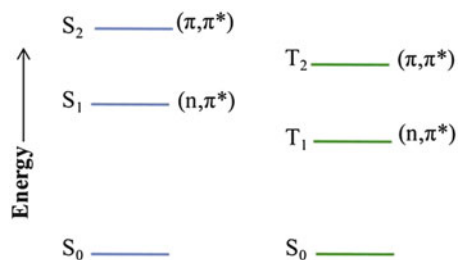


Fig. 9.3 Relative energy content of the ground state (S_0) and excited n,π^* (S_1 and T_1) and π,π^* (S_2 and T_2) states for the carbonyl group ($-\text{C}=\text{O}$)

point of view. The σ^* orbital has a node between the atoms forming the σ bond, and this causes the breaking of the bond when an electron is promoted to this orbital [8–10].

Electronic configurations and electronic states: The molecule electronic configuration is reached by adding electrons to orbitals that are available or vacant and are characteristic of the molecular system. The ground state is defined as the state of lowest energy and is so characterized because the electrons are distributed among the orbitals of lowest energy according to the Aufbau, Pauli, and Hund rules [8, 9]. Excitation by absorption of a photon of appropriate energy will promote an electron from one of the occupied low-energy MOs to one of high energy, a vacant antibonding orbital.

The ground state configuration: In the ground state, each of the orbitals in this configuration contains two electrons. In general the energy order of the molecular orbitals, the number of available electrons and the Pauli and Aufbau principles are employed to create the ground-state configuration of a molecule. Physically, the total electron distribution of a configuration may be approximated as the superposition of all one-electron AOs that make up the configuration of the molecule [8, 9].

Excited state configurations and transitions between states: As previously mentioned, in general the transitions involving σ and σ^* orbitals are not used because of the occurrence of photodegradation or photochemical transformation. Thus, transitions involve in general n , π , and π^* orbitals. The excitation of an n electron into a π^* orbital is called an $n-\pi^*$ transition and the resulting excited state is called an n,π^* state. Similarly, excitation of π electrons into a π^* state is called a $\pi-\pi^*$ transition and creates a π,π^* state. The Pauli principle demands that any ground state configuration in which the electrons are paired in orbitals must be a ground-state singlet; the spins of the two electrons in each orbital are paired, and this is defined as a ground-state singlet (S_0). In the excited state, two electrons are orbitally unpaired, with each electron in a different orbital. As a result, the Pauli principle establishes no prohibition regarding the spin of these two electrons. Then, either of two states can be produced: (1) a singlet excited state in which there is no net spin because electron spins are paired as in the ground state, or (2) a triplet state (T_n), where the two electrons, which are orbitally unpaired and now possess parallel spins, may result from the same electronic configuration of the orbitals (Figs. 9.3 and 9.4). That means that each of the excited n,π^* and π,π^* states may be either a singlet (S) or a triplet (T).

Despite the large number of electrons that even small molecules possess, most of the photoinitiated processes involve only the lowest excited states and one or two electrons located in the highest energy occupied bonding molecular orbitals (HOMO). Each particular excited state has a characteristic energy, lifetime and electronic distribution. In reality, a molecule in one of its electronic excited states is a different chemical species than that at ground-state. The excited states are expected to be considerably more reactive because of their high energy content and peculiar electronic distribution

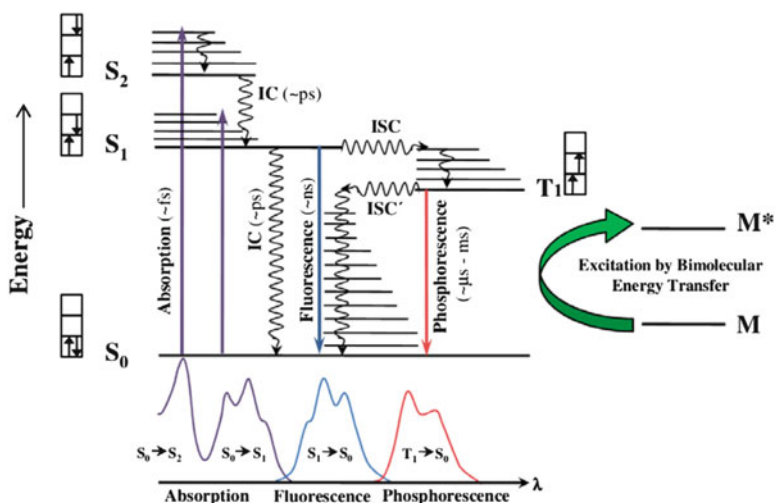


Fig. 9.4 Modified Jablonski diagram. Electronic states of a molecule and the transitions between them. The states are arranged vertically by energy and grouped horizontally by spin multiplicity. Radiative transitions are indicated by *straight arrows* and nonradiative transitions by *squiggly arrows*. The vibrational ground states of each electronic state are indicated with *thick lines*, the higher vibrational states with *thinner lines*

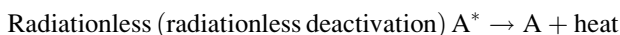
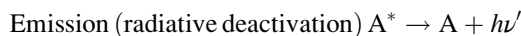
(paired or unpaired electrons in two different orbitals). The peculiar character of the photoinitiated processes is that energy necessary to produce such activation is supplied by the photons of the light source (lamp; laser).

Energy level diagrams: State or energy level diagrams are quite satisfactory for describing electronic transitions that take place upon absorption of a photon (Fig. 9.4). Nowadays this presentation is called “the modified Jablonski diagram” in honor of Prof. A. Jablonski, who illustrated the electronic states of a molecule and the transitions between them (the molecular absorption and luminescence process) with this sort of display for the first time in 1933 [14]. In these diagrams the energy of the lowest vibrational level of each electronic state is shown (thick lines), and the other vibrational levels of each electronic state (thinner lines) are also detailed, relative to the energy of the lowest vibrational level of the electronic ground state. The energy levels are represented by horizontal lines such that the vertical distance between any two of these lines corresponds to the energy difference between the states. The energy is shown at the left, on the y axis, and the ground state, S_0 , is arbitrarily assigned as a relative energy value zero. The singlet and triplet states (states with different multiplicity) are indicated separated on the left and right hand sides of the diagrams, but the abscissa has no physical meaning in these diagrams. The electronic transitions indicated in the diagrams could represent absorption or emission of light (photons) and are represented conventionally by a solid line, while radiationless transitions are represented by a squiggly arrow. For each transition the triplet state is of lower energy than the corresponding singlet state. This fact results from the Pauli principle that establishes that orbitally unpaired electrons with parallel spin cannot occupy the same orbital. Thus, the electron–electron repulsion is drastically reduced. This restriction is not operating for the corresponding singlet state, and stronger repulsion occurs, so that this state has a higher energy than the corresponding triplet.

Photochemical processes: All photochemical reactions involve electronically excited states at some point (step). Each excited state has a definite energy, lifetime, and structure. These properties may be somewhat different as we go from one state to another. In addition, as mentioned earlier, the excited

states are different chemical entities than the ground state and are expected to behave differently. To understand the photochemical processes, information relating to the energies, lifetime, and structures of the electronically excited states should be taken into account.

Electronically excited state: The excitation energy acquired by a molecule of analyte A upon absorption of a photon (in the reaction $A + h\nu \rightarrow A^*$ (*S* or *T*)) may be dissipated in any of the three following general processes.

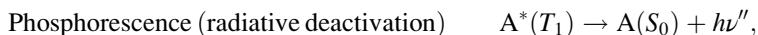
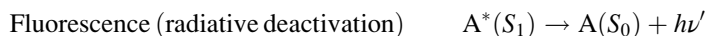


9.3 Deactivation of Excited States

9.3.1 Unimolecular Processes

Radiative deactivation and light emission: The radiative lifetime of an excited state may be often defined in terms of a first-order decay process. It is important to differentiate between the inherent radiative lifetime τ^0 of a state (the reciprocal of the rate constant for the disappearance of this state if emission were the only path of energy dissipation), and the measured lifetime τ , which is the reciprocal of the sum of the rate constants of the number of competing deactivation first-order (or pseudo-first-order) processes that really take place [11–13].

The time scale of a photochemical sequence is set by the rate of spontaneous radiative emission to the ground state A_0 (S_0) from A^* in S_1 or T_1 state; i.e., no reaction that competes for deactivation of these states can require much longer time than τ^0 for emission, otherwise the latter process will dominate. Fluorescence is the phenomenon of emission from A^* in the lowest singlet state S_1 to the ground state A in S_0 (Fig. 9.4). The inherent fluorescence lifetime of S_1 varies from picoseconds to nanoseconds and microseconds for most bio and organic molecules. Phosphorescence is the emission from the A^* in triple state T_1 to ground state A in S_0 state (Fig. 9.4). The inherent phosphorescence lifetime of T_1 varies for most molecules from 10^{-6} to 10^{-3} to 10 s.



where $h\nu'' < h\nu'$ and $\lambda_p > \lambda_f$, with λ_p and λ_f representing the wavelengths of phosphorescence and fluorescence emission, respectively (Fig. 9.4) [11–13].

Radiationless processes and heat emission: A radiationless process converts one electronic state to another without absorption or emission of radiation. Excesses of vibrational energy that result from a radiationless process are carried away rapidly as heat, by collision with the surrounding molecules in fluid (liquid or gas state) or quasi-solid systems or may induce ablation of solids (see details in Sects. 9.5 and 9.6). Two important types of radiationless processes are:

1. Internal conversion (IC)—the intramolecular radiationless conversion between different electronic states of the same multiplicity (singlet–singlet, i.e., S_2 to S_1 ; S_1 to S_0 (Fig. 9.4); triplet–triplet, i.e., T_2 to T_1 ; T_1 to T_0) (not shown).
2. Intersystem crossing (ISC)—the intramolecular radiationless conversion between singlet and triplet states (singlet–triplet, i.e., S_1 to T_1 ; triplet–singlet, i.e., T_1 to S_0) (Fig. 9.4).

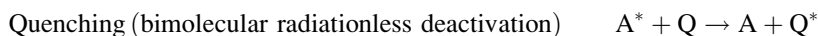
All radiationless transitions involve some type of energy transfer (heat transfer) from the excited molecule A^* to its environment. This energy may be transferred in large portions (conversion of electronic energy to vibrational energy in the form of heat. Figure 9.4, i.e., IC among different electronic states: S_1 to S_0 ; ISC among different electronic states: T_1 to S_0) or in relative small portions (conversion of electronic energy to vibrational, rotational, and translational energy. Figure 9.4, i.e., IC among vibrational excited states of an electronic state, see details in S_2 state or in T_1 state).

Photochemical reactions: The molecule photochemistry or molecule photoreactions are a special case in which unstable species produced from electronically excited states and/or the same excited state are involved in a chemical reaction. Then, chemical compounds (products) other than the irradiated and electronically excited analyte A , appear in the irradiated system. A mechanistic investigation of a photoreaction should indicate whether the reactive state is S_1 and/or T_1 or whether the deactivation of these states produces hot ground states (molecules in the ground state produced in upper vibrational levels of S_0), unstable radicals, anionic radicals, tautomers, etc., which yield the final products of the reaction.



9.3.2 Bimolecular Processes

The bimolecular deactivation, called quenching of the excited state is any deactivation process that involves the interaction of the excited molecule A^* with another molecule component of the surrounding or, in general, of the system. If a particular molecule is dramatically efficient at promoting the quenching process, it is possible to suppress all the other deactivation processes of the species A^* (see Fig. 9.4; on the right side, the bimolecular process M to M^* , where M is an energy acceptor molecule). Then, together with the possible unimolecular deactivation steps detailed in Fig. 9.4, the following reaction needs to be taken into account:

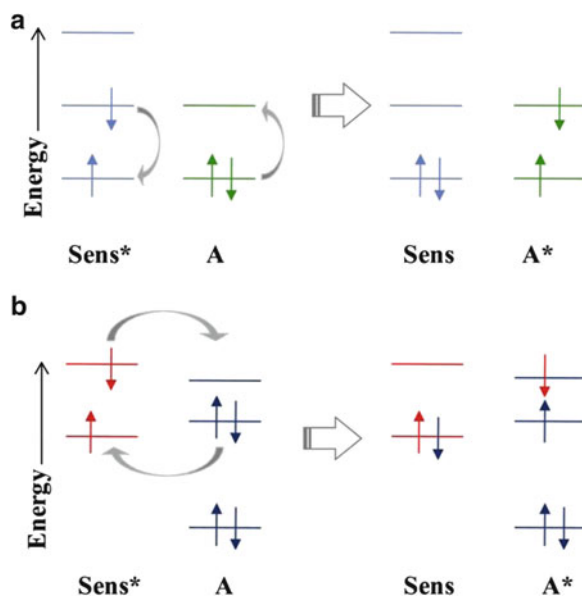


After formation of Q^* (which may be a singlet or triplet), the Q^* can disappear through emission (fluorescence or phosphorescence), or by radiationless (heat) or photoreaction processes.

Mechanism of Energy Transfer: The intermolecular energy transfer defines the radiationless, one-step transfer of electronic excitation from a donor molecule (or sensitizer) in the excited state ($Sens^*$) to an acceptor molecule A , where now A is working as quencher. The peculiarity of this mechanisms is that the energy of the excited state A^* must be lower than that of $Sens^*$ (at least slightly lower), as a condition for the energy transfer process to be efficient. Furthermore the process must occur within the time τ that the molecule of the sensitizer remains in the $Sens^*$ state.

Two different mechanisms have been suggested to explain the electronic energy transfer and the corresponding theory established [12, 15].

Fig. 9.5 Bimolecular energy transfer. Energy restriction for the pair energy donor (Sens*) energy acceptor (A). Process (a) without exchange of electrons and (b) with exchange of electrons



1. The transfer takes place only if the two molecules approach each other to be in molecular contact (a distance shorter than their collision diameters).
2. The transfer occurs between molecules separated by distances longer than their collision diameters.

Clearly, the rates of transfers that proceed by mechanism (1) are limited by the diffusion of the molecules in the surrounding environment (liquid, gas, solid) and decreases in viscous media because of the slower rate of diffusion. In contrast, the rates of transfers occurring by mechanism (2) are no so limited and would be expected to be independent or not affected by the viscosity of the medium. This process does not depend on direct encounter of acceptor A and sensitizer Sens* during the lifetime of the latter. Several years ago, Förster [16] showed that the necessary interaction occurs between the quantum mechanical transition moments (dipole–dipole) that also determine the absorption and emission properties of individual molecules. This interaction is strongest if the corresponding dipole transitions in both Sens* emission and A absorption are allowed (singlet–singlet or triplet–triplet transition). This mechanism is also called “resonance energy transfer” (nowadays named Förster resonance energy transfer, FRET).

In connection with the former mechanism, the contact energy transfer is possible when Sens* and A are close enough so that their electron clouds overlap. In the overlap region the electrons are indistinguishable, so that an excited electron of Sens* has the probability of appearing on A. Some sort of mechanism of electrons exchange and energy transfer operates, although no ionic species is produced as a result (Fig. 9.5b).

If the exchange energy transfer leads to an electron transfer from one species to the other, the so-called “photoinduced electron transfer” (PET) occurs. As a result, from a neutral Sens* and A pair, a cation-radical/anion-radical pair is produced (Fig. 9.6).

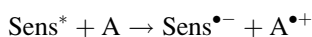
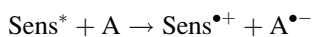
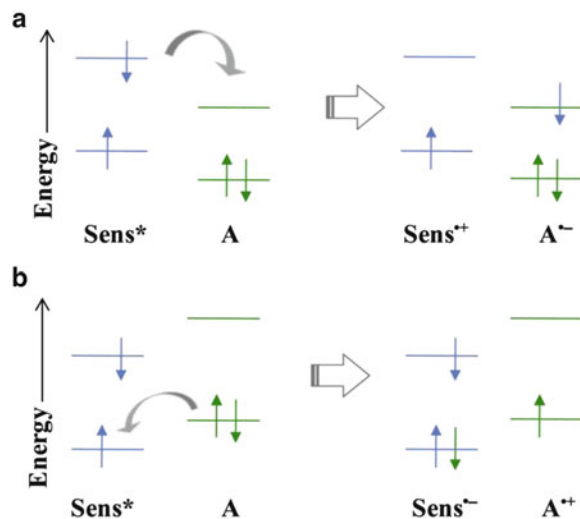


Fig. 9.6 Bimolecular photoinduced electron transfer (PET). Energy restriction for the pair neutral Sens^* and A. Production of (a) $\text{Sens}^{++}/\text{A}^{-}$ pair and (b) $\text{Sens}^{\cdot-}/\text{A}^{\cdot+}$ pair



Furthermore, as a result of the molecular interaction, the exchange of a hydrogen moiety can occur from the Sens^* to A (or from A to Sens^*), and a pair of neutral radical species (highly reactive species) can be formed:

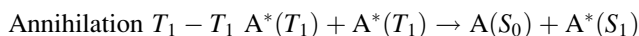


If the exchange of hydrogen occurs simultaneously with the electron transfer (net proton transfer) the following processes can take place:



9.3.3 Bimolecular Triplet-Triplet Annihilation

The bimolecular interaction between two electronically excited molecules is so small because several factors such as short lifetime and low concentration of excited states that make molecular collision-interaction almost impossible or low probable. However, under certain conditions, two long-lived triplets $\text{A}^*(T_1)$ may collide with one another and simultaneous annihilation takes place, producing one molecule at the ground state $\text{A}^*(S_0)$ and the other at the excited singlet state $\text{A}^*(S_1)$:



Then, if straight deactivation of $\text{A}^*(S_1)$ by emission occurs, the fluorescence of A^* would be observed, but with a lifetime τ_f similar to or higher than the triplet state of A. The cause of the longer τ_f value is that the original excitation has resided for a while in A^* as T_1 , with a longer τ_p .

The yield of this delayed fluorescence depends upon the square of the intensity of the exciting light, because two photons are necessary to produce one molecule in the excited singlet state ($\text{A}^*(S_1)$).

Fig. 9.7 Homo-bimolecular T_1 - T_1 annihilation ($A^*(T_1)$ with $A^*(T_1)$)

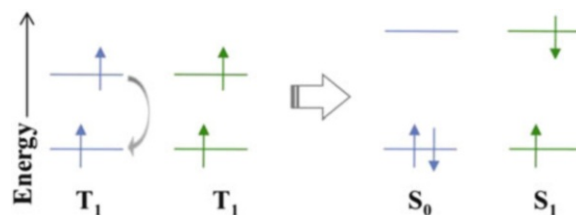
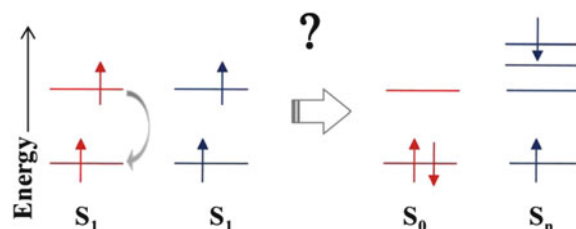


Fig. 9.8 Possible homo-bimolecular S_1 - S_1 annihilation ($A^*(S_1)$ with $A^*(S_1)$)



The triplet-triplet annihilation mechanism requires that part of the energy from two separately absorbed photons be transferred to the same molecule. This mechanism can be used to produce an excited singlet state $A^*(S_1)$, capable of emitting a photon of higher energy (lower wavelength) than that of the absorbed photons. This phenomenon can occur as a homo-bimolecular annihilation (A^* with A^*) and hetero-bimolecular annihilation (A^* with B^* , with A and B different molecule species) (Fig. 9.7).

The possibility of this bimolecular event opens some very attractive and challenging photochemical theoretical areas for the applications and understanding of processes starting from an electronically excited molecule. Triplet-triplet annihilation has been described as a very efficient process in the gas state, solid crystals and solid solutions. Although the development of higher energy molecular sources is a most attractive feature, in the current state of the art the photochemistry associated with this topic is still quite unexplored. Recently, some authors have used a similar annihilation but involving S_1 states (S_1 - S_1 annihilation) mechanism to explain some of the photochemical events that would occur in MALDI [4]. In the MALDI process high-density S_1 states may be formed for the matrix at the laser spot and S_1 - S_1 annihilation may occur, yielding a matrix in an S_n state with higher energy content (Fig. 9.8); however, concrete experiments showing S_1 - S_1 annihilation processes have not yet been described in the literature.

9.4 Nanomaterials

Because of their unique electronic nature, semiconductor and metal nanoparticles (i.e., TiO_2 ; CdS; Au; Ag; etc.) are at the center of scientific interest; they follow quantum mechanical rules instead of the laws of classical physics that govern bulk materials behavior. In general, we call these compounds nanoparticles, which implies that predominantly they do not exhibit classical bulk properties, while, on the other hand, differing from molecules by the fact that in some way they represent pieces of matter with properties related to the bulk material they originate from. This section of the chapter is called Nanomaterials (nanoparticles-quantum dots), as it deals with these very special properties of matter in the nanosize regime. Understanding the behavior of quantum-confined electrons in very small particles

is the basis for the understanding of physical properties among which the optical are of interest for their application in soft ionization-assisted laser desorption methods for mass spectrometry. Tanaka et al. used fine metal powder as photosensitizer in their early work [1]. Recently, diverse nanomaterials (i.e., carbon nanotubes; nanoparticles) have been extensively used as photosensitizers (matrices) in MALDI MS also called SALDI MS (surface assisted laser desorption ionization mass spectrometry) [3, 4, 17].

In the last decade, new directions of modern research, broadly defined as nanoscale science and technology, have emerged [18]. Materials science and technology are evolving at fast speed and are currently producing the most significant contributions to nanoscale research, a field driven by the desire to fabricate materials with novel or improved properties, such as, strength, electrical and thermal conductivity, optical response, elasticity, or wear resistance.

In connection with optical response, the behavior of nanoscale materials can be remarkably different from that of bulk materials and from their atomic counterparts and quantum mechanics can help in rationalizing this. For this reason nanomaterials are also defined or named quantum dots.

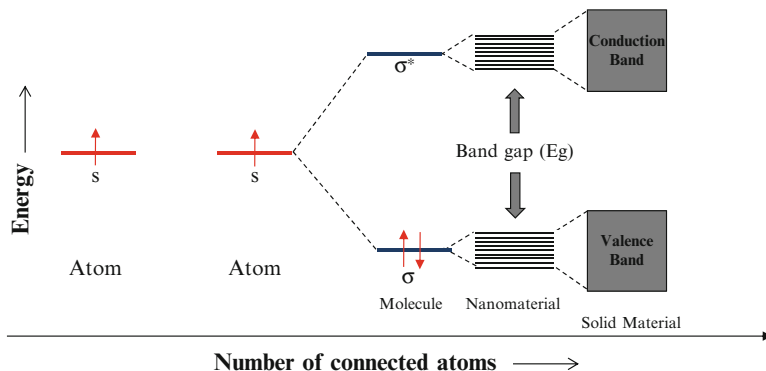
9.4.1 Electronic Excitation of Nanomaterials

A fundamental aspect of quantum mechanics is the particle-wave duality, introduced by de Broglie, according to which any particle can be associated with a matter wave whose wavelength is inversely proportional to the particle's linear momentum. Whenever the size of a physical system becomes comparable to the wavelength of the particles that interact with such a system, the behavior of the particles is best described by the rules of quantum mechanics [8]. All the information we need about the particle is obtained by solving the Schrödinger equation. The solutions of this equation represent the possible physical states in which the system can be found.

From Atoms to Molecules and Quantum Dots: From a chemist's point of view, the basic building blocks of matter are atomic nuclei and electrons. In an atom, electrons orbit around the single nucleus, and the number of electrons depends on the element. In the simplest case of the hydrogen atom, one electron orbits around one proton. The electronic states of the hydrogen atom can be calculated analytically [9, 19]. When more than one electron is involved, however, the calculation of the energy levels becomes more complicated, because in addition to the interaction between the nucleus and the electron, electron–electron interactions have also to be taken into account. Although the energy states of many-electron atoms can no longer be derived analytically, approximations such as the Hartree–Fock method are available [19]. Each electron can be ascribed to an individual orbit or AO, with an associated discrete energy level, as discussed, previously. The next bigger structure obtained from the combination of several atoms is the molecule. Now electrons are shared between the atoms, and are called MOs [9]. Only the lowest energy (bonding) MOs are occupied, and this explains the relative stability of molecules in the ground state (see discussion in Sect. 9.2) [19]. Using the same principle, it is possible to derive the electronic structure of more complex systems such as large molecules or atomic clusters. When combining atoms to form a molecule, we start from discrete energy levels of the AOs and we still end up obtaining discrete levels for the MOs [9]. When the size of a polyatomic system gradually increases, the calculation of its electronic structure in terms of combinations of AOs becomes unfeasible [20]. As an example in Fig. 9.9 the MO σ and σ^* formed by combination of AO s is shown (i.e., H–H bond in H₂).

Absorption and Emission spectra: In chemistry, size-dependent optical properties of colloidal semiconductor particles have been observed since the beginning of the last century (1920–1930), although it was only toward its end that this fact was rationalized in terms of size quantization [21]. The most striking effect in semiconductor nanoparticles is the widening of the band gap (E_g) between

Fig. 9.9 Comparison of energy for the atomic orbital s , the molecular orbitals σ and σ^* , and the band gap of nanomaterials absorbing in similar UV region



the highest occupied electronic states (the top of the original valence band) and the lowest unoccupied states (the bottom of the original conduction band) (see Fig. 9.9) [22]. This directly affects the optical properties of quantum dots as compared to the corresponding bulk material [23]. As an example, in Fig. 9.9 the relative energy of the AOs s and the MOs σ and σ^* formed by linear combination of the former is compared with the energy gap of a nanomaterial. This nanomaterial requires for electronic excitation a similar wavelength (energy) as the electrons located in the ligand σ bond for a σ to σ^* electronic transition.

The minimum energy needed to create an electron–hole pair in a quantum dot (an exciton) is defined by E_g . Light with energy lower than E_g cannot be absorbed by the quantum dot. Because the band gap depends on the size of the quantum dot, the onset of absorption is also size-dependent [21, 22]. In UV absorption experiments it is shown that smaller quantum dots have an absorption spectrum that is shifted to shorter wavelengths with respect to larger quantum dots and to bulk material. Excitons (electronic excited states) in semiconductors have a finite lifetime, τ , because of the recombination of the photoexcited electron–hole pair (deactivation process). In quantum dots, the energy released upon exciton deactivation is too large to be dissipated by vibrational modes. Preferentially it is released by photon emission. Radiative decay through photon emission, in other words fluorescence, is a highly probable decay channel in quantum dots [24]. Certainly, the possibility of radiationless deactivation (prompt heat emission) cannot be excluded [25]. As is the case of organic fluorophores, the range of energies emitted from a quantum dot sample after excitation is centered at a value that is smaller than that required to excite the sample (and which must be at least as large as its band gap). In other words, the wavelength of the fluorescence is longer than that of the absorbed light [9].

Many applications of the quantum-mechanical aspects of quantum dots can be found in optics. As in the more general case of atoms or molecules, quantum dots can be excited either optically or electrically. Regardless of the nature of the excitation, quantum dots may emit photons when they relax from an excited state to the ground state. Based on these properties, quantum dots may be used as lasing media, as single photon sources, as optically addressable charge storage devices, or as fluorescent labels.

Nanotechnology has already become part of our daily lives, even if we do not realize this. The most revolutionary outcomes can be expected when their electronic properties—the most valuable properties of nanoparticles—are exploited [26]. The fascinating nature of these properties will bring about a real technological revolution. Meanwhile, knowing some of the most important basic facts about nanoparticles is important for the understanding of current applications and for predicting future ones based on their special properties.

9.5 Radiationless Deactivation: Photoacoustic Spectroscopy (Laser-Induced Optoacoustic Spectroscopy)

Like many other current spectroscopic techniques that use laser light sources, the field of photoacoustics is much older than the development of the first laser in 1960. In 1881, Graham Bell proposed a spectrophone “for the purpose of examination of the absorption spectra of bodies in those portions of the spectrum that are invisible.” This instrument is based on the experiments of transmission of sound without a cable connection. The field then lay largely dormant until the middle of the 1970s when Rosencwai and Gersho laid the theoretical basis for the photoacoustic effect in solids, the so-called R–G theory [27].

The basic principle of all photothermal (PT) techniques is the absorption of light in a sample with the subsequent change of its thermal state. This may result in a change in temperature or other thermodynamical parameter of the sample related with the temperature. Measurement of either the temperature, pressure or density change that occurs due to optical (light) absorption is ultimately the basis of all the PT spectroscopic methods. PT analysis can be considered as an indirect absorption measurement as the measured quantity is not an optical signal (light). It is important to note here that the classical light absorption measurement is also not a direct measurement. Although an optical value (light), more specifically transmitted light, is being measured in this case, the amount of absorbed light is determined from the difference between the incident and transmitted energy, and therefore the measurement is indirect. The sample heating that produces the PT signal is correlated directly to the absorbed electromagnetic energy (light). In contrast to classical transmission spectroscopy (UV–Visible absorption spectroscopy), neither scattered nor reflected light contributes to the signal.

The most straightforward detection scheme for a photoacoustic signal is the observation of temperature change at the irradiated sample surface. The more common technique is detection of the emitted thermal radiation from the sample surface, which represents the temperature distribution within the sample. If the temperature rise in the absorbing sample volume occurs faster than this volume can expand, the result is a local pressure increase (wave). This pressure wave can be considered as a sound wave. PT techniques based on the measurement of this sound wave are called photoacoustic (PA) techniques. In a gaseous sample a microphone can be used as a detector, whereas pressure fluctuations in a solid or a liquid sample can be probed by pressure-sensitive detectors such as piezo transducers [28–30] (Figs. 9.10 and 9.11).

Although any kind of UV–Visible light source can induce a PT effect, lasers are the preferred source nowadays (and the technique is laser-induced optoacoustic spectroscopy, LIOAS) because of two reasons: (1) the PT signal, to a first approximation, is proportional to the temperature rise of the

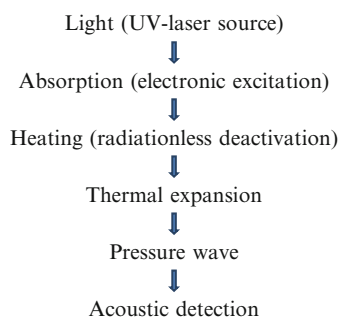


Fig. 9.10 Schematic top-down steps of a photoacoustic or laser-induced optoacoustic experiment to characterize radiationless deactivation processes

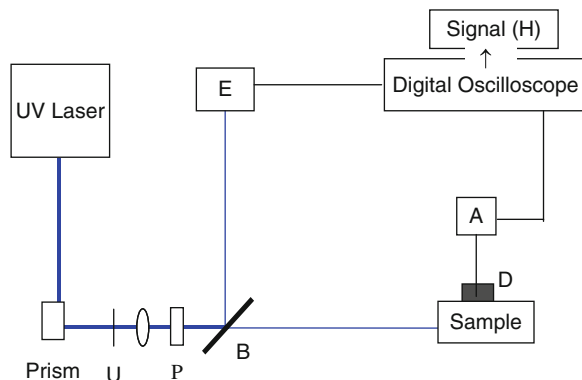


Fig. 9.11 Laser-induced optoacoustic spectroscopy (LIOAS): diagram of the experimental setup. Note the perpendicular arrangement between the incident laser beam on the sample container (cell) and detector (oscilloscope). E energy meter, U pin hole, P polarizer, B beam splitter, D ceramic detector (piezoelectric transducer), A amplifier, H amplitude of the first maximum registered by the oscilloscope

sample and thus is proportional to the absorbed energy, i.e., the laser pulse energy; (2) for many applications the selectivity of the PT analysis, as many other optical absorption analytical techniques, depends on the bandwidth of the excitation wavelength.

PT techniques are calorimetric in essence. Thus, after the absorption of energy in the form of radiation (E_a), simple energy balance considerations lead to the general rule that establishes the relationship between the various forms of dissipation of energy by the excited species [30].

$$E_a = \phi_f E_f + \alpha E_a + \phi_{st} E_{st} \quad (9.8)$$

In this equation, E_a is the absorbed molar energy. On the right hand side of the equation, the first term is the energy dissipated in the form of fluorescence, expressed as the product of fluorescence quantum yield, ϕ_f , times the molar energy of the fluorescing state, E_f . The second term is the fraction α of energy deposited in the medium as a result of the rapid heat released, i.e., within the heat-integration time of the experiment, vibrational relaxation including relaxation to the fluorescing state (see the Jablonski diagram, Fig. 9.4). This heat release is referred to as prompt heat. The third term is the energy stored by species living longer than the heat integration time and is expressed as the product of the quantum yield of formation, ϕ_{st} , times the molar energy content E_{st} . These species may be stable products or entities living longer than the time resolution of the experiment. When other deactivation processes take place (i.e., phosphorescence), other terms should be included that take into account the energy involved in such process(es) (molar energy of the phosphorescing state, E_p) and the phosphorescence quantum yield ϕ_p .

$$E_a = \phi_f E_f + \alpha E_a + \phi_{st} E_{st} + \phi_p E_p \quad (9.9)$$

For the mathematical treatment of LIOAS experimental data several assumptions are made that allow the evaluation of the thermal deactivation of excited electronic species. A design for optoacoustic experiments has evolved in which the detector is externally pressed to a cuvette wall in a plane parallel to the propagation direction of the exciting laser beam. This design is based on long experience with fluorescence measurements of dilute solutions, and it employs readily available fluorescence cuvettes that are cleaned and easily handled. Because the acoustic wave propagates perpendicularly to the laser beam direction, this arrangement is designated as a right-angle configuration.

In this arrangement and with low absorbance (A), the heat source has a cylindrical geometry with dimensions equal to the laser beam diameter and the cuvette length, and it expands radially. The equations necessary to handle this problem were developed by Landau and Lifschitz [31] to treat the general problem of sound generation by a cylindrical light source.

Taking into account that the changes in pressure P are much smaller than the original pressure, and that the thermal conductivity is quite small, the pressure wave $P(r,t)$ can be expressed by the inhomogeneous differential equations developed by Landau and Lifschitz [31].

$$(\nabla^2 P - v_a^{-2} \partial^2 P / \partial t^2) = -\beta / C_P \cdot \partial^2 Q / \partial t^2, \quad (9.10)$$

where ∇^2 is the Laplace function (Laplacian), $\beta = 1/V \cdot \partial V / \partial T$ is the coefficient of volumetric expansion ($V =$ volume, $T =$ temperature), C_P is the caloric capacity at constant pressure, v_a is the speed of sound in the medium studied and $Q = Q(r,t)$ the heat emitted, at a time t and at a distance r from the heat source.

This equation expresses the form of the pressure wave generated by the heat pulse, providing a description of the laser-induced optoacoustic signals in LIOAS. This equation neglects any damping of the acoustic wave by the viscosity of the solvent. Generally, these effects are small. Equation (9.11) is obtained by solving (9.10) for the pulse pressure sensed by the detector $P(r,t)$, (r , distance; t , time)

$$P(r,t) = \beta E_a / 8\pi^{1/2} C_P (\nu_a / r)^{1/2} \tau_{\text{ef}}^{-3/2} d\phi_0(\xi) / dt \quad (9.11)$$

For the calculation of the magnitude of the pressure wave as function of the time and distance from the detector, (9.12) is used:

$$|P(r,t)| \propto \beta E_a / 8\pi^{1/2} C_P (\nu_a / r)^{1/2} \tau_{\text{ef}}^{-3/2}, \quad (9.12)$$

where r is the distance of the detector from the source, which should be shorter than the length of the cylindrical heat source (the cuvette) for the problem to be considered as two dimensional ($\tau_a = R/\nu_a$ acoustic transit time; $\tau_a' = 2R/\nu_a$ effective acoustic transit time, where R is the radius or section of the laser).

Equation (9.13) was derived for the case of rapid and total radiationless deactivation of the excited species. In this case the pressure is determined by the absorbed energy E_a , which for very dilute solutions is proportional to the laser energy E_1 and the absorbance A ; in a more precise manner,

$$E_a = E_1(1 - 10^{-A}) \quad \text{and} \quad \tau_{\text{ef}}(\tau_1^2 + \tau_a^2)^{1/2} \quad (9.13)$$

with $\tau_a = R/\nu_a$. Again, two cases should be distinguished here: thin beams (long laser pulses), for which τ_1 dominates, and wide beams (time with of the laser pulse; shorter pulses τ_1) in which case τ_a (acoustic time transit) dominates.

Two procedures have been developed to apply LIOAS in determining the properties of electronically excited molecules by making use of the various parameters of the signal, which vary when energy-storing species with τ_{st} (from (9.8)) $> \tau_1'$ are produced in the sample.

According to one of the procedures, the amplitude of the first maximum, H , is used as a measure of the prompt heat delivered to the medium. This procedure is based on the fact that H is related through

an instrumental constant to $P(r,t)$ from (9.14), and that H decreases when energy-storing species are produced in the system.

$$H = KanE_a \quad (9.14)$$

The factor α was introduced for heat delivered promptly, in which K contains the thermoelastic parameters from (9.11), as well as instrumental constants, and n is the number of Einsteins contained in the laser pulse of molar energy E_l . The fraction of heat dissipated promptly originates from all processes with a deactivation lifetime shorter than τ_a' such as vibrational deactivation in the excited singlet or triplet states (IC), internal conversion of the excited state to the ground state (IC), charge transfer, intersystem crossing (ISC), and other chemical transformations (see the Jablonski scheme, Fig. 9.4).

Calorimetric References: In particular when using acoustic detection (LIOAS, LIOAC, PAC) and for the determination of the value of α (9.8) and (9.14), calibration of the experimental setup is required, by which the quantitative relationship between the heat released and the signal is determined. This is normally performed by using calorimetric references. A calorimetric reference is ideally a substance with an absorption spectrum overlapping that of the sample, which does not fluoresce (or does so with a known energy E_f and yield ϕ_f), delivers all the absorbed energy to the medium as heat within the observation time ($\alpha = 1$, (9.14)), and is measured under identical conditions as those employed for the sample, including the geometrical parameters [30, 32, 33].

Whenever possible, it is advisable to measure both reference and sample solutions at various concentrations (absorbances, A), to avoid technical problems related to the matching of absorbances. For studies in the liquid phase, the slopes of the linear plots of the PT (i.e., optoacoustic or thermal-lensing) H signal vs. laser fluence are, in turn, plotted against the fraction of absorbed fluence ($1-10^{-A}$) for solutions of various absorbances A , of sample and reference. The ratio of the slopes of the latter plots affords α for the sample under study. This essentially means eliminating the factor K in (9.14). As already stated, the possibility of multiple photon excitation should be carefully eliminated by performing the experiment for the calorimetric reference over a wide laser-fluence (F) range (again in this case the fluence should be varied by introducing neutral density filters in the laser-beam path, thus avoiding the perturbation of the beam profile).

$$H/F = K\alpha(1 - 10^{-A}), \quad (9.15)$$

where K is an experimental constant containing the thermoelastic properties of the solution and instrumental factors, A is the sample absorbance value and α is the fraction of energy released to the medium as prompt heat, within the time resolution of the experiment.

The α value for a sample, α^S , is calculated as the ratio of the fluence-normalized optoacoustic signal for the sample and for the reference, using the same absorbance for sample and analyte H^S/H^R .

Then, combining with (9.15) the following expression is obtained:

$$H^S/H^R = \alpha^S/\alpha^R, \quad (9.16)$$

and the value of α^S for the specific studied sample is obtained. In this context, the α values for some classical MALDI matrix materials have been reported (2,5-dihydroxybenzoic acid, 2,4,6-trihydroxyacetophenone, *trans*-3,5-dimethoxy-4-hydroxycinnamic acid, *trans*- α -ciano-4-hydroxycinnamic acid, 9H-pirido[3,4-b]indole (*nor*-harmane) and 1-methyl-9H-pirido[3,4-b]indole

(harmaline) [34]; 9-aminoacridine, 3-aminoquinoline, 2-(2-aminoethylamino)-5-nitropyridine and 3,4-dihydro-7-methoxy-1-methyl-9H-pyrido[3,4b]indole (harmaline) [35]). It is interesting to mention that these α values are quite high. Preferential radiationless deactivation from the electronic excited state seems to be a common behavior of crystalline organic MALDI matrices, at least in acetonitrile solution.

9.6 Ablation

Upon irradiation of condensed materials with laser pulses at high fluence (where fluence is defined as laser energy per pulse per unit area), massive material ejection is observed. This phenomenon has been named ablation. A plot of the quantity of the removed material as a function of laser fluence usually shows sigmoid dependence, although the exact shape may differ considerably depending on the system properties and irradiation parameters [28].

Despite its apparent violent nature, this efficient material removal method has provided the basis for a wide spectrum of highly successful applications, such as microelectronics [28, 29], medicine [28, 29, 36, 37], removal of microscopic particles from surfaces with applications in laser cleaning of technologically important substrates and components, restoration of painted artwork [28, 29, 38], analytical chemistry (desorption/ionization methods in mass spectrometry, i.e., LDI and MALDI) [3, 4, 28, 29, 39]. In some of these applications, UV ablation is employed to effect the appropriate shaping or processing of the substrate via the removal of unwanted material [28, 29]. In either case, ablation offers the outstanding advantage of micrometer precision in the removed depth, with little thermal or other degradation of the ejected or remaining material. Further advantages include a high degree of reproducibility, the capability of interfacing with a variety of laser-based techniques for online monitoring of the process, etc. [28].

Despite the widespread and highly successful applications, several aspects of laser ablation of molecular substrates induced with nanosecond or shorter pulses remain poorly understood [28, 39, 40]. The first and foremost problem to be elucidated remains the issue of the fundamental mechanisms responsible for material ejection, i.e., how the absorbed light energy induces material ejection. Generally, the whole process is described phenomenologically from the dependence of the etched depth (or the amount of the removed material) on laser fluence. Usually, the fluence at which a sharp increase is observed in the etching depth is considered to be the threshold for ablation. Even the existence of a threshold is very difficult to predict theoretically; the question raised is if ablation can be identified with specific physical characteristics that distinguish it from processes at lower fluence or if it is adequately specified only in terms of the amount of material removed.

Unfortunately, for several applications, only the amount of removed material is of concern [28]. The difficulties encountered in trying to establish the fundamental physical processes underlying the phenomenon can be easily understood taking into account the various steps involved in material ejection.

Rationalizing the ablation: To begin with, energy must be transferred into the system via absorption [28]. Typically, experimental fluencies of ~ 100 mJ/cm² or higher are required to induce material ejection by nanosecond laser pulses. Given a typical cross section of $\sim 10^{-18}$ cm²/molecule, multiphoton processes and other nonlinearities in the absorption process, such as bimolecular annihilation of electronically excited states (see the Sect. 9.3 in this chapter), and others, become highly likely. Establishing the absorbed energy experimentally is no easy task, because the extensive material ejection during the laser pulse results in significant scattering and absorption of the incident light by the ejected material. In fact, the extensive material ejection severely limits the use of any

spectroscopic technique in probing processes on the substrate (at least up to microsecond time scales after the nanosecond laser pulse). Following light absorption, material ejection can be induced by different ways. At least for nanosecond pulses, a good percentage of the absorbed energy can be expected to decay into thermal energy, since the typical radiationless decay constants, k_{ic} , for organic molecules are $\sim 10^{-12}$ – 10^{-9} s (see the Jablonski diagram, Fig. 9.4). In view of the low thermal conductivity of molecular systems, high surface temperature changes may be attained, and desorption–evaporation rates can be substantial (thermal mechanism). However, given the very short time scale of irradiation, phase transformations under nonequilibrium conditions may occur (explosive boiling and/or phase change explosion), resulting in quantitative and even qualitative differences from simple thermal processes.

Unfortunately, the dynamic optical, thermophysical, and other properties under these conditions can be quite different than those of a uniformly heated system, which further complicates the quantitative analysis and even the interpretation of the results. The fast change in temperature implies also a volume change and thus a high-amplitude pressure generation, which can result in material ejection via an essentially mechanical rupture named spallation, of the upper layers of the substrate. To make the matter worse, upon UV excitation, most organic molecules photodecompose (photochemical reaction) with a quite high quantum efficiency. Besides, the formation of gaseous photoproducts that exert a high pressure upon expansion and/or the high amount of energy that is liberated by exothermic reactions can contribute to material ejection (photochemical and photomechanical mechanism).

These processes necessarily occur in parallel; thus, the question is to identify the process responsible for material ejection. Clearly, the different processes will result in different features and effects, and thus the specification of their contribution is intimately related to the question of the nature of ablation. The relative importance of the processes can be approximately assessed via some simple criteria. Assuming a thermal energy pulse and photo-inert systems, the relative importance of thermal-versus-mechanical processes depends on the ratio of pulse duration to thermal (τ_{th}) and stress relaxation (τ_{ac}) times [28, 41].

These times (τ) are given, respectively, by $\tau_{th} = \lambda_{abs}^2/\chi$ and $\tau_{ac} = \lambda_{abs}/c_S$, where λ_{abs} is the optical penetration depth (assumed to be much smaller than the laser beam radius, so that a one-dimensional analysis can be used), χ is the thermal diffusivity, and c_S is the speed of sound. The two terms represent, respectively, the time for heat diffusion (τ_{th} , thermal equilibration) and for the acoustic wave (τ_{ac} , and thus mechanical relaxation) within the optical penetration depth. Typically, for molecular solids, λ_{abs} in UV is in the range from 100 to 5 μm , and $\chi \sim 10^{-7}$ m^2/s , so $\tau_{th} \sim 1$ μs and $\tau_{ac} < 1$ ns. In the case of UV excitation, it is assumed that the time scale of electronic energy deactivation, τ_{ic} , is fast enough compared to the previously mentioned times (τ_{th} and τ_{ac}) (internal conversion, IC, processes, see Jablonski diagram Fig. 9.4; i.e., S_n to S_1 ; S_1 to S_0 ; T_n to T_1). The $\tau_{ic} \leq \tau_{th}$ condition is expected to be fulfilled for most molecular systems, but the $\tau_{ic} \leq \tau_{ac}$ condition may not be.

For laser pulse durations shorter than τ_{th} (thermal confinement regime), the temperature profile is determined by the laser light distribution, i.e.,

$$\Delta T(z) = \alpha F_{\text{las}} e^{-\alpha z} / \rho C_P, \quad (9.17)$$

where $\Delta T(z)$ is the temperature jump induced at depth z from the surface, α is the absorption coefficient, ρ the mass density, F_{las} the laser fluence, and C_P the heat capacity, light reflection and scattering being neglected. Since the maximum possible temperature is attained within the target volume, thermal desorption–evaporation rates can be significant and can account for the high material

removal rates observed at high laser fluencies. Furthermore, under this condition, the extent of thermal dissipation and damage adjacent to the irradiated area is limited.

This limited damage has been one of the key factors in the success of nanosecond UV laser processing of molecular substrates. Georgiou and Koubenakis [41], in their detailed review discuss several still unclear aspects of the theory and experiments connected with ablation. Briefly, they concluded that: (a) the current arguments (theoretical and experimental) do not explain some of the unique features of the phenomenon, which have been crucial for the widespread implementation of UV-MALDI-MS, i.e., how fragile molecules are ejected with minimal fragmentation. It now appears that, at least for simple systems (photo-inert and with low cohesive energy) and nanosecond pulses, these unique features may be associated with a nonequilibrium phase transformation, namely, explosive boiling. In this case, an additional criterion may be introduced to establish whether material ejection is the result of simple thermal desorption or of ablation, or in other words, whether the rate of homogeneous bubble formation is competitive with evaporative cooling rates or with the rate of energy consumed for bubble formation in the presence of nuclei promoting heterogeneous nucleation. (b) For even shorter laser pulses, such that $\tau_{\text{Las}} < \tau_{\text{ac}}$ (stress-confinement regime), heating is effected under nearly isochoric conditions, leading to possibly the most efficient generation of a thermoelastic wave. In the presence of an interface with a lower acoustic impedance medium (i.e., liquid, air), this wave contains—because of reflection at the interface—both compressive and tensile stresses. Such a high-amplitude bipolar stress wave can lead to ejection of material via essentially mechanical rupture of the upper layers (spallation).

Despite their appealing simplicity, the above criteria clearly serve only as approximate guidelines. In most cases, there is a competition or synergy between the various processes, and the question which one dominates will depend sensitively on the characteristics of the substrate (in particular, cohesive energy). Evidently, it is very difficult to specify or control experimentally all the different aspects involved in the phenomenon. Similarly, for the theoretical description, analytical treatments have to be restricted and to consider only individual processes, but unfortunately, this simplification in mathematical formalism might miss essential aspects of the phenomenon.

Several interesting features of material ejection in the irradiation of molecular solids at high laser fluencies have been indicated by molecular dynamics (MD) simulations based on the breathing sphere model [28, 42]. However, even here, because enormous computing power is required to simulate the laser–matter interaction, several simplifications are made in the representation of the molecules and irradiation conditions. In view of these difficulties, the existence of a wide range of uncertainties and controversies concerning the mechanisms of ablation is not surprising.

Photomechanical ablation model: There is experimental evidence that under certain conditions photomechanical effects play a role in laser ablation. One observation is that the energy density threshold for tissue ablation with nanosecond laser pulses can be up to one order of magnitude lower than that needed for complete vaporization. These low thresholds point strongly to mechanical effects being implicated in removal. Another observation is that ablation with these short laser pulses is accompanied by the emission of strong acoustic waves into the ablated material. These acoustic transients can be a consequence of ablation, for example, due to the recoil momentum of vaporized and ejected material, in which case no waves are generated below the ablation threshold. If acoustic transients are generated below the ablation threshold by mechanisms other than recoil momentum, it is possible that their amplitude becomes so high that they actively cause material fracture and removal, and only in such a case we can say that there is photomechanical ablation [28, 40, 43].

Thermoelastic stress is caused by the heating and thermal expansion of a material. If the heat generated by absorption of light remains confined in the irradiated volume during the laser pulse and

cannot escape via heat conduction, a condition named thermal confinement is obtained. The criterion is that the pulse duration has to be shorter than a characteristic thermal relaxation time τ_{th} , given by

$$\tau_{\text{th}} = d^2/4\chi \quad (9.18)$$

where d is the smallest dimension of the heated volume (either the beam diameter or the optical penetration depth, whichever is smaller) and χ is the thermal diffusivity. Thermal confinement maximizes the temperature in the heated volume and is an important prerequisite to efficiently generate thermoelastic stress. In a liquid, the overpressure p (“pressure” from now on), which is the difference between the actual and the equilibrium pressure, depends on the relative volume change $\Delta V/V$ and the temperature change ΔT

$$p = -B(\Delta V/V) + B\beta\Delta T \quad (9.19)$$

where B is the bulk modulus and β the volume expansion coefficient.

For an isotropic solid, the equivalent equation is the stress–strain relationship [28, 40, 43, 44]

$$\sigma_{ij} = (3B/1 + \nu)[(1 - 2\nu)\epsilon_{ij} + \nu\epsilon_{kk}\delta_{ij}] - B\beta\Delta T \quad (9.20)$$

where σ_{ij} and ϵ_{ij} are the components of the stress and strain tensor, respectively, ν is the Poisson ratio, and δ the Kronecker symbol. Here we use the convention that compressive stress has a negative sign. The relative volume change is:

$$\Delta V/V = \epsilon_{kk} = \epsilon_{11} + \epsilon_{22} + \epsilon_{33} \quad (9.21)$$

From both relationships it follows that the maximum pressure or stress, $B\beta\Delta T$, is achieved if the heating takes place in a way that all displacements in the medium that would give rise to a volume change or any strain are zero. This condition is called stress or inertial confinement and is achieved if the heating pulse is much shorter than the characteristic time of acoustic relaxation, τ_{ac} , and $\tau_{\text{ac}} = d/c_s$,

where c_s is the speed of sound. Stress and pressure lead to displacements in the medium. Using the equation of motion, one obtains for a liquid the scalar thermoelastic wave equation that is most conveniently given in terms of the velocity potential ϕ

$$\nabla^2\phi - c^{-2}(d^2/dt^2) = \beta S/\rho C \quad (9.22)$$

where ρ is the density, C the specific heat capacity, and S the heat generated per unit time and volume. The relationships between pressure, particle velocity ν , and velocity potential are given by

$$\nu = \text{grad } \phi, \text{ and } p = -\rho(d\phi/dt).$$

The corresponding wave equation for the displacement vector u in an isotropic solid is [28, 43, 44]

$$\rho(d^2u/dt^2) - [E\nabla^2u/2(1 + \nu)] - [E\nabla(\nabla u)/2(1 + \nu)(1 - 2\nu)] = -B\beta\nabla(\Delta T), \quad (9.23)$$

where E is Young’s modulus of the solid. A good description of the temporal evolution of thermoelastic stresses in a solid has been given by Albagli et al. [45, 46] according to which four regimes are distinguished:

1. A heating phase under stress or inertial confinement. The maximum stress $B\beta\nabla(\Delta T)$ is achieved, which serves as the initial condition for the second regime.
2. A transient regime, in which the forces caused by the thermal stress lead to displacements that propagate as longitudinal and transverse acoustic waves. The time scale for the emission of acoustic waves from the heated zone is τ_{ac} .
3. A quasi steady-state regime, in which the system reaches mechanical equilibrium and the net forces in any direction become zero. Because of the nonuniform temperature distribution caused by heating a confined volume within the medium, the individual stress components are not zero. The existence of the third regime requires that $\tau_{ac} \ll \tau_{th}$, a condition that is always satisfied with the exception of extremely small values of d (in the subnanometer range). The quasistatic stresses strongly depend on the shape of the heated volume. For example, a rectangular laser beam profile generates much higher temperature gradients and stresses than a beam with a Gaussian radial profile.
4. A thermal diffusion regime with a time scale of τ_{th} , in which the excess heat diffuses out of the irradiated volume and the thermoelastic stresses decay to zero.

Because liquids cannot support shear waves or any quasistatic stresses arising from thermal deformations, only regimes 1 and 2 occur in liquids and only longitudinal waves are generated. In solids, both transient and quasistatic stresses can contribute to ablation. The transient stress acts in a similar way as in liquids, but additional stress components, such as radial stress right at the surface, develop [47]. It is also possible to generate only the third and fourth regimes without transient stresses, as long as $\tau_p \ll \tau_{th}$. Quasistatic stresses mainly develop in regions where the temperature gradient is high [46]. A top-hat laser beam with sharp edges in the radial irradiance profile will therefore mainly cause strong stresses right at the rim of the laser beam. Alternatively, a difference in thermal expansion coefficients, for example, at the interface of a coating and a substrate with a smaller thermal expansion coefficient, can cause stresses that initiate ablation of the coating [48]. Considering that dynamic fracture needs some incubation time, and that quasistatic thermoelastic stresses act on the material for periods that are orders of magnitude longer than the transient stresses, even low amplitudes of quasistatic stress might play an important role in ablation [28, 43, 46].

9.7 Conclusion

The previous discussion directly indicates that the study of the UV-MALDI process is highly interdisciplinary, encompassing questions from the fields of photophysics and photochemistry, thermodynamics, optics, hydrodynamics, etc. As a result of this interdisciplinary character, the particular study of UV laser ablation can be expected to result in new knowledge about photophysics and photochemistry of both molecules (organic molecules, organic ionic liquids, silicon polymers) and nanomaterials that are currently used as MALDI matrix [3, 4]. This is clearly indicated by the fact that the wide range and high success of the applications of the phenomenon could not have been expected by considerations of conventional photochemistry alone [6, 7], although complementary knowledge from this field of science was of much help. To the contrary, by any conventional photophysical and photochemical criterion, the high irradiances employed in the process would have been expected at first sight to result in chemical decomposition or other still unknown and not well studied effects [6, 7, 28, 29]. This current situation suggests the need to introduce new concepts that may have far-reaching scientific impact. Indeed, important issues concerning nonequilibrium phase transformations, electronic excitation and deactivation processes, material dynamics, etc. have

already been raised and studied in the field [28, 29] (see also articles and references in the special issue on ablation, *Chem Rev* 103(2) 2003, [39]).

Although the power of UV ablation is illustrated in the processing of complex polymers, biopolymers, tissues, painted artwork, etc., the study of the processes underlying the phenomenon in realistic analyte–matrix systems raises significant difficulties [28, 29, 36, 40]. Ablation studies on simple molecular systems may provide a useful starting point by enabling detailed probing and elucidation of the processes: i.e., laser-induced material ejection from liquids has been extensively studied in its own right [28, 29]; It has also provided a basis for understanding processes in complex systems, in particular tissues [28, 29, 36].

References

1. Tanaka K, Waki H, Ido Y, Akita S, Yoshida Y, Yoshida T (1998) Protein and polymer analyses up to m/z 100,000 by laser ionization time-of-flight mass spectrometry. *Rapid Commun Mass Spectrom* 2:151–153
2. Karas M, Hillenkamp F (1998) Laser desorption/ionization of proteins with molecular masses exceeding 10,000 daltons. *Anal Chem* 60:2299–2301
3. Hillenkamp F, Peter-Katalinić J (eds) (2007) MALDI MS. A practical guide to instrumentation, methods and applications. Wiley-VCH, Weinheim
4. Cole RB (2010) Electrospray and MALDI mass spectrometry. Fundamentals, instrumentation, practicalities, and biological applications. Wiley, London
5. Phipps C (ed) (2007) Laser ablation and its applications, 2nd edn. Springer, New York
6. Klessinger M, Michl J (1995) Excited states and photochemistry of organic molecules. VCH, New York
7. Turro NJ, Ramamurthy V, Scaiano JC (2010) Modern molecular photochemistry of organic molecules. University Science Books, Sausalito
8. Cohen-Tannoudji C, Diu B, Laloë F (1997) Quantum mechanics. Wiley, New York
9. Atkins PW (1986) Physical chemistry. Oxford University Press, Oxford
10. Birks JB (1975) Organic molecular photophysics vols I and II. Wiley, Chichester
11. Simons JP (1971) Photochemistry and spectroscopy. Wiley-Interscience, London
12. Valeur B (2002) Molecular fluorescence. Wiley-VCH, Weinheim
13. Zander C, Enderlein J, Keller RA (2002) Single molecule detection in solution. Wiley-VCH, Berlin
14. Jablonski A (1935) Über den mechanismus der photolumineszenz von farbstoffphosphoren. *Z Phys* 94:38–46
15. Lakowicz JR (ed) (1991) Topics in fluorescence spectroscopy, vol 1 and 2. Plenum, New York
16. Cheung HC (1991) Resonance energy transfer. In: Lakowicz JR (ed) Topics in fluorescence spectroscopy, vol 2. Plenum, New York
17. Chiang CK, Chen WT, Chang HT (2011) Nanoparticle-based mass spectrometry for the analysis of biomolecules. *Chem Soc Rev* 40:1269–1281
18. Lane N (2001) The grand challenges of nanotechnology. *J Nanopart Res* 3:95–103
19. Karplus M, Porter RN (1970) Atoms and molecules; an introduction for students of physical chemistry. W. A. Benjamin, New York
20. Harrison WA (1980) Electronic structure and the properties of solids. Freeman, San Francisco
21. Brus LE (1984) Electron–electron and electron–hole interactions in small semiconductor crystallites: the size dependence of the lowest excited electronic state. *J Chem Phys* 80:4403–4409
22. Gaponenko SV (1998) Optical properties of semiconductor nanocrystals. Cambridge University Press, Cambridge
23. Harrison WA (1989) Electronic structure and the properties of solids: the physics of the chemical bond. Dover Publications, Dover
24. Klimov VI, McBranch DW, Leatherdale CA, Bawendi MG (1999) Electron and hole relaxation pathways in semiconductor quantum dots. *Phys Rev B* 60:13740–13749
25. Vertes A (2007) Laser–matter interaction in novel regimes. In: Phipps C (ed) Laser ablation and its applications. Springer, New York
26. Schmid G (ed) (2004) Nanoparticles: from theory to application. Wiley-VCH, Weinheim
27. Rosenzweig A, Gersho A (1976) Theory of photoacoustic effect in solids. *J Appl Phys* 47:64–69
28. Phipps C (ed) (2006) Laser ablation and its applications, 1st edn. Springer, New York
29. Bäuerle D (2011) Laser processing and chemistry, 4th edn. Springer, New York
30. Braslavsky SE, Heibel GH (1992) Time-resolved photothermal and photoacoustic methods applied to photoinduced processes in solution. *Chem Rev* 92:1381–1410, and references therein

31. Landau LD, Lifschitz EM (1959) Fluid mechanics. Pergamon, Oxford, Chap VIII
32. Van Haver P, Viaene L, Van der Auweraer M, De Schryver FC (1992) References for laser-induced opto-acoustic spectroscopy using UV excitation. *J Photochem Photobiol A Chem* 63:265–277
33. Murgida DH, Erra-Balsells R, Bilmes GM (1996) New photocalorimetric references for UV excitation. *Chem Phys Lett* 250:198–202
34. Mesaros M, Tarzi OI, Erra-Balsells R, Bilmes GM (2006) The photophysics of some UV-MALDI matrices studied by using spectroscopic, photoacoustic and luminescence techniques. *Chem Phys Lett* 426:334–340
35. Petroselli G, Gara PD, Bilmes GM, Erra-Balsells R (2012) Photoacoustic and luminescence characterization of nitrogen heterocyclic aromatic UV-MALDI matrices in solution. *Photochem Photobiol Sci* 11:1062–1068
36. Vogel A, Venugopalan V (2003) Mechanisms of pulsed laser ablation of biological tissues. *Chem Rev* 103:577–644
37. Vèkey K, Telekes A, Vertes A (eds) (2008) Medical applications of mass spectrometry. Elsevier, Amsterdam
38. Colombini MP, Modugno F (eds) (1988) Organic mass spectrometry in art and archaeology. Wiley, Florencia
39. Georgiou S, Hillenkamp F (eds) (2003) Introduction: laser ablation of molecular substrates. *Chem Rev* 103:317–319
40. Dreisewerd K (2003) The desorption process in MALDI. *Chem Rev* 103:395–425
41. Georgiou S, Koubenakis A (2003) Laser-induced material ejection from model molecular solids and liquids: mechanisms, implications, and applications. *Chem Rev* 103:349–393
42. Zhigilei LV, Leveugle E, Garrison BJ, Yingling YG, Zeifman MI (2003) Computer simulation of laser ablation of molecular substrates. *Chem Rev* 103:321–347
43. Paltauf G, Dyer PE (2003) Photomechanical processes and effects in ablation. *Chem Rev* 103:487–518
44. Royer D, Dieulesaint E (2000) Elastic waves in solids I, II. Springer, Berlin
45. Itzkan I, Albagli D, Dark M, Perelman L, von Rosenberg C, Feld MS (1995) The thermoelastic basis of short pulsed laser ablation of biological tissue. *Proc Natl Acad Sci U S A* 92:1960–1964
46. Albagli D, Dark M, von Rosenberg C, Perelman L, Itzkan I, Feld M (1994) Laser-induced thermoelastic deformation: a three-dimensional solution and its application to the ablation of biological tissue. *Med Phys* 21:1323–1332
47. Albagli D, Dark M, Perelman LT, von Rosenberg C, Itzkan I, Feld MS (1994) Photomechanical basis of laser ablation of biological tissue. *Opt Lett* 19:1684–1686
48. Koulikov SG, Dlott DD (2001) Ultrafast microscopy of laser ablation of refractory materials: ultra low threshold stress-induced ablation. *J Photochem Photobiol A Chem* 145:183–194

Kenzo Hiraoka

10.1 SIMS and Cluster SIMS

Secondary ion mass spectrometry (SIMS) is one of the most powerful techniques for material analysis. Sputtering of a solid induced by atomic ion bombardment leads to linear cascade collisions resulting in damage under the surface. Static SIMS, a technique in which the primary ion beam dose is restricted so that only 1 % of the surface is impacted by a primary ion, allows molecular information to be extracted from the sample that is representative of its chemistry [1]. A number of studies have shown that the sputtering and secondary ion formation efficiency improve with increasing the mass of the primary particles [2–16]. The projectiles such as $\text{Cs}^+(\text{CsI})_n$ [2], (SF_5^+) [13], massive glycerol cluster [17–20], C_{60}^+ [9], Au_3^+ [10, 11], and Bi_3^+ [21, 22] have enabled the acquisition of SIMS spectra with highly enhanced sensitivity. It has been shown that some of the cluster ion beams have the potential to increase the secondary ion yields by more than three orders of magnitude compared with Ga [9, 21].

Colla et al. used molecular-dynamics (MD) simulation to study sputter effects induced by 16 keV Au_n ($n = 1, 2, 4, 8, 12$) cluster impact on an Au{111} surface [5]. Because of the high stopping power of Au in Au, this system is characterized by compact cascades and large deposited energy density. With the exception of bombardment by Au_1 , sputtering lasts at least 8 ps, a pronounced crater is formed as a rule, and large clusters emitted from the crater rim contribute substantially to sputtering. Sputter yield and crater size are strongly positively correlated in each individual impact event. For larger cluster impact ($n \geq 4$), fluctuation in these two quantities shrink, giving the events a macroscopic appearance.

Postawa et al. performed MD simulations for the sputtering of Ag{111} by 15 keV Ga and C_{60} [12].

Figure 10.1 shows the cross-sectional views of temporal evolution of collision events leading to ejection of atoms under 15 keV Ga and C_{60} bombardment [12]. It is obvious that the nature of the energy deposition process is very different for these two projectiles. The atomic Ga projectile penetrates deeper into the crystal creating a cylindrical damage area. In contrast, the bombardment event with C_{60} creates a mesoscale crater with a concomitant pressure wave in the solid. The impact leads to nearly simultaneous motion and high disorder in a relatively shallow volume of the crystal below the surface within tens of picoseconds. A significant amount of the projectile's energy is

K. Hiraoka (✉)

Clean Energy Research Center, University of Yamanashi, Takeda-4-3-11, Kofu 400-8511, Yamanashi, Japan
e-mail: hiraoka@yamanashi.ac.jp

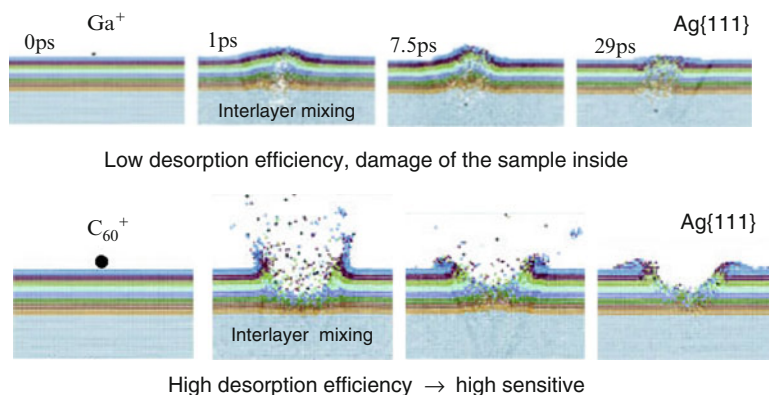


Fig. 10.1 Cross-sectional view of temporal evolution of collision events leading to ejection of atoms under 15 keV Ga and C₆₀ bombardment of a Ag{111} surface at normal incidence. The view is from the side of a portion of a $10 \times 10 \times 10 \text{ nm}^3$ microcrystallite containing 612,000 atoms (reproduced with permission from [12])

deposited close to the surface, leading to the emission of numerous particles. The crater has an almost circular (doughnut) shape surrounded by a rim.

The work of Mahoney et al. is considered pioneering because massive multiple-charge glycerol clusters with masses of 10^6 – 10^7 u and excess charges of ~ 200 via electrohydrodynamic (EHD) emission were generated in vacuum using a 1.5 M solution of ammonium acetate in glycerol [17–20]. This method of massive cluster impact (MCI) has enabled the production of high secondary-ion yields from biological samples without the use of a liquid matrix. Dry samples of molecules as large as cytochrome c were observed to be efficiently desorbed without significant fragmentation by the MCI beam of glycerol clusters. Signals from protonated molecules retained a significant proportion of their initial intensity, meaning that little radiation damage was accumulated on the irradiated biological samples. MCI not only demonstrated good performance in the picomole/nanomole range for the desorption of highly polar and fragile molecules such as proteins and deoxyoligonucleotides, but it also allowed the observation of a noncovalent complex in the form of a deoxyoligonucleotides duplex [23]. Although this method was found to afford extremely soft ionization/desorption conditions for peptides and proteins [17–20], stable ion currents can only be obtained for several hours until the lens electrodes become contaminated by accumulated glycerol, at which time source cleaning is necessary.

Aksyonov and Williams developed the technique of impact desolvation of electrosprayed microdroplets (IDEM), which uses the charged droplets generated by vacuum electrospray [24]. Analytes were dissolved in an electrolyte solution that was electrosprayed in vacuum, producing highly charged micron and submicron-sized droplets. Water-based solutions rapidly evaporate in vacuum, resulting in freezing and plugging of the capillary. To avoid freezing, the capillary was heated with a nichrome wire. The electrosprayed microdroplets were accelerated by 5–10 kV to velocities of several kilometer per second and allowed to impact a target. The energetic impacts led to desorption of analyte molecules dissolved in the droplets. Oligonucleotides (2- to 12-mer) and peptides (bradykinin, neurotensin) yielded single- and double-charged protonated molecules with no detectable fragmentation. It was found that in IDEM the polarity of the microdroplets appeared to be unrelated to ion formation. This issue was investigated by changing the polarity of the electrospray source and mass spectrometer independently. The target could then be irradiated by positive or negative microdroplets and positive or negative ions could be extracted from the target, leading to possible microdroplet/analyte ion polarity combinations: +/+, +/–, –/–, and –/+ . The main

conclusion was that whatever the polarity of the primary droplet, the mass spectrum of secondary ions of a given polarity was the same, and this indicates that the charge brought by the microdroplet into the ionization region is negligible compared with the charging produced by the impact itself [24].

The gas cluster ion beam (GCIB) technology has been proposed by Yamada et al. as a material processing technique [25, 26]. In GCIB gas clusters are generated by supersonic gas expansion. For example, Ar_n clusters with n ranging from a few hundreds to more than 1,000 could be formed using a Laval nozzle of 0.1 mm diameter and Ar stagnation pressure of $\sim 1 \times 10^6$ Pa. The cluster ions are accelerated by up to 80 kV [27, 28].

A characteristic feature of GCIB processing is its inherent ability for fast etching without roughening the surface. For example, Lee et al. [29] performed organic depth profiling of a nanostructured delta layer reference material, consisting of ultrathin “delta” layers of Irganox 3114 (~ 2.4 nm) embedded between thick layers of Irganox 1010 (~ 46 or 91 nm), using large argon cluster ions. Major benefits can be obtained using Ar GCIB, including a constant high sputtering yield throughout a depth of ~ 390 nm, together with an extremely low sputter-induced roughness of less than 5 nm. These results indicate the potential to achieve high depth resolution and suggest that Ar GCIB may have a major role to play in the depth profiling of organic materials.

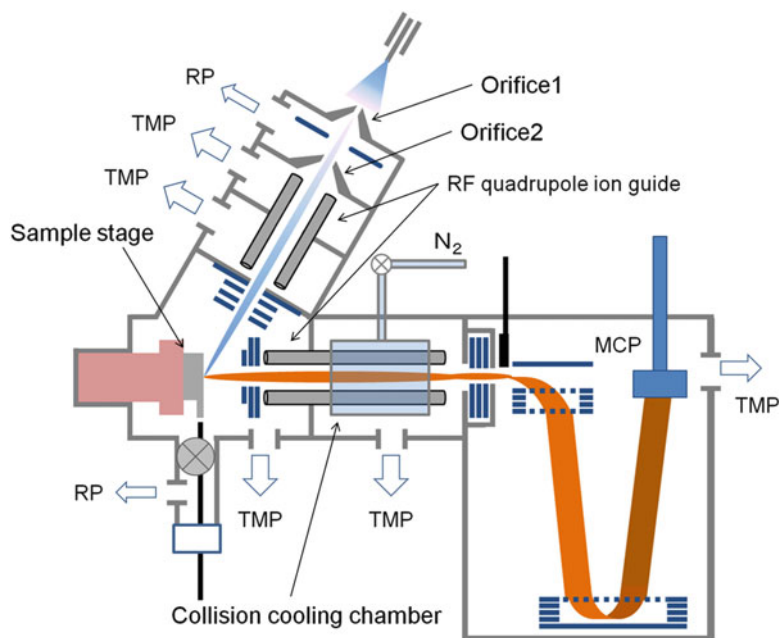
Rabbani et al. performed a systematic study of the suitability of Ar GCIB with the general composition Ar_n^+ , where $n = 60\text{--}3,000$, as primary particles in TOF-MS analysis [28]. They assessed the potential of the Ar GCIB for molecular depth-profiling in terms of damage accumulation and sputter rate and also as analysis beams where spectral quality and secondary ion yields were important. With direct comparison with C_{60}^+ on the same sample and in the same instrument on polymers, polymer additives, and biopolymer samples, including lipids and small peptides, it was found that bombardment with large Ar clusters shows reduced damage accumulation compared with C_{60} , with an approximately constant sputter rate as a function of cluster size. Further, with large argon clusters the changes observed in the mass spectra are indicative of a more gentle ejection mechanism. With increasing Ar cluster size a reduction in the ionization of secondary species is observed. GCIB has a place in dual beam depth-profile studies of organic systems, where they will be valuable as sputtering beams inducing only low damage (although not zero-damage). A downside of this approach is that most of the material sputtered is not available for analysis [28].

The continuing trend of scaling down in microelectronic circuit technology has led to a drastic reduction in film thickness, which increases the demands for very high depth resolution, ideally for a multilayer system. A simple analysis of recent applications indicates that to provide meaningful results aimed at the semiconductor community the depth resolution target should be in the order of 0.5 nm. However, a technique that is capable of atomic and molecular level etching and has been less explored will be described in the following sections. This technique is the electrospray droplet impact (EDI), which uses the atmospheric pressure electrospray as a cluster source. The basic idea of EDI is similar to that of MCI developed by Mahoney [17–20], with the difference that the former utilizes an electrospray of aqueous solution at atmospheric pressure to form charged water droplet projectiles instead of vacuum electrospray of glycerol. EDI has several new characteristic features, such as the fact that no special sample preparation is necessary, that it is maintenance-free, and has capability for atomic and molecular level etching, with little damage accumulation and high efficiency for secondary ion formation.

10.2 Experimental Method

MCI cannot avoid the contamination of the lens electrode system because it uses the less volatile glycerol [17–20]. This problem can be solved by using more volatile solvents. Impact desolvation of electrosprayed microdroplets (IDEM), introduced by Aksyonov and Williams involves vacuum

Fig. 10.2 Schematic diagram of the electrospray droplet impact (EDI)/secondary ion mass spectrometer. This apparatus was also equipped with a rare gas fast atom bombardment (FAB) gun (not shown)



electrospray using water-based solvents [24]. However, these solvents evaporate quickly in vacuum, resulting in freezing and plugging of the capillary. To avoid the problems encountered in MCI and IDEM, this author and colleagues have developed the EDI technique that uses the atmospheric pressure electrospray instead of vacuum electrospray [30–32] that is discussed in Chap. 8 of this monograph. Because EDI adopted the ambient electrospray, a stable electrospray could be maintained for days of continuous operation.

The conceptual experimental setup of an EDI ion source coupled with an orthogonal time-of-flight mass spectrometer is displayed in Fig. 10.2 [30].

The charged liquid droplets generated by electrospraying 1 M acetic acid or 0.01 M trifluoroacetic acid aqueous solution at atmospheric pressure are introduced into the first vacuum chamber through an orifice with 400 μm diameter. The voltages applied to the stainless steel capillary (i.d. 0.1 mm, o.d. 0.2 mm) are +3 kV in the positive mode and -2.5 kV in the negative mode electrospray. The charged droplets sampled through the orifice are transported into a first quadrupole ion guide for collimation, and accelerated by 0.5–10 kV after exiting the ion guide. The electrospray droplets (i.e., the multiply charged massive clusters) are allowed to impact the solid sample prepared on a stainless steel substrate with the angle of 60° to the surface normal. The total current of the electrospray charged droplets irradiated on the target was measured to be ~ 1 nA using a Faraday cup installed at the target position.

The nozzle shown in Fig. 10.3 is used to form the electrosprayed charged droplets.

The flow rate of the liquid for electrospray is 50 $\mu\text{L}/\text{min}$. The electrospray is nebulized with dry N_2 gas with the flow rate of ~ 8 L/min. The tip of the inner capillary is located about 5 mm in front of the ion sampling orifice of the first vacuum chamber. The linear velocity of the nebulizing gas through the tip nozzle is estimated to be roughly ~ 400 m/s. This suggests that the nebulizing gas flow velocity coaxial to the capillary is close to the sonic velocity, i.e., the sonic spray condition [33, 34] is nearly established.

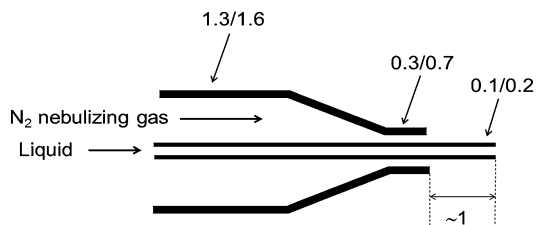


Fig. 10.3 Double cylindrical capillary system used for the formation of charged droplets. The values of the i.d./o.d. ratio are shown

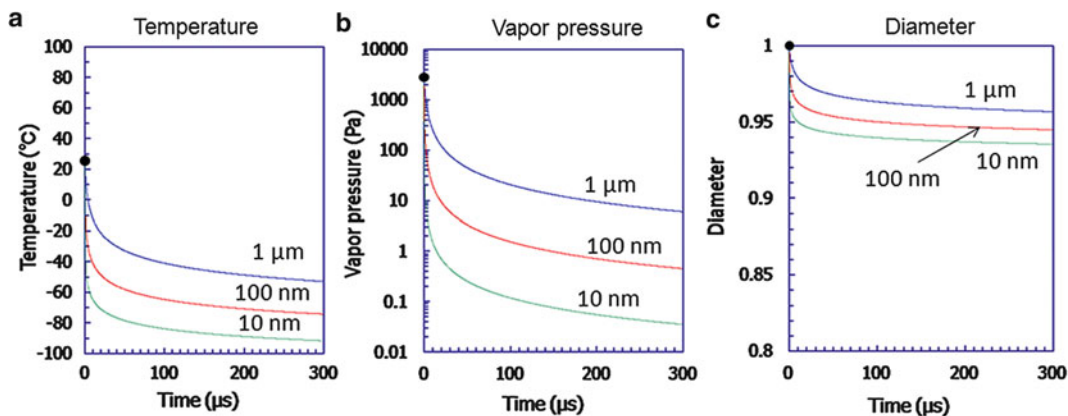


Fig. 10.4 Calculated temperature (a), vapor pressure (b), and diameter (c) of water droplets sampled through the ion sampling orifice with the original diameters of 1 μm , 100 nm and 10 nm as a function of time. Time 0 corresponds to when the droplets pass through the ion sampling orifice into vacuum. The time of flight of the droplets from the ion sampling orifice to the target is about 200 μs . The temperature and vapor pressure of the droplets at time 0 are assumed to be 25 $^{\circ}\text{C}$ and 3,000 Pa (i.e., the vapor pressure of water at 25 $^{\circ}\text{C}$). The diameter of the droplets at time 0 is normalized as 1 for the three sizes

Because the water droplets generated at atmospheric pressure are sampled in vacuum, their evaporative weight loss in vacuum needs to be estimated. The collision frequency of gas molecules hitting a unit area of the surface ν (s^{-1}) is given by (10.1).

$$\nu = \frac{nv}{4}, \quad (10.1)$$

where n is the number density of molecules, and v is the velocity of the gas molecule at T . The value of ν (s^{-1}) may be approximated to the number of molecules evaporating from the liquid droplet surface into the gas phase at the saturated vapor pressure at T . By knowing ν (s^{-1}), the temperature change of the droplet in vacuum can be estimated using the Clausius–Clapeyron equation:

$$\log \frac{P_2}{P_1} = \frac{L_v}{2.303R} \left(\frac{1}{T_1} - \frac{1}{T_2} \right), \quad (10.2)$$

where P is the vapor pressure and L_v is the heat of vaporization of the liquid. Figure 10.4 shows the calculated temperature, vapor pressure, and diameter of the droplets with the original diameters of 1 μm , 100 nm and 10 nm as a function of time.

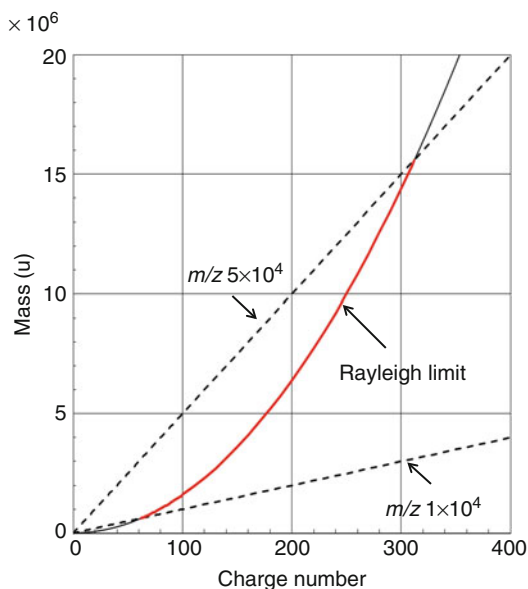


Fig. 10.5 Relationship between the mass (u) and the number of charges of the droplet calculated by the Rayleigh limit equation, $z = (\gamma\epsilon_0 r^3)^{0.5} \times 8\pi/e$. The intersects of the two *dotted straight lines* with $m/z 1 \times 10^4$ and 5×10^4 with the Rayleigh limit function line give the estimated values of masses and the charge numbers of the droplets with $m/z 1 \times 10^4$ and 5×10^4 , respectively (reproduced with permission from [32])

The temperature of the droplets decreases steeply resulting in a corresponding steep decrease in vapor pressure (Fig. 10.4a, b). Because of the rapid decrease in vapor pressure, the diameters of the droplets decrease only slightly (Fig. 10.4c), suggesting that the water droplets introduced into the vacuum nearly maintain their original mass and the evaporative weight loss is at most 20 %. In addition, the free-jet expansion of the N_2 carrier gas containing charged droplets through a small orifice brings about a rapid temperature drop. Thus, the evaporative weight loss of the electrospayed droplets in vacuum in the EDI experiment may be kept to a minimum.

The first RF quadrupole ion guide shown in Fig. 10.2 is adjusted for sampling charged droplets in the m/z range 1×10^4 to 5×10^4 . From the principles of mass spectrometry analysis, only m/z values can be evaluated for the charged particles, but not independent values of m or z . However, in the experimental system in Fig. 10.2, using electrospay as a source of charged projectiles, the m and z values may be roughly estimated. It is generally accepted that the charge states of the primary electrospayed droplets and their offspring droplets are close to the Rayleigh limit. The relation between the charge number z and radius of the droplet r is given by the Rayleigh equation:

$$z = (\gamma\epsilon_0 r^3)^{0.5} \times \frac{8\pi}{e}, \quad (10.3)$$

where γ is the surface tension, ϵ_0 is the vacuum permittivity, and e is the electronic charge. From the surface tension of water ($\gamma = 72 \times 10^{-3} \text{ J m}^{-2}$), $\epsilon_0 = 8.9 \times 10^{-12} \text{ C}^2 \text{ J}^{-1} \text{ m}^{-1}$, and the density of the droplet (assumed to be equal to that of water, 1 g cm^{-3}), the relationship between the mass (u) and the number of charges of the droplet can be calculated as displayed in Fig. 10.5 [32].

From the values of m/z in the range of 1×10^4 and 5×10^4 , the masses of the droplets and the number of charges are calculated to be in the range of 6.2×10^5 to 1.6×10^7 u, and 62–311,

respectively. The radii of the droplets are estimated to be in the range 5–20 nm. As an example, the kinetic energy and velocity of a typical projectile $[(\text{H}_2\text{O})_{90,000} + 100\text{H}]^{100+}$ accelerated by 10 kV are 1×10^6 eV and 12 km/s, respectively.

The diameter of the droplets beam can be adjusted in the range of 2–0.05 mm using the ion beam focusing lenses.

10.3 Atomic and Molecular Level Etching by EDI

The best sample for testing the ability for the shallow surface etching may be self-assembled monolayers.

Figure 10.6a shows the EDI mass spectra for a self-assembled monolayer of $\text{Au-S-(CH}_2)_6\text{-NH}_2$ formed on a gold substrate as a function of irradiation time [35]. At the beginning of the measurement $[\text{M} + \text{H}]^+$, $[2\text{M} + \text{H}]^+$, and $[\text{M} + \text{H} + \text{Au}]^+$ (M denotes $\text{HS-(CH}_2)_6\text{-NH}_2$) are observed as major ions and the intensity of Au^+ is weaker. Besides, no fragment ions originating from M are observed in the low m/z region. This clearly indicates that only the top-layer organic molecule is selectively ionized/desorbed.

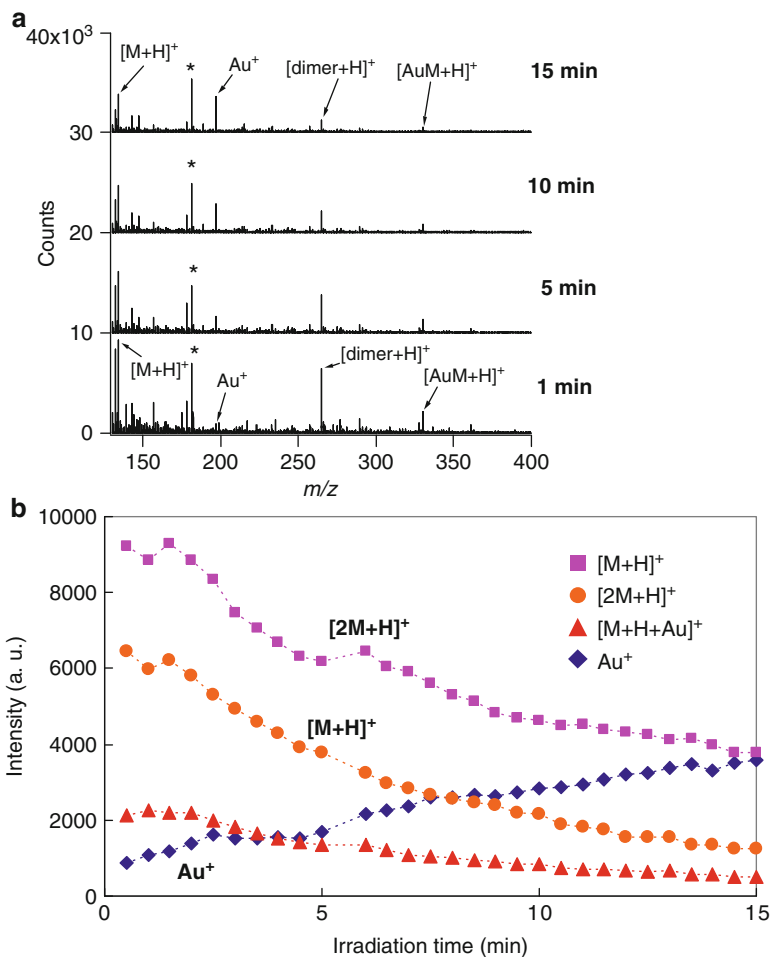


Fig. 10.6 (a) EDI mass spectra for the self-assembled monolayer $\text{Au-S-(CH}_2)_6\text{-NH}_2$ as a function of irradiation time after the start of the measurement. M stands for $\text{HS-(CH}_2)_6\text{-NH}_2$. (b) Ion intensities for the major ions as a function of irradiation time. The peak with asterisk denotes $\text{H}^+(\text{CH}_3\text{COOH})_3$ at m/z 181. This ion originates from the electro sprayed 1 M CH_3COOH aqueous solution. All other small peaks originate from contaminants (reproduced with permission from [35])

Figure 10.6b shows the intensities of the major ions as a function of irradiation time. The decrease in the abundance of the ions $[M + H]^+$, $[2M + H]^+$, and $[M + H + Au]^+$ is accounted for by the gradual growth of Au^+ originating from the Au substrate. Au cluster ions (Au_n^+) were not detected with prolonged irradiation in Fig. 10.6a. Only the appearance of the monomer ion Au^+ indicates that the exposed gold substrate suffers only from atomic level etching by EDI. In summary, no ablation, but atomic and molecular level etching takes place in EDI. This is in marked contrast to the results obtained by SIMS using atomic ions as projectiles. Wolf et al. measured the 12 keV Ga^+ ion SIMS mass spectra for self-assembled monolayers of $CH_3(CH_2)_{13}SH$ formed on an Au surface [36]. They observed Au^+ , Au_3^+ , Au_nS^+ with $n = 1-5$, $Au_6S_2H_2^+$, $Au_7S_3H_2^+$, $Au_8S_2H^+$, etc. in their SIMS mass spectrum. It is apparent that Au ablation takes place in Ga^+ SIMS to give gold cluster ions. Czerwiński et al. performed computational simulation of C_{60} bombardment of a self-assembled monolayer of octanethiol molecules on Au{111} [16]. They predicted that almost all ejected octanethiol molecules were fragmented.

Figure 10.7a–d shows the EDI mass spectra for bradykinin films with ~1,000, 100, 10, and 1 ML (monolayer) thickness, respectively [37].

The film thickness was crudely estimated from the amounts on the samples deposited on the 3 mm-diameter stainless steel substrate assuming that the film was uniformly deposited. In the mass spectra in Fig. 10.7, the protonated molecule ion $[M + H]^+$ is observed as a base peak with some fragment ions with *b* and *y* series. It should be noted that the relative intensities of the *b* and *y* fragment ions increase gradually with increasing film thickness. That is, in EDI thicker samples are subject to more fragmentation.

Figure 10.7e shows the sum of the intensities of $[M + H]^+$ and $[M + 2H]^{2+}$ for the samples with four film thicknesses as a function of irradiation time. The ion intensities of $\{[M + H]^+ + [M + 2H]^{2+}\}$ for the 10 pmol (~1 ML) sample decrease exponentially, i.e., about half of the deposited samples is desorbed in ~3 min. It should be noted that for films with thickness values larger than 10 ML the ion intensities are almost independent of irradiation time for at least 10 min. This suggests that the thickness of solid bradykinin desorbed by a single collisional event in EDI is less than 10 ML. In Fig. 10.7e, the ion intensities at the start of the measurement are of the order of the sample thicknesses of $1 \geq 10 > 100 > 1,000$ ML. That is, the thinnest sample gives the strongest ion signal with the least fragmentation (see Fig. 10.7a–d), indicating that in EDI the ionization and/or desorption efficiencies decrease with increasing film thickness. A similar trend was observed for gramicidin S [30].

Because EDI has surface etching ability at the molecular level, the technique is applicable for removing contaminants from the surface of the samples. Figure 10.8 presents the EDI and FAB (fast atom bombardment) mass spectra for the drug FK506 (tacrolimus, immunosuppressant) [30].

Figure 10.8a shows the EDI mass spectrum for 1 nmol FK506 deposited on stainless steel substrate. The ions $[M + K]^+$, $[M + Na]^+$, $[M + H]^+$, $[M - H_2O + H]^+$, and $[M - 2H_2O + H]^+$ were observed. The appearance of $[M + H]^+$, $[M + Na]^+$, and $[M + K]^+$ indicates that EDI is a soft ionization method, but the appearance of the dehydrated ions, $[M - 2H_2O + H]^+$ and $[M - H_2O + H]^+$, also indicates that degradation of the sample molecule takes place to some extent in this technique. Figure 10.8b shows the FAB mass spectrum just after the FAB gun was turned on (the EDI gun was off). No molecular ions of FK506 could be detected. However, weak signals of $[M + Na]^+$, and $[M + K]^+$ with strong chemical noise appeared at 10 s after firing the FAB gun in Fig. 10.8c. The molecular ions disappeared at 20 s after the start of FAB operation in Fig. 10.8d (dose of $\sim 10^{13}$ atoms/cm² of 5 keV Xe). The periodic peaks appearing in Fig. 10.8d are spaced by 13 or 14 u, indicating that the sample surface of FK506 was severely damaged and polymerized radiation products accumulated on the surface of the sample. Figure 10.8e shows the EDI spectrum at 20 s after the damaged sample was bombarded by the electrospayed droplets (the FAB gun was off).

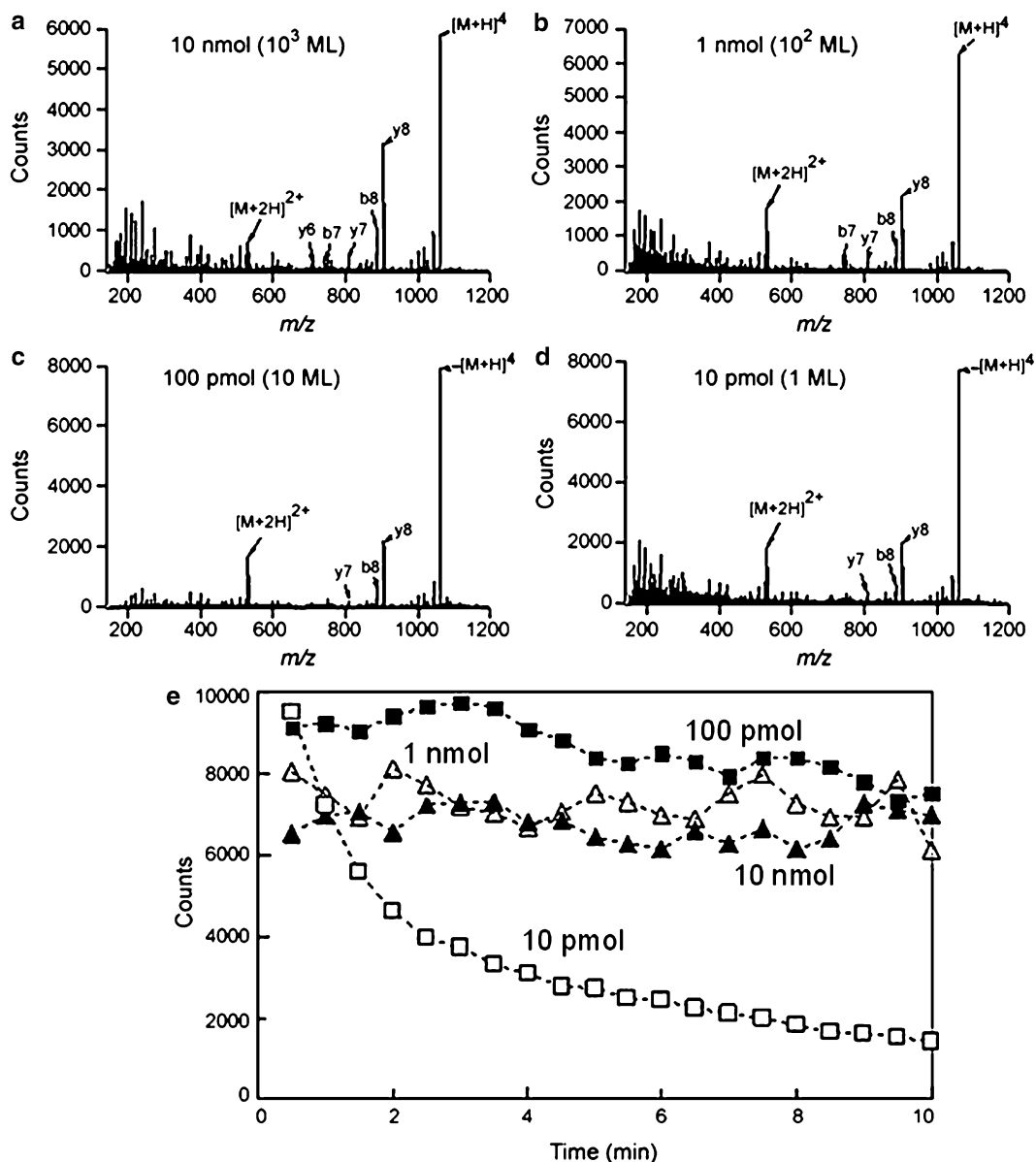


Fig. 10.7 EDI mass spectra for bradykinin with sample amounts of (a) 10 nm, (b) 1 nmol, (c) 100 pmol, and (d) 10 pmol. (e) Sum of the intensities of $[M + H]^+$ and $[M + 2H]^{2+}$ for the four films plotted as a function of irradiation time (reproduced with permission from [37])

Figure 10.8e is almost the same as the original FK506 in Fig. 10.8a. The observed recovery of the mass spectrum for FK506 indicates that EDI has the ability for shallow surface cleaning. From the experimental results described above, it is evident that EDI can sputter only the topmost surface molecules without damaging the sample underneath the surface. This kind of almost damage-free self-cleaning effect was also observed in MCI [38]. The molecular-level cleaning of the contaminants on the sample surface may be useful in sample pretreatment for surface analysis such as X-ray photoelectron spectroscopy (XPS), Auger electron spectroscopy (AES), electron microscopy.

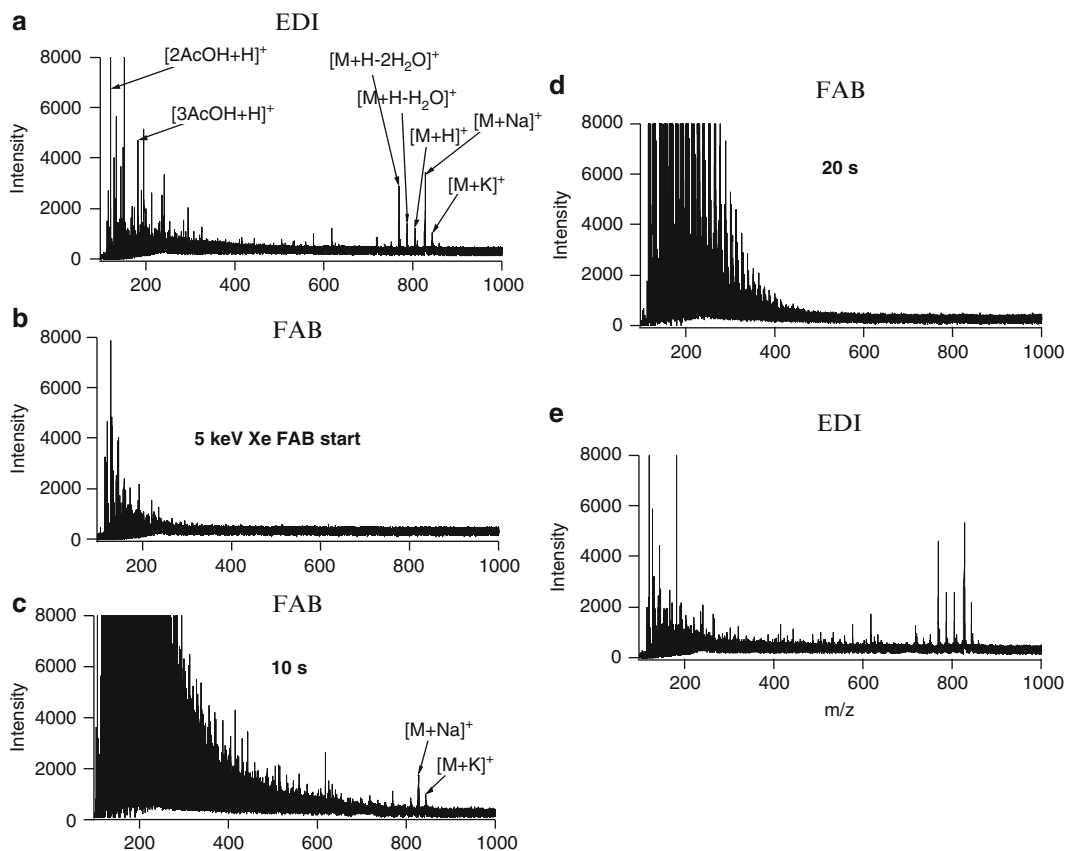


Fig. 10.8 EDI and FAB mass spectra for 1 nmol of FK506. (a) EDI mass spectrum for FK506; $[M + K]^+$, $[M + Na]^+$, $[M + H]^+$, $[M - H_2O + H]^+$, and $[M - 2H_2O + H]^+$ were observed. (b) FAB mass spectrum right after the FAB gun initiation (5 keV Xe FAB with a beam of about 0.1 μ A); only small m/z fragment ions but no molecular ions could be detected for FK506. (c) FAB mass spectra at 10 s after FAB gun ignition; strong growth of chemical noise as well as the appearance of $[M + Na]^+$ and $[M + K]^+$ was observed. (d) FAB mass spectrum at 20 s after the FAB gun ignition; the intensities of chemical noise decreased and molecular ions of FK506 disappeared. (e) EDI mass spectrum after the sample was irradiated by Xe FAB for 20 s; the original mass spectrum for FK506 was restored (reproduced with permission from [30])

10.4 Application of EDI to Synthetic Polymers and Biological Samples

EDI was applied to various synthetic polymers such as polystyrene (PS) [39–43], polyethylene terephthalate (PET) [35], polyvinyl chloride (PVC) [44], polyimide (PI) [45], and polymethyl methacrylate (PMMA) [46]. The EDI mass spectra were found to be composed of fragment ions that reflect the molecular units of the polymer backbones.

Polyimide (PI) is known to be a difficult sample for depth profiling because of the selective etching of O and N, resulting in accumulation of graphitic carbon on the sample surface after etching by atomic ion bombardment. In this respect, PI is an appropriate sample to examine whether selective etching takes place by EDI. The surface properties of polymers are very important in many applications, and very often they are different from their bulk. Among the analytical techniques used to probe surface chemical properties of polymers, XPS has been the most essential.

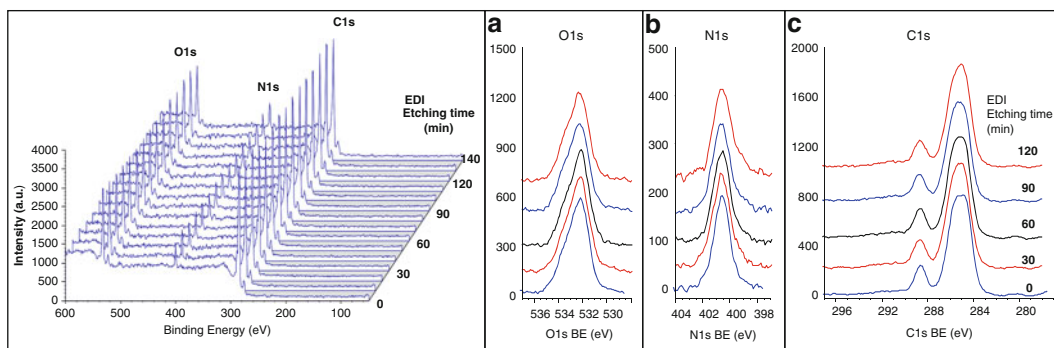


Fig. 10.9 XPS spectra for a 0.05 mm-thick PI film as a function of EDI irradiation time. *Left panel:* XPS survey spectra. *Right panel:* (a) O1s XPS spectra, (b) N1s spectra, (c) C1s spectra (reproduced with permission from [45])

Figure 10.9 shows the XPS spectra for PI as a function of EDI irradiation time. The intensities of O1s, N1s, and C1s remain unchanged for an irradiation time of 140 min, indicating that selective etching of O and N does not take place in EDI [45]. In the separate experiment, the marked selective etching was observed when PI was irradiated with 500 eV Ar^+ ions [45]. This clearly indicates the superiority of EDI over atomic ions for etching.

Figure 10.10a–d shows the surface topological changes for PI etched by EDI for 0 (as received), 30, 60, and 90 min, respectively [45].

The PI surface becomes rougher (in terms of short-wavelength roughness) with 30 min EDI etching (Fig. 10.10b) compared to the as received sample (Fig. 10.10a). This may be caused by the preferential etching of defects over the harder microcrystalline domains in the near-surface region of the PI sample. After 60 min (Fig. 10.10c), the surface is smoother than after 30 min, and this is likely to have been caused by selective etching and also by the collapse of sharp protrusions formed with 30 min EDI etching (Fig. 10.10b). After EDI etching for 90 min, the surface becomes rougher than after 60 min. That is, surface roughening and smoothing repeat periodically. Such a trend was also observed for PMMA [46].

Figure 10.11 shows the EDI mass spectrum for PI [45].

The most probable chemical structures for the major ions are shown in the figure. All the major ions observed reflect the molecular units of the PI backbone. The possible PI fragmentation processes are shown in Fig. 10.12 [45].

All the major ions in Fig. 10.11 are explained by molecular elimination from the backbone of PI. PI is synthesized by condensation polymerization reactions (dehydration) of amines and carboxylic acids. The model shown in Fig. 10.12 suggests that the ions with m/z 167, 283, and 299 are formed by hydration of precursor fragments formed from PI. The hydration in fragmentation processes is highly probable because the PI sample was irradiated with water droplets.

One of the most appropriate samples for evaluating EDI is PET because its damage characteristics have been studied under bombardment with various projectiles, such as C_{60}^+ , Au_3^+ , and Au^+ ions [47]. The EDI mass spectra measured for PET immediately after and 60 min after the start of EDI are shown in Fig. 10.13a, b [37].

High-mass ions of monomer units up to tetramer (m/z 769) are observed. Note that the mass spectra do not change after 60 min irradiation, although ion intensities decreased to about half their initial values. The decrease in ion signal intensities is attributed either to surface charging or to the topological changes induced by EDI irradiation.

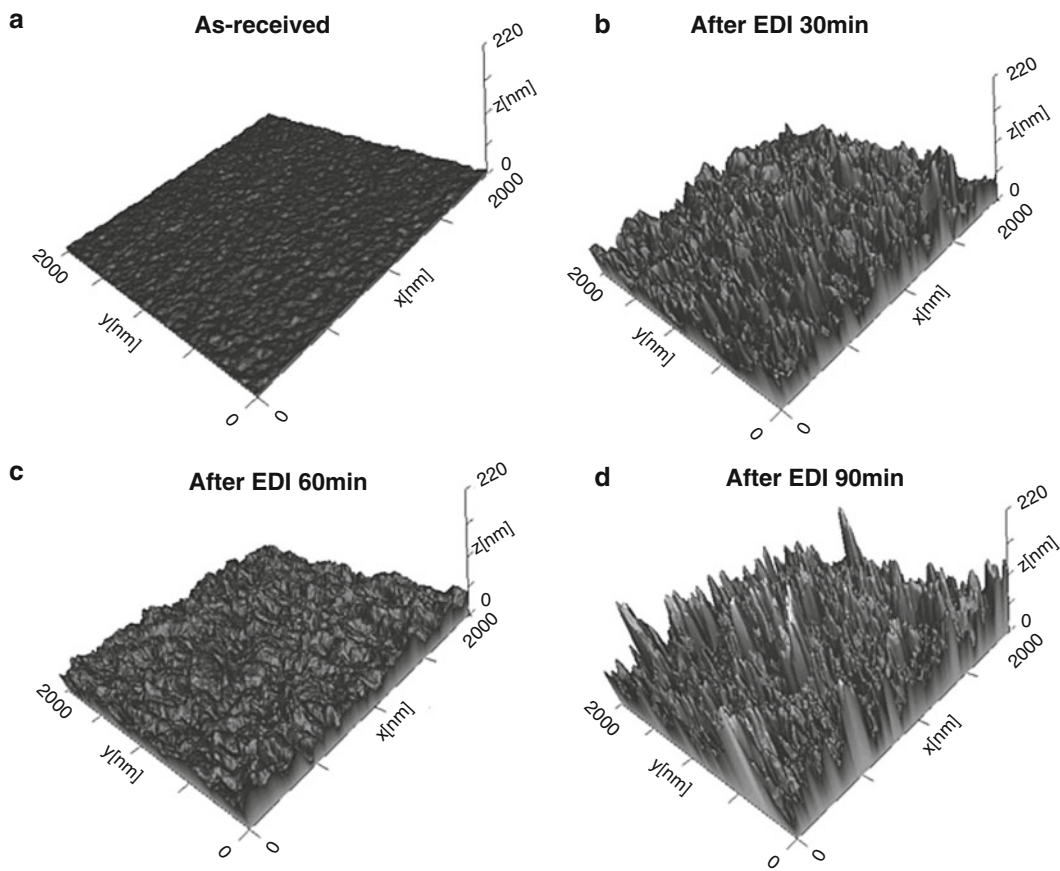


Fig. 10.10 Surface topologies of PI etched by EDI for (a) 0 min (as received), (b) 30 min, (c) 60 min, and (d) 90 min as measured by atomic force microscopy (AFM); the incidence angle of the EDI beam was 60° to the surface normal. The surface roughness values in an area of $2 \times 2 \mu\text{m}^2$ were 2, 13, 7, and 21 nm, respectively, for EDI irradiation times of 0 (as received), 30, 60, and 90 min (reproduced with permission from [45])

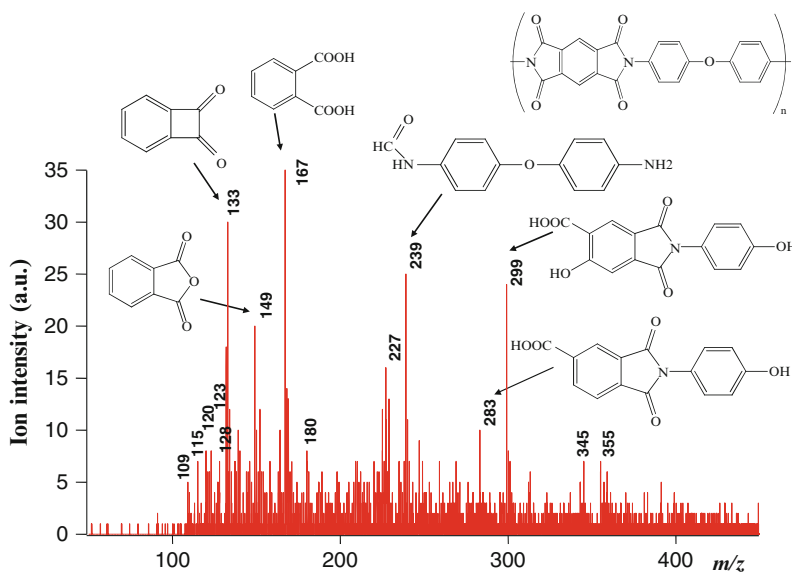


Fig. 10.11 EDI mass spectrum for PI. The ions with m/z below 100 were cut off by the ion guide used in the mass spectrometer (reproduced with permission from [45])

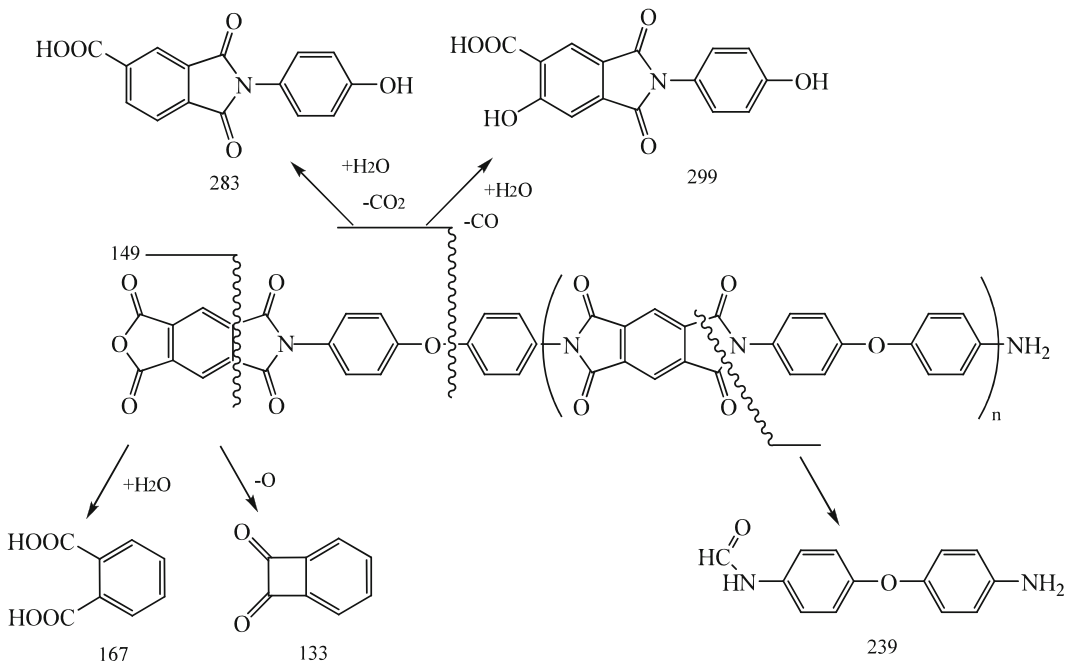


Fig. 10.12 Possible fragmentation processes for PI etched by EDI (reproduced with permission from [45])

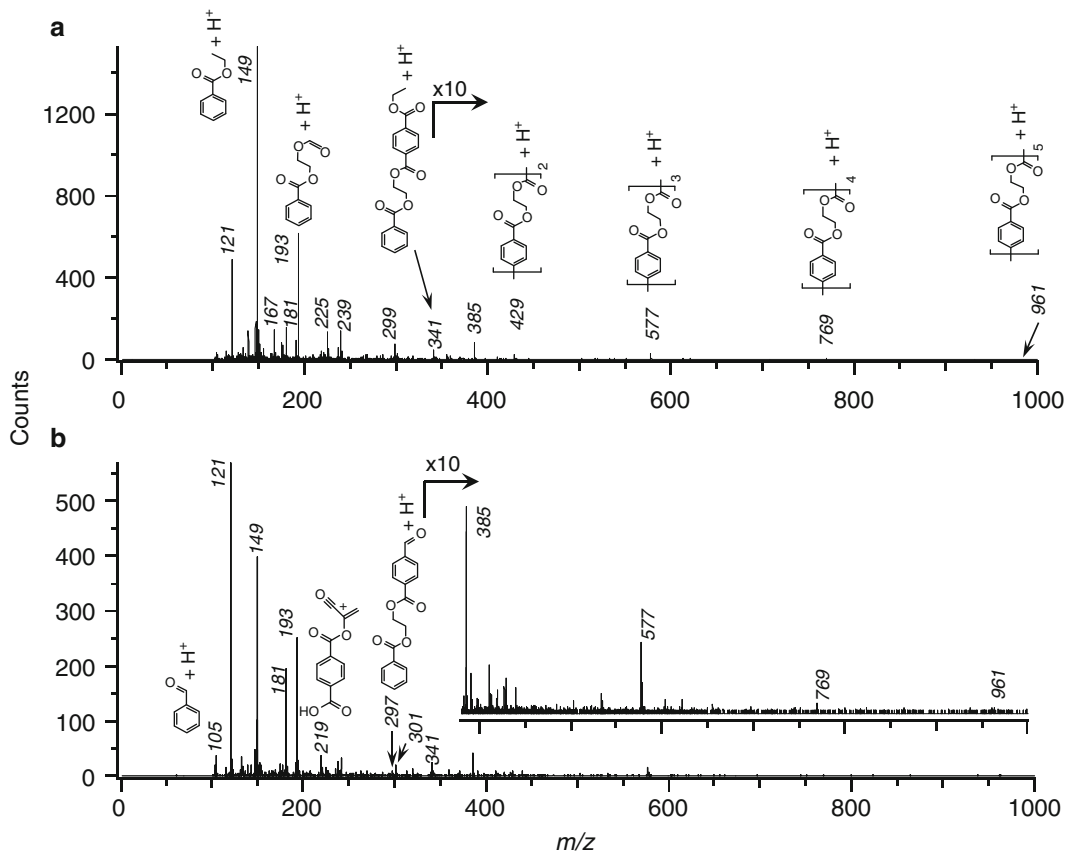


Fig. 10.13 EDI mass spectra for a 0.1 mm-thick PET film measured after the start of the measurement (a) immediately after, and (b) 60 min (reproduced with permission from [37])

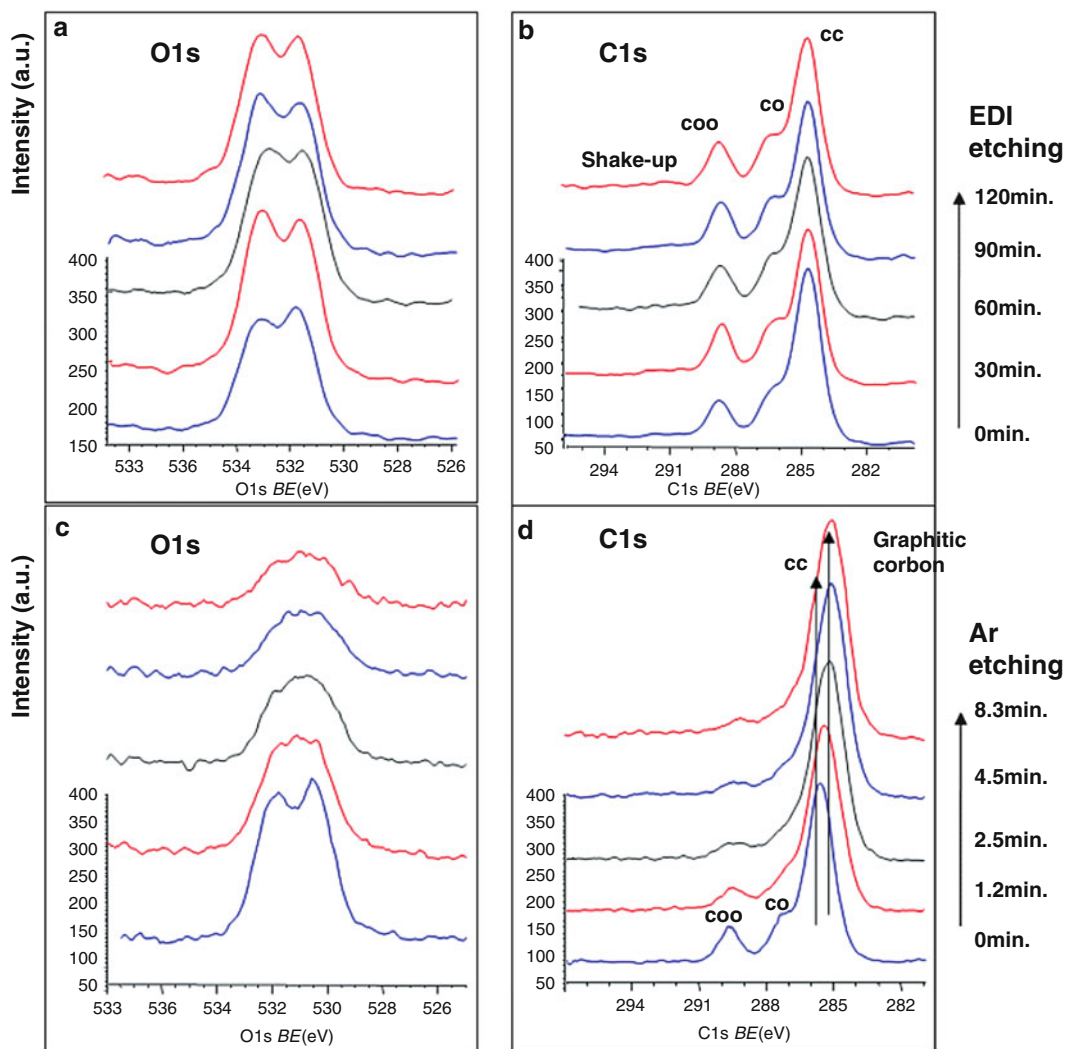


Fig. 10.14 XPS spectra for 0.1 mm-thick PET film: (a) and (b) measured as a function of EDI irradiation time for O1s and C1s, respectively; (c) and (d) measured as a function of 1 keV Ar⁺ irradiation time for 8.3 min for O1s and C1s, respectively. The etching rate of EDI for PET is determined to be 2 nm/min. The sputtered depth in 120 min EDI irradiation is about 240 nm. BE stands for binding energy, in eV (reproduced with permission from [37])

Figure 10.14a, b shows the O1s and C1s XPS spectra of PET measured as a function of EDI irradiation time [37].

The spectrum before etching (0 min) differs slightly from the spectra after EDI irradiation. This may be caused either by surface contamination by some hydrocarbons or to modification of the polymer surface induced by the self-diffusion of molecules on the top surface.

The spectra in Fig. 10.14a, b show no recognizable change up to 120 min EDI irradiation. For comparison, we also measured the XPS spectra for a PET film bombarded with 1 keV Ar⁺. Figure 10.14c, d shows the O1s and C1s spectra as a function of 1 keV Ar⁺ irradiation time up to 8.3 min. The peak intensities of O1s and of C1s for COO and CO spectra decrease rapidly and the peak of C–C shifts to that of most graphitic carbon with irradiation time. It is apparent that rapid deoxygenation, dehydrogenation, and graphitization take place under 1 keV Ar⁺ bombardment. This is a marked contrast to the fact that the chemical components of PET surface are little modified by EDI.

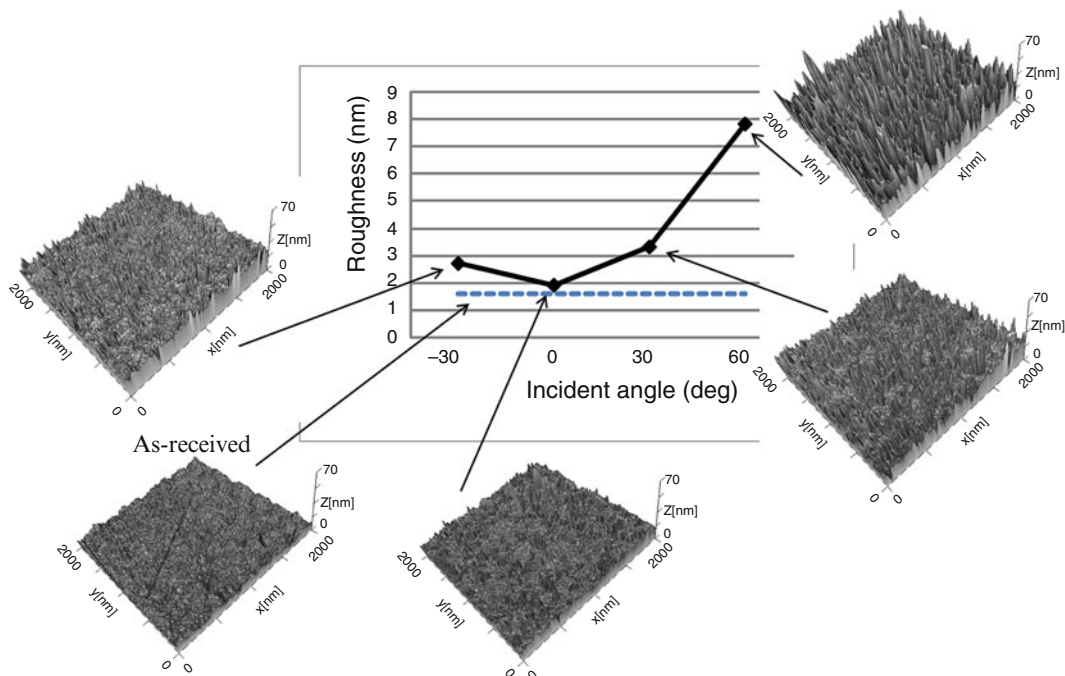


Fig. 10.15 Surface roughness of a 0.1 mm-thick PET film etched by EDI as measured by AFM as a function of beam angle with -30° , 0° , $+30^\circ$, and $+60^\circ$ to the surface normal. EDI irradiation time was 30 min for each measurement. The dashed line indicates the original sample roughness before EDI irradiation

Figure 10.15 shows the AFM images of 0.1 mm thick PET film etched by EDI measured as a function of beam angle to the surface normal.

The roughness of the sample irradiated with EDI for 30 min with the beam angle of 0° is nearly the same as that of the as-received sample. With increasing beam angle, the roughness increases rather steeply from 1.7 nm at 0° to 7.2 nm at 60° . It is evident that to suppress surface roughening, a small incident beam angle is preferable. It is well known that ion beam bombardment at oblique incidence often produces modulation on the surface of solid samples [48]. In EDI, the surface roughening effect for soft materials may be more serious than in other SIMS techniques because EDI uses high-momentum water droplet projectiles.

The mass spectra and XPS spectra were also measured for other polymers such as PS [40–43], PVC [44], and PMMA [46]. For all the synthetic polymers examined, no change was observed in either SIMS mass spectra or XPS spectra for the prolonged EDI irradiation. It is evident that the treated polymers did not undergo any recognizable surface damage or accumulation of radiation products by EDI irradiation. That is, for all the polymers analyzed, nonselective molecular-level etching is realized without leaving any noticeable damage as far as the XPS measurement is concerned.

EDI/SIMS was applied to mouse brain as the biological tissue sample [49]. In the positive mode of operation, various kinds of PC (phosphatidylcholine) and GalCer (galactosylceramide) could be detected. In the separate experiments, MALDI measurements were also performed using 2,5-dihydrobenzoic acid (DHB) as a matrix for comparison with EDI. The S/N ratios for the positive mode mass spectra obtained by EDI and MALDI were similar for PC and GalCer. That is, the detection sensitivities of EDI and MALDI are about the same. In contrast, negative-mode mass spectra obtained by EDI and MALDI present some distinct differences, as shown in Fig. 10.16 [49].

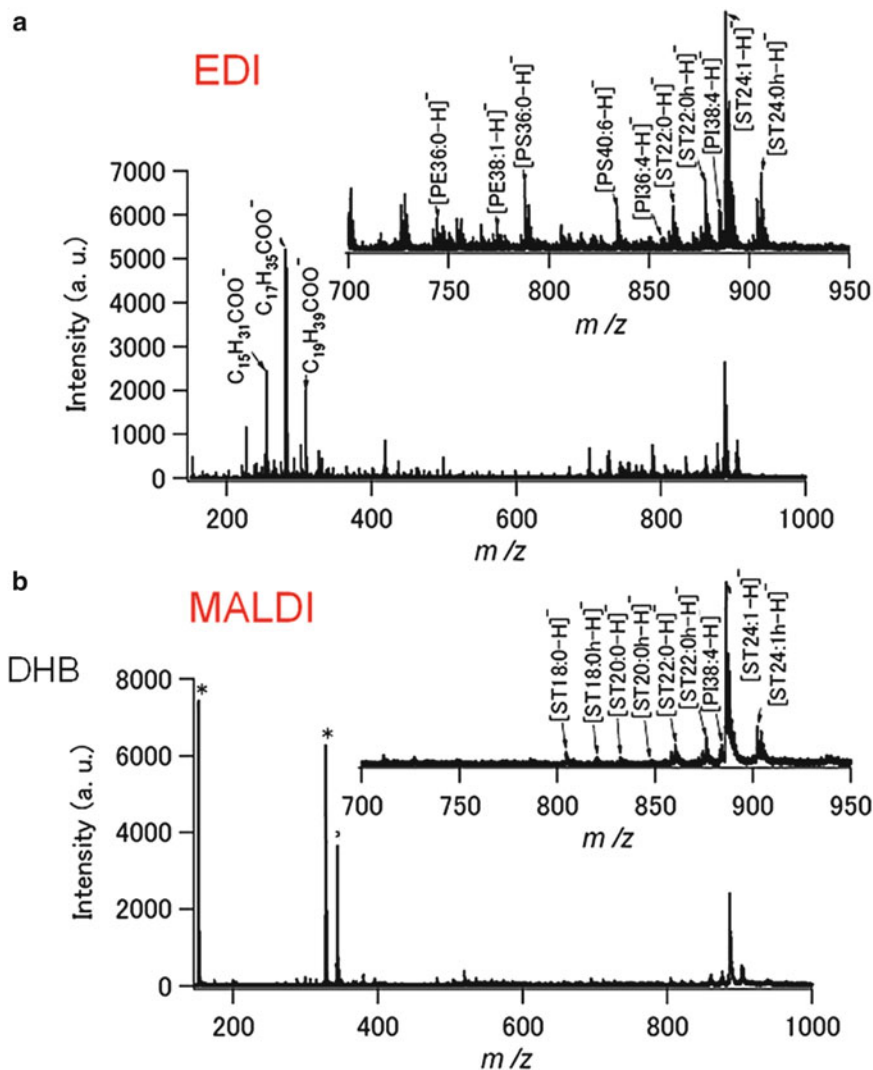


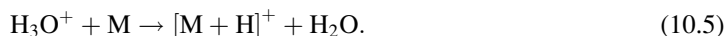
Fig. 10.16 Negative mode mass spectra of homogenized mouse brain obtained by (a) EDI, and (b) MALDI (matrix: 2,5-dihydrobenzoic acid (DHB)). In the MALDI mass spectrum, peaks marked with *asterisks* originate from the matrix (DHB) (reproduced with permission from [49])

PE (phosphatidylethanolamine), PS (phosphatidylserine), PI (phosphatidylinositol), and ST (sulfatide) are detected in the EDI mass spectrum, whereas PE and PS are absent in MALDI mass spectrum. That is, EDI is capable of more non-selective ionization for the biological molecules.

One of the characteristic features of EDI is its capability to form strong negative, as well as positive ions for many organic compounds, e.g., amino acids [50], peptides [31], pigments [51]. For example, both basic and acidic amino acids gave strong negative ions of the type $[M-H]^-$ as well as positive ions of the type $[M+H]^+$ approximately with equal abundance [50], suggesting that EDI has some unique nature for the formation of secondary ions. The efficient formation of positive and also of negative ions may be ascribed to the disproportionation proton transfer reaction of water molecules, i.e., the occurrence of electrolytic dissociation reaction of water molecules in the colliding interface [35, 50, 51].

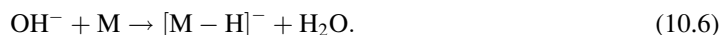


For the colliding system, the endoergic reaction (10.4) may be one of the primary routes for energy dissipation. The H_3O^+ , hydronium ion, is known to be a very strong acid, and is likely to transfer its proton to the analyte M to form the protonated molecule $[\text{M} + \text{H}]^+$ at the collision interface.



The occurrence of reaction (10.5) explains the strong appearance of $[\text{M} + \text{H}]^+$ for molecules that have larger proton affinities than H_2O (691 kJ/mol).

The OH^- in reaction (10.4) is also known to be a very strong base and it deprotonates from M to form $[\text{M}-\text{H}]^-$.

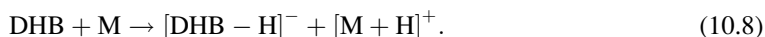


In a sense, the very strong acid H_3O^+ and also the very strong base OH^- are inherently incorporated in the supersonic collisional events in EDI.

In EDI mass spectra, some compounds give strong radical cations and anions (e.g., C_{60} [50], coronene, and organic pigments [51]) in addition to $[\text{M} + \text{H}]^+$ and $[\text{M}-\text{H}]^-$ ions. For example, mass spectra for C_{60} , C_{60}^+ and C_{60}^- ions are observed in EDI with approximately equal abundances [50]. Some of these ions may be formed by the disproportionation electron transfer reaction (10.7) caused by the supersonic collision in EDI [51].



In the MALDI mass spectrum in Fig. 10.16, PE and PS are not detected when DHB (a typical matrix for MALDI) is used. The ion formation mechanism for MALDI using DHB as a matrix may be ascribed to reaction (10.8). It should be recognized here that DHB is one of the organic acids and acts as a protonating reagent.



The $[\text{DHB}-\text{H}]^-$ ion, the reaction product in reaction (10.8), may act as the deprotonating reagent for the formation of the negative ion of the analyte.



However, the basicity of $[\text{DHB}-\text{H}]^-$ is much weaker than that of OH^- because the negative charge in $[\text{DHB}-\text{H}]^-$ is dispersed in the molecular ions (i.e., energy stabilization due to charge delocalization) and the occurrence of reaction (10.9) is much less likely than reaction (10.6). This may explain the absence of the negative ions of PE and PS in the MALDI mass spectrum in Fig. 10.16.

10.5 Application of EDI to Inorganic Materials

EDI has been applied to alkali halides [52], TiO_2 [53], Si [37], SiO_2 [37], InP [37], TiO_2 [54], Ta_2O_5 [54] and CuO [55]. As an example, the results obtained for native SiO_2 (2 nm) on Si (SiO_2/Si) [37] will be discussed. In the positive ion mode, the major ions observed are $[n\text{SiO}_2 + \text{H}]^+$ with $n = 1$ and 2.

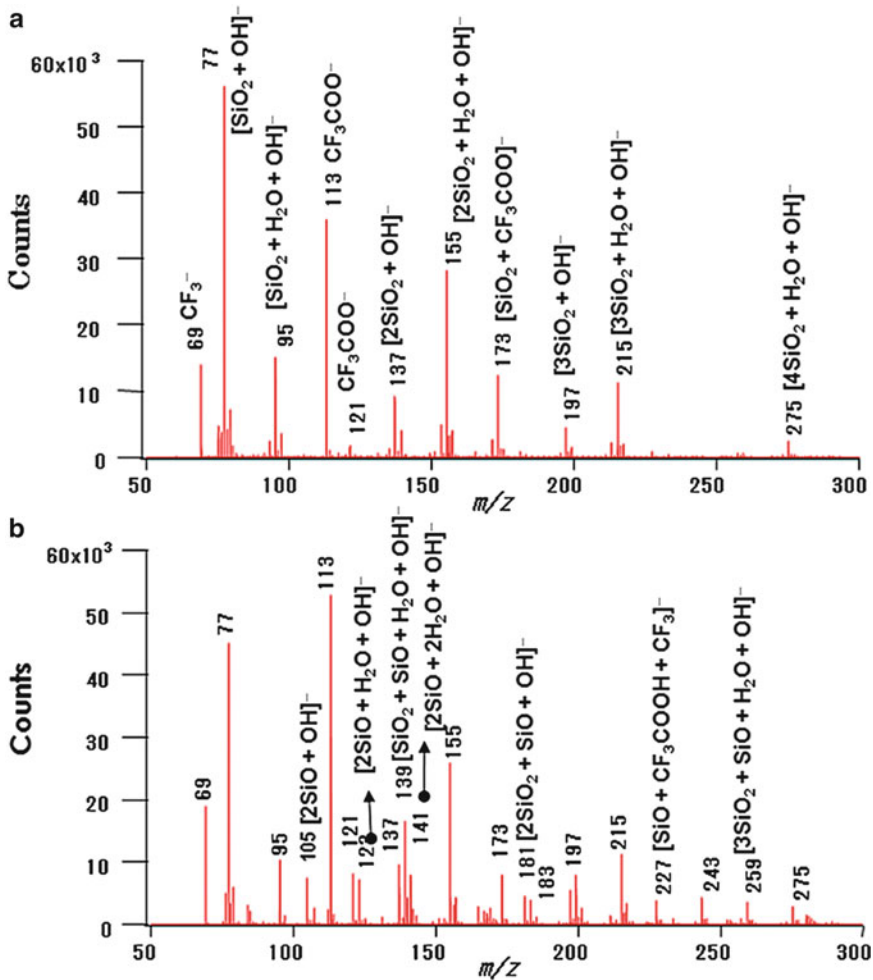


Fig. 10.17 (a) Negative mode EDI mass spectrum of a 2 nm-thick film of native SiO₂ on Si obtained immediately after EDI irradiation. The thickness of SiO₂ was measured by spectroscopic ellipsometry. Major peaks are assigned as m/z 69: CF₃⁻, m/z 77: [SiO₂ + OH]⁻, m/z 95: [SiO₂ + H₂O + OH]⁻, m/z 113: CF₃COO⁻, m/z 121: [SiO₂ + SiO + OH]⁻, m/z 137: [2SiO₂ + OH]⁻, m/z 139: [SiO₂ + SiO + H₂O + OH]⁻, m/z 155: [2SiO₂ + H₂O + OH]⁻, m/z 173: [SiO₂ + CF₃COO]⁻, m/z 197: [3SiO₂ + OH]⁻, m/z 215: [3SiO₂ + H₂O + OH]⁻, and m/z 275: [4SiO₂ + H₂O + OH]⁻. (b) Negative-mode EDI mass spectrum obtained after 30 min EDI irradiation for the film in (a). New peaks that were not observed in (a) are assigned as m/z 105: [2SiO + OH]⁻, m/z 123: [2SiO + H₂O + OH]⁻, m/z 141: [2SiO + 2H₂O + OH]⁻, m/z 181: [2SiO₂ + SiO + OH]⁻, m/z 227: [SiO + CF₃COOH + CF₃]⁻, and m/z 259: [3SiO₂ + SiO + H₂O + OH]⁻ (reproduced with permission from [37])

With EDI irradiation for 30 min, no distinct change was observed in the mass spectra although the pristine Si should be exposed with this EDI irradiation time. Thus, no clear-cut information was obtained about the etching rate for the 2-nm SiO₂ layer on Si. In contrast, the negative-mode EDI mass spectra showed a remarkable change as a function irradiation time. Figure 10.17a shows the negative EDI mass spectrum for the SiO₂/Si layer immediately after the start of EDI irradiation [37].

The major ions in Fig. 10.17a are assigned as m/z 77: [SiO₂ + OH]⁻, m/z 95: [SiO₂ + H₂O + OH]⁻, m/z 137: [2SiO₂ + OH]⁻, m/z 155: [2SiO₂ + H₂O + OH]⁻, m/z 173: [SiO₂ + CF₃COO]⁻, m/z 197: [3SiO₂ + OH]⁻, m/z 215: [3SiO₂ + H₂O + OH]⁻, and m/z 275: [4SiO₂ + H₂O + OH]⁻. Thus, all the major ions contain n -SiO₂ with $n = 1-4$. Two other major ions at m/z 69 and 113 are assigned as

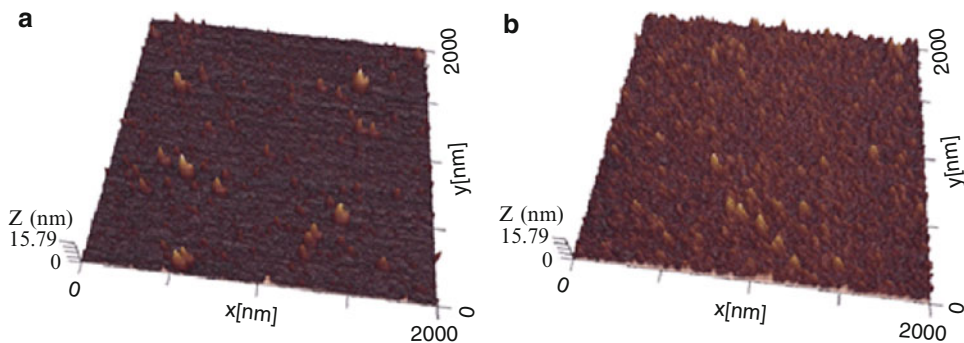


Fig. 10.18 (a) AFM image ($2 \times 2 \mu\text{m}^2$) for SiO_2 (2 nm)/Si as received. (b) AFM image ($2 \times 2 \mu\text{m}^2$) for SiO_2 /Si etched by EDI for 30 min. The incidence beam angle is 60° to the surface normal. (reproduced with permission from [37])

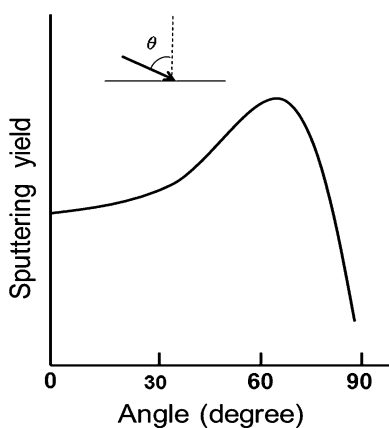


Fig. 10.19 Conceptual idea of the relation between the sputtering yield and the beam incidence angle (θ) to the surface normal

CF_3^- and CF_3COO^- . The CF_3COO^- ion originates from the projectile generated by electro spraying 0.01 M CF_3COOH aqueous solution. The CF_3^- ion at m/z 69 may be formed by the dissociation of the trifluoroacetate ion CF_3COO^- , $\text{CF}_3\text{COO}^- \rightarrow \text{CF}_3^- + \text{CO}_2$.

Continuous EDI irradiation caused the gradual appearance of new peaks that were not apparent when EDI just started. Figure 10.17b shows the negative-mode EDI mass spectrum observed with 30 min EDI irradiation. The newly observed peaks and their assignments are: m/z 105: $[\text{2SiO} + \text{OH}]^-$, m/z 123: $[\text{2SiO} + \text{H}_2\text{O} + \text{OH}]^-$, m/z 141: $[\text{2SiO} + \text{2H}_2\text{O} + \text{OH}]^-$, m/z 181: $[\text{2SiO}_2 + \text{SiO} + \text{OH}]^-$, m/z 227: $[\text{SiO} + \text{CF}_3\text{COOH} + \text{CF}_3]^-$, and m/z 259: $[\text{3SiO}_2 + \text{SiO} + \text{H}_2\text{O} + \text{OH}]^-$. All of these peaks contain $n\text{SiO}$ with an n value of either 1 or 2. These ions were only observed when the Si substrate was exposed bare by EDI irradiation. Since it took about 10 min to remove the native 2 nm SiO_2 , the etching rate for SiO_2 was estimated to be about 0.2 nm/min.

Figure 10.18 shows the AFM images for SiO_2 (2 nm)/Si(100), before and after 30 min EDI etching. The surface roughness of as-received SiO_2 (2 nm)/Si(100) was 0.6 nm. After 30 min etching, the surface roughness increased to 1.1 nm at ~ 6 nm sputtering depth [37].

Figure 10.19 shows the general trend of the variation of the sputtering yield with beam angle [48].

The apparatus shown in Fig. 10.2 adopted the beam angle of 60° to the surface normal. Ion bombardment with off-normal incidence ($\theta \neq 0$) often produces periodic height modulations on the

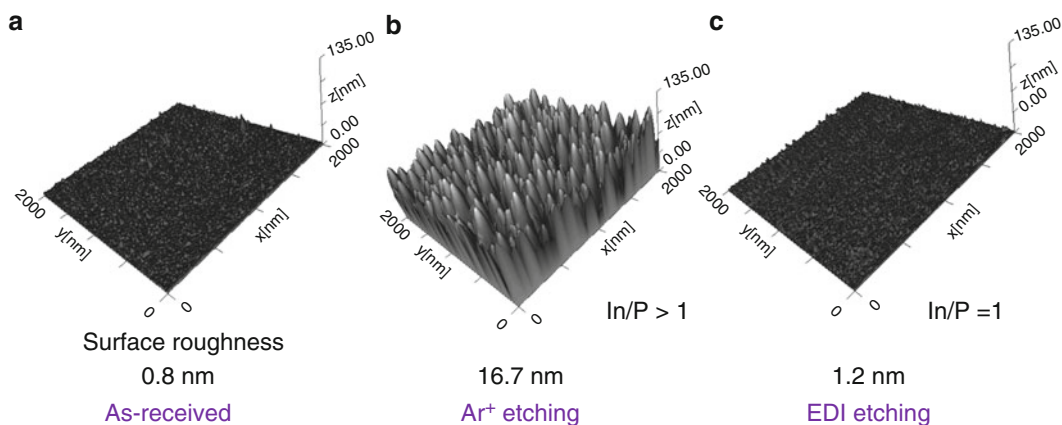


Fig. 10.20 AFM images ($2 \times 2 \mu\text{m}^2$) for InP: (a) as received; (b) etched by 3 keV Ar^+ (etching depth of ~ 60 nm as calibrated for SiO_2) with the incidence beam angle of 45° to the surface normal; (c) etched by EDI (etching depth of ~ 48 nm as calibrated for SiO_2) with the incidence beam angle of 60° to the surface normal (reproduced with permission from [37])

surface of solid samples, e.g., etching cone or ripple formation [56]. The surface roughness induced by EDI irradiation may be reduced by increasing or decreasing the beam angle from $\sim 60^\circ$ (see Fig. 10.15). An alternative way to suppress surface roughening is to rotate the substrate [57, 58].

InP is used in high-power and high-frequency electronics because of its superior electron mobility with respect to the more common semiconductors Si and GaAs. For the surface analysis of InP, it is of paramount importance to avoid the selective etching of P with respect to In and also to suppress the growth of etching cones on the surface.

In the positive mode of EDI/SIMS, only In^+ but no cluster ions of the type In_n^+ were detected. The changes in surface topology for InP (111) etched with 3 keV Ar^+ and EDI were examined by AFM. Figure 10.20a–c shows the AFM images of InP (111) as received, etched by 3 keV Ar^+ (etching rate: 2 nm/min as calibrated for SiO_2) for 30 min, and etched by EDI (etching rate: ~ 0.2 nm/min, as calibrated for SiO_2) for 240 min, respectively [37].

Growth of etching cones is observed on the surface of InP (111) etched by Ar^+ (Fig. 10.20b). The formation of etching cones mainly composed of In is generally observed when InP is analyzed by atomic ion SIMS. It was suggested that etching cones formed as a result of the heat effect [37]. The surface of InP (111) etched by EDI (Fig. 10.20c) is much smoother than that etched by Ar^+ (Fig. 10.20b), suggesting that the heat effect that leads to the formation of the etching cone is almost negligible in EDI. From the AFM images in Fig. 10.20c, the surface roughness (1.2 nm) after EDI etching (~ 48 nm etching depth as calibrated for SiO_2) increased only slightly compared with the sample as received (0.8 nm). In contrast, higher roughness by more than one order of magnitude (16.7 nm) was observed for InP etched by 3 keV Ar^+ (~ 60 nm etching depth as calibrated for SiO_2). The relative concentrations of In and P for InP etched by 3 keV Ar^+ and EDI were measured by XPS. The ratio of In/P increases from 1 to 1.7 for 3 keV Ar^+ etching. Apparently, under 3 keV Ar^+ , P was etched preferentially over In, but for EDI etching the ratio In/P remained 1 (Fig. 10.21), indicating that InP is not selectively etched for either In or P.

It was also found that the full-width at half-maximum (FWHM) of the In $3d_{5/2}$ and P 2p peaks of the XPS spectra were the same before and after EDI etching, indicating that the crystalline structure of InP (111) is preserved and that EDI does not induce amorphization. Similar results were obtained for SiO_2/Si and HF-treated Si [59].

Transition metal oxides have many practical applications such as catalysts, electric or magnetic devices, and anticorrosion coatings. It is well known that when the transition metals oxides are etched

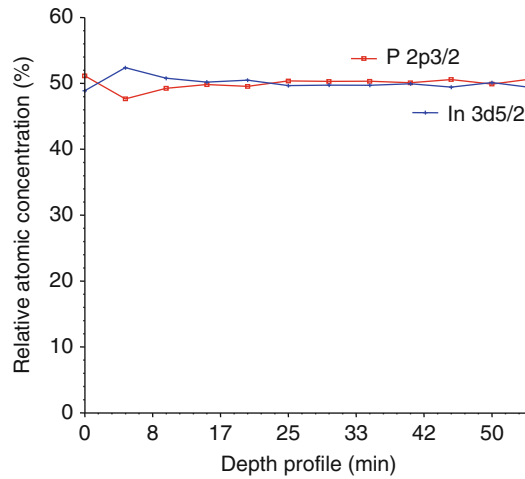


Fig. 10.21 Depth profile for InP measured by XPS

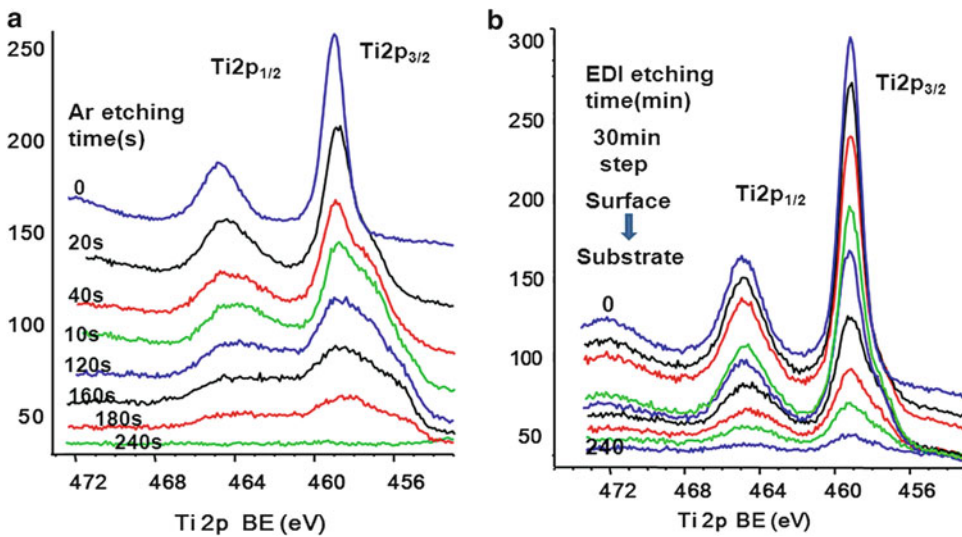


Fig. 10.22 XPS depth analysis of a 20 nm thin film of TiO_2 deposited on Si(001) substrate etched by (a) 500 eV Ar^+ , and (b) EDI (reproduced with permission from [55])

by Ar^+ , reduction is observed as alternation of the composition or chemical state of the oxides [60–63]. These alternations hinder the determination of oxidation states in depth analysis in XPS. In the case of TiO_2 and Ta_2O_5 , the oxides are reduced by Ar^+ etching and the XPS peaks of the less oxidative components appear at the expense of those of the original oxides [64–67]. In addition, Ar^+ etching would be accompanied by widening of FWHM in XPS peaks because of the change in morphologies, e.g., from crystalline to amorphous. To suppress the reduction by Ar^+ irradiation, the effects of lower energy and glancing angles of the Ar^+ beams were examined [67]. However, the deoxidative etching by Ar^+ could not be avoided.

As an example for metal oxides, Fig. 10.22 shows the XPS depth analysis of a 20 nm thin film of TiO_2 deposited on a Si substrate. Figure 10.22a shows the Ti 2p spectra etched by Ar^+ as a function of 500 eV Ar^+ irradiation time [55].

It took about 240 s to sputter-off the entire TiO_2 layer deposited on the Si substrate. Under Ar^+ irradiation, the peak broadens and the peak position shifts to lower binding energy with time because of selective sputtering of O in TiO_2 . Figure 10.22b shows the depth analysis of Ti 2p for the 20 nm TiO_2 on Si by EDI. As shown, the intensities of Ti 2p peaks decreased monotonically without changes in peak shape. It took about 200 min to etch-off the TiO_2 layer. Thus, the EDI etching rate for TiO_2 under these experimental conditions was estimated to be ~ 0.1 nm/min. Despite the fact that the XPS spectra for bulk TiO_2 do not show any recognizable change by EDI, a small shoulder peak at ~ 458 eV is observed for $\text{TiO}_2(20 \text{ nm})/\text{Si}$ sample (Fig. 10.22b). It seems likely that a Ti suboxide has formed near the TiO_2 -Si interface. That is, EDI is capable of characterizing nanoscale multilayer systems. In fact, a thin metallic Cu layer with a thickness of a few nm formed between the CuO overlayer and the Si substrate was clearly detected for the sample CuO (10 nm)/Si [54].

10.6 Estimation of the Useful Yields

As described above, the chemical modifications caused by EDI irradiation are below the detection limit of XPS. In addition, desorption of samples is only limited to the atomic- and molecular-level thickness (Figs. 10.6 and 10.7). Although etching is only limited to the subsurface layer, the relatively high secondary ion yields are a characteristic feature of EDI, suggesting that this technique has a high useful yield. To obtain more information on ionization efficiencies, measurements of the limit of detection for neutral and ionic compounds were conducted.

The EDI mass spectrum for 10 fmol gramicidin S deposited directly on a stainless steel sample stage (Fig. 10.2) is displayed in Fig. 10.23 [31].

In this spectrum, the protonated molecule ion $[\text{M} + \text{H}]^+$ could be detected as a major ion with an S/N ratio of about 30 with little fragment ions. The left inset shows the ion intensity for $[\text{M} + \text{H}]^+$ as a function of irradiation time. The $[\text{M} + \text{H}]^+$ ion could be detected as late as 30 min after the start of irradiation.

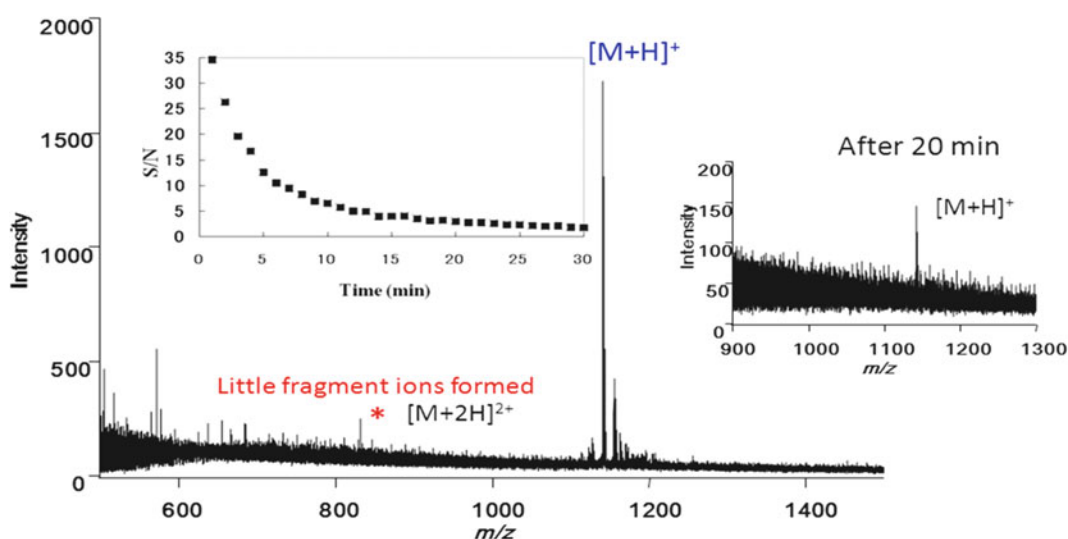


Fig. 10.23 EDI mass spectrum for 10 fmol gramicidin S. (reproduced with permission from [31])

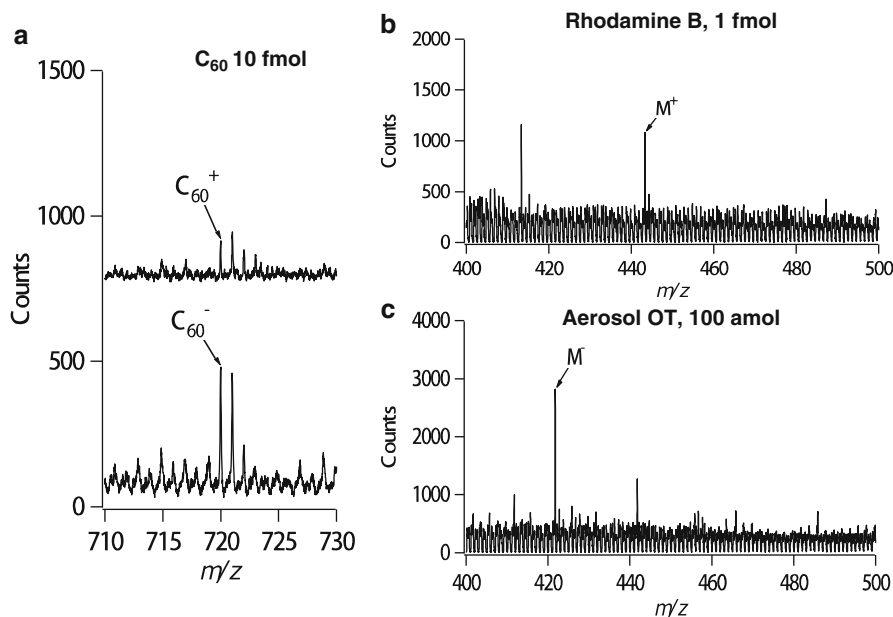


Fig. 10.24 EDI mass spectra for (a) 10 fmol of C₆₀, (b) 1 fmol of rhodamine B, and (c) 100 amol of Aerosol OT (sodium bis(2-ethylhexyl) sulfosuccinate), deposited directly on the sample stage (reproduced with permission from [68])

It was generally observed that dyes and surface-active agents give a lower detection limit (detectable with higher sensitivities) with EDI than neutral compounds. This may be attributed to the fact that dyes and surface-active agents have ionic forms and only their desorption may lead to the formation of gaseous ions. Figure 10.24a–c shows the positive and negative mode mass spectra for 10 fmol C₆₀, the positive mode mass spectrum for 1 fmol rhodamine B (a cationic surfactant), and the negative mode mass spectrum for 100 amol Aerosol OT (sodium bis(2-ethylhexyl) sulfosuccinate, an anionic surfactant) [68].

The limits of detection for rhodamine B and Aerosol OT are 1 fmol and 100 amol, respectively (see Fig. 10.24). On the other hand, the limits of detection for neutral compounds, such as gramicidin S and C₆₀ were found to be higher, i.e., about 10 fmol. The higher detection limit for neutral compounds is to be expected, because the detection of neutral molecules requires ionization. Here, if we assume that (1) desorption efficiencies are about the same for gramicidin S, C₆₀, rhodamine B and Aerosol OT, and (2) desorption of ionic compounds directly gives the secondary ion signals, the useful yield (i.e., total ions generated divided by the total molecules desorbed) may be estimated to be 0.1 (1 fmol/10 fmol for rhodamine B) or 0.01 (100 amol/10 fmol for aerosol OT). For the additional experiments, the positive- and negative-mode EDI mass spectra were measured for the binary mixtures of C₆₀/rhodamine B (1/1) and C₆₀/Aerosol OT (1/1), respectively. For sample preparation, the equimolar samples were crushed/mixed in a mortar and deposited on the sample stage as a thin film. This sample preparation method was adopted from the solvent-free MALDI [69–71]. The ratios of [C₆₀⁺]/[total positive ions originated from rhodamine B] for the sample of C₆₀/rhodamine B (1/1) and [C₆₀⁻]/[total negative ions originating from Aerosol OT] for the sample of C₆₀/Aerosol OT (1/1) were measured to be 0.18 and 0.16, respectively. These large values argue for the high ionization efficiency of EDI [72].

10.7 Mechanism for Ionization/Desorption in EDI

Beuhler and Friedman studied the sputtering of C, Cu, and Au surfaces with energetic water cluster ions [3]. Water cluster ions were prepared by free jet or nozzle expansion of weakly ionized plasma of water vapor in He carrier gas. Water clusters containing $\sim 3,000$ H_2O molecules with energies up to 240 keV were used as projectiles. The ion yields in cluster sputtering were shown to be a very small fraction of the total sputtered products. Very similar distributions of secondary ions and relatively large yields of energetic atomic ions and smaller yields of polyatomic ions were observed.

Takaoka et al. also investigated irradiation effects using water cluster ions [73]. Water clusters were generated by injecting water vapor through a nozzle into vacuum. The peak size of the clusters was 2,500. At the acceleration voltage of 9 keV the sputtering yield was 17.8 atoms/projectile for Si and 17.1 molecules/projectile for SiO_2 , i.e., approximately ten times larger than the yield with Ar monomer ion irradiation. They found that the thickness of the SiO_2 layer on pristine Si increased with increasing the acceleration voltage of the water cluster ions. The thickness of SiO_2 generated with cluster irradiation at an acceleration voltage of 9 keV was about 11 nm. The formation of the oxide layer was suggested to be a result of OH radical injection onto the Si substrate during irradiation of the water cluster [73].

The experimental results using water clusters obtained by Takaoka et al. [72] are in marked contrast to those obtained by EDI although these two techniques use water clusters as projectiles. In EDI, no SiO_2 formation was observed when HF-treated pristine Si was irradiated [59]. In addition, the native SiO_2 on Si (i.e., SiO_2 (2 nm)/Si) was etched off and pristine silicon appeared after that [59].

The velocities of the water cluster projectiles used in Beuhler's and Takaoka's experiments were ~ 30 and ~ 6 km/s, respectively, and these values are of the same order as those measured in EDI (~ 12 km/s). The major difference between EDI and the latter two techniques that use water clusters is the cluster size, i.e., a typical water cluster is composed of $\sim 90,000$ H_2O molecules in the projectile in EDI, $[(\text{H}_2\text{O})_{90,000} + 100\text{H}]^{100+}$. It seems likely that cooperative collision phenomena take place in EDI.

A hypothetical model describing the ionization/desorption induced by EDI [45] is shown in Fig. 10.25.

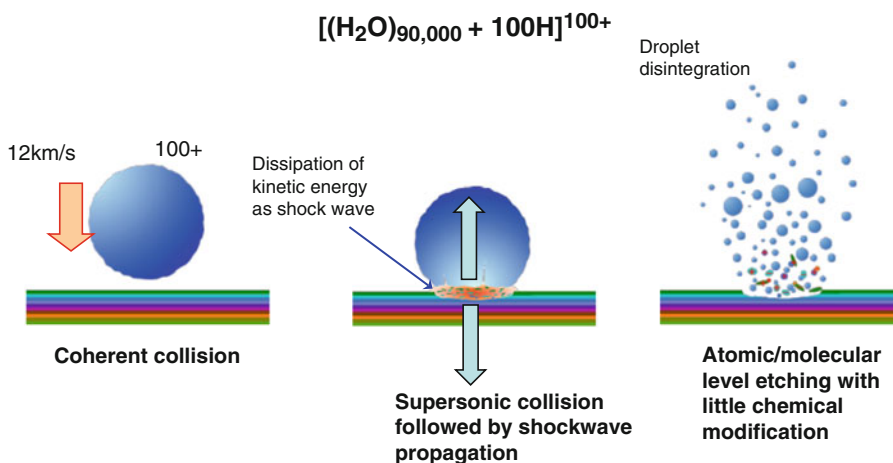


Fig. 10.25 Hypothetical model for the ionization/desorption taking place in EDI (reproduced with permission from [45])

Water droplets with a diameter of ~ 10 nm impact the sample surface with a velocity of ~ 12 km/s, which is higher than the sound velocity in various solids. For example, the sound velocity in polystyrene, ice, and Si is ~ 2.4 , ~ 3.2 , and ~ 8.4 km/s, respectively. Thus, a supersonic collision must take place at the moment of impact. Because H is the lightest atom among all elements, some of the kinetic energies of the impinging droplets would be preserved by the backscattering of H atoms on the surface of the water droplet at the instant of supersonic collision. Immediately following the collision, an enormous pressure would be exerted at the colliding interface because of the high momentum of the water droplet impact. The force F exerted on the surface is expressed as

$$F = \frac{dp}{dt}, \quad (10.10)$$

where dp is the momentum change of the projectile (i.e., $p = m \times v$) during the collision, and dt is the interaction time of the droplet with the surface. The water droplet is composed of a rather tight hydrogen bond network. Thus, the supersonic collision may be followed by shockwave propagation through the hydrogen bond network in the water droplet. If one assumes that the shockwave velocity propagating in the water droplet is roughly the same as the projectile velocity [18], the transit time of the shockwave through a water droplet with 10 nm diameter may be 1 ps (i.e., $10 \text{ nm}/(12 \times 10^3 \text{ m/s}) \approx 10^{-12} \text{ s}$). Because the shockwave has an open end at the opposite edge of the droplet, the droplet may be disintegrated as finer microclusters within ~ 1 ps (Fig. 10.25). In fact, a broad distribution of the water cluster ions was observed as secondary ions in EDI [32]. Some of the kinetic energy of the droplets ($\sim 10^6$ eV) may dissipate as kinetic energies of the disintegrated microdroplets. That is, the dissipation process of the kinetic energy of the projectile should be largely nonthermal.

The high ionization efficiency of EDI indicates that at the colliding interface the kinetic energy of the droplet is efficiently converted into internal energies of the species. When an enormous pressure is exerted on the colliding interface at the moment of supersonic collision, the wave functions of the species at the colliding interface overlap and quasidelectronic states will be formed originating from the exchange repulsion (Note that electrons are fermions). As the particles recede from each other, transitions to the excited electronic states can occur at potential energy curve crossings [74]. Thus, the formation of quasidelectronic states opens new channels for ionization and dissociation of the species taking part in the collision, and this may be one of the major dissipation channels for the kinetic energies brought about by the impinging water droplets.

Figure 10.26 shows the conceptual idea for the curve-crossing mechanism for collisional activation [75, 76].

The reaction coordinate for an impinging molecule m is shown in one dimension, and the m - N coordinate is shown as orthogonal to it. Two electronic states of m are shown, which cross at some point along the m - N coordinate leading to the electronic excitation of m , $m \rightarrow m^*$. The electronically excited m^* will lead to the ionization and fragmentation of m . The excitation energy of ΔE necessary for the reaction $m \rightarrow m^*$ at the crossing point is much smaller than its value when the distance between m and N is larger. Such electronic excitations via the curve-crossing mechanism are likely in EDI.

The most characteristic feature of EDI is the ability for atomic- and molecular-level surface etching with little chemical modification and damage accumulation on the etched surface. Similar results were obtained by the technique called MCI (massive cluster impact) developed by Mahoney et al. [17–20]. To explain the ionization/desorption mechanism, they proposed the macroscopic shockwave model for sputtering by primary cluster beams that impact with velocities exceeding the velocity of sound in the target materials. Upon supersonic cluster impact, the molecules comprising the matrix are set in in-phase coherent motion by a strong compression planar pressure wave. Instantaneously, a shockwave is propagated through the cluster causing its disintegration shortly after impact.

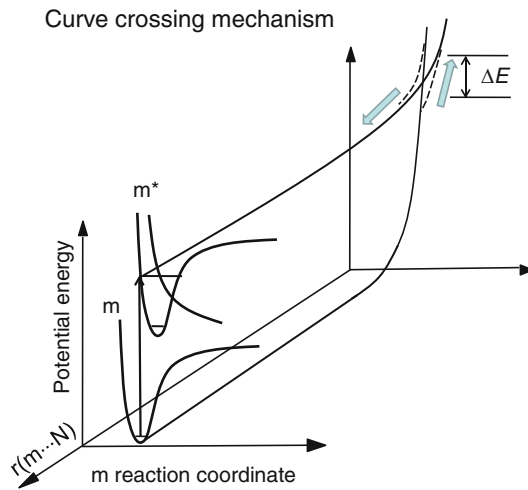


Fig. 10.26 Conceptual idea for the curve-crossing mechanism for collisional activation of the impinging molecule m in collision with N (reproduced with permission from [75])

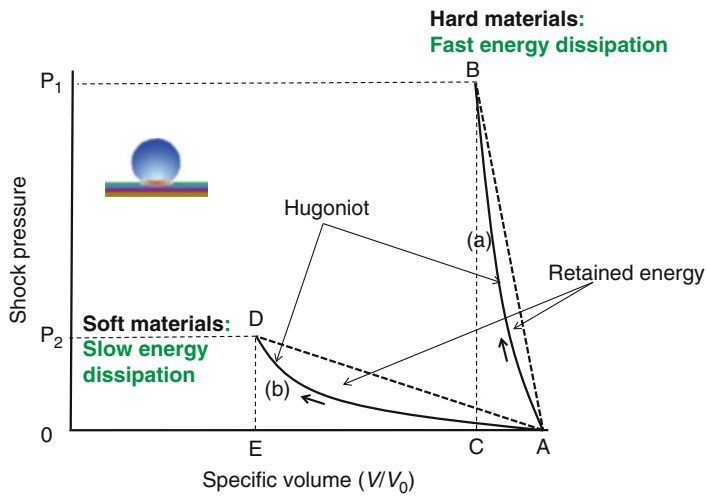


Fig. 10.27 Hugoniot curves for hard and soft materials

In EDI, it was found that the ionization efficiencies decrease with increase in film thickness of the organic layers, as shown in Fig. 10.7. This suggests that the ionization processes may change depending on the hardness or densities of the target materials.

To obtain a conceptual idea how the initial impact energy is partitioned between the bombarding cluster and the target material, Hugoniot curves are shown in Fig. 10.27 [18].

The cluster and the target material are compressed by the supersonic collision from an initial P_0, V_0 state (A) to the final P , and V state (B or D). The intermediate points on the Hugoniot curve AB or AD represent the locus of P, V states reached by discontinuous pressure jumps across the shock front. The colliding system will relax from B or D to certain values of P and V by rarefaction of the shockwave. In Fig. 10.27a, b two cases, of hard (a) and soft (b) target materials, are shown as examples.

The shockwave is supported by the collisions of atoms and molecules, and thus, the thickness of the shock front is mainly determined by the number of collisions that form the shockwave. In (a), the dense collision takes place in a shorter time and a higher force will act on the colliding interface (10.10). This results in high ionization efficiency (Fig. 10.26). For a soft target (b), the projectile will interact with the target for longer time and shock pressure will be lower than in case (a). This will lead to the lower ionization efficiencies. The subsurface material containing ionic products will be desorbed by the rarefaction of the shockwave, i.e., the in-phase coherent upward collective motion of the ionized target species.

In collisional phenomena, the kinetic energy of the center of mass of the system is conserved [76]. The maximum kinetic energy that can be converted into internal energies for the colliding system (KE_{rel}) is given by (10.11):

$$KE_{\text{rel}} = \left(\frac{N}{m + N} \right) KE_{\text{lab}}, \quad (10.11)$$

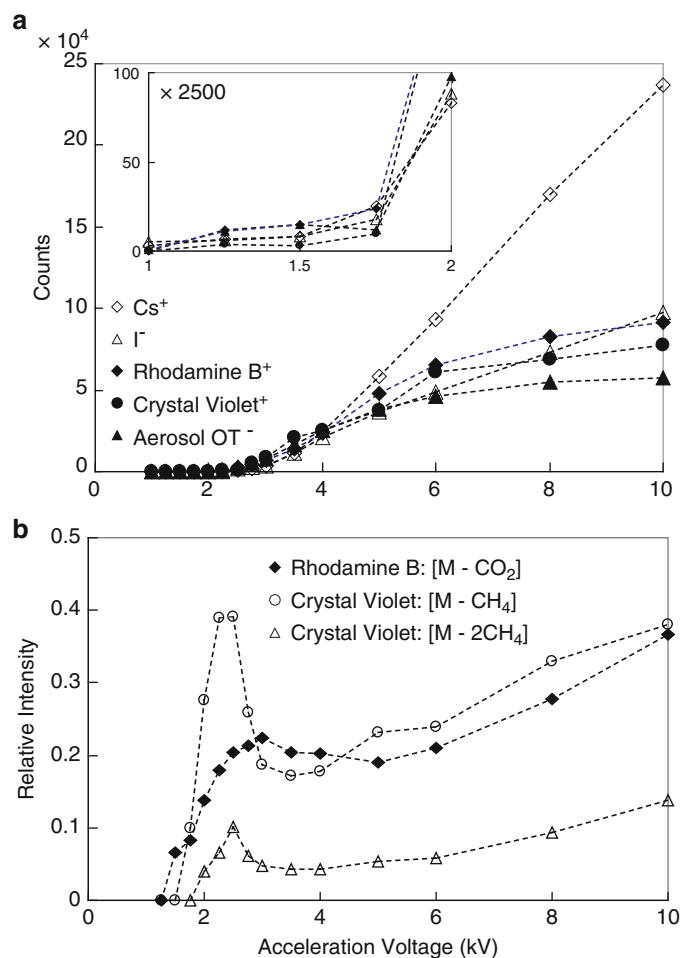
where m is the mass of the projectile, N is the mass of the target, KE_{rel} is the relative kinetic energy, and KE_{lab} is the laboratory collision energy. When the EDI cluster projectile with mass m bombards hard solid materials, such as metals or semiconductors, N is much larger than m , and thus, KE_{rel} can be approximated to be KE_{lab} . That is, efficient conversion of the kinetic energy of the projectile to the internal energies of colliding system is guaranteed. This is the case in Fig. 10.27a. In the case of soft target materials, however, the effective mass N becomes smaller, and this must result in smaller E_{rel} compared with E_{lab} . A longer interaction time of the water cluster projectile with the soft materials may result in fewer nonthermal collisions than for hard materials. But still, EDI is capable of etching soft materials such as synthetic polymers, peptides, and proteins with little chemical modification and damage accumulation, as described above.

The supersonic collision-induced ionization in EDI takes place only when the velocity of the projectile becomes larger than the sound velocity of the target sample. Thus, the ionization efficiency in EDI depends strongly on the acceleration voltage of the charged water droplets. Figure 10.28 shows the variation in secondary ion abundances with acceleration voltage for samples of CsI, rhodamine B, crystal violet, and aerosol OT [35]. Because the primary cluster ion current (~ 1 nA) is almost independent of the acceleration voltage in the range 0.5–10 kV, the ion intensities in Fig. 10.28 represent the relative ionization efficiencies in EDI as a function of acceleration voltage.

In the inset in Fig. 10.28a for CsI, ion signals for both Cs^+ and I^- start to be observed at about 1 kV, but their abundances are nearly voltage-independent up to 1.75 kV and show a steep increase after that. Similar trends are also observed for other samples shown in Fig. 10.28a. That is, there are two threshold behaviors for secondary ion formation, i.e., low-energy and high-energy regimes [35]. In the low-energy regime, only desorption takes place, but no ionization. Ionization of neutral molecules such as C_{60} is only observed in the high-energy regime [35]. From the inset in Fig. 10.28a, ionization/desorption because of the supersonic collision starts at the acceleration voltage of ~ 1.75 kV.

In Fig. 10.28, Cs^+ and I^- show more or less linear increase in the high-energy regime in the range of 3–10 kV. This indicates that the desorption efficiency of Cs^+ and I^- from CsI increases linearly with the kinetic energy of the projectile. However, the general trend for molecular compounds is different. The ion intensities of molecular ions M^+ for rhodamine B, crystal violet, and aerosol OT show a linear increase from 3 to 5 kV but start to deviate from linearity and the increment becomes smaller at higher acceleration voltage. Since the plateau at the higher accelerating voltage is only observed for molecular samples but not for CsI, this is likely to be a result of the fragmentation of the molecular ions M^+ . Figure 10.28b displays the relative abundances of fragment ions to molecular ions

Fig. 10.28 (a) Secondary ion abundances as a function of acceleration voltage for the charged water projectiles for samples of CsI, rhodamine B, crystal violet, and aerosol OT when electrospray droplet projectiles are generated in the positive mode of operation. Inset: Ion abundances expanded in the range of +0.5 to +2 kV. The amount of sample loaded on the metal substrate is 100 pmol. (b) Relative abundances of fragment ions to molecular ions M^+ as a function of acceleration voltage for rhodamine B and crystal violet (reproduced with permission from [35])



M^+ as a function of acceleration voltage for rhodamine B and crystal violet. Fragment ions are only observed above 1.75 kV in the high-energy regime. The absence of fragment ions in the low-energy regime (below 1.75 kV) indicates that the ions observed in the low-energy regime are those dissolved/sputtered by the impinging water droplet. In Fig. 10.28b the relative abundances of fragment ions show initial step increases that reach maxima at 2 or 3 kV, then decrease to their minima, and then increase again linearly after ~4 kV. The appearance of the peaks at 2–3 kV and the subsequent gradual increase after ~4 kV suggest that there are at least two mechanisms for the formation of fragment ions. In the inelastic collision, the Massey's adiabatic criterion (10.12) is known to be a good approximation:

$$R_M = \frac{t_c}{\tau}, \quad (10.12)$$

where R_M is the Massey parameter, t_c is the interaction time of collision, and τ is the period of electronic, vibrational, or rotational motion. For $R_M > 1$, the collision takes place adiabatically and the efficiency of the energy transfer from kinetic to internal energy is small. For $R_M = 1$, the

efficiency reaches maximum because of the resonant energy transfer. For $R_M < 1$, the interaction time becomes too short for efficient energy transfer. A crude estimate of the transit time of the water droplet $[(\text{H}_2\text{O})_{90,000} + 100\text{H}]^{100+}$, for example, in 5 \AA is about 10^{-13} s with the acceleration voltage of 2–3 kV. This value roughly corresponds to the period of molecular vibration. It seems likely that the peaks observed at 2–3 kV in Fig. 10.28b are a result of the resonant vibrational excitation that leads to the molecular elimination from M^+ . With further increase in acceleration voltage above 5 kV, the interaction time upon supersonic collision becomes shorter and electronic excitation will become more important for fragmentation.

The sputter rates by EDI are limited, because only atomic- and molecular-level etching takes place. The etching rates with EDI were determined experimentally for several materials, for example, $\sim 2 \text{ nm/min}$ for bradykinin [50, 77], 3–5 nm/min for PS [42, 43], 2 nm/min for PET, 0.2 nm/min for SiO_2 [37], 0.12 nm for TiO_2 [54], 0.7 nm/min for Ta_2O_5 [54], and 0.3 nm/min for CuO/Cu [55]. Roughly, the etching rates for organic materials (synthetic polymers and peptides) are about one order of magnitude higher than for inorganic materials (metal, metal oxides, and SiO_2).

Lee et al. measured the sputter rate (Y) for Irganox 1010 (antioxidant, tetrakis-(methylene-(3,5-di-(tert)-butyl-4-hydrocinnamate))methane) as $120 \text{ nm}^3/\text{ion}$ by using 10 keV Ar_{700}^+ [29]. This value is more than two orders of magnitude larger than the value of $0.76 \text{ nm}^3/\text{ion}$ obtained for Si with 20 keV $\text{Ar}_{2,000}^+$ [78]. Therefore, the rather small difference in etching rates for hard and soft materials obtained with EDI is unique.

For Ar_n^+ , the cluster is held together by weak van der Waals forces, and thus, the dissipation of the collision energy through the shockwave propagation should be much less efficient compared with water cluster, which is held together by strong hydrogen bonds. Thus, the kinetic energy of the Ar_n^+ projectile is likely to be converted to an out-of-phase random motion of Ar atoms at the colliding interface leading to lateral motion [79]. That is, numerous particles acquire high lateral momentum and are ejected in the lateral direction. This leads to the high sputter rate with the surface smoothing ability. That is, Ar cluster sputtering induces under-cosine angular distribution [79]. In contrast, such a lateral sputtering is less likely in EDI. EDI is capable of shallow surface etching with high ionization efficiency, but the etching rate is relatively low due to the low beam flux.

10.8 Conclusion and Perspective

The continuing scaling-down trend leads to a drastic reduction in film thickness, thus increasing the demands for very high depth-resolution, ideally a multilayer system with the depth-resolution in the order of 0.5 nm. To achieve these demands, several cluster SIMS techniques have been developed. This chapter has dealt with the EDI method, which uses the largest projectile ever developed so far for cluster/SIMS. In EDI, almost damage-free atomic- and molecular-level etching is possible. In addition, secondary ions are produced with high efficiency. The useful yields (total number of ions divided by total neutral species desorbed) of EDI are estimated to be roughly 1–10 %. The soft surface etching ability of EDI indicates that no ablation takes place in the collision of the water droplet with the surface. In other words, the projectile does not penetrate into the target, i.e., the destructive momentum transfer from the droplet to the target is minor. This unique nature must originate from the water droplet used as projectile. At the instance of supersonic collision, the H atoms on the surface of the droplets will backscatter because the H atom has the smallest mass among all elements, i.e., there is an elastic shock front forming at the instance of the supersonic collision. In fact, the single-acceptor units (i.e., H sites of H_2O) dominate the water surface because of the anticooperative effects at double donor (i.e., O sites) and double acceptor hydrogen bond configurations [80, 81]. At the instant of the supersonic collision, all the H_2O molecules in the droplet have the same direction and the same

velocity towards the target resulting in a coherent collision at the colliding interface. At the instant of supersonic collision, the enormous pressure rise exerted at the colliding interface induces the electronic excitation for molecules at the colliding interface and secondary ions are generated with high efficiencies. The water and target molecules are compressed and they displace their positions with in-phase motion. The resultant shockwave propagation through the water droplet and the target contributes to the efficient energy dispersion, and this explains the high ionization efficiency and the soft etching ability of EDI. In summary, the unique nature of EDI is ascribed to the characteristic nature of the water molecule, as two thirds of the water molecule H_2O are H atoms. Because of the high polarity of the water molecule, a strong hydrogen bond network is formed in the condensed phase, and EDI takes its beneficial characteristics from this unique nature of H_2O .

The characteristic features for EDI may be summarized as follows.

- EDI utilizes the water droplet projectiles, typically represented as $[(\text{H}_2\text{O})_{90,000} + 100\text{H}]^{100+}$.
- No special sample pretreatment is necessary.
- Because EDI uses volatile water droplets, the EDI/SIMS apparatus is free from contamination and maintenance-free for years of everyday operation.
- The kinetic energy of the droplet is about 10^6 eV. Because the velocity of ~ 12 km/s is higher than the sound velocities in solids, the supersonic collision takes place in EDI, resulting in the ionization/desorption of the sample atoms and molecules.
- In general, the molecular ions with the molecular masses below 1,000 u are observed as base peaks with much weaker fragment ions.
- In EDI, atomic- and molecular-level etching takes place with little damage left on the surface after EDI irradiation.
- From the limits of detection for neutral and ionic compounds, the useful yields (defined as the total number of ions generated divided by the total number of neutral species desorbed) of EDI are estimated to be roughly ~ 0.1 .

Based on these characteristic features, if the diameter of the beam of the water droplet projectiles could be focused to submicron dimensions, EDI could become a useful method for 3D nanoimaging for nanomaterials [82].

References

1. Benninghoven A (1970) *Z Physik* 230:403
2. Blain MG, Della-Negra S, Joret H, Le Beyec Y, Schweikert EA (1989) *Phys Rev Lett* 63:1625
3. Beuhler RJ, Friedman L (1989) *Int J Mass Spectrom Ion Process* 94:25
4. Appelhans AD, Delmore JE (1989) *Anal Chem* 61:1087
5. Colla TJ, Aderjan R, Kissel R, Urbassek HM (2000) *Phys Rev B* 62:8487
6. Garrison BJ, Delcorte A, Krantzman KD (2000) *Acc Chem Res* 33:69
7. Eusepi F, Tomsic A, Gebhardt CR (2003) *Anal Chem* 75:5124
8. Davies N, Weibel DE, Blenkinsopp Lockyer PN, Hill R, Vickerman JC (2003) *Appl Surf Sci* 203:223
9. Weibel D, Wong S, Lockyer N, Blenkinsopp P, Rowland H, Vickerman JC (2003) *Anal Chem* 75:1754
10. Tempez A, Schultz JA, Della-Negra S, Depauw J, Jacquet D, Novikov A, Lebeyec Y, Pautrat M, Caroff M, Ugarov M, Bensaoula H, Gonin M, Fuhrer K, Woods A (2004) *Rapid Commun Mass Spectrom* 18:371
11. Touboul D, Halgand F, Brunelle A, Kersting R, Tallarek E, Hagenhoff B, Laprevote O (2004) *Anal Chem* 76:1550
12. Postawa Z, Czerwiński B, Szerwczyk M, Smiley EJ, Winograd N, Garrison B (2004) *J Phys Chem B* 108:7831
13. Mahoney CM, Roberson SV, Gillen G (2004) *Anal Chem* 76:3199
14. Novikov A, Caroff M, Della-Negra S, Depauw J, Fallavier M, Beyec YL, Pautrat M, Schultz JA, Tempez A, Woods AS (2005) *Rapid Commun Mass Spectrom* 19:1851
15. Winograd N (2005) *Anal Chem* 143A-149A
16. Czerwiński B, Samson R, Garrison BJ, Winograd N, Postawa Z (2006) *Vacuum* 81:167
17. Mahoney JF, Perel J, Ruatta SA, Martino PA, Husain S, Lee TD (1991) *Rapid Commun Mass Spectrom* 5:441
18. Mahoney JF, Perel J, Lee TD, Martino PA, Williams P (1992) *J Am Soc Mass Spectrom* 3:311

19. Mahoney JF, Cornett DS, Lee TD (1994) *Rapid Commun Mass Spectrom* 8:403
20. Cornett DS, Lee TD, Mahoney JF (1994) *Rapid Commun Mass Spectrom* 8:996
21. Kollmer F (2004) *Appl Surf Sci* 231–232:153
22. Touboul D, Kollmer F, Niehuis E, Brunelle A, Lapr evote O (2005) *J Am Soc Mass Spectrom* 16:1608
23. Fabris D, Wu Z, Fenslau CC (1995) *J Mass Spectrom* 30:140
24. Aksyonov SA, Williams P (2001) *Rapid Commun Mass Spectrom* 15:2001
25. Yamada I, Matsuo J, Toyoda N, Kirkpatrick A (2001) *Mater Sci Eng R34*:231
26. Toyoda N, Matsuo J, Yamada I (2004) *Nucl Instrum Methods Phys Res B* 216:379
27. Seki T, Matsuo J (2007) *Surf Coat Technol* 201:8646
28. Rabbani S, Barber AM, Fletcher JS, Lockyer NP, Vickerman JC (2011) *Anal Chem* 83:3793
29. Lee JLS, Ninomiya S, Matsuo J, Gilmore IS, Seah MP, Shard AG (2010) *Anal Chem* 82:98
30. Hiraoka K, Asakawa D, Fujimaki S, Takamizawa A, Mori K (2006) *Eur Phys J D* 38:225
31. Hiraoka K, Mori K, Asakawa D (2006) *J Mass Spectrom* 41:894
32. Mori K, Asakawa D, Sunner J, Hiraoka K (2006) *Rapid Commun Mass Spectrom* 20:2596
33. Hirabayashi A, Sakairi M, Koizumi H (1994) *Anal Chem* 66:4557
34. Hirabayashi A, Sakairi M, Koizumi H (1995) *Anal Chem* 67:2878
35. Asakawa D, Mori K, Hiraoka K (2008) *Appl Surf Sci* 255:1217
36. Wolf KV, Cole DA, Bemasek SL (2002) *Anal Chem* 74:5009
37. Hiraoka K, Sakai Y, Iijima Y, Asakawa D, Mori K (2009) *Appl Surf Sci* 255:8947
38. McMahon JM, Dookeran NN, Todd PJ (1995) *J Am Soc Mass Spectrom* 6:1047
39. Asakawa D, Chen LC, Hiraoka K (2009) *J Mass Spectrom* 44:945
40. Sakai Y, Iijima Y, Takaishi R, Asakawa D, Hiraoka K (2009) *J Surf Anal* 15:283
41. Sakai Y, Iijima Y, Takaishi R, Asakawa D, Hiraoka K (2009) *J Vac Sci Technol A* 27:743
42. Sakai Y, Iijima Y, Asakawa D, Hiraoka K (2010) *Surf Interface Anal* 42:658
43. Sakai Y, Iijima Y, Mukou S, Hiraoka K (2011) *Surf Interface Anal* 43:167
44. Hiraoka K, Iijima Y, Sakai Y (2011) *Surf Interface Anal* 43:236
45. Hiraoka K, Sakai Y, Iijima Y (2010) *J Vac Sci Technol A* 28:510
46. Hiraoka K, Takaishi R, Asakawa D, Sakai Y, Iijima Y (2009) *J Vac Sci Technol A* 27:748
47. Conlan XA, Gilmore IS, Henderson A, Lockyer NP, Vickerman JC (2006) *Appl Surf Sci* 252:6562
48. Carter G (2001) *J Phys D: Appl Phys* 34:R1
49. Asakawa D, Yoshimura K, Takeda S, Hiraoka K (2010) *J Mass Spectrom* 45:437
50. Asakawa D, Fujimaki S, Hashimoto Y, Mori K, Hiraoka K (2007) *Rapid Commun Mass Spectrom* 21:1579
51. Kudaka I, Asakawa D, Mori K, Hiraoka K (2008) *J Mass Spectrom* 43:436
52. Mori K, Hiraoka K (2008) *Int J Mass Spectrom* 269:95
53. Sakai Y, Iijima Y, Hiraoka K (2008) *Surf Sci* 15:172
54. Sakai Y, Ninomiya S, Hiraoka K (2011) *Surf Interface Anal* 43:1605
55. Sakai Y, Ninomiya S, Hiraoka K (2012) *Surf Interface Anal* 44:938
56. Bradley RM, Harper JME (1988) *J Vac Sci Technol A* 6:2390
57. Zalar A (1985) *Thin Solid Films* 124:223
58. Zalar A (1986) *Surf Interface Anal* 9:41
59. Sakai Y, Iijima Y, Mori K, Hiraoka K (2008) *Surf Interface Anal* 40:1716
60. Nagiub HM, Kelly R (1975) *Rad Effects* 25:1
61. Kim KS, Battering WE, Amy JW, Winograd N (1974) *J Electron Spectrosc Relat Phenom* 5:351
62. Hashimoto S, Hirokawa K, Fukuda Y, Suzuki K, Suzuki T, Usuki N, Gennai N, Yoshida S, Koda M, Sezaki H, Horie H, Tanaka A, Ohtsubo T (1992) *Surf Interface Anal* 18:799
63. Bardy U, Tamura K, Owari M, Nihei Y (1988) *Appl Surf Sci* 32:352
64. Kelly R (1980) *Surf Sci* 100:85
65. Hofmann S, Sanz JM (1982–1983) *J Trace Microprobe Technol* 1:213
66. McCafferty E, Wightman JP (1999) *Appl Surf Sci* 143:92
67. Hashimoto S, Tanaka A (2001) *J Surf Anal* 8:192
68. Asakawa D, Hiraoka K (2009) *J Mass Spectrom* 44:461
69. Przybilla L, Brand J-D, Yoshimura K, R ader HJ, M ullen K (2000) *Anal Chem* 72:4591
70. Trimpin S, Rouhanipour A, Az R, R ader HJ, M ullen K (2001) *Rapid Commun Mass Spectrom* 15:1364
71. Trimpin S, Grimsdale AC, R ader HJ, M ullen K (2002) *Anal Chem* 74:3777
72. Hiraoka K, Asakawa D, Takaishi R (2013) doi:1002/sia
73. Takaoka G, Nakamura K, Noguchi H, Kawashita M (2006) *Surf Interface Anal* 38:1534
74. Rabalais JW, Chen J-N (1986) *J Chem Phys* 85:3615
75. Levsen K, Schwarz H (1983) *Mass Spectrom Rev* 2:77
76. McLuckey SA (1992) *J Am Soc Mass Spectrom* 3:599

-
77. Asakawa D, Hiraoka K (2012) *Surf Interface Anal* 44:227
 78. Seki T, Matsuo J (2007) *Nucl Instrum Methods Phys Res B* 257:666
 79. Toyoda N, Kitani H, Hagiwara N, Aoki T, Matsuo J, Yamada I (1998) *Mater Chem Phys* 54:262
 80. Ojamäe L, Hermansson K (1994) *J Phys Chem* 98:4271
 81. Wilson KR, Cavalleri M, Rude BS, Schaller RD, Nilsson A, Pettersson LGM, Goldman N, Catalano T, Bozek JD, Saykally RJ (2002) *J Phys Condens Matter* 14:L221
 82. Ninomiya S, Chen LC, Suzuki H, Sakai Y, Hiraoka K (2012) *Rapid Commun Mass Spectrom* 26:863

Index

A

Ablation, 174, 180, 191–196, 206, 227
Acceptor, 128, 181, 182, 227
Acid-catalyzed dehydration reaction, 135
Acidity, 110, 123, 129, 130
Acoustic wave, 188, 189, 192, 193, 195
Activated complex, 36
Activation barrier, 114, 116
Acupuncture needle, 159, 164
Adiabatic ionization energy, 158
AES. *See* Auger electron spectroscopy (AES)
AFM. *See* Atomic force microscopy (AFM)
Alkaline ion, 117
Ambient electrospray, 202
Ambient FD, 169
Ambient imaging mass spectrometry, 163
Amorphization, 218
Amphiphilic molecule, 155
Analyte, 110, 111, 115, 116, 121, 129, 130, 135–138, 154, 164, 166, 173, 174, 180, 181, 190, 196, 200, 215
Angular momentum, 18, 37, 38, 47, 50, 62
Antibonding orbital(s), 65, 69, 70, 73, 77, 176–178
Antibonding π^* orbital, 121
APCI. *See* Atmospheric-pressure chemical ionization (APCI)
Appearance potential, 34, 43
Aprotic solvent, 133
Arn cluster, 201
ASD. *See* Auger stimulated desorption (ASD)
Associative ionization, 138
Asymmetric TOF distribution, 34, 45, 46
Atmospheric-pressure chemical ionization (APCI), 110, 111, 115, 121, 123, 124, 132, 135–142, 151
Atmospheric-pressure penning ionization, 140
Atomic force microscopy (AFM), 210, 213, 217, 218
Atomic ion bombardment, 199, 208
Atomic level etching, 206
Attractive force, 12–14, 16, 111, 170
Aufbau principle, 176, 178
Auger cascade, 65
Auger decay, 62–66, 68, 70, 71, 73, 74, 76, 77
Auger electron spectroscopy (AES), 66, 207

Auger stimulated desorption (ASD), 65, 73
Autoionization, 56, 58, 59, 82–85, 87, 139
Averaged dipole orientation (ADO) theory, 22, 113, 114
Average free time (τ), 93, 94

B

Backscattering, 223
Band gap, 185, 186
Basicity, 110, 128, 215
Beam angle, 213, 217, 218
Billiard-like collision, 111
Bimolecular process, 181–183
Bimolecular reaction, 112
Binding energy, 4, 61, 62, 75, 141, 209, 212, 220
Bohr radius, 8
Boltzmann constant, 113
Boltzmann distribution, 36
Bond dissociation energy, 129
Bond energy, 110, 117, 130, 133–135, 141
Born-Oppenheimer approximation, 83, 84, 86
Bound state, 117
Bovine milk, 161–163
Breakdown curve, 34, 40–44
Breathing sphere model, 193
Bronsted-Lowry classification, 128
Bubble formation, 193
Buffer gas, 92, 93, 99, 100, 105, 115, 118–120, 130, 137
Bulk measurement method, 89

C

Canonical ensemble, 29, 36
Canonical rate constant, 33, 36
Capillary-based ES, 149, 160, 164, 166
Capture collision
capture collision rate constant, 112, 116, 117, 123
capture limit rate constant, 111–113
Carbenium ion, 131
Carbon nanotube, 104, 185
Cathode ray tube, 109
Center-of-mass collision, 41
Center-of-mass system, 1–3, 13
Centrifugal force, 18–21, 37

- Centrifugal force (*cont.*)
 central force potential, 17
Centrifugal potential, 18–19
Charge delocalization, 128, 131, 215
Charged residue, 154
Charged residue mechanism, 154
Charge transfer, 74, 111, 119, 190
 charge transfer reaction, 111
Chemical ionization, 110, 115
Chemical modification, 220, 222, 223, 225
Chemical noise, 208
Chemical shift, 61, 66, 74
Chiral detection, 105–106
Chiral effect, 90
CID. *See* Collision-induced dissociation (CID)
Clausius-Clapeyron equation, 203
Closed shell, 117
Cluster impact, 199, 200, 223
Clustering reaction, 111, 115, 117–119, 122,
 132, 134–136
Cluster ion, 41, 42, 110, 123, 130, 132–136,
 143, 199, 201, 206, 218, 222, 223, 225
 cluster ion beam, 199, 201
Coherent collision, 222, 228
Coherent motion, 223
Collective motion, 225
Collisional activation, 29, 223, 224
Collisional cooling, 117
Collisional deactivation, 29, 115, 138, 139, 141
Collision cross section, 6–11, 13, 26, 90, 92, 95
Collision diameter, 182
Collision frequency, 92, 93, 95, 96, 111, 137, 203
Collision-induced dissociation (CID), 1, 41, 99
Collision process, 91–94, 98
Collision theory, 1–26
Compensation voltage (CV), 102, 103
Competitive reaction, 41–44
Complex conjugate, 175
Concentration-sensitive, 158
Concentric hemispherical analyzer, 66
Conduction band, 155, 186
Conductivity, 157, 185, 189, 192
Cone-jet mode, 156
Configuration interaction, 59
Consecutive reaction, 40–41
Conservation of angular momentum, 37, 47
Cooperative collision phenomena, 222
Core electron, 61–78
 core electron excitation/ionization, 61–65
Core excited state, 63, 65, 68, 71, 74–77
Corona discharge, 140, 151, 155, 156, 158
Coster-Kronig transition, 65
Coulomb attraction force, 157
Coulomb repulsion, 60, 65, 73, 147
Covalent entrance channel, 139
Crater, 199, 200
Cross section, 92, 95, 96, 98–100, 102, 103,
 105, 121, 130, 139, 191, 199, 200
Curve crossing mechanism, 223, 224
CV. *See* Compensation voltage (CV)
Cylindrical mirror analyzer (CMA), 68
- D**
Damage accumulation, 201, 223, 225
Dc corona discharge, 140, 151, 156, 158
Deactivation, 29, 73, 115, 118, 138, 139,
 141, 174, 180–184, 186–192, 195
De Broglie's material wave, 2
De Broglie wavelength, 155
Debye, 112–114, 125, 157, 158
Debye length, 157, 158
Deca process, 62–65, 77, 82, 84–86, 180
Degeneracy of reaction path, 33
Degenerate, 177
Dehydrogenation, 212
Delayed fluorescence, 183
Delta function, 56, 58, 100
Delta layer, 201
Density functional theory (DFT), 75
Deoxygenation, 212
Deprotonated ion, 137
Depth analysis, 219, 220
Depth profiling, 201, 208
Depth resolution, 151, 201, 227
Desorption-ablation, 174
Desorption efficiency, 70, 225
DFT. *See* Density functional theory (DFT)
D_{2h} symmetry, 132
Diabatic crossing, 139
Differential cross section, 9, 13–16
Differential pumping system, 98–101
Dipolar molecule, 113, 115
Dipole moment, 10, 12, 22, 111, 113, 114, 125, 136
Discrete energy, 115, 175, 185
Disintegration of the charged droplet, 151–153
Dispersion voltage (DV), 102, 103, 159
Displacement reaction, 122, 132
Disproportionation electron transfer reaction, 215
Disproportionation proton transfer reaction, 214
Dissipation channel, 114, 223
Dissipation process, 223
Dissociation limit, 47, 48, 121
Dissociative electron attachment, 121, 130
Dissociative recombination, 85
Distonic intermediate, 43
Donor, 115, 125, 128, 181, 182, 227
Double-minimum potential, 123
 double-well potential, 123
Downsizing of electrospray, 159
Drift time, 99, 100, 104, 105
Droplet disintegration, 153, 154, 167
Droplet fission, 151, 152
DV. *See* Dispersion voltage (DV)
- E**
EDI. *See* Electrospray droplet impact (EDI)
Effective oscillator, 33
Effective potential, 18, 20, 37

- Effective temperature, 97
EICO. *See* Electron-ion coincidence (EICO) spectroscopy
Eigenfunction, 23, 176
Eigen value, 175
Elastic collision, 97, 226
Elastic shock front, 227
Electrical atomization, 145
Electrical breakdown, 145, 155–158
Electric double layer, 157, 158
Electric flux, 146
Electric sneeze, 150, 151
Electroactive, 157
Electrochemical reaction, 145–150, 156–158, 161
Electrode potential, 148
Electrohydrodynamic (EHD) emission, 200
Electrolytic dissociation, 129, 214
Electron affinity, 110, 122, 123
Electron attachment, 119, 121, 130
Electron avalanche, 155
Electron capture, 22, 119, 120, 130
 electron capture cross section, 130
Electron cloud, 111, 182
Electronegative, 125, 140
Electron–electron coincidence spectroscopy, 68
Electron–hole pair, 186
Electronic shell, 117
Electron-ion coincidence (EICO) spectroscopy, 68
Electron ionization, 3, 9, 22, 31, 55, 56, 60, 63, 68, 110, 111, 115, 138, 140
Electron irradiation, 130, 131
Electron microscope, 156
Electron mobility, 218
Electron-scavenging SF₆, 156
Electron spectroscopy for chemical analysis (ESCA), 66
Electron temperature, 120
Electron transfer, 5, 9, 19, 22, 26, 114, 138, 182, 183, 215
Electron transfer dissociation, 5
Electron tunneling, 168, 169
 electron tunneling process, 155, 168, 169
Electrophoretic charge separation, 147
Electrospray (ES), 115, 123, 124, 145–170, 200–202, 204–206, 217, 226
 electrospray ionization (ESI), 99, 100, 103, 123, 128, 140, 145, 147–149, 153–157, 159–161, 166, 168
Electrospray droplet impact (EDI), 201, 202, 204–228
Electrostatic pressure, 150, 158
Electrostatic unit, 114
Element-selectivity, 61, 62, 75–77
E/N, 91
Endothermic reaction, 123
Energy continuum, 82, 83
Energy dispersion, 228
Energy disposal, 47–53
Energy transfer, 114, 115, 117, 118, 138, 181, 182, 226, 227, 874
Enthalpy change, 123–125, 129, 130, 132, 135
Entropy barrier, 115, 116, 123
Entropy change, 123–125, 132, 134
Equilibrium constant, 124, 136
Equilibrium interatomic distance, 121
Equivalent core model, 75
ES. *See* Electrospray (ES)
ESI. *See* Electrospray ionization (ESI)
Etching
 etching cone, 218
 etching rate, 212, 216–218, 220, 227
Evaporative cooling, 193
EXAFS. *See* Extended X-ray absorption fine structure (EXAFS)
Excess charge, 147–154, 158, 161, 167, 169, 200
Excess energy, 30, 31, 33, 39, 49, 56, 63, 77, 78, 114, 115, 117, 139
Excess internal energy, 118
Exchange repulsion, 223
Excited dimer (excimer), 141
Exciton, 186
Exothermic reaction, 21, 123, 136, 192
Extended X-ray absorption fine structure (EXAFS), 63
F
FAB. *See* Fast atom bombardment (FAB)
FAIMS. *See* Field asymmetric waveform ion mobility spectrometry (FAIMS)
Fano profile, 59
Faraday cup, 202
Fast atom bombardment (FAB), 202, 206, 208
Femtosecond laser, 67, 73
Femtosecond laser mass spectrometry (FLMS), 67
Fermi level, 155, 169
Fermion, 223
Feschbach resonance, 86
FI. *See* Field ionization (FI)
Field asymmetric waveform ion mobility spectrometry (FAIMS), 102–103, 106
Field desorption, 145, 151, 166–169
Fieldemission type cold cathode, 156
Field-induced ion desorption, 168
Field ionization (FI), 35, 145, 166, 168–170
Field ion microscopy, 151
Filter for MS, 103
First order reaction, 110
Flow-rate sensitive, 158
Fluence, 173, 190–192
Fluorescence, 63, 67, 82, 176, 180, 181, 183, 186, 188
Förster resonance energy transfer, 182
Forward rate constant, 124
Fragment ion, 34, 37, 43, 46, 55, 58–60, 66, 110, 205, 206, 208, 220, 225, 226, 228
Franck-Condon factor, 26, 58, 114
Franck-Condon Principle, 31
Free energy change, 124, 125, 136
Free jet expansion, 204
Free time, 8, 9, 26, 92–95
Fullerene, 41, 42, 89, 90, 104, 105
G
Gas breakdown, 156, 160
Gas chromatography-chemical ionization mass spectrometry (GC-CIMS), 115
Gas cluster ion beam (GCIB), 201

- Gas jet stream, 136
Gas phase acidity, 128–130
Gaussian function, 100
Gauss's law, 146
Glancing angle, 219
Glory scattering, 16
Graphatization, 208, 212
Guanidino group, 128
- H**
Half-cell, 147
Half-life of reaction, 137
Hamiltonian, 2, 23, 30, 31, 175, 176
Hamiltonian equation, 30
Hard sphere, 96, 98
Harmonic oscillator, 29–31
Hartree-Fock method, 185
Heat bath, 152
Heat diffusion, 192
Heat of formation, 123
Heat of vaporization, 203
Hemispherical analyzer, 34, 66
Heteroatom, 176, 177
Hetero-bimolecular annihilation, 184
Highest occupied molecular orbital (HOMO), 64, 125, 169, 178
High field condition, 91, 96–98
High harmonic generation (HHG), 78
High-pressure ESI ion source, 156
High-pressure mass spectrometry, 129
 high-pressure mass spectrometer, 124
HOMO. *See* Highest occupied molecular orbital (HOMO)
Homo-bimolecular annihilation, 184
HTR. *See* Hydride transfer reaction (HTR)
Hückel theory, 176
Hugoniot curve, 224
Human breast cancer, 166, 167
Human milk, 161, 163
Hund's rule, 178
Hybrid orbital, 177
Hydride
 hydride affinity, 110
 hydride transfer reaction (HTR), 116–117, 122, 123, 131
Hydrogen atom transfer reaction, 115
Hydrogen bond network, 135, 223, 228
- I**
IEM. *See* Ion evaporation mechanism (IEM)
Impact desolvation of electrosprayed microdroplets (IDEM), 200–202
Impact parameter, 1, 13–16, 18–20, 22, 23
IMS/MS, 89, 96, 98–100, 104–106
Induced dipole, 10, 12, 22, 111, 113, 132
Induced dipole moment, 10, 12, 22
Induction period of ES, 161
Inductive effect, 128, 131, 134
Inertial confinement, 194, 195
Information theory, 49
 information quantity, 52
Infrared laser-assisted ES, 154
Innerorbital excited state, 83
Inner shell electron, 61
In-phase coherent motion, 223
Instability criterion, 145
Interfacial layer, 155
Intermediate complex, 116, 117, 122, 123, 137, 139
Internal conversion, 32, 49, 180, 190, 192
Internal energy, 1, 3, 4, 17, 22, 25, 26, 29, 37, 38, 40–42, 48, 49, 58, 81, 83, 99, 115, 118, 120, 121, 139–142, 223, 225, 226
Internal equilibrium, 32
Internal freedom, 92, 96, 98
Internal pressure P_y force, 154
Internal standard, 138
Interstellar medium, 117
Intersystem crossing, 190, 1891
Ion chemistry, 123, 139
Ion cyclotron mass spectrometry, 129
Ion-dipolar molecule interaction, 113
Ion-dipole interaction, 111, 115
Ion-dipole potential, 37
Ion evaporation mechanism (IEM), 154, 155
 ion evaporation regime, 168, 169
Ionic strength, 8
Ion-induced dipole interaction, 111
Ion injection system, 98, 99, 102
Ionization continuum state, 58
Ionization cross section, 9, 10, 56, 81, 139
Ionization efficiency, 55–60, 138, 158, 220, 221, 223–225, 227, 228
Ionization energy, 9, 43, 56, 58, 59, 81–85, 87, 110, 114, 138–140, 169
Ionization quantum yield, 139
Ionization threshold, 60, 62, 70
Ionizing light source, 55, 60
Ion mobility spectrometry, 89–106
Ion/molecule clustering reaction, 111, 117, 134
Ion/molecule reaction, 13, 18, 19, 21, 60, 109–142, 170
Ionosphere, 85
Ion pair formation, 119, 139
Ion sampling orifice, 160, 202, 203
Isoelectronic, 75, 117
Isotope effect, 90, 139
Isotopomer, 103
Isotropic fragmentation, 46
- J**
Jablonski diagram, 179, 188, 192
- K**
Kassel's equation, 31
Kinetic energy release, 1, 4–6, 32.34.39, 40, 46–47, 51
Knife edge, 146
- L**
Laboratory collision energy, 225
Langevin cross section, 19–22
Langevin ion-molecule reaction model, 37

- Langevin theory, 112, 113
Langmuir-Blodgett film, 155
Laplacian, 189
Laser induced optoacoustic spectroscopy (LIOAS), 187–191
Laval nozzle, 136, 201
Le Chaterier's law, 135
Lennard-Jones potential, 11–13
Life time, 29, 46, 76, 77, 85, 90, 91, 111, 115–118, 120, 138, 178–180, 182, 183, 186, 190
 life-time of the excited ion, 115
Limit of detection, 158, 220
Linear cascade collision, 199
Linear combination of atomic orbitals(LCAO), 175
Linear ion trap (LIT), 101
LIOAS. *See* Laser induced optoacoustic spectroscopy (LIOAS)
Liquid metal ion source, 151, 167
Locking constant, 113
Lone-pair electrons, 127, 128
Loose complex, 116
Loose transition, 36
Low field condition, 91–99
Luminescence spectroscopy, 176
- M**
Macroscopic shockwave model, 223
MALDI. *See* Matrix-assisted laser desorption ionization (MALDI)
Massey criterion, 22–25
 Massey's adiabatic criterion, 24, 226
Massive cluster impact (MCI), 200–202, 207, 223
Massive glycerol cluster, 199
Massive multiple-charge glycerol cluster, 200
Matrix-assisted laser desorption ionization (MALDI), 103, 115, 123, 124, 140, 145, 163, 164, 173–196, 213–215, 221
 MALDI-imaging-MS, 163, 164
Matter wave, 2, 22, 185
MCI. *See* Massive cluster impact (MCI)
McLafferty rearrangement, 43
Mean free path, 8, 26, 156
Mean free time, 8, 9, 26, 92
Metallofullerene, 104–105
Metastable atom bombardment (MAB), 140
Metastable decay, 34, 46
Metastable dissociation, 34, 45–46
Microcanonical
 microcanonical rate constant, 33, 36
 microcanonical transition state theory, 33
Micro-channel plate(MCP), 67
Microdroplet, 151, 152, 166–168, 200, 201, 223
Mobility, 1, 4, 89–106, 167, 218
Molecular-dynamics (MD) simulation, 199
Molecular elimination, 209, 227
Molecular imaging, 162
Molecular level etching, 201, 205–208, 213, 222, 227, 228
Molecular scalpel, 65, 66, 78
Momentum transfer, 95, 98, 114, 227
Monochromatic light, 57
Morphology, 219
Morse potential, 12, 13
MO theory, 176, 177
Motion of precession, 113
MS/MS, 8
Multiple-jet mode, 156
Multiple photon excitation, 190
Multiplicity, 179, 181
Multiply-charged massive clusters, 202
- N**
Nano-ESI, 145, 149, 153, 154, 158–161, 166, 168
Nanomaterial, 89, 103, 104, 151, 184–186, 195, 228
Nanoparticle, 164, 184–186
Nano-particle MALDI, 164
Native protein structure, 156
Near-edge X-ray absorption fine structure (NEXAFS), 63, 66, 69, 70
Nebulizing gas, 202
Needle electrode, 146, 151
Negative adsorption, 155
Negative ion, 119–123, 128–130, 147, 148, 155, 156, 200, 214, 215, 221
Negative-mode CI, 120, 121, 129, 130
Negative temperature dependence, 118
Neutral dissociation, 58, 82, 83, 85, 87, 139
NEXAFS. *See* Near-edge X-ray absorption fine structure (NEXAFS)
Nonbonding, 127, 128, 176, 177
Non-bonding lone-pair electron, 127, 128
Non-covalent complex, 200
Non-degenerate, 177
Non-equilibrium phase transformation, 193, 195
Non-ionization process, 82
Non-polar molecule, 111–113, 115, 170
Non-selective ionization, 214
Normal Auger decay, 63, 64
Nozzle expansion, 222
 $n-\pi^*$ transition, 178
Nucleophilic 2nd order reaction, 122
Number density, 137, 203
- O**
Observable, 63, 175
Off-spring droplet, 152, 154
OH radical injection, 222
Operator, 175
Optical penetration depth, 192, 194
Optical transition, 138
Optoacoustic, 176, 187–191
Orbiting cross section, 20, 21
Orbiting trajectory, 19, 20
Orbiting transition state, 37
Orthogonal time-of-flight mass spectrometer, 202
Oscillator strength, 139
Oxidation reaction, 147

P

- Parent ion, 45, 46, 49, 55, 58–60
 Participator Auger decay, 63–65
 Particle-wave duality, 185
 Partition function, 52
 Paschen's law, 156
 Pauli principle, 176, 178, 179
 π electron orbital, 176
 Penning ionization, 85, 138–142
 Permanent dipole, 111–114, 170
 permanent dipole moment, 113, 114
 Permittivity of vacuum, 13
 PESI. *See* Probe electrospray ionization (PESI)
 Phase space, 30, 31, 36–40, 49
 Phosphatidylcholin, 162–164, 166, 167, 213
 Phosphorescence, 176, 180, 181, 188
 Photoabsorption cross section, 81, 139
 Photoacoustics, 187–191
 Photoacoustic spectroscopy, 187–191
 Photochemical activation, 174
 Photochemistry, 139, 175–177, 181, 184, 195
 Photoelectric effect, 155
 Photoelectron, 34, 35, 43, 53, 55, 63–66, 68, 70, 155, 207
 photoelectron emission, 155
 Photoelectron-photoion coincidence spectroscopy (PEPICO), 34, 68
 Photoelectron spectroscopy, 63, 66, 207
 Photoexcitation, 56, 186
 Photoinduced electron transfer, 182, 183
 Photoion(ization), 31, 34, 35, 55–60, 68
 photoionization cross section, 81, 139
 photoionization quantum yield, 81, 82, 85–87, 140
 Photoion-photoion coincidence (PIPICO) spectroscopy, 68
 Photomechanical ablation, 193
 Photon factory, 67
 Photosensitizer, 173, 185
 Piantibonding(π^*), 176
 Pi-bonding(π), 176
 Piezo transducer, 187
 Plume, 147, 173
 Pneumatically-assisted ES, 154
 Point charge, 112, 113
 Point ion emission source, 151
 Poisson's equation, 150, 158
 Polarizability, 11, 13, 19, 21, 73, 112–114, 188
 Polarization dependence, 73
 Polar molecule, 113–114, 170
 Polygonal-line, 56
 Positive adsorption, 155
 Potential crossing, 26
 Potential energy curve, 83, 85, 120, 122
 potential energy curve crossing, 223
 Potential energy surface, 44, 75
 Potential gradient, 76, 155, 157
 Potential surface, 30, 36, 37, 39
 Precession motion, 114, 115
 Predissociation, 58, 85, 140
 Preferential etching, 209
 Pressure equilibrium constant, 136
 Pressure wave, 187, 189, 199, 223
 Pretzel phase, 41, 42
 Primary ion, 60, 131, 151, 199
 Primary particle, 199, 201
 Principle of maximum entropy, 52–53
 Probe electrospray ionization (PESI), 145, 154, 158–166, 168, 169
 PESI-imaging-MS, 163
 Probe ES, 154
 Product ion, 34, 40, 43, 45, 110, 111, 114, 115, 131, 137, 138, 170
 Projectile, 37, 199, 201, 204–206, 209, 213, 217, 222, 223, 225–228
 Proline cluster, 106
 Protic solvent, 133
 Proton acceptor, 128
 Proton affinity, 110, 123–128, 215
 Proton donor, 115, 128
 Proton-sandwich dimer, 134
 Proton transfer reaction, 110, 113–116, 123–125, 129, 131, 214
 Pseudo-crossing, 26
 Pseudo-first order, 137, 180
 Pseudo-second order, 119
- Q**
 QET. *See* Quasi-equilibrium theory(QET)
 QMS. *See* Quadrupole mass spectrometer(QMS)
 Quadrupole ion guide, 202, 204
 Quadrupole mass spectrometer(QMS), 67, 74, 99, 100
 Quantum-confined electron, 184
 Quantum dot, 184–186
 Quantum yield for ionization, 139
 Quasibound orbital, 62, 63
 Quasielectronic state, 223
 Quasi-equilibrium Theory(QET), 32, 36, 49
 Quencher, 181
- R**
 Radiation damage, 200
 Radiationless deactivation, 180, 181, 186–191
 Radiationless process, 180
 Radiationless transition, 32, 49, 58, 179, 181
 Radiative deactivation, 180
 Radiative lifetime, 138, 180
 Radical, 38, 40–44, 46, 47, 51, 129, 169, 170, 181–183, 215, 222
 Radio frequency (RF), 100–102, 106, 204
 Radius of curvature, 146, 149, 152
 Rainbow scattering, 16
 Rarefaction of shockwave, 224, 225
 Rare gas-halide molecule, 140
 Rare gas ion, 114
 Rayleigh limit, 149, 151–154, 158, 167, 204
 Reactant ion(s), 110, 111, 114, 115, 130, 135–138
 Reaction barrier, 37
 Reaction coordinate, 31, 36, 40, 223
 Reaction rate theory, 110
 Reactive quenching, 140
 Recoil momentum, 193

- Recombination energy, 114, 115
Reduced mass, 3, 13, 14, 17, 112, 113
Reduction reaction, 147, 148
Repulsive potential, 11, 77, 85
 repulsive potential energy curve, 85
Resolution, 34, 43, 58, 62, 63, 66, 89, 98–106,
 151, 162, 188, 190, 201, 227
Resonance line, 55, 60
Resonant Auger decay, 63, 68, 71
Resonant core excitation, 65, 71, 72, 77
Resonant electron transfer, 22
Resonant energy transfer process, 114
Resonant vibrational excitation, 227
Retarding grid, 34
Reverse rate constant, 124
RF. *See* Radio frequency (RF)
R-G theory, 187
Rice-Ramsberger-Kassel-Markus (RRKM) theory,
 29, 32, 33, 36–40, 48, 50, 51
Rigid transition state, 39
Ripple formation, 218
Rotational autoionization, 84, 85
Rotational symmetry number, 125
Roughening, 201, 209, 213, 218
Rovibronic state, 114, 138
RRKM. *See* Rice-Ramsberger-Kassel-Markus
 (RRKM) theory
Rydberg state, 56, 63, 67, 83
- S**
Sackur-Tetrode equation, 134
Scaling down, 201, 227
Scaling law, 48–49
Scanning tunneling microscopy (STM), 151, 159
Scattering cross section, 6–11, 16
Schrödinger equation, 175, 185
Secondary electron, 66
Secondary ion mass spectrometry (SIMS),
 123, 124, 151, 199–228
Secondary ion yield, 199–201, 220, 222
Second order reaction, 110, 111, 132
Selection rule, 62
Selective etching, 208, 209, 218
Selective ionization, 115, 214
 σ electron donor base, 125
Self-assembled monolayer, 69, 205, 206
Self-cleaning effect, 207
Self-diffusion, 212
Sensitizer, 181, 182
Shake-off ionization, 65, 70
Shake-up ionization, 65, 70
Shell structure, 132
Shock front, 224, 225, 227
Shockwave propagation, 222, 223, 227, 228
Sigma antibonding(σ^*), 176
Sigma bonding(σ), 176
SIMS. *See* Secondary ion mass spectrometry (SIMS)
Single-bunch operation, 67
Single collisional event, 206
Singlet-singlet transition, 182
Singlet state, 175, 179, 180, 183, 184
Sinusoidal distortion, 101
Site-selective bond breaking, 69–75, 77
Site selectivity, 62, 65, 68–71, 74, 75, 77
Size quantization, 185
 S_N2 reaction, 122
Soft etching, 228
Soft ionization, 67, 137, 169, 185, 200, 206
Solvated ion, 132, 167
Solvation energy, 134
Solvent-free MALDI, 221
Sonic spray, 202
Sonic velocity, 202
Sound velocity, 223, 225
Sound wave, 187
Space-charge field, 157
Space coordinate, 175
Spallation, 192, 193
Spectator Auger decay, 63, 64
Spectroscopic ellipsometry, 216
 sp^2 hybridization, 131
Spin coordinate, 175
Spontaneous ionization, 82
Sputtering, 199, 201, 207, 212, 217, 220, 222,
 223, 226, 227
 sputtering depth, 217
Sputter rate, 201, 227
Sputter yield, 199
SRIG. *See* Stacked ring ion guide (SRIG)
Stacked ring ion guide (SRIG), 101, 102
Stagnation pressure, 201
Standard electrode potential, 148
State density, 31
State-selected ion/molecule reaction, 60
Statistical phase space (PS) theory, 49
Steady-state concentration, 117
Step function, 56, 62, 63
Steric hindrance, 115
Stopping power, 199
Stress confinement, 193
Structural information, 91, 98, 106
Subsurface, 220, 225
Superexcitation, 83, 85
Superexcited state, 83
 superexcited state of first kind, 83
 superexcited state of second kind, 83
Supersonic cluster impact, 223
Supersonic collision, 215, 223–225, 227, 228
Supersonic gas expansion, 201
Supporting electrolyte, 157
Suppression, 145, 154, 155, 157–158, 164, 166
Suppression effect, 145, 154, 157, 164, 166
Surface-active ion
 surface-active agent, 164, 221
 surface activity, 154, 155, 166
Surface charge density, 146, 147, 152, 153
Surface charging, 209
Surface cleaning, 207

- Surface etching ability, 206, 227
Surface roughening, 209, 213, 218
Surface smoothing, 227
Surface tension, 145, 149, 150, 154–156,
159, 167, 204
Surface topology(s), 209, 210, 218
Surprisal, 49–53
Symmetry number, 125
Synchrotron orbit radiation, 140
Synchrotron radiation (SR), 61, 65–67, 73
- T**
Taylor cone, 145, 147, 149–152, 158–160, 167, 168
Taylor cone angle, 159
Td, 98
Temperature constant, 51
Tensile stress, 193
Tetrahedral structure, 127
Thermal activation, 174
Thermal confinement, 192, 194
Thermal diffusivity, 192, 194
Thermalized electron, 120
thermal electron, 120, 121, 130
Thermal lensing, 190
Thermal relaxation time, 194
Thermal velocity, 95, 100
Thermochemical data, 123–136
Thermodynamic(s), 34, 48, 110, 132, 135,
173, 187, 195
Thermoelastic wave, 193, 194
Third-body collision, 118, 120, 132
Third order, 110, 111, 118
third order reaction, 110
Three-body collisional deactivation, 141
Three-center-two-electron bond, 109,
110, 125, 132
Threshold energy, 56, 86
Threshold law, 55–58, 60
Threshold photoelectron-photoion coincidence
(TPEPICO), 34–35, 38–41, 43, 47, 49, 53
threshold photoelectron, 34–35, 43
Tight complex, 116
Tight intermediate complex, 116
Tight transition, 36, 39
Time of flight mass spectrometry (TOF-MS), 67,
100, 201
TOF-MS. *See* Time of flight mass spectrometry
(TOF-MS)
Topological change, 209
Total angular momentum, 37
TPEPICO. *See* Threshold photoelectron-photoion
coincidence (TPEPICO)
Trace analysis, 136–137
Transition moment, 182
Transition probability, 24, 26, 58, 59, 63
Transition state, 33, 36, 37, 39, 40
Translational energy, 37, 118, 132, 181
Translational entropy, 134
Translational freedoms of motion, 134
Travelling wave, 101–102
Travelling wave ion mobility spectrometry system
(TWIMS), 101, 102
Triacylglyceride, 166, 167
Trimolecular reaction, 110, 111
Triplet excimer, 141
Triplet state, 175, 178, 179, 181, 183, 190
Triplet-triplet annihilation, 183–184
Triplet-triplet transition, 182
Tunneling electron emission, 155
Tunneling emission of electron, 155
Tunneling ionization process, 151
TWIMS. *See* Travelling wave ion mobility spectrometry
system (TWIMS)
- U**
Unbound state, 117
Under-cosine angular distribution, 227
Uneven fission process, 152
Unified statistical theory, 40
Unimolecular decomposition, 115
Unimolecular dissociation, 29–53, 131
Unimolecular fragmentation, 111
Unimolecular process, 180
Unimolecular rate constant, 33
Unimolecular reaction, 29, 30, 32, 33
Unoccupied orbital, 63, 64
Unpaired electron, 133, 179
Useful yield, 220–221, 227, 228
UV-visible absorption spectroscopy,
176, 177
- V**
Vacuum electrospray, 200–202
Vacuum level, 169
Vacuum permittivity, 146, 204
Vacuum UV light source, 34
Valence electron, 61, 63–65
Valence excitation, 65, 68, 77
Valence orbital, 63–65
Van der Waals force, 20, 227
Van't Hoff plot, 124, 125
Vibrational autoionization, 84, 85
Vibrational degrees of freedom, 37, 48
Vibrational progression, 59, 62
- W**
Water cluster ion, 222, 223
Work function, 155, 156, 169, 170
- X**
XAFS. *See* X-ray absorption fine structure (XAFS)
XANES. *See* X-ray absorption near-edge structure
(XANES)
XAS. *See* X-ray absorption spectroscopy (XAS)
XESD. *See* X-ray induced electron-stimulated
desorption (XESD)
XFEL. *See* X-ray free electron laser (XFEL)
X-ray absorption edge, 62

X-ray absorption fine structure (XAFS), 63
X-ray absorption near-edge structure (XANES), 63
X-ray absorption spectroscopy (XAS), 62, 63
X-ray fluorescence emission, 63
X-ray free electron laser (XFEL), 78
X-ray induced electron-stimulated desorption (XESD),
71, 72, 78

Y

Young's modulus, 194

Z

Z+1 approximation, 75
Zero kinetic energy, 56, 83
Zero point energy, 83